

**SEARCH FOR DARK MATTER WITH THE ATLAS DETECTOR AND  
DEVELOPMENT OF A TRACK RECONSTRUCTION ALGORITHM FOR  
THE ATLAS INNER TRACKER**

4 by

Minh-Tuan Pham

6 A dissertation submitted in partial fulfillment of  
7 the requirements for the degree of

8 Doctor of Philosophy

(Physics)

10 at the

11 UNIVERSITY OF WISCONSIN-MADISON

12 2025

<sup>13</sup> Date of final oral examination: 07/25/2025

<sup>14</sup> The dissertation is approved by the following members of the Final Oral Committee:

15 Sau Lan Wu, Professor, Physics

16 Sridhara Dasu, Professor, Physics

17 Paolo Calafiura, Doctor, Physics

18 Melinda Soares-Futardo, Professor, Astronomy

19

## **TABLE OF CONTENTS**

	Page
<b>21 List of figures . . . . .</b>	<b>4</b>
<b>22 LIST OF FIGURES . . . . .</b>	<b>4</b>
<b>23 List of tables . . . . .</b>	<b>12</b>
<b>24 LIST OF TABLES . . . . .</b>	<b>12</b>
<b>25 1 Introduction . . . . .</b>	<b>16</b>
<b>26 I Search for dark matter interpreted in a Two-Higgs-Doublet 27 Model with a pseudoscalar mediator using <math>139 \text{ fb}^{-1}</math> of <math>\sqrt{s} = 13</math> 28 TeV proton-proton collision data at the ATLAS detector</b>	<b>19</b>
<b>29 2 Theoretical background . . . . .</b>	<b>20</b>
30     2.1 The Standard Model of Particle Physics . . . . .	20
31     2.2 Electroweak symmetry breaking and the Higgs mechanism . . . . .	21
32     2.3 Standard Model Higgs boson production and decay . . . . .	25
33     2.4 Extension of the Standard Model Higgs sector . . . . .	29
<b>34 3 The ATLAS experiment . . . . .</b>	<b>31</b>
35     3.1 The ATLAS detector . . . . .	31
36         3.1.1 The Inner Detector . . . . .	33
37         3.1.2 The Calorimeter system . . . . .	37
38         3.1.3 The muon spectrometer . . . . .	39
<b>39 4 Combination of dark matter searches interpreted in 2HDM+<math>a</math> . . . . .</b>	<b>41</b>
40     4.1 Theoretical considerations . . . . .	41
41     4.2 Benchmark scenarios . . . . .	45
42         4.2.1 Scenario 1: Exploration of two $m_a - m_A$ planes . . . . .	46
43         4.2.2 Scenario 2: Exploration of two $m_A - \tan\beta$ planes . . . . .	46
44         4.2.3 Scenario 3: Exploration of two $m_a - \tan\beta$ planes . . . . .	47

		Page
45	4.2.4 Scenario 4: Variation of the pseudo-scalar mixing angle $\sin \theta$ . . . . .	47
46	4.2.5 Scenario 5: Variation of the Dark Matter mass $m_\chi$ . . . . .	47
47	4.2.6 Scenario 6: Variation of the $m_a - m_\chi$ . . . . .	48
48	4.3 Data and simulated event samples . . . . .	49
49	4.4 Experimental signatures . . . . .	53
50	4.4.1 $E_T^{\text{miss}} + Z(\ell\ell)$ signature . . . . .	55
51	4.4.2 $E_T^{\text{miss}} + h(b\bar{b})$ signature . . . . .	57
52	4.4.3 $E_T^{\text{miss}} + h(\gamma\gamma)$ signature . . . . .	60
53	4.4.4 $E_T^{\text{miss}} + h(\tau\tau)$ signature . . . . .	61
54	4.4.5 $E_T^{\text{miss}} + tW$ signature . . . . .	62
55	4.4.6 $E_T^{\text{miss}} + j$ signature . . . . .	64
56	4.4.7 $h \rightarrow$ invisible signature . . . . .	65
57	4.4.8 Additional searches using $36 \text{ fb}^{-1}$ of $\sqrt{s} = 13 \text{ TeV}$ $pp$ collision data .	66
58	4.4.9 $tbH^\pm(tb)$ signature . . . . .	67
59	4.4.10 $t\bar{t}t\bar{t}$ signature . . . . .	68
60	4.4.11 Exotic Higgs boson decays $h \rightarrow aa \rightarrow f\bar{f}f'\bar{f}'$ . . . . .	69
61	4.5 Systematic uncertainties . . . . .	71
62	4.6 Statistical combination of results . . . . .	72
63	4.6.1 Statistical analysis . . . . .	72
64	4.6.2 Uncertainties and their correlations . . . . .	74
65	4.6.3 The impact of uncertainties . . . . .	74
66	4.7 Results on combined constraints on the 2HDM+ $a$ . . . . .	75
67	4.7.1 Scenario 1: $m_a - m_A$ planes . . . . .	75
68	4.7.2 Scenario 2: $m_A - \tan \beta$ planes . . . . .	80
69	4.7.3 Scenario 3: $m_a - \tan \beta$ planes . . . . .	82
70	4.7.4 Scenario 4: Variation of $\sin \theta$ . . . . .	83
71	4.7.5 Scenario 5: Variation of $m_\chi$ . . . . .	86
72	4.7.6 Scenario 6: $m_a - m_\chi$ plane . . . . .	88
73	4.8 Conclusion . . . . .	90
74	<b>II Track reconstruction with geometric deep learning using graph neural networks in the ATLAS Inner Tracker</b>	<b>92</b>
76	<b>5 The High Luminosity Large Hadron Collider</b> . . . . .	<b>93</b>
77	<b>6 The ATLAS Inner Tracker</b> . . . . .	<b>96</b>
78	6.1 Overview of the Inner Tracker . . . . .	96
79	6.2 Simulation of the Inner Tracker . . . . .	100

	Page
80            6.2.1    Simulation of the Pixel Detector . . . . .	101
81            6.2.2    Simulation of the Strip Detector . . . . .	103
82        6.3    Particle interaction with detector material . . . . .	104
83            6.3.1    Energy loss of heavy particles . . . . .	105
84            6.3.2    Energy loss of electrons and positrons . . . . .	108
85            6.3.3    Multiple Coulomb scattering . . . . .	111
86        6.4    Simulated samples . . . . .	114
87 <b>7    The ATLAS track reconstruction chain</b> . . . . .	115
88            7.1    Clusterization and space point formation . . . . .	115
89            7.2    The least-square fit . . . . .	120
90            7.3    Iterative track fit . . . . .	123
91            7.4    Combinatorial Kalman Filter . . . . .	125
92            7.5    Computational cost of track reconstruction . . . . .	127
93 <b>8    Track reconstruction with Graph Neural Networks</b> . . . . .	130
94            8.1    Overview . . . . .	131
95            8.2    Target, non-target particles and evaluation metrics . . . . .	132
96            8.3    Graph construction methods . . . . .	136
97            8.3.1    The Module Map Method . . . . .	136
98            8.3.2    The Metric Learning approach . . . . .	140
99            8.4    Result . . . . .	144
100 <b>9    Edge classification</b> . . . . .	148
101            9.1    Introduction to graph neural networks . . . . .	148
102            9.2    The filter network . . . . .	149
103            9.2.1    Method . . . . .	149
104            9.2.2    Results . . . . .	156
105            9.3    The Interaction Network . . . . .	159
106            9.3.1    Methods . . . . .	159
107            9.3.2    Results . . . . .	164
108 <b>10   Graph segmentation</b> . . . . .	173
109            10.1    Connected components . . . . .	173
110            10.2    The Walkthrough algorithm . . . . .	177

	Page
<b>111 11 Track reconstruction performance . . . . .</b>	<b>182</b>
112   11.1 Extraction of track parameters . . . . .	183
113   11.2 Track matching and performance metrics . . . . .	186
114   11.3 Results . . . . .	188
115     11.3.1 Reconstruction performance of the GNN-based algorithm under nom- 116       inal and relaxed track selections . . . . .	191
117     11.3.2 Reconstruction efficiency . . . . .	194
118     11.3.3 Track fake rate . . . . .	198
119     11.3.4 Parameter resolution . . . . .	200
<b>120 12 Computational performance . . . . .</b>	<b>209</b>
121   12.1 An inference pipeline . . . . .	210
122   12.2 Neural Network optimization techniques . . . . .	210
123     12.2.1 Automatic mixed precision (AMP) . . . . .	211
124     12.2.2 Just-In-Time (JIT) compilation . . . . .	212
125   12.3 Optimized performance . . . . .	213
126   12.4 Pipeline computational performance . . . . .	218
127   12.5 Toward computational performance in production environment . . . . .	220
<b>128 13 Conclusion . . . . .</b>	<b>222</b>
<b>129 Bibliography . . . . .</b>	<b>247</b>

## <sup>130</sup> LIST OF FIGURES

Figure	Page
<sup>131</sup> 2.1 Production cross-section of the Standard Model Higgs boson produced by $pp$ <sup>132</sup> collision as a function of $M_H$ at $\sqrt{s} = 13$ TeV . . . . .	<sup>25</sup>
<sup>133</sup> 2.2 Leading-order Higgs boson production mechanisms . . . . .	<sup>27</sup>
<sup>134</sup> 2.3 Leading-order Higgs boson decay mechanisms . . . . .	<sup>28</sup>
<sup>135</sup> 3.1 The ATLAS detectors and its components [31] . . . . .	<sup>32</sup>
<sup>136</sup> 3.2 The ATLAS pixel detector and detector module. Figures taken from reference [33]	<sup>35</sup>
<sup>137</sup> 3.3 Overview of the strip module of the SCT in the barrel layers. Figures taken from <sup>138</sup> reference [37] . . . . .	<sup>36</sup>
<sup>139</sup> 3.4 (a) Layout of the ATLAS calorimetry system, and (b) sketch of a barrel module <sup>140</sup> of the electromagnetic calorimeter [38]. . . . .	<sup>38</sup>
<sup>141</sup> 3.5 (a) Layout of the ATLAS Muon Spectrometer system, and (b) a sideview of one <sup>142</sup> quadrant of the MS [39]. . . . .	<sup>40</sup>
<sup>143</sup> 4.1 Representative production mechanisms and final state of the $E_T^{\text{miss}} + Z(\ell\ell)$ sig- <sup>144</sup> nature, including gluon-gluon fusion resonant (a) and non-resonant production, <sup>145</sup> and (c) $b$ -initiated production. . . . .	<sup>55</sup>
<sup>146</sup> 4.2 Production mechanisms and final state of the $E_T^{\text{miss}} + h(b\bar{b})$ signature includ- <sup>147</sup> ing gluon-gluon fusion resonant (a) and non-resonant production, $b\bar{b}$ -associated <sup>148</sup> production (c) and $b\bar{b}$ -initiated production (d). . . . .	<sup>58</sup>
<sup>149</sup> 4.3 Production mechanisms and final state of the $E_T^{\text{miss}} + tW$ signature. . . . .	<sup>64</sup>
<sup>150</sup> 4.4 Production mechanisms and final state of the $E_T^{\text{miss}} + j$ signature, including gluon- <sup>151</sup> gluon fusion production (a) and $b\bar{b}$ -initiated production (b). . . . .	<sup>64</sup>
<sup>152</sup> 4.5 Production mechanisms and final state of the $tbH^\pm(tb)$ signature. . . . .	<sup>68</sup>

Figure	Page
153 4.6 Production mechanisms and final state of the $t\bar{t}t\bar{t}$ , $E_T^{\text{miss}} + b\bar{b}$ , and $E_T^{\text{miss}} + t\bar{t}$ signatures. . . . .	68
155 4.7 Production mechanisms and final state of the $h \rightarrow aa \rightarrow f\bar{f}f'\bar{f}'$ signature. . . . .	69
156 4.8 Observed and expected exclusion regions at 95% CL over the $(m_a, m_A)$ plane evaluated at 2HDM+ $a$ mixing angles $\sin\theta = 0.35$ (subfigures (a), (c)), and $\sin\theta = 0.7$ (subfigures (b), (d)). The observed and expected contours are respectively shown in solid and dashed lines in all subsequent figures. In (a) and (b), the observed and expected exclusion limits from each of the three statistically combined signatures are shown along with the combined limits. The green and yellow shared bands respectively correspond to the $\pm 1$ and $\pm 2$ standard deviation uncertainty in the combined expected limits. In (c) and (d), the combined exclusion contours are overlaid along those of additional channels not included in the statistical combination. In all subfigures, a dashed grey region indicates the region where the width of any of the Higgs boson exceeds 20% of its mass [40]. . . . .	78
168 4.9 Observed and expected exclusion regions at 95% CL over the $(m_A, \tan\beta)$ plane evaluated at 2HDM+ $a$ mixing angles $\sin\theta = 0.35$ (a), and $\sin\theta = 0.7$ (b). The statistical combined contours are shown along with those from individual searches. In both subfigures, a dashed grey region indicates the region where the width of any of the Higgs boson exceeds 20% of its mass [40]. . . . .	81
173 4.10 Observed and expected exclusion regions at 95% CL over the $(m_a, \tan\beta)$ plane evaluated at 2HDM+ $a$ mixing angles $\sin\theta = 0.35$ (a), and $\sin\theta = 0.7$ (b). The statistical combined contours are shown along with those from individual searches. In both subfigures, a dashed grey region indicates the region where the width of any of the Higgs boson exceeds 20% of its mass [40]. . . . .	82
178 4.11 Observed and expected exclusion limits at 95% CL for the 2HDM+ $a$ as a function of $\sin\theta$ plane evaluated under benchmark scenarios 4. In subfigures (a) and (b), the results are derived at $\tan\beta = 1$ , while in (c) and (d) they are derived at $\tan\beta = 0.5$ or $\tan\beta = 50$ . (a) and (c) represent the sensitivity at low pseudo-scalar mass, in particular $m_A = 600$ GeV and $m_a = 200$ GeV, and (b) and (d) the high-mass regime, namely $m_A = 1.0$ TeV and $m_a = 350$ GeV. The combined exclusion is shown along with individual searches. In all subfigures, a dashed grey region indicates the region where the width of any of the Higgs boson exceeds 20% of its mass [40]. . . . .	84

## Figure

## Page

187	4.12 Observed and expected exclusion limits at 95% CL for the 2HDM+ $a$ as a function 188 of the dark matter particle mass $m_\chi$ evaluated under benchmark scenario 5 189 following $m_A = 1.0$ TeV, $m_a = 400$ GeV, $\tan\beta = 1.0$ , and $\sin\theta = 0.35$ . The 190 limits are expressed in terms of the ratio of the excluded cross-section to the 191 nominal cross-section of the signal model. The results from several individual 192 searches are shown along with the combined limits. The relic density for each 193 $m_\chi$ assumption, calculated with MADDM [105], is superimposed on the plot in 194 dashed line [40]. . . . .	87
195	4.13 Observed and expected exclusion limits at 95% CL for the 2HDM+ $a$ as a function 196 of $m_a$ and $m_\chi$ evaluated under benchmark scenario 6 following $m_A = 1.2$ TeV, 197 $\tan\beta = 1.0$ , and $\sin\theta = 0.35$ . The relic density contour for the case $\Omega_c h^2 = 0.12$ , 198 calculated with MADDM [105], is superimposed on the plot in dashed line. The 199 shaded regions mark the region where the model predicts a relic density greater 200 than the observed value $\Omega_c h^2 = 0.12$ . The island around ( $m_\chi \approx 100$ , $m_a \approx 100$ ) 201 GeV corresponds to the resonant enhancement of the process $\chi\bar{\chi} \rightarrow ah \rightarrow \text{SM}$ 202 that depletes the relic density [40]. . . . .	89
203	5.1 Distribution of pile-up multiplicity ( $\mu$ ) in proton–proton collision at the ATLAS 204 interaction point during Run 2 and the data taking period in 2022 of Run 3. 205 The dashed line represents a rescaled Run 2 distribution such that its integral is 206 the same as that of the Run 3 distribution. $\langle\mu\rangle$ denotes the distribution mean. 207 Figure taken from reference [106]. . . . .	94
208	6.1 A schematic view of the ITk layout (a), and of the pixel detector layout (b), 209 both in one quadrant. Only active elements are visible in both figures. Pixel and 210 strip elements are respectively shown in green and blue. The IP is located at the 211 origin. The horizontal axis is parallel to the beam line, and the vertical axis is 212 the radius measured from the IP [107]. . . . .	97
213	6.2 Overview of the endcap petal (upper) and barrel stave (lower) in the strip detector. 214 Sensor modules shown in blue are mounted directly on a rigid carbon-fiber 215 sandwich structure. Only one half of a stave is shown [108]. . . . .	101
216	6.3 Location of the materials for one quadrant of the ITk layout 03-00-00. The pixel 217 subsystem is shown in green and surrounded by the strip subsystem shown in 218 blue. The location of the materials are indicated by black regions [12]. . . . .	102
219	6.4 An illustration of the GEANT4 geometry model of the outer barrel longeron stave 220 with mounted inclined and flat modules. Figure taken from reference [109]. . . . .	103

Figure	Page
221 6.5 Displays of the GEANT4 geometry model of the strip barrel staves (left) and the 222 endcap petals (right). Figure taken from reference [109]. . . . .	104
223 6.6 The mass stopping power of positive muons in copper as a function of the muon 224 momentum spanning nine orders of magnitude. The solid curves indicate the 225 total stopping power of all dissipative effects. The region of interest in HEP 226 ranges from 100 MeV to 100 GeV, well within the so-called Bethe region, in 227 which the stopping power is strongly dependent on $\beta$ (see text for definition). 228 Figure taken from reference [22]. . . . .	107
229 6.7 Contribution of radiative and collisional components in the total energy loss of 230 electrons in copper as functions of electron energy. At a critical value $E_c = 19.63$ 231 MeV, radiative loss becomes the dominant mechanism. The energy range of 232 electrons in HEP detectors is well within the Bremsstrahlung regime [22]. . . . .	110
233 6.8 Integrated material budget encountered on a particle's path in unit of radiation 234 length as a function of pseudorapidity based on (a) the ITk and (b) the ID. The 235 particle assumes a straight trajectory from the origin. (c) is a comparison between 236 the amount of material that must be traverse before the particle accumulates 237 enough hits to be deemed reconstructible. . . . .	112
238 6.9 Schematic of the calculation of macroscopic mean deflection angle caused by 239 multiple scattering [22]. . . . .	113
240 7.1 Formation of a pixel clusters from multiple cells. The particle deposits its energy 241 in 7 cells, 5 of which receive charges exceeding the detection threshold and enter 242 the clusterization [124]. . . . .	116
243 7.2 The passage of a particle through a pixel sensor segmented in two dimensions. 244 The energy deposit in each sensor cell is measured as a signal when it exceeds a 245 measurement threshold. The true intersection point is estimated from the signal 246 cells grouped together, called a cluster [124]. . . . .	117
247 7.3 A pair of strip sensors are used to reconstruct a 3-dimensional estimate of the 248 particle's true impact point (a). Ambiguity arises when more than one particle 249 hit a strip module, leading to more combinations than particles (b) [124]. . . . .	118
250 7.4 Average number of lone strip clusters per track as a function of the particle 251 pseudorapdity $\eta$ . . . . .	119

Figure	Page
252 7.5 Tracking efficiency (left) and track parameter resolution (right) as functions of 253 the truth particle's pseudorapidity, evaluated at $\langle \mu \rangle = 200$ . The bottom plots 254 show the ratio of the corresponding metric observed in the fast chain to that in 255 the default chain [133]. . . . .	129
256 8.1 The GNN4ITk algorithm consists of three distinct stages. The first stage con- 257 struct a graph from the set of space points in an event, each acting as a node. 258 The second stage identifies edges connecting consecutive nodes on a particle 259 tracks from other edges. The last stage construct track candidates by segment- 260 ing the graph using the output of the second stage. The algorithm's output 261 consists of individual track candidates each as a set of space points believed to 262 belong to the same particle. . . . .	132
263 8.2 Distributions of the production vertex position on the transverse plane (a) and 264 along the $z$ -axis (b) of simulated particles in $t\bar{t}$ -events at $\langle \mu \rangle = 200$ for non- 265 primary and primary particles. Primary vertices are restricted to a small region 266 around the interaction point, whereas non-primary vertices can occur throughout 267 the detector. . . . .	133
268 8.3 Distributions of transverse momentum $p_T$ (a) and pseudorapidity (b) of simulated 269 particles in $t\bar{t}$ -events at $\langle \mu \rangle = 200$ separated according into hard-scattering and 270 pile-up particles. Soft pile-up particles have low $p_T$ , whereas hard-scattering 271 particles have a wider $p_T$ distribution. The former is two orders of magnitude 272 more abundant than the latter. . . . .	135
273 8.4 Principle of the Module Map method for graph construction. On the left, hits 274 from target particles on 9 detector modules in a $t\bar{t}$ event is observed and module 275 connections are recorded. By observing the trajectory of target particles in 90000 276 $t\bar{t}$ events, a list of all pairs of detector modules sequentially traversed by a particle 277 is built. During reconstruction of a new unobserved event on the right, the space 278 points residing on the pairs of modules which appear in the module map are 279 connected by an edge. A set of selections are applied to reduce the number of 280 edges and eliminate outliers. . . . .	137

Figure	Page
281 8.5 Principle of deep metric learning. Starting from (a) labelled data which are 282 difficult to separate in real space, (b) a distance metric is defined to measure 283 the similarity between data points in an embedding space, in this case a simple 284 Euclidean distance. (c) A transformation from real to embedding space is learned, 285 such that examples of the same class are close together, whereas those of different 286 classes are pushed away from each other. (d) The transformation is a simple feed- 287 forward network applied to all instances of the dataset. (e) After training, 288 examples of different classes are well-separated, and clusterizable [147]. . . . .	141
289 8.6 Graph construction efficiency of the Module Map approach as a function of $\eta$ (up- 290 per) and $p_T$ (lower), using the MinMax selection (left) and MeanRMS selection 291 (right). . . . .	145
292 8.7 Graph construction efficiency of the Metric learning approach as a function of $\eta$ 293 (a) and $p_T$ (b), averaged over 1000 $t\bar{t}$ events. . . . .	146
294 9.1 GRAPH SAGE sampling and aggregation mechanism. [153] . . . . .	151
295 9.2 Edge efficiency of the Filter network on graphs constructed by the Metric Learn- 296 ing method as a function of $\eta$ (a) and $p_T$ (b). . . . .	157
297 9.3 Edge efficiency (a) and purity (b) of the Filter network on graphs constructed by 298 the Metric Learning method as functions of the $(z, r)$ -coordinates of the inner hit. 168	
299 9.4 The number of space points per $(z, r)$ -bin averaged over 50 $t\bar{t}$ events. The bin- 300 width is 15 mm in both $z$ - and $r$ -direction. . . . .	169
301 9.5 Edge efficiency of the INTERACTION GNN as a function of $\eta$ (left) and $p_T$ (right), 302 evaluated on graphs created using the Module Map method with MeanRMS 303 (upper) and MinMax selections (lower). . . . .	170
304 9.6 Edge efficiency of the INTERACTION GNN on graphs constructed by the <b>Module</b> 305 <b>Map MeanRMS</b> as a function of the $(z, r)$ -coordinates of the inner hit. . . . .	171
306 9.7 Edge purity of the INTERACTION GNN on graphs constructed by the <b>Module</b> 307 <b>Map MeanRMS</b> as a function of the $(z, r)$ -coordinates of the inner hit. . . . .	172
308 10.1 A distribution of the GNN edge classification scores. 200 graphs constructed 309 using the Metric Learning approach are used. . . . .	174

Figure	Page
--------	------

310    10.2 Illustration of the Connected Component method. (a) The input graph contains 311    two particle tracks and a single hits, all color-coded. The three objects are 312    merged by two fake edges in red. (b) Edges whose score falls under a threshold 313    is eliminated. (c) The remaining connected components are considered as track 314    candidates. . . . .	176
315    10.3 Different scenarios encountered by the Walkthrough algorithm. (a) A starting 316    node as a single outgoing edge. (b) The starting node has several outgoing edges 317 $\{e_{12}, e_{13}, e_{14}\}$ . Edge $e_{12}$ has the highest score, and neither lower-score edges 318    exceed the minimum score $s_{add}$ to create an alternative path. Only edge $e_{12}$ 319    is admitted. (c) The starting node has several outgoing edges $\{e_{12}, e_{13}, e_{14}\}$ , in 320    which $e_{12}$ and $e_{13}$ exceed $s_{add}$ . Two candidate paths stemming from the junction 321    are considered, the longer of which is admitted. . . . .	180
322    10.4 An ambiguity occurs when two candidate paths have equal lengths. The path 323    stemming from the higher edge score at the junction is selected. . . . .	181
324    11.1 A track represented in two different parametrizations, both being particular in- 325    stances of the general ATLAS parametrization in equation (11.1). The perigee 326    parametrization (left) is defined with respect to the global $z$ -axis, while the planar 327    parametrization (right) is defined with respect to the coordinate axes of a 328    local measuring surface [160]. . . . .	184
329    11.2 A comparison of the GNN-based track candidates selected by the nominal and 330    the relaxed criteria in representative performance metrics. Top plots show the 331    efficiency as functions of the truth pseudorapidity $\eta$ (a) and transverse momen- 332    tum $p_T$ (b). Bottom plots show the rate of fake tracks as functions of $\eta$ (c) and 333    the pile-up level $\mu$ (d). . . . .	192
334    11.3 Tracking efficiency as functions of the truth pseudorapidity $\eta$ (a) and transverse 335    momentum $p_T$ (b). The bottom plots show the ratio of the GNN-based curves 336    to the CKF-based curve. . . . .	195
337    11.4 Tracking efficiency as a function of the pile-up level $\langle \mu \rangle$ . The bottom plots show 338    the ratio of the GNN-based curves to the CKF-based curve. . . . .	197
339    11.5 The proportion of reconstructed tracks reconstructed by the GNN4ITk and CKF 340    chains having matching probability less than 0.5 as a function of the track pseu- 341    dorapidity $\eta$ (a) and the truth pile-up (b). The bottom plots show the ratio of 342    the GNN-based curves to the CKF-based curve. . . . .	199

Figure	Page
343 11.6 Transverse (a) and longitudinal (b) impact parameter resolution shown as histograms of $\sigma(d_0)$ and $\sigma(z_0)$ respectively. Note that the resolution of parameter 344 $x$ is inversely proportional to $\sigma(x)$ . . . . .	201
346 11.7 The number of hits from the inner most pixel layer as a function of reconstructed 347 pseudorapidity $\eta$ . . . . .	202
348 11.8 Transverse impact parameter resolution $\sigma(d_0)$ of as a function of truth $\eta$ , evaluated 349 on tracks reconstructed by the GNN4ITk and the CKF chains. The bottom 350 plots show the ratio of the GNN-based curves to the CKF-based curve. . . . .	202
351 11.9 Longitudinal impact parameter resolution $\sigma(z_0)$ of as a function of truth $\eta$ , evaluated 352 on tracks reconstructed by the GNN4ITk and the CKF chains. The bottom 353 plots show the ratio of the GNN-based curves to the CKF-based curve. . . . .	203
354 11.10 Transverse momentum resolution shown as a histogram of $\sigma(p_T)$ (a) and a function 355 of the truth pseudorapidity $\eta$ (b). . . . .	205
356 11.11 Hit content of selected track candidates, demonstrated by the average number 357 pixel clusters (a), pixel holes (b), strip clusters (c) and strip holes (d). These 358 quantities are shown as functions of the reconstructed pseudorapidity $\eta$ . . . . .	207
359 12.1 Computational efficiency of the INTERACTIONGNN in terms of the execution 360 time (left vertical axis) and peak memory (right vertical axis), measured using 361 the baseline configuration, and configuration optimized with automated mixed 362 precision (AMP), Just-In-time computation (JIT), and a combination of the two 363 techniques. All measurements use graphs constructed with the Module Map 364 MinMax method. . . . .	214
365 12.2 GPU time of the INTERACTIONGNN as a function of the number of space points 366 in a $t\bar{t}$ event (a) and as a histogram (b), measured using the baseline configura- 367 tion, and configurations optimized with automated mixed precision (AMP), 368 JIT compilation, and a combination of both techniques. Each dashed line in 369 (a) displays the best-fit second-order polynomial to the corresponding config- 370 uration. The fitted coefficients are exhibited in table 12.2. All measurements 371 are performed on an NVIDIA-A100 GPU with 80 GB of memory, using graphs 372 constructed with the Module Map MeanRMS method. . . . .	216

## 373 LIST OF TABLES

	Table	Page
374    2.1   Standard Model Higgs boson decay branching ratios and uncertainty at $M_H =$		
375    125.09 GeV . . . . .		28
376    4.1   Summary of the parameter settings for the different 2HDM+ $a$ benchmark sce-		
377    narios explored in this summary. . . . .		50
378    4.2   Details of the MADGRAPH5_AMC@NLO generation set-up used for the 2HDM+ $a$ sig-		
379    nals, for the signatures considered in this publication. The Pseudoscalar_2HDM		
380    UFO model is used for all simulated samples except those for the $tbH^\pm(tb)$		
381    search, which relies on the UFO of reference [51]. The $h \rightarrow$ invisible and		
382 $h \rightarrow aa \rightarrow f\bar{f}f'\bar{f}'$ signatures are not listed here as no signal samples are re-		
383    quired for the re-interpretation, which in those cases relies on the branching		
384    ratio limits [40]. . . . .		51
385    4.3   Summary of input analyses used in the different benchmark scenarios [40]. . . .		54
386    4.4   Selection criteria used to defined resolved and merged signal regions for the		
387 $E_T^{\text{miss}} + h(b\bar{b})$ signature [13]. . . . .		59
388    4.5   Selection criteria used to define low- and high- $m_R$ signal regions for the $E_T^{\text{miss}} +$		
389 $h(\tau\tau)$ signature [63]. . . . .		63
390    4.6   Impact from different sources of uncertainties on the best-fit signal strength ex-		
391    press in $\Delta\mu$ on the signal at ( $m_A = 800$ GeV, $m_a = 450$ GeV, $\tan\beta = 1$ , $\sin\theta =$		
392    0.35), estimated by fixing the corresponding NPs to their best-fit values, and		
393    subtracting the resulting uncertainty from the total uncertainty in quadrature.		
394    The statistical uncertainty component is obtained by fixing all NPs except the		
395    floating background normalization factors, and quantifies the impact of the limit		
396    data yields in the signal and control regions. The total uncertainty is not the		
397    quadratic sum of the individual contribution due to correlations between systematic		
398    uncertainties [40]. . . . .		76

Table	Page
399 5.1 The integrated luminosity delivered to the ATLAS detector by the LHC as of 400 September 2, 2024. . . . .	93
401 6.1 Representative parameters of the pixel flat barrel and inclined rings in the ITk 402 layout 03-00-00. Note that while all pixel layers have rings, only the OB features 403 inclined rings. The fifth column provides the number of flat sensors mounted on 404 a complete stave in the central barrel of each layer. The number of inclined rings 405 is given by $2 \times$ the number of rings on each of the barrel [107]. . . . .	99
406 6.2 Representative parameters of the pixel endcaps in the ITk layout 03-00-00. The 407 radius in the second column refers to the radius of the circle formed by the 408 innermost point of the sensors on each ring. The number of rings is twice the 409 number of rings on each of the barrel [107]. . . . .	100
410 6.3 Characterization of the strip barrel, including the number of staves, radius, tilt 411 angle, and strip length in the ITk layout 03-00-00 [107]. . . . .	102
412 7.1 The CPU required in $\text{HS06} \times \text{seconds}$ to reconstruct a Run 2 data event using the 413 corresponding software release at average pile-up 90 using. The total reconstruc- 414 tion time is broken down into inner tracking, Calorimeter and Muon Spectrometer 415 reconstruction, and Monitoring. Numerical figures taken from reference [132]. . .	127
416 7.2 The CPU required in $\text{HS06} \times \text{seconds}$ to reconstruct a $t\bar{t}$ MC event with $\langle \mu \rangle = 140$ 417 and 200 in the ITk. The total track reconstruction time, evaluated for both the 418 default and an optimized CKF-based chains, is broken down into individual steps, 419 most significant of which are clustering, space point formation, CKF-based track 420 finding and ambiguity resolution. An Intel Xeon E5-2620v2 processor with 2.1 421 GHz and six physical cores per CPU was used. The CPU time is multiplied by 422 an HS06 factor of 17.8 for single-thread running. Numerical figures taken from 423 reference [133]. . . . .	128
424 8.1 Input features into the Metric Learning model include the global coordinates 425 of the reconstructed space point $(r, \phi, z)$ and features describing the number 426 of cells, the total charge deposit in the clusters from which the space point is 427 reconstructed. A pixel space point is formed from a single cluster, and a strip 428 space point from two clusters. The subscript $i \in \{1, 2\}$ of the cluster features 429 denote the cluster index. The cluster shape is a vector pointing from the cell 430 where the particle enters the detector element to one where it exits. To preserve 431 the same input vector shape, pixel cluster features of are duplicated at each node.	143

Table	Page
432 8.2 Hyperparameters used to train the Metric Learning model. . . . .	144
433 9.1 Hyperparameters used to train the Filter network. . . . .	156
434 9.2 Comparison of the three graph construction methods: Module Map MINMAX, 435 Module Map MEANRMS and Metric Learning. The constructed graphs become 436 input to the INTERACTIONGNN. . . . .	158
437 9.3 Edge-level input features to the INTERACTIONGNN. The subscripts $i$ and $j$ 438 respectively denote the source and destination nodes connected by an edge. . . .	160
439 9.4 Hyperparameters used to train the INTERACTIONGNN. . . . .	163
440 9.5 Performance of the GNN4ITk algorithm after the across three graph construction 441 methods. Edges are classified using the INTERACTIONGNN with a threshold of 442 0.5 on the classification score. The edge efficiency is cumulative throughout the 443 pipeline. The number of edges is the size of the remaining edge set after the 444 score cut. . . . .	166
445 10.1 Edge efficiency and fake reduction rate at representative values of GNN edge 446 score cut. . . . .	175
447 11.1 Nominal track selection criteria featured in reference [107]. . . . .	189
448 11.2 Relaxed selections adapted to GNN-based tracks. Modified criteria with respect 449 to those in table 11.1 are highlighted in boldface. The rest is identical to reference 450 [107]. . . . .	190
451 11.3 The total number of reconstructed tracks by the GNN4ITk and the CKF chains 452 having matching probability less than 0.5 over 1000 $t\bar{t}$ events. . . . .	193
453 11.4 Minimally modified selections adapted to GNN-based tracks. Modified criteria 454 with respect to those in table 11.1 are highlighted in boldface. The rest is identical 455 to reference [107]. . . . .	194
456 12.1 Latency improvement over eager computation at full precision of each optimiza- 457 tion, measured using the baseline configuration, and configurations optimized 458 with automated mixed precision (AMP), JIT compilation, and a combination 459 of both techniques. All measurements use graphs constructed with the Module 460 Map MeanRMS method. . . . .	215

Table	Page
461 12.2 The coefficients of a second-order polynomial fit to the GPU time shown in 462 figure 12.2 for each optimization technique. The GPU time $t$ in units of seconds 463 is assumed to depend on $x = \frac{ V }{10^6}$ , where $V$ is the set of nodes, as $t = Ax^2 + Bx + C$ . . . . .	217
464 12.3 Per-event run time of each stage in the GNN4ITk algorithm. The latency of graph 465 construction and edge classification is evaluated on an NVIDIA-A100 GPU with 466 80GB of memory, and of graph segmentation on the AMD EPYC 7763 CPU, 467 using graphs constructed with the Module Map MeanRMS method. . . . .	219

<sup>468</sup> **Chapter 1**

<sup>469</sup> **Introduction**

<sup>470</sup> This thesis is organized into two parts. The first part describes a statistical combination  
<sup>471</sup> of three most sensitive dark matter searches and a summary of other analyses interpreted  
<sup>472</sup> in the Two-Higgs-Doublet Model extended by a pseudoscalar mediator (2HDM+ $a$ ) using  
<sup>473</sup>  $139 \text{ fb}^{-1}$  of proton-proton collision data at center-of-mass energy  $\sqrt{s} = 13 \text{ TeV}$  collected by  
<sup>474</sup> the ATLAS detector during Run 3 of the Large Hadron Collider. The second reports the  
<sup>475</sup> development of an algorithm for charged-particle track reconstruction using Graph Neural  
<sup>476</sup> Networks (GNNs) for the ATLAS Inner Tracker (ITk), commissioned for the High Luminosity  
<sup>477</sup> phase of the Large Hadron Collider (HL-LHC). A brief introduction and motivation of each  
<sup>478</sup> part is provided in this chapter.

<sup>479</sup> The existence of Dark Matter (DM) enjoys well-established acceptance among particle  
<sup>480</sup> physicists and cosmologists, supported by a wealth of evidence from astrophysical observa-  
<sup>481</sup> tions [1, 2, 3, 4, 5, 6, 7, 8]. Although DM accounts for an estimated 85% of the mass in the  
<sup>482</sup> universe, no known particle candidate in the Standard Model can explain it. Thus, an expla-  
<sup>483</sup> nation of its nature is a central focus of the physics programme in the collider experiments  
<sup>484</sup> such as ATLAS and CMS [9]. Among the proposed hypotheses, Weakly-Interacting Massive  
<sup>485</sup> Particles [10] (WIMPs)  $\chi$  gain much interest for experimental detection of DM, which typi-  
<sup>486</sup> cally targets the associated production of a visible mediator decaying to stable particles and

<sup>487</sup> a large missing transverse momentum with magnitude  $E_T^{\text{miss}}$ . The result of these indirect  
<sup>488</sup> searches is usually interpreted in the context of a simplified model that involves a fermionic  
<sup>489</sup> DM particle connected to the visible sector via a vector, axial-vector, scalar, or pseudo-scalar  
<sup>490</sup> mediator  $a$ . It contains a minimal set of free parameters, including the masses and coupling  
<sup>491</sup> strength of the DM and mediator particles.

<sup>492</sup> The Two-Higgs-Doublet Model [11] (2HDM) plus a pseudo-scalar mediator  $a$  is the sim-  
<sup>493</sup> plest gauge-invariant and renormalizable extension of the simplified pseudo-scalar DM model,  
<sup>494</sup> offering a rich phenomenology and a more complete benchmark. It is identified by the LHC  
<sup>495</sup> Dark Matter Working Group along with a set of recommended scans to explore its parame-  
<sup>496</sup> ter space through LHC searches [12]. A variety of analyses using  $137 \text{ fb}^{-1}$  of proton-proton  
<sup>497</sup> collision data collected at the center-of-mass energy up to 13 TeV by the ATLAS detector  
<sup>498</sup> and targetting diverse visible signatures provide constraints on the 2HDM+ $a$ . The first  
<sup>499</sup> part of this thesis presents a statistical combination of the three most sensitive analyses and  
<sup>500</sup> a summary of the remaining searches. The statistical combination considers  $E_T^{\text{miss}} + X$ -type  
<sup>501</sup> signatures where  $X$  is either a SM Higgs boson decaying into a pair of  $b$ -quarks [13] or a  
<sup>502</sup>  $Z$ -boson decaying into a pair of leptons [14], and a search for associated production of a top  
<sup>503</sup> and a bottom quark with a charged Higgs boson decaying into a top and a bottom quark [15].  
<sup>504</sup> The result from searches targeting signatures are summarized in the result.

<sup>505</sup> These searches for DM leave a sizeable part of the parameter space unexcluded and  
<sup>506</sup> await more data to derive better constraints on the 2HDM+ $a$ . In general, searches for  
<sup>507</sup> exotic phenomena at the LHC are often statistically limited, motivating a substantial boost  
<sup>508</sup> in the rate of data collection. The HL-HLC will help satisfy the demand for data with  
<sup>509</sup> up to 3-fold increase in instantaneous luminosity  $\mathcal{L}$ , reaching  $7.5 \times 10^{34} \text{ cm}^{-2}\text{s}^{-1}$  [16]. The  
<sup>510</sup> integrated luminosity delivered to each of the general-purpose detectors will total  $4000\text{fb}^{-1}$   
<sup>511</sup> at the end of Run 5,  $\sim 10$  times the amount of data collected during the nominal LHC runs.  
<sup>512</sup> This upgrade will bring unprecedented opportunities for physics discovery and precision

513 measurements, and at the same time many challenges to all aspects of data processing, from  
514 simulation to reconstruction.

515 In particular, the elevated luminosity leads to an increased number of proton-proton  
516 interactions in a bunch crossing. As a result, events characterized by a large momentum  
517 transfer and often producing interesting physics, or hard scatters, are more likely to occur,  
518 they are accompanied by a larger background of soft inelastic collisions, or pile-up. The  
519 expected pile-up  $\langle \mu \rangle$  will increase from  $\sim 50$  in Run 3 to 140 at the end of Run 4, peaking at  
520 200 in Run 5, and with it a steep increase in event complexity as well as the necessary CPU  
521 resources to for event reconstruction. The computing budget dedicated to reconstruction  
522 is typically dominated by inner tracking, which is why both many LHC experiments are  
523 investigating methods based on modern hardware accelerators (GPUs, FPGAs) as a poten-  
524 tial solution to this problem. In this direction, a tracking algorithm centered on GNNs is  
525 identified as a promising approach whose development and evaluation are reported in the  
526 second part of this thesis.

527

# Part I

528

Search for dark matter interpreted in

529

a Two-Higgs-Doublet Model with a

530

pseudoscalar mediator using  $139 \text{ fb}^{-1}$  of

531

$\sqrt{s} = 13 \text{ TeV}$  proton-proton collision

532

data at the ATLAS detector

<sup>533</sup> **Chapter 2**

<sup>534</sup> **Theoretical background**

<sup>535</sup> This chapter presents an overview of the Standard Model [17, 18] (SM) of Particle Physics  
<sup>536</sup> which describes the particle nature of visible matter in the universe and unifies the elec-  
<sup>537</sup> tromagnetic, weak and strong interactions. Since a complete account of this monumental  
<sup>538</sup> achievement far exceeds the scope of this document, only aspects of the theory most relevant  
<sup>539</sup> to the rest of the thesis will be introduced. Interested readers are invited to peruse classic  
<sup>540</sup> texts on the subject for further details [19, 20, 21]. We describe at the end some of the SM's  
<sup>541</sup> limitations, which motivate the exploration of the extended Higgs sector, part of what is  
<sup>542</sup> known as Beyond Standard Model (BSM) physics.

<sup>543</sup> **2.1 The Standard Model of Particle Physics**

<sup>544</sup> Elementary particles in the SM are typically grouped by their spin. There are three  
<sup>545</sup> generations of spin- $\frac{1}{2}$  particles called fermions, several spin-1 gauge bosons which mediate  
<sup>546</sup> their interaction, and a spin-0 Higgs boson to account for other particles' mass. Two types of  
<sup>547</sup> fermions exist; the first is the leptons, which include the electron ( $e$ ), the muon ( $\mu$ ) and the  
<sup>548</sup> tau lepton ( $\tau$ ), and their associated neutrinos, denoted  $(\nu_e, \nu_\mu, \nu_\tau)$ . The second type consist  
<sup>549</sup> of three generations of quarks, each consisting of a pair, namely up ( $u$ ) and down ( $d$ ), charm  
<sup>550</sup> ( $c$ ) and strange (also sideways) ( $s$ ), and top ( $t$ ) and bottom ( $b$ ).

With the exception of neutrinos, all SM fermions carry an electric charge and couple to the *electromagnetic* field via the photon. Leptons carry integer charge  $\pm 1$ , while quarks carry fractional charges  $\mp \frac{1}{3}e$  and  $\mp \frac{2}{3}e$ .

Unlike leptons, quarks also carry  $SU(3)$  color charge and couple to the gluon field, just like electrically charged particles coupling to the electromagnetic field. The spin-1 gluon also carries color charges and mediate the strong force between quarks and other gluons. It is due to the strong interaction that quarks always appear in bound states of a pair or a triplet called hadron, of which the proton and the neutron are examples, despite having same-sign electric charges. The color charge of bound quarks in hadrons cancel each other, so hadrons are color-neutral.

All fermions participate in the weak interaction mediated by the  $W^\pm$  and the  $Z$  bosons and responsible for decays of the muon and the tau lepton to the electron, and of quarks to lighter quarks, the most well-known example of which in nuclear physics is  $\beta$  decay, and the top quark decaying to the bottom quark in particle physics. Unlike the photon and the gluon, the weak vector bosons are massive particles, whose mass is generated by their interaction to the Higgs field whose quantized particle is the Higgs boson. The discovery of the Higgs boson in 2012 completed the Standard Model and affirmed its internal consistency.

## 2.2 Electroweak symmetry breaking and the Higgs mechanism

In the standard model, the left-handed leptons transform as an  $SU(2)$  doublet, and the right-handed leptons transform as an  $SU(2)$  singlet. Their Lagrangian must be invariant under the corresponding generic transformation

$$E_L \rightarrow e^{\frac{i}{2}(\alpha^a(x)\sigma^a + \beta(x))} E_L, \quad E_R \rightarrow e^{i\beta(x)/2} E_R, \quad (2.1)$$

where  $\alpha^a(x)$  and  $\beta(x)$  are arbitrary differentiable functions, and  $\sigma^a$  the Pauli matrices. To account for lepton masses, a scalar field invariant under local  $SU(2) \otimes U(1)$  transformation

<sup>574</sup> is introduced

$$\phi = \begin{pmatrix} \phi^+ \\ \phi^- \end{pmatrix}, \quad \phi \rightarrow e^{\frac{i}{2}(\alpha^a(x)\sigma^a + \beta(x))} \phi, \quad (2.2)$$

<sup>575</sup> from which its covariant derivative follows

$$D_\mu = \partial_\mu - i\frac{g_2}{2}W_\mu^a\sigma^a - i\frac{g_1}{2}B_\mu, \quad (2.3)$$

<sup>576</sup> where  $A_\mu^a$  and  $B_\mu$  are the  $SU(2)$  and  $U(1)$  gauge bosons. The most general Lagrangian for  
<sup>577</sup> a renormalizable scalar field respecting these symmetries can be written as

$$\mathcal{L}_{\text{Higgs}} = |D_\mu|^2 + \mu^2\phi^\dagger\phi - \frac{\lambda}{2}(\phi^\dagger\phi)^2. \quad (2.4)$$

<sup>578</sup> The configuration which minimizes the Higgs potential, assuming  $\mu^2 > 0$ , is such that

$$\phi^\dagger\phi = \frac{\mu^2}{\lambda} = v^2. \quad (2.5)$$

<sup>579</sup> The number  $v$  is known as the vacuum expectation value (VEV) of the Higgs field. Selecting  
<sup>580</sup> the simplest configuration, and adding a fluctuation field around the minimum, we get

$$\langle\phi\rangle = \frac{1}{\sqrt{2}} \begin{pmatrix} 0 \\ v \end{pmatrix}, \quad \phi = \frac{1}{\sqrt{2}} \begin{pmatrix} 0 \\ v + H(x) \end{pmatrix}, \quad (2.6)$$

<sup>581</sup> and evaluating the kinetic term in (2.4), we obtain terms suggestive of the mass eigenstates  
<sup>582</sup> of the electroweak bosons

$$|D_\mu\phi|^2 = \frac{1}{2}(\partial_\mu H)^2 + \frac{g_2^2}{8}(v + H)^2|W_\mu^1 + iW_\mu^2|^2 + \frac{1}{8}(v + H)^2|g_2W_\mu^3 - g_1B_\mu|^2. \quad (2.7)$$

<sup>583</sup> By defining the mass eigenstates as

$$W_\mu^\pm = \frac{1}{\sqrt{2}}(W_\mu^1 \mp iW_\mu^2), \quad Z_\mu = \frac{g_2W_\mu^3 - g_1B_\mu}{\sqrt{g_1^2 + g_2^2}}, \quad A_\mu = \frac{g_2W_\mu^3 + g_1B_\mu}{\sqrt{g_1^2 + g_2^2}} \quad (2.8)$$

<sup>584</sup> and the corresponding masses as

$$M_W = \frac{g_2 v}{2}, \quad M_Z = \frac{v\sqrt{g_1^2 + g_2^2}}{2}, \quad m_A = 0 \quad (2.9)$$

585 and writing (2.7) as

$$|D_\mu \phi|^2 = \frac{1}{2}(\partial_\mu H)^2 + M_W^2 \left(1 + \frac{H}{v}\right)^2 W_\mu^+ W^{\mu-} + \frac{M_Z^2}{2} \left(1 + \frac{H}{v}\right)^2 Z_\mu Z^\mu + \frac{M_A^2}{2} A_\mu A^\mu, \quad (2.10)$$

586 we “create” mass for the vector bosons, while maintaining a massless photon. It is convenient  
587 to introduce the electroweak mixing angle  $\theta_W$  such that

$$\tan \theta_W = \frac{g_1}{g_2} \Rightarrow \cos \theta_W = \frac{m_W}{m_Z}, \quad (2.11)$$

588 and that

$$\begin{pmatrix} Z_\mu \\ A_\mu \end{pmatrix} = \begin{bmatrix} \cos \theta_W & -\sin \theta_W \\ \sin \theta_W & \cos \theta_W \end{bmatrix} \begin{pmatrix} W_\mu^3 \\ B_\mu \end{pmatrix}. \quad (2.12)$$

We can rewrite the covariant derivative in (2.4) using the mass eigenstates

$$D_\mu = \partial_\mu - i \frac{g_2}{2} W_\mu^a \sigma^a - i \frac{g_1}{2} B_\mu \quad (2.13)$$

$$= \partial_\mu - \frac{ig_2}{\sqrt{2}} (W_\mu^+ T^+ + W_\mu^- T^-) - i \frac{1}{\sqrt{g_1^2 + g_2^2}} Z_\mu (g_2^2 T^3 - g_1^2 Y) \quad (2.14)$$

$$- i \frac{g_1 g_2}{\sqrt{g_1^2 + g_2^2}} A_\mu (T^3 + Y) \quad (2.15)$$

589 where  $T^a = \sigma^a/2$ ,  $T^\pm = (T^1 \pm iT^2)$ ,  $Y$  a general  $U(1)$  charge. Defining the coefficient  
590 of the electromagnetic interaction  $e = \frac{g_1 g_2}{\sqrt{g_1^2 + g_2^2}}$ , and the electric charge quantum number  
591  $Q = T^3 + Y$ , we retrieve a covariant derivative where the couplings of all electroweak bosons  
592 can be described by the familiar electric charge and the mixing angle

$$D_\mu = \partial_\mu - \frac{ig_2}{\sqrt{2}} (W_\mu^+ T^+ + W_\mu^- T^-) - \frac{ig_2}{\cos \theta_W} (T^3 - \sin \theta_W Q^2) - ie A_\mu Q \quad (2.16)$$

593 By spontaneously breaking the symmetry  $SU(2)_L \times U(1)_Y \rightarrow U(1)_Q$ , three Goldstone bosons  
594 (three degrees of freedom) are absorbed by the  $W^\pm$  and  $Z$  boson, making them massive. The  
595 remaining  $U(1)_Q$  symmetry is unbroken, so its generator, the photon, remains massless.

596 Fermion mass is generated by treating the same scalar field  $\phi$  and its isodoublet  $\tilde{\phi} =$   
597  $i\sigma^2\phi*$ . Take for example the first generation of fermion, introduce the  $SU(2)_L \times U(1)_Y$   
598 invariant Yukawa Lagrangian

$$\mathcal{L}_F = -\lambda_e \bar{L} \phi e_R - \lambda_d \bar{Q} \phi d_R - \lambda_u \bar{Q} \tilde{\phi} u_R + h.c., \quad (2.17)$$

<sup>599</sup> and repeat the same procedure, we get

$$\mathcal{L}_F = -\frac{1}{\sqrt{2}}\lambda_e(v + H)\bar{e}_L e_R + \dots, \quad (2.18)$$

<sup>600</sup> and the fermion mass

$$m_f = \frac{\lambda_f v}{\sqrt{2}} \quad (2.19)$$

<sup>601</sup> After symmetry breaking, the Higgs Lagrangian can be written as

$$\mathcal{L}_H = \frac{1}{2}(\partial_\mu H)^2 - \lambda v^2 H^2 - \lambda v H^2 - \frac{\lambda}{4}H^4, \quad (2.20)$$

<sup>602</sup> from which the Higgs boson mass reads

$$M_H^2 = 2\lambda v^2 = -2\mu^2. \quad (2.21)$$

<sup>603</sup> The triple and quartic terms give rise to the Higgs self-interaction vertices with coupling

<sup>604</sup> strength given in terms of its mass and VEV by

$$g_{HHH} = \frac{3M_H^2}{v}, \quad g_{HHHH} = \frac{3M_H^2}{v^2}. \quad (2.22)$$

<sup>605</sup> The Higgs coupling to gauge bosons can easily be read from terms in (2.10) following

<sup>606</sup>  $M_V(1 + \frac{H}{v})^2$ , and hence,

$$g_{HV} = \frac{2M_V^2}{v}, \quad g_{HHV} = \frac{2M_V^2}{v^2}. \quad (2.23)$$

<sup>607</sup> Similarly, the Higgs coupling to fermion is proportional to the fermion mass

$$g_{Hff} = \frac{m_f}{v} \quad (2.24)$$

<sup>608</sup> In addition, the vacuum expectation value  $v$  is fixed in terms of the Fermi constant  $G_F$ ,

<sup>609</sup> experimentally determined from muon decay

$$M_W = \frac{g_2 v}{2} = \left( \frac{\sqrt{2}g_2^2}{8G_F} \right)^{1/2} \Rightarrow v = \sqrt{\frac{1}{\sqrt{2}G_F}} \approx 246 \text{ GeV}. \quad (2.25)$$

### 610 2.3 Standard Model Higgs boson production and decay

611 From the Higgs coupling structure derived from 2.2, we can examine the main production  
 612 mechanisms of the Higgs boson in  $pp$  collision at the LHC. Figure 2.1a shows the production  
 613 cross sections of the SM Higgs boson during  $pp$  collision at center-of-mass energy  $\sqrt{s} = 13$   
 614 TeV as a function of the Higgs mass. The most important production mechanisms include  
 615 gluon-gluon fusion ( $ggF$ ), vector boson fusion ( $qqH$ ), associated production with a vector  
 616 boson  $VH$ , ( $V = W, Z$ ), associated production with a pair of top (bottom) quarks  $t\bar{t}H$  ( $b\bar{b}H$ ),  
 617 and associated production with a single top quark ( $tH$ ).

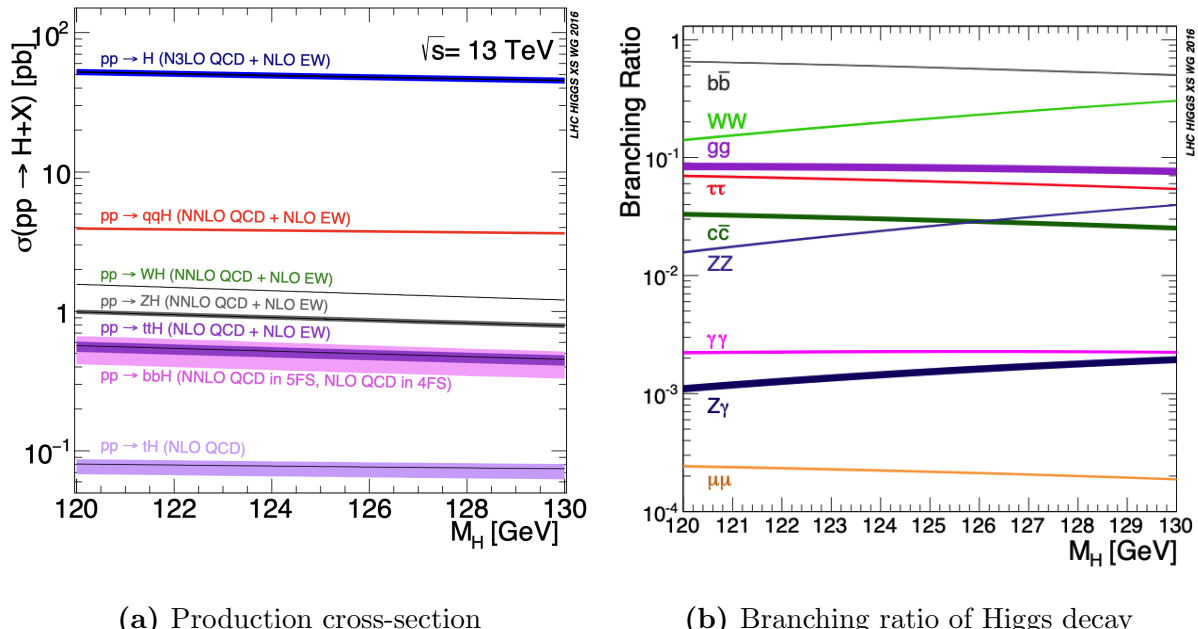


**Figure 2.1:** Production cross-section of the Standard Model Higgs boson produced by  $pp$  collision as a function of  $M_H$  at  $\sqrt{s} = 13$  TeV

618 The most dominant production mechanism is gluon-gluon fusion, whose cross-section  
 619 far exceeds those of other mechanism. The Feynman diagram for this process is shown in  
 620 figure 2.2a. The gluon is massless and only indirectly couples to the Higgs boson through  
 621 a triangular heavy quark loop, to which the largest contribution comes from the top quark.

622 The diagram still has a large magnitude, thanks to the strong coupling of the Higgs boson  
623 and the gluon to the top quark at this energy scale.

624 Production via vector boson fusion (*VBF*) sees the second largest cross-section, thanks  
625 to large couplings between the Higgs and the  $W/Z$  bosons and between the vector bosons  
626 to heavy quarks, albeit an order of magnitude smaller than  $\sigma_{ggF}$ . Its tree-level diagram is  
627 shown in figure 2.2b. The final state is characterized by two forward jets from hadronized  
628 heavy quarks, along with products from various Higgs decay signatures. This process is  
629 particularly important in measurements of the  $g_{HVV}$  coupling.

630 The leading diagram for associated Higgs production with a vector boson initiated by  
631 a pair of quarks ( $qq \rightarrow VH$ ) is shown in figure 2.2c. Another much smaller  $gg$ -initiated  
632 production also contribute at next-to-leading order. The Higgs boson is produced via Hig-  
633 gsstrahlungs from the vector boson. The latter can decay leptonically or hadronicall, but  
634 analyses in the leptonic channel often benefit from efficient lepton triggers, and high-quality  
635 lepton reconstruction.

636 Finally, we mention the mechanism of associated production with a top quark pair, shown  
637 in figure 2.2d, which is small but of paramount importance in probing the Higgs coupling  
638 to the top quark. Unlike the case of other third-generation fermions, namely the tau lepton  
639 and the bottom quark, the Higgs decay to the top quark is kinematically forbidden due to  
640 the latter's large mass. Therefore, the top quark Yukawa coupling  $y_t$  can only be measured  
641 through the  $pp \rightarrow t\bar{t}H$  production process.

642 Another consequence of the Higgs coupling structure described in 2.2 equally important  
643 to the study of the Higgs boson at the LHC is the consideration of its decay channels.  
644 Being one of the heaviest SM particles, the Higgs boson has a lifetime of approximately  
645  $10^{-22}s$ . Tree-level Higgs boson decay is induced by its coupling to quarks, whose primary  
646 channels include  $H \rightarrow b\bar{b}/c\bar{c}$ , to leptons, namely  $H \rightarrow \tau\bar{\tau}/\mu\bar{\mu}$ , and to vector bosons, namely  
647  $H \rightarrow WW/ZZ$ . In addition, notable loop-induced decays include  $H \rightarrow gg/\gamma\gamma/Z\gamma$ . Figure

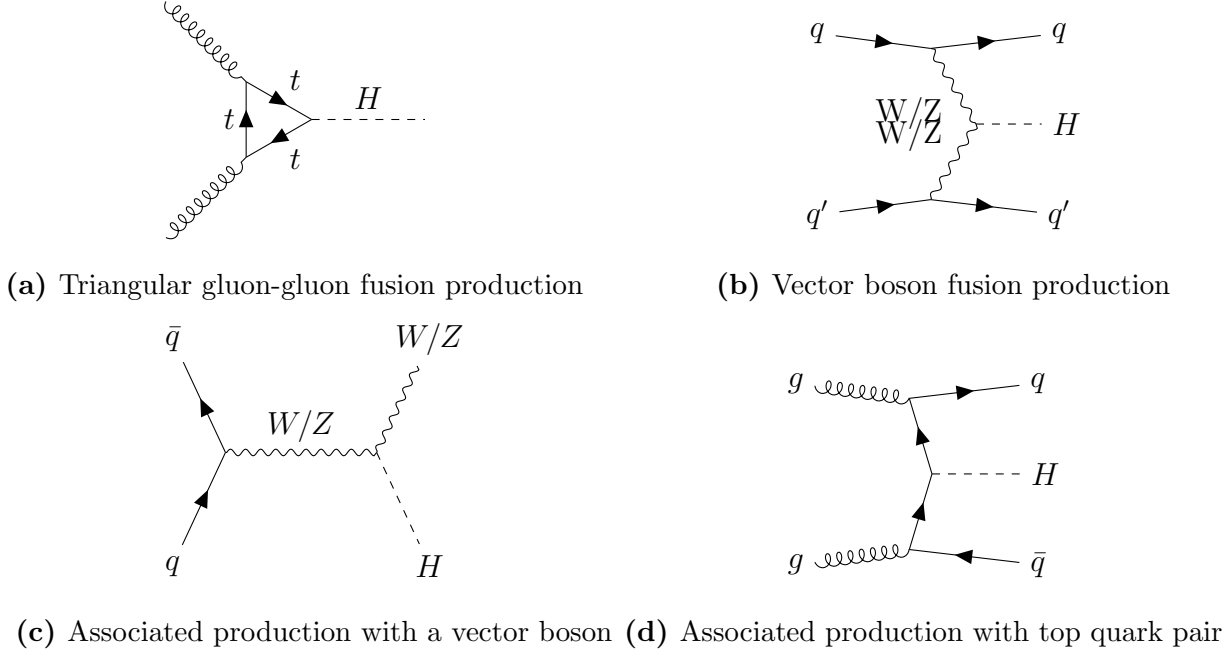


**Figure 2.2:** Leading-order Higgs boson production mechanisms

648 2.1b shows the branching ratios of primary Higgs decay channels as a function of the Higgs  
 649 mass near  $m_H = 125$  GeV. Table 2.1 specifies the branching ratio measured at Higgs mass  
 650  $M_H = 125.09$  GeV.

651 Since a decay to the top quark is forbidden, it is not surprising that the most dominant  
 652 decay mode is via Yukawa coupling to the second heaviest quark,  $H \rightarrow b\bar{b}$ , whose branching  
 653 ratio is 57.5% at  $m_H = 125.09$  GeV. Among other fermions, decay into a pair of tau leptons  
 654 is the second largest, followed by decays into second-generation fermions (figure 2.3a). The  
 655 decay to a pair of vector boson proceeds through tree-level processes (figure 2.3b), whereas  
 656  $H \rightarrow \gamma\gamma$  is mediated by a  $W$  boson (figure 2.3d) or a heavy quark loop (figure 2.3c). Despite  
 657 having a small branching ratio,  $H \rightarrow \gamma\gamma$  is an important channel for precision measurement  
 658 of the Higgs mass due to the high resolution of the reconstructed photon invariant mass.

Decay channel	Branching ratio (%)
$H \rightarrow b\bar{b}$	$57.5 \pm 1.9$
$H \rightarrow WW$	$21.6 \pm 0.9$
$H \rightarrow gg$	$8.56 \pm 0.86$
$H \rightarrow \tau\bar{\tau}$	$6.30 \pm 0.36$
$H \rightarrow c\bar{c}$	$2.9 \pm 0.35$
$H \rightarrow ZZ$	$2.67 \pm 0.11$
$H \rightarrow \gamma\gamma$	$0.228 \pm 0.011$
$H \rightarrow Z\gamma$	$0.155 \pm 0.014$
$H \rightarrow \mu\bar{\mu}$	$0.022 \pm 0.001$

**Table 2.1:** Standard Model Higgs boson decay branching ratios and uncertainty at  $M_H = 125.09$  GeV

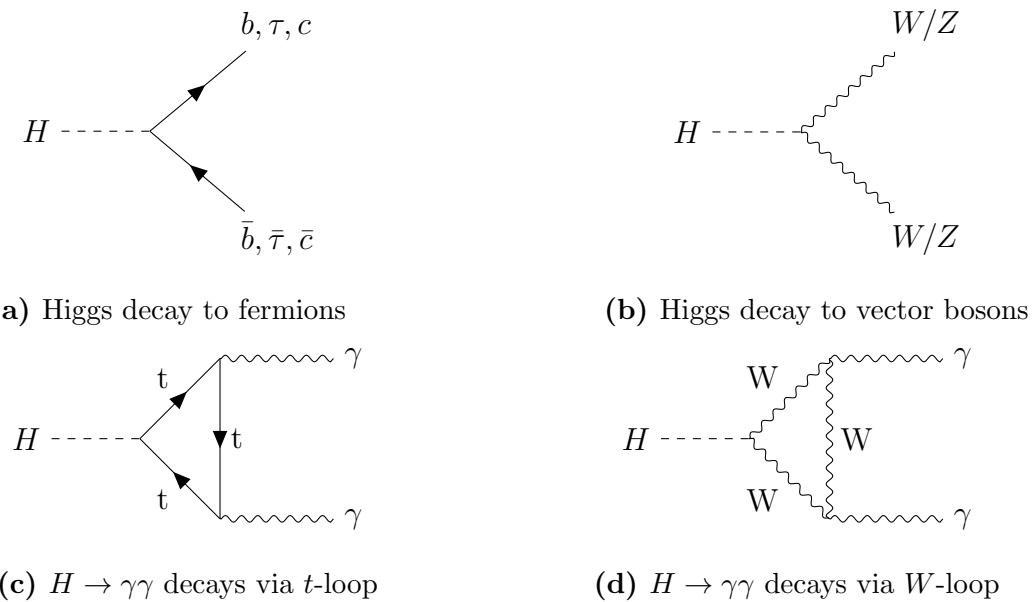


**Figure 2.3:** Leading-order Higgs boson decay mechanisms

## 659 2.4 Extension of the Standard Model Higgs sector

660 Until now, we have given a theoretical description of the simplest possible scalar struc-  
 661 ture of the Higgs field, namely a single  $SU(2)$  doublet  $\phi$ . This assumption is motivated  
 662 almost entirely by simplicity, and there exist a number of extensions to the SM Higgs sector  
 663 which satisfy the experimental constraint on its scalar structure [22]. The simplest of such  
 664 extensions consists of an additional scalar Higgs doublets—known as the Two-Higgs-Doublet  
 665 Model (2HDM).

666 The model is motivated by several considerations, the best known of which is supersymme-  
 667 try, which is explored in reference [23]. Briefly speaking, supersymmetric quarks of charges  
 668  $2/3$  and  $-1/3$  cannot acquire their mass through coupling to a single Higgs doublet. More-  
 669 over, the cancellation of anomalies requires the existence of an additional Higgs doublet.  
 670 Therefore, the Minimal Supersymmetric Standard Model (MSSM) must contain two Higgs  
 671 doublets, as prescribed by the 2HDM.

672 In addition, while the SM cannot account for the baryon-antibaryon asymmetry of the  
 673 early universe, the 2HDM, thanks to the flexibility of their scalar mass spectrum and ad-  
 674 ditional sources of CP violation, can provide stronger theoretical explanation of this phe-  
 675 nomenon. Aspects of electroweak baryogenesis in the 2HDM are explored in reference [24,  
 676 25, 26, 27, 28, 29]. A comprehensive review of the rich phenomenology of the 2HDM can be  
 677 found in reference [30].

678 In the context of dark matter (DM) searches at the LHC, the 2HDM extended by a  
 679 pseudo-scalar mediator  $a$ , denoted by 2HDM+ $a$ , constitutes an attractive benchmark model  
 680 [12]. The pseudo-scalar mediates the interactions between the visible sector of the 2HDM and  
 681 the dark sector, assumed to include a single fermionic DM particle  $\chi$ . Chapter 4 presents a  
 682 combination and summary of dark matter searches using  $139\text{ fb}^{-1}$  of  $pp$  collision data at  $\sqrt{s} =$   
 683  $13\text{ TeV}$  collected by the ATLAS detector throughout LHC Run 2. Relevant phenomenological

<sup>684</sup> consideration of the 2HDM+*a* is presented in 4.1, along with important model parameters  
<sup>685</sup> and experimental signatures to be examined by DM searches in ATLAS, many of which are  
<sup>686</sup> introduced earlier in this chapter.

687 **Chapter 3**

688 **The ATLAS experiment**

689 **3.1 The ATLAS detector**

690 The ATLAS (A Toroidal LHC ApparatuS) detector is a general-purpose detector, along  
691 with CMS, designed to observe any new physics phenomena that the LHC can discover. It  
692 is a cylindrical structure constructed around the beam pipe at one of the collision points on  
693 the LHC, comprised of an Inner Detector (ID), an electromagnetic calorimeter, a hadronic  
694 calorimeter, and a muon spectrometer. Being the largest of the LHC detectors, it spans 44m  
695 in length and 25m in height, as shown in figure 3.1.

696 The detector's geometry facilitates the use of a right-handed cylindrical coordinate system  
697 to describe locations and directions, with the nominal interaction point (IP) at the origin.  
698 The  $z$ -axis points along the beam pipe, parallel to the direction of the incoming protons.  
699 The  $x$ -axis points from the IP towards the center of the LHC. Any position is described  
700 by  $(r, \phi, z)$ , where  $\phi \in [-\pi, \pi]$ . Particle momentum can be represented by a four-vector  
701  $p = (E, p_x, p_y, p_z)$ . In practice, however, the rapidity, define as

$$y = \frac{1}{2} \ln \left( \frac{E + p_z}{E - p_z} \right) \quad (3.1)$$

702 is commonly used in lieu of the longitudinal momentum, because differences in rapidity is  
703 invariant under a Lorentz boost along  $z$ . For massless or very energetic particles, the rapidity

<sup>704</sup> is well approximated by the pseudorapidity defined from the polar angle  $\theta$

$$\eta = -\ln \tan\left(\frac{\theta}{2}\right). \quad (3.2)$$

<sup>705</sup> Both  $y$  and  $\eta$  are symmetric about  $z = 0$ . A particle moving entirely on the transverse plane  
<sup>706</sup> has  $y = \eta = 0$ , and one moving parallel to the  $z$ -axis has  $\eta = \pm\infty$ . Obviously, no detector  
<sup>707</sup> can cover the entire  $4\pi$  steradians of solid angle around the IP. The range of pseudorapidity  
<sup>708</sup> observable by a detector is called the *acceptance*. Each subsystem of ATLAS has a different  
<sup>709</sup> acceptance, in particular,  $|\eta| < 2.5$  in the ID, and  $|\eta| < 4.8$  for the calorimeters. Since the  
<sup>710</sup> pseudorapidity represents the polar angle, it is sufficient to describe a particle by  $(E, p_T, \eta, \phi)$ ,  
<sup>711</sup> where  $p_T = \sqrt{p_x^2 + p_y^2}$  is the transverse momentum.

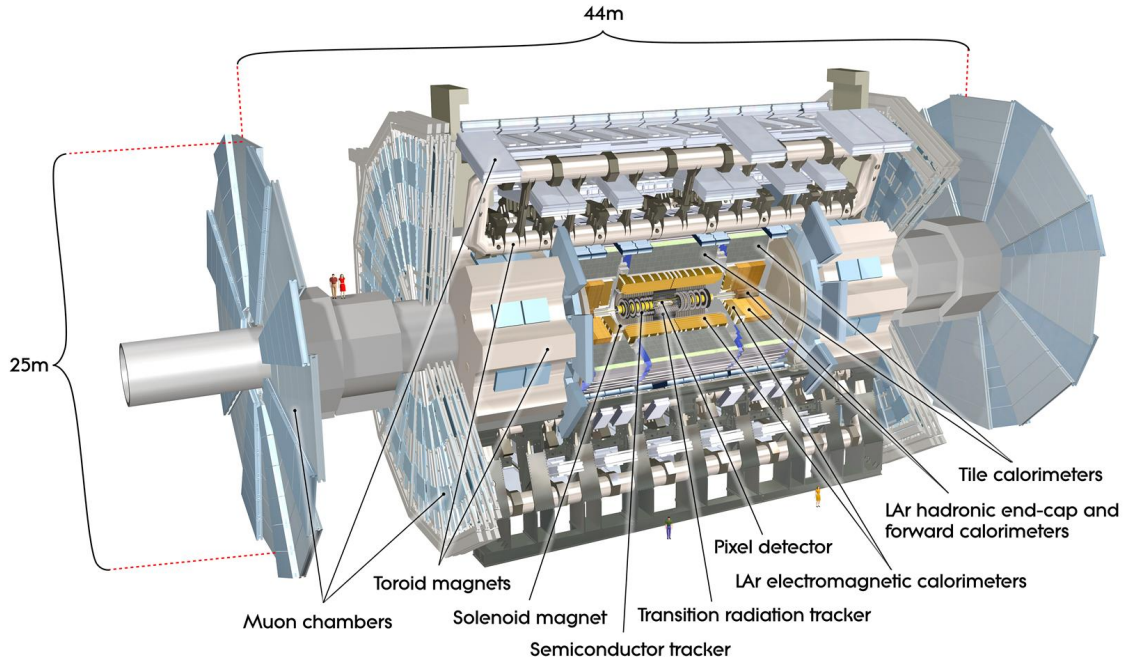


**Figure 3.1:** The ATLAS detectors and its components [31]

### 712 3.1.1 The Inner Detector

713 f Immediately surrounding the interaction point is the Inner Detector, consisting of 3  
714 subsystems constructed from two sensor technologies. These subsystems include a Pixel  
715 detector, a Semi-Conductor Tracker (SCT), and a Transition Radiation Tracker (TRT), in  
716 order of increasing radial distance from the IP. The first two use silicon sensors to detect  
717 the passage of a charged particle and the latter a collection of gas-filled straw tube and a  
718 tungsten wire to collect the secondary radiation engendered from the particle.

719 The ID is responsible for precise measurements of discrete points along the path of a  
720 charged particle, from which its trajectory (tracks) is reconstructed. Tracks are essential  
721 inputs to reconstruct physics objects charged leptons, jets, as well as the identification of  
722 jets from heavy quarks.

723 A crucial part of the ID's function is the estimation of particle momentum and impact  
724 parameters. In the presence of a homogeneous magnetic field of 2T permeating the ID along  
725 the  $z$ -axis, charged particles move in helical orbits, whose radius depends on the transverse  
726 momentum  $p_T$

$$R = \frac{p_T}{qB}. \quad (3.3)$$

727 In principle, by fitting a helix through measurements on a track, one obtains an estimate of  
728 the curvature and thus  $p_T$ . Extrapolating this helix to the point of closest approach to the  
729 IP, called the *perigee*, yields an estimate of the primary and longitudinal impact parameters  
730 ( $d_0, z_0$ ) respectively. This procedure is described in detail in chapter 7.

731 Being the first sub-detector to observe particles after they are created in the entire de-  
732 tector, the ID has the best position to characterize their kinematics to the highest possible  
733 resolution. In particular, the relative momentum resolution  $p_T\sigma(\frac{q}{p_T})$  is  $O(1\%)$ , while the  
734 impact parameter resolutions can reach  $\sigma(d0) \approx 25\mu m$  and  $\sigma(z0) \approx 40\mu m$ . This level of

735 resolution is remarkable considering the physical dimensions of ATLAS, which can only be  
736 achieved through meticulous custom designs of the subsystems described below.

### 737 3.1.1.1 The Pixel Detector

738 The pixel detector (figure 3.2a) is the innermost part of the ID, consisting of 3 barrel  
739 layers extending from a radius of  $r = 50.5\text{ mm}$  up to  $r = 122.5\text{ mm}$ , and 3 end-cap disks  
740 on each sides of the barrel. Each of these physical layers provides a structure onto which  
741 detector modules are mounted. Each barrel layer consists of supporting staves, and each  
742 end-cap of 8 sectors circularly arranged around the  $z$ -axis. In total, the pixel detector has  
743 1744 identical modules, each composed of an array of silicon sensor and 16 front-end chips  
744 which read out the electrical signal created by the passage of a charge particle [32].

745 A sensor element is fabricated from a detector-grade n-type silicon wafer implanted with  
746 high positive ( $p^+$ ) and negative ( $n^+$ ) dose regions on each side. At the  $p^+ \text{-} n$  junction, holes  
747 from the  $p^+$  region neutralize free electrons in the  $n$ -typed bulk, creating a depletion zone  
748 devoid of free charge carriers. Operated in a reverse bias, this region is enlarged over the  
749 whole sensor bulk volume. Although containing no free charge carrier, the  $pn$ -junction is  
750 easily ionized by a traversing particle, creating electron-hole pairs. Primary electrons directly  
751 created by the traversing particle are often energetic enough to induce secondary ionization  
752 and amplify the signal. Electron-hole pairs are separated by the biasing electric field and drift  
753 toward their corresponding electrodes. As electrons approach the anode, they are multiplied  
754 and measured by the read-out chips.

755 The sensitive part of a pixel module is approximately  $2 \times 6\text{ cm}^2$  in size, segmented into  
756 highly granular pixels of dimensions  $50 \times 400\text{ }\mu\text{m}^2$ , totalling 47268 pixels. Nearly every pixel  
757 corresponds to a readout channel, providing the pixel detector approximately 80 million  
758 channels. With the inclusion of the Insertable B-Layer (IBL), the total number of channels

759 the smallest pixel dimension is reduced to  $50 \times 250 \mu\text{m}^2$ , and the total number of read-  
 760 out channels increased to 94 million. This high level of granularity enables high precision  
 761 measurements very close to the beam pipe.

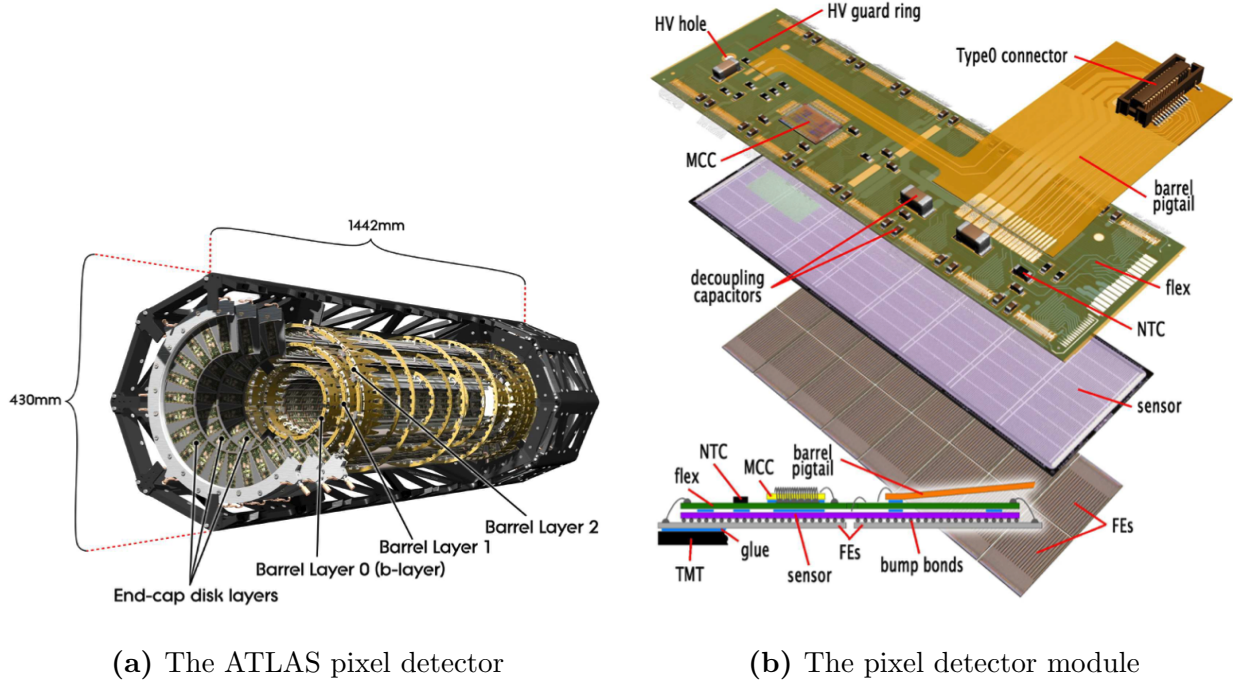


**Figure 3.2:** The ATLAS pixel detector and detector module. Figures taken from reference [33]

### 762 3.1.1.2 The Semi-Conductor Tracker

763 Surrounding the Pixel volume is the Semi-Conductor Tracker (SCT), consisting of four  
 764 barrel layers and eighteen symmetric end-cap disks, both featuring a total of 4088 strip  
 765 modules [34, 35]. Figure 3.3b provides an overview of a strip module used in the barrel layers.  
 766 Each detector module consists of two pairs of single-sided microstrips with  $80 \mu\text{m}$  pitch. Each  
 767 single strip sensor is capable of detecting particle intersection in one dimension, information  
 768 from a pair of strips must be combined to provide three-dimensional point information with  
 769 space-point resolution of  $16 \mu\text{m}$  in the  $(R - \phi)$  direction and  $580 \mu\text{m}$  in the  $z$ -direction [36].

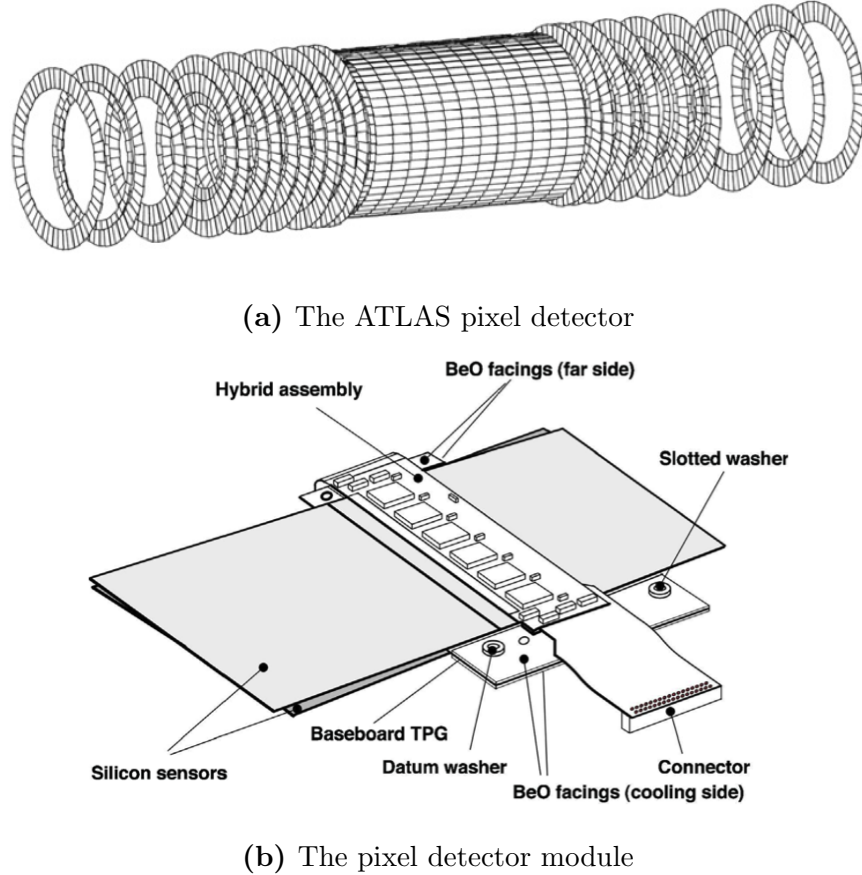


**Figure 3.3:** Overview of the strip module of the SCT in the barrel layers. Figures taken from reference [37]

### 770 3.1.1.3 The Transition Radiation Tracker

771 The Transition Radiation Tracker (TRT) is the outermost component of the Inner De-  
 772 tector. It comprises of approximately 300000 straw tubes that are 4 mm in diameter, and  
 773 covers up to  $|\eta| = 1$  in the barrel and  $|\eta| = 2$  in the end-cap layers. Each high  $p_T$  track  
 774 passing through the TRT leaves 30 – 36 hits and reach a resolution of 130  $\mu\text{m}$  in the  $(R - \phi)$   
 775 direction.

776 In each straw tube, a tungsten wire is located at the center and surrounded by a gas  
 777 mixture spreading the volume of the tube. When a charged particle passes through the

<sup>778</sup> tube, it ionizes the ambient gas and creates an pairs of electrons and positive gas ions. An  
<sup>779</sup> electric field exists between the outer tube and the central wire, which act as electrodes,  
<sup>780</sup> separating the charges. As they reach the wire, the charges are amplified and detected. To  
<sup>781</sup> enhance electron identification, the straw tubes are surrounded by polymer fibers (barrel)  
<sup>782</sup> and foils (end-caps), which facilitate transition radiation at the interface between materials.

### <sup>783</sup> 3.1.2 The Calorimeter system

<sup>784</sup> The second group of detector subsystems, the calorimeters, is dedicated to the measure-  
<sup>785</sup> ment of particle energies and directions. There exist two types of calorimeters: electromag-  
<sup>786</sup> netic and hadronic. They detect particle through alternating layers of passive and active  
<sup>787</sup> materials. In the passive layers, also called the absorber, an energetic particle deposits a  
<sup>788</sup> large portion of its kinetic energy and induces a large number of secondary particles, includ-  
<sup>789</sup> ing electrons, photons, and hadrons, depending on the type of calorimeter. These particles  
<sup>790</sup> are then stopped and measured by the active layers.

<sup>791</sup> The electromagnetic calorimeter targets electrons/positrons and photons, which create  
<sup>792</sup> electromagnetic showers as they interact with the inactive material. In the electric field near  
<sup>793</sup> the atomic nuclei that make up the material, electrons and positron undergo Bremsstrahlung  
<sup>794</sup> and emit secondary photons, which induces electron pair production and generates more  
<sup>795</sup> high-energy charged particles. A reaction chain in which Bremsstrahlung photons induce  
<sup>796</sup> electrons/positrons, which emits more Bremsstrahlung photons, creates a shower of charged  
<sup>797</sup> particles in the passive material.

<sup>798</sup> In the case of the hadronic calorimeters, a hadron interacts with the atomic nuclei of a  
<sup>799</sup> dense material through which it passes and produces secondary hadrons, mostly pions, which  
<sup>800</sup> then drive the reaction chain, similar to the electromagnetic counterpart. In addition, neutral  
<sup>801</sup> pion decays to high-energy photon and leptonic decays can also induce electromagnetic sub-  
<sup>802</sup> shower within a hadronic shower.

### 3.1.2.1 The electromagnetic (EM) calorimeter

The passive absorber material in the ATLAS electromagnetic calorimeter comprises of lead, and the active material of liquid argon. The passive layers are interspersed with active layers in an accordion pattern. The barrel covers a pseudorapidity range up to  $|\eta| = 1.475$  and the endcaps  $1.375 < |\eta| < 3.2$ . The central region of the EM calorimeter consists of three layers and a pre-sampler with a fine granularity ( $\eta \times \phi = 0.025 \times 0.1$ ). The first sampling layer features a segmentation of  $\eta \times \phi = 0.025/8 \times 0.1$ , while the second and third sampling layers are segmented into  $\eta \times \phi = 0.025 \times 0.025$  and  $\eta \times \phi = 0.025 \times 0.05$ , respectively. Angular segmentation allows measurements of particle directions, and depth segmentation measurements of shape. This information is useful in discriminating electrons and photons from jets. Figure 3.4b shows a sketch of the EM calorimeter module in the barrel.

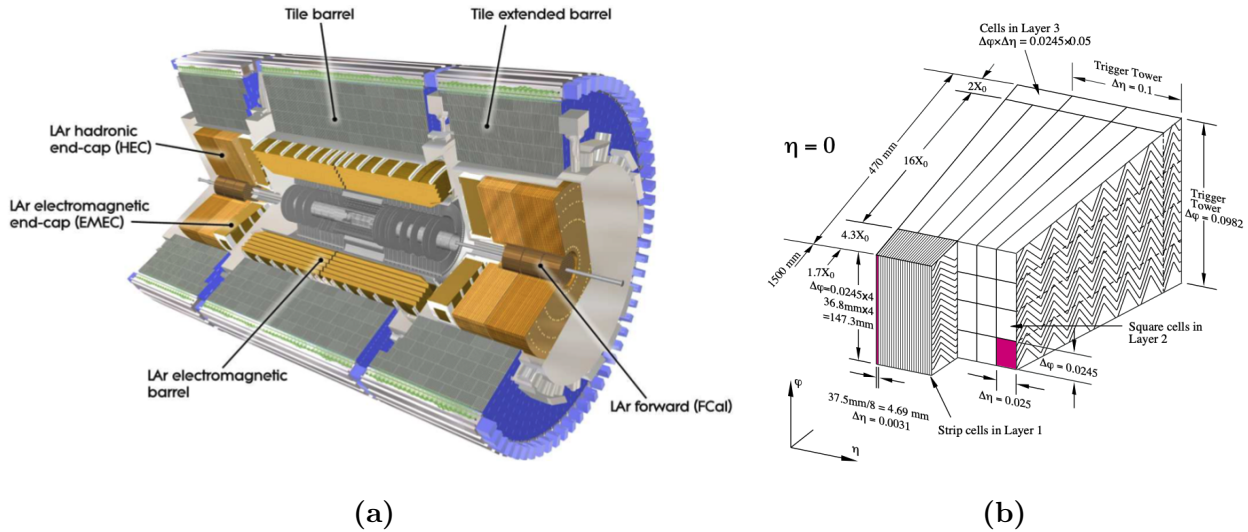


**Figure 3.4:** (a) Layout of the ATLAS calorimetry system, and (b) sketch of a barrel module of the electromagnetic calorimeter [38].

### **3.1.2.2 The hadronic calorimeter**

The hadronic calorimeter uses iron absorbers and plastic scintillating tiles as active material in the barrel region. It covers a pseudorapidity range of  $|\eta| < 1.0$  in the barrel and  $0.7 < |\eta| < 1.7$  in the extended barrel. It also comprises of three layers of increasing radii. The effective granularity varies between  $\eta \times \phi = 0.1 \times 0.1$  and  $0.2 \times 0.1$ .

The endcap and forward regions (figure 3.4a) of the hadronic calorimeter uses copper/tungsten as absorber and liquid argon as the active material. They cover a pseudorapidity range of up to 4.9. The forward calorimeter is split into an electromagnetic and a hadronic component.

### **3.1.3 The muon spectrometer**

Unlike other particles, muons produced with energy in the range of 0.1–100 GeV typically seen in ATLAS do not strongly interact with detector material in the detector subsystems described in the previous sections. Despite leaving energy clusters in the ID, they traverse the calorimeters intact and are therefore measured by a dedicated muon system. The muon spectrometer is composed of four subsystems that use different technologies to track muons at high precision and perform fast triggers. It is immersed in a toroidal magnetic field ranging from 2.0 to 6.0 T, providing enough bending power to resolve the muon transverse momentum. Figure 3.5 shows the overall layout of and a side view of a quadrant of the MS, including its subsystems.

To measure the curvature of muon tracks along the bending direction of the toroidal field, the MS uses a number of aluminum tubes 30 millimeters in diameter filled with Ar and having a central tungsten/rhenium alloy wire, similar to the TRT. The outer surface and the central wire of these Monitored Drift Tubes (MDTs) are kept at a potential difference of 3 kV to ensure a drifting time of less than 700 ns. The MDTs are divided into 1200 chambers

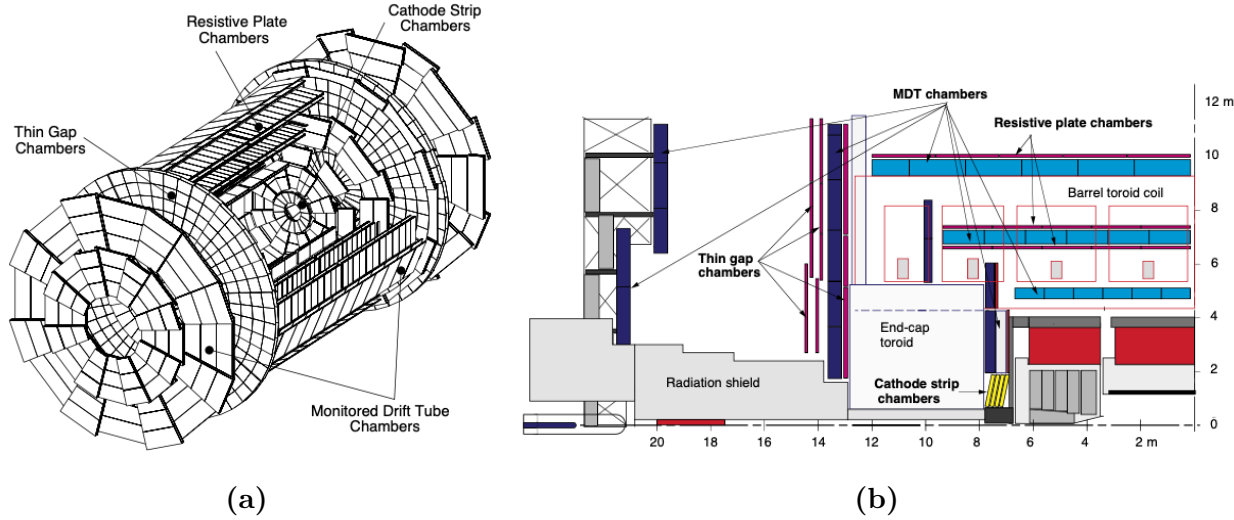


**Figure 3.5:** (a) Layout of the ATLAS Muon Spectrometer system, and (b) a sideview of one quadrant of the MS [39].

838 cover a pseudorapidity range up to  $|\eta| = 2.7$ , each chamber providing 6 to 8 measurements  
839 along the track.

At larger  $|\eta|$ , the Cathode Strip Chambers (CSCs) have a higher granularity than the MDTs to resolve large backgrounds in the forward region. They cover  $2.0 < |\eta| < 2.7$  and have short drift times of around 40 ns. The CSCs provide 4 simultaneous measurements of  $\eta$  and  $\phi$ .

The Resistive Plate Chambers (RPCs), used in the barrel and the Thin Gap Chambers (TGCs), used in the endcap regions are both gaseous detectors and together make up the muon trigger system. They respectively cover  $|\eta| < 1.05$  and  $1.05 < |\eta| < 2.4$ .

847 **Chapter 4**

848 **Combination of dark matter searches interpreted in 2HDM+ $a$**

849 This chapter presents the combined searches for dark matter particles in the context of  
850 a Two-Higgs-Doublet Model (2HDM) extended by a pseudoscalar mediator  $a$  using proton-  
851 proton collision data collected at the ATLAS detector during LHC Run 2. We start with a  
852 discussion of the signal model as an extension of the Standard Model Higgs sector detailed  
853 in section 2.2, and introduce the fermionic dark matter particle  $\chi$  connected to the visible  
854 sector via  $a$ . In all analyses, no significant deviations from SM predictions are observed, and  
855 the data is used to derive exclusion limits on the signal model as functions of its parameters  
856 A statistical combination of the most sensitive channels carries out the limit setting over six  
857 benchmark scenarios given in section 4.2. An overview of the experimental signatures tar-  
858 geted by these searches, a description of systematic uncertainty, and the statistical method  
859 are provided in sections 4.4, 4.5 and 4.6, respectively. Finally, the results are presented  
860 in section 4.7. This analysis, in which the author is a contributor, has been published in  
861 reference [40].

862 **4.1 Theoretical considerations**

863 The benchmark model used to interpret the data extends the Standard Model with a  
864 second complex Higgs doublet, already postulated in several UV-complete BSM theories [41,  
865 42]. After electroweak symmetry breaking, the model contains 5 Higgs bosons: a light CP-  
866 even boson  $h$ , a heavier CP-even boson  $H$ , a CP-odd boson  $A$  and a two charged bosons

<sup>867</sup>  $H^\pm$ . The 2HDM allows some freedom in the choice of Higgs-fermion coupling structure, for  
<sup>868</sup> example, 2HDM type-I which couples only one Higgs doublet to fermions, and 2HDM type-  
<sup>869</sup> II, which couples the neutral member of one Higgs doublet to only up-type quarks and the  
<sup>870</sup> neutral member of the other to down-type quarks. This search assumes the type-II structure,  
<sup>871</sup> along with the alignment and decoupling limits, so that the lighter CP-even states  $h$  can be  
<sup>872</sup> identified with the SM Higgs boson [43]. The Lagrangian of the 2HDM can be written as

$$\mathcal{L}_{2HDM} = (D_\mu \Phi_1)^\dagger (D^\mu \Phi_1) + (D_\mu \Phi_2)^\dagger (D^\mu \Phi_2) - V(\Phi_1, \Phi_2) \quad (4.1)$$

where the covariant derivative  $D_\mu$  is given by

$$D_\mu = \partial_\mu - ig \frac{\tau^i}{2} W_\mu^i - i \frac{g'}{2} Y B_\mu,$$

<sup>873</sup> in which  $\tau^i$  are Pauli matrices and  $Y$  is the hypercharge. The potential is

$$\begin{aligned} V(\Phi_1, \Phi_2) &= m_{11}^2 \Phi_1^\dagger \Phi_1 + m_{22}^2 \Phi_2^\dagger \Phi_2 - (m_{12}^2 \Phi_1^\dagger \Phi_2 + h.c.) \\ &\quad + \frac{\lambda_1}{2} (\Phi_1^\dagger \Phi_1)^2 + \frac{\lambda_2}{2} (\Phi_2^\dagger \Phi_2)^2 + \lambda_3 (\Phi_1^\dagger \Phi_1)(\Phi_2^\dagger \Phi_2) + \lambda_4 (\Phi_1^\dagger \Phi_2)(\Phi_2^\dagger \Phi_1) \\ &\quad + \left\{ \frac{\lambda_5}{2} (\Phi_1^\dagger \Phi_2)^2 + [\lambda_6 (\Phi_1^\dagger \Phi_1) + \lambda_7 (\Phi_2^\dagger \Phi_2)] (\Phi_1^\dagger \Phi_2) + h.c. \right\} \end{aligned} \quad (4.2)$$

<sup>874</sup> The scalar field vacuum expectation values occur at

$$\langle \Phi_i \rangle = \frac{1}{\sqrt{2}} \begin{pmatrix} 0 \\ v_i \end{pmatrix}, \quad v_i \in \mathbb{R}, \quad (4.3)$$

<sup>875</sup> with the following conditions

$$\begin{aligned} m_{11}^2 &= m_{12}^2 t_\beta - \frac{1}{2} v^2 (\lambda_1 c_\beta^2 + \lambda_{345} s_\beta^2 + 3 \lambda_6 s_\beta c_\beta + \lambda_7 s_\beta^2 t_\beta) \\ m_{22}^2 &= m_{12}^2 (t_\beta)^{-1} - \frac{1}{2} v^2 (\lambda_2 s_\beta^2 + \lambda_{345} c_\beta^2 + \lambda_6 c_\beta^2 (t_\beta)^{-1} + 3 \lambda_7 s_\beta c_\beta), \end{aligned} \quad (4.4)$$

where

$$t_\beta = \frac{v_2}{v_1}, \quad \lambda_{345} = \lambda_3 + \lambda_4 + \lambda_5, \quad v = \sqrt{v_1^2 + v_2^2} = 246 \text{ GeV}$$

<sup>876</sup> After spontaneous symmetry breaking, three of the original eight scalar degrees of freedom  
<sup>877</sup> are absorbed by the  $W^\pm$  and the  $Z$  bosons, leaving five physical Higgs bosons as described

878 above. The physical masses of the CP-odd and charged Higgs states are given by

$$\begin{aligned} m_A^2 &= \frac{m_{12}^2}{s_\beta c_\beta} - \frac{v^2}{2} \left( 2\lambda_5 + \frac{\lambda_6}{t_\beta} + \lambda_7 t_\beta \right) \\ m_{H^\pm}^2 &= m_A^2 + \frac{v^2}{2} (\lambda_5 - \lambda_5) \end{aligned} \quad (4.5)$$

879 The two CP-even Higgs states mix according to the squared-mass matrix

$$\mathbf{M}^2 = m_A^2 \begin{pmatrix} s_\beta^2 & -s_\beta c_\beta \\ -s_\beta c_\beta & c_\beta^2 \end{pmatrix} + \mathbf{B}^2 \quad (4.6)$$

where

$$\mathbf{B}^2 = v^2 \begin{pmatrix} \lambda_1 c_\beta^2 + 2\lambda_6 s_\beta c_\beta + \lambda_5 s_\beta^2 & (\lambda_3 + \lambda_4) s_\beta c_\beta + \lambda_6 c_\beta^2 + \lambda_7 s_\beta^2 \\ (\lambda_3 + \lambda_4) s_\beta c_\beta + \lambda_6 c_\beta^2 + \lambda_7 s_\beta^2 & \lambda_2 s_\beta^2 + 2\lambda_7 s_\beta c_\beta + \lambda_5 c_\beta^2 \end{pmatrix}.$$

880 Diagonalizing  $\mathbf{M}^2$  furnishes the physical CP-even Higgs states, whose squared-masses are  
881 the eigenvalues

$$m_{H,h}^2 = \frac{1}{2} \left[ \mathbf{M}_{11}^2 + \mathbf{M}_{22}^2 \pm \sqrt{(\mathbf{M}_{11}^2 - \mathbf{M}_{22}^2)^2 + 4\mathbf{M}_{12}^2} \right], \quad (4.7)$$

882 and the mixing angle

$$s_{2\alpha} = \frac{2\mathbf{M}_{12}^2}{\sqrt{(\mathbf{M}_{11}^2 - \mathbf{M}_{22}^2)^2 + 4\mathbf{M}_{12}^2}}, \quad c_{2\alpha} = \frac{(\mathbf{M}_{11}^2 - \mathbf{M}_{22}^2)^2}{\sqrt{(\mathbf{M}_{11}^2 - \mathbf{M}_{22}^2)^2 + 4\mathbf{M}_{12}^2}}. \quad (4.8)$$

883 The 2HDM, though being a BSM model, does not natively contain a dark sector. Therefore,  
884 a fermionic dark matter particle  $\chi$  is included, and connected to the Higgs sector by a pseudo-  
885 scalar CP-odd mediator  $a$ , with Yukawa-like couplings to both SM and DM fermions. The  
886 mediator mixes with the pseudo-scalar  $A$  of the 2HDM with a mixing angle  $\theta$ .

887 With the inclusion of the fermionic dark matter and the pseudo-scalar mediator, the  
888 phenomenology of the model is fully determined by 14 independent parameters:

- 889 1. the mass of Higgs bosons  $m_h$ ,  $m_H$ ,  $m_A$ ,  $m_{H^\pm}$ ,
- 890 2. the mass of the pseudo-scalar mediator  $m_a$ ,

- 891     3. the mass of the dark matter particle  $m_\chi$  ,
- 892     4. the Yukawa coupling  $g_\chi$  between  $a$  and  $\chi$ ,
- 893     5. the electroweak VEV  $v$ ,
- 894     6. the ratio of the VEVs of the two Higgs doublets  $\tan \beta$  ,
- 895     7. the mixing angle  $\alpha$  of the CP-even Higgs states  $h$  and  $H$ ,
- 896     8. the mixing angle  $\theta$  of the CP-odd states  $A$  and  $a$ ,
- 897     9. the quartic coupling  $\lambda_3$  of the pure 2HDM potential,
- 898     10. the quartic couplings of the potential terms between the doublet and singlet fields  $\lambda_{P1}$ ,
- 899       and  $\lambda_{P2}$

900 Some of these parameters are constrained by electroweak and flavour measurements, as well  
 901 as phenomenological considerations [11, 12]. Some parameters are chosen to simplify the  
 902 model and reduce the space of independent parameters. Reference [12] contains detailed  
 903 descriptions of the 2HDM+ $a$  benchmark scenarios recommended by the LHC Dark Matter  
 904 working group.

905 This analysis scans over a total of 5 parameters, including  $m_A$  ,  $m_a$  ,  $\tan \beta$  ,  $\sin \theta$  , and  
 906  $m_\chi$  . Other parameters are set to constant in all benchmark scenarios. The coupling  $g_\chi$  is  
 907 set to 1, having negligible effect on the shape of the kinematic distribution of interest. The  
 908 alignment and decoupling limits are assumed, effectively assigning  $m_h = 125$  Gev,  $v = 246$   
 909 GeV, and  $\cos(\beta - \alpha) = 0$ . The quartic coupling  $\lambda_3$  is set to 3 to guarantee the stability of  
 910 the Higgs potential for the chosen range of the heavy Higgs bosons. In addition, they are  
 911 fixed to the same value, i.e.  $m_A = m_H = m_{H^\pm}$ . The heavy CP-even Higgs  $H$  is chosen to  
 912 have the same mass as the charged Higgs to avoid the constraints from electroweak precision  
 913 measurements, and the same mass as the CP-odd Higgs to reduce the number of independent

914 parameters [11]. The other quartic couplings are also fixed at 3 to maximize the trilinear  
915 couplings between the CP-odd and the CP-even neutral sates.

916 The phenomenology of the 2HDM+ $a$  is particularly rich, and this analysis combines a  
917 large number of signatures as illustrated in table 4.3. These signatures can be broadly catego-  
918 rized into those involving invisible and visible mediator decays, the former being represented  
919 by  $E_T^{\text{miss}} + X$ . An overview of the signatures considered are given in section 4.4, and further  
920 details can be found in the referenced publications. The dominant production mode for the  
921 majority of signatures is  $gg$ -initiated production. Figures 4.1a, 4.1b respectively summarize  
922  $gg$ -initiated resonant and non-resonant production mechanisms of the  $E_T^{\text{miss}} + Z(\ell\ell)$  final  
923 state. Similarly, the  $E_T^{\text{miss}} + h(b\bar{b})$  signature, as well as other  $E_T^{\text{miss}} + h$  signatures, can be  
924 produced both resonantly and non-resonantly via  $gg$  fusion, as seen on figures 4.2a and 4.2b.  
925 In addition,  $gg$ -initiated production of the  $E_T^{\text{miss}} + j$  signature is shown in figures 4.4a, and  $t\bar{t}$ -  
926 or  $b\bar{b}$ -associated resonant  $A/H$  production leading to  $t\bar{t}t\bar{t}$ ,  $b\bar{b}b\bar{b}$ ,  $t\bar{t}b\bar{b}$ ,  $E_T^{\text{miss}} + t\bar{t}$ , or  $E_T^{\text{miss}} + b\bar{b}$   
927 signatures in Figure 4.6. Figure 4.5 shows the production of a charged Higgs associated with  
928 and decaying into a pair of  $tb$  quarks, designated  $tbH^\pm(tb)$ , and figure 4.7 shows loop-induced  
929 Higgs production of a SM Higgs boson decaying into a pair of mediators  $aa$  resulting in 2  
930 pairs of fermionic DM or SM particles.

931 The second largest production mode is  $bb$ -initiated production, whose primary signatures  
932 include  $E_T^{\text{miss}} + Z(\ell\ell)$ ,  $E_T^{\text{miss}} + h(b\bar{b})$ , and  $E_T^{\text{miss}} + j$ . Representative Feynman diagrams  
933 are respectively shown in in figures 4.1c, 4.2d, 4.4b. Finally, the leading diagram for the  
934  $E_T^{\text{miss}} + tW$  signature is shown in figure 4.3. The interplay between these signatures depends  
935 on the 2HDM+ $a$  model parameters.

## 936 4.2 Benchmark scenarios

937 The parameter space is examine through a total of 6 representative benchmark scenarios,  
938 in which one or two parameters are varied while the others are fixed. Table 1 summarizes

939 these scenarios, demarcated to demonstrate the rich phenomenology of the 2HDM+ $a$  and to  
940 examine the interplay between the signatures described in the previous section.

#### 941 4.2.1 Scenario 1: Exploration of two $m_a$ – $m_A$ planes

942 This scenario evaluates constraints on 2HDM+ $a$  as a function of the pseudo-scalar masses  
943  $m_a$  and  $m_A$ , highlighting the complex dependence of the model phenomenology on the  
944 pseudo-scalar mass hierarchy, which governs the production and decay modes that are kine-  
945 matically accessible and favoured. In this scan,  $\tan \beta$  is fixed to 1.0 which favours couplings  
946 to up-type quarks, particularly the top quark, while the  $a/A$  mixing angle is fixed to two  
947 values  $\sin \theta = 0.35$  and  $\sin \theta = 0.7$ , and thus two parameter planes are explored. These  
948 angles respectively correspond to low and almost maximal mixing between the CP-odd Higgs  
949 and the pseudo-scalar mediator connected to the dark sector.

#### 950 4.2.2 Scenario 2: Exploration of two $m_A$ – $\tan \beta$ planes

951 This scenario evaluates the constraints while simultaneously varying  $m_A$  and  $\tan \beta$  for  
952 the same choices of mixing angle  $\sin \theta$  in 4.2.1. The pseudo-scalar mass  $m_a$  is fixed to  
953 250 GeV to kinematically prevent on-shell decays of the mediator into a pair of top quarks  
954 and enlarge the branching ratio of the decay into the fermionic DM particle  $a \rightarrow \chi\chi$  up  
955 to 100%. This benchmark scenario highlights the dependence of the couplings of the CP-  
956 odd Higgs  $A$  on the value of  $\tan \beta$  as a function of its mass. In particular, low values of  
957  $\tan \beta$  correspond to stronger coupling to up-type quarks, while higher values of  $\tan \beta$  favour  
958 couplings to down-type quarks and charged leptons. In addition, it examines the interplay  
959 between  $gg$ -initiated, top-loop induced and  $b\bar{b}$ -initiated production modes.

### 960 4.2.3 Scenario 3: Exploration of two $m_a - \tan \beta$ planes

961 Similar to 4.2.2, constraints on 2HDM+ $a$  are evaluated as a function of the pseudo-  
 962 scalar mass  $m_a$  and Higgs doublet VEV ratio  $\tan \beta$ . The CP-odd Higgs mass is fixed at  
 963  $m_A = 600$  GeV, allowing for the decays  $A \rightarrow t\bar{t}$  and favouring it at low  $\tan \beta$ . The value of  
 964  $m_A$  is motivated by constraints on the mass of the charged Higgs  $m_{H^\pm} = m_A$  derived from  
 965 precision measurements of  $B$ -meson decays [44, 11]. Two parameter planes corresponding  
 966 to  $\sin \theta = 0.35$  and  $\sin \theta = 0.7$  are examined, similar to the previous scenarios.

### 967 4.2.4 Scenario 4: Variation of the pseudo-scalar mixing angle $\sin \theta$

968 This benchmark scenario highlights the interplay between the  $E_T^{\text{miss}} + Z$  and  $E_T^{\text{miss}} + h$   
 969 signatures arising from invisible mediator decays, and signatures that probe visible mediator  
 970 decays. The couplings  $g_{Aha}$ ,  $g_{HZa}$  which affect  $E_T^{\text{miss}} + h$  and  $E_T^{\text{miss}} + Z$  production scale with  
 971  $\sin \theta \cos \theta$  and  $\sin \theta$  respectively, and the coupling  $g_{at\bar{t}}$  which plays a dominant role in the  
 972 leading  $E_T^{\text{miss}} + X$  production modes, scales with  $\sin \theta$ . As  $\sin \theta \rightarrow 0$ , the sensitivity of the  
 973  $E_T^{\text{miss}} + X$  signatures vanishes.

### 974 4.2.5 Scenario 5: Variation of the Dark Matter mass $m_\chi$

975 The value of  $m_\chi$  has a strong effect on parameters in cosmological dark matter models,  
 976 such as the relic density, and on the sensitivity of direct and indirect detections of DM.  
 977 This benchmark scenario provides a basis to compare the sensitivity of collider searches to  
 978 those of non-collider experiments and cosmological observations in the context of 2HDM+ $a$ .  
 979 Constraints are evaluated by varying  $m_\chi$  and fixing other free parameters to  $\sin \theta = 0.35$ ,  
 980  $m_A = 600$  GeV,  $m_a = 400$  GeV, and  $\tan \beta = 1.0$ . A similar benchmark scenario was  
 981 examined in reference [12] under a different set of pseudo-scalar mass parameters, which is

982 fully excluded by a previous ATLAS publication [45],. The current choices of  $m_a$  and  $m_A$   
 983 represent an unexplored region in the parameter space.

984 **4.2.6 Scenario 6: Variation of the  $m_a - m_\chi$**

985 This scenario illustrates the interplay between searches for invisible and exotic decays of  
 986 the Higgs boson  $h$  in the context of 2HDM+ $a$ . Other free parameters are set to  $\sin \theta = 0.35$   
 987 and  $\tan \beta = 1.0$  for consistency with other benchmark scans, and  $m_A = 1200$  to satisfy  
 988 the constraint on the coupling  $g_{haa}$  from measurements of the total Higgs boson decay width  
 989 [46]. This is a strong constraint for  $m_a < m_h/2$ , satisfied only by a relatively narrow range  
 990 of  $m_A$  in the chosen subspace of other free parameters.

991 In all benchmark scenarios, unless varied, the DM mass is fixed at  $m_\chi = 10$  GeV to  
 992 ensure a significant branching ratio for its decay from the pseudo-scalar  $a$  for  $m_a > 100$   
 993 GeV. As long as  $m_\chi < m_a/2$ , the value of  $m_\chi$  has little impact on the sensitivity of the  
 994 searches considered in this analysis. Consequently, it is possible to match the observed relic  
 995 density across a range of model parameter space through an appropriate choice of  $m_\chi$   
 996 without much effect on the experimental signatures.

997 Various theoretical constraints are considered in selecting the ranges of the parameters  
 998 that are varied in these benchmark scenarios. First, in some regions of the parameter space, the  
 999 scalar potential is not bounded from below at large  $m_A$ , occurring, for example, in scenario  
 1000 1a for  $(m_A \gtrsim 1250, m_a = 100)$  GeV and  $(m_A \gtrsim 1550, m_a = 1000)$  GeV. However, these  
 1001 constraints could be substantially relaxed if the quartic couplings take values closer to the  
 1002 perturbative limit or in more general 2HDM models [12, 11, 47]. Therefore, they should not  
 1003 be understood as a strong limit on the validity of the model predictions that were used to  
 1004 derive the exclusion contours. Second, given the parameter choices, the  $aah$  coupling exceeds  
 1005 the unitary limit of  $4\pi$  for large  $m_A$ , for instance, in scenario 1a, for  $(m_A \gtrsim 1250, m_a = 100)$   
 1006 GeV and  $(m_A \gtrsim 1550, m_a = 1000)$  GeV. In this region, the width of the additional heavy

1007 Higgs bosons grows substantially and the theoretical predictions are subject to additional  
1008 uncertainties from the treatment of the width. Therefore, regions where the relative width  
1009  $\Gamma/m$  of at least one heavy Higgs boson or of the pseudo-scalar mediator  $a$  exceeds 20% are  
1010 marked as shaded areas in the summary plots in Section 4.2.6. This conservative approach  
1011 to large widths follows reference [45].

1012 Table 4.1 summarizes the benchmark scenarios examined in this analysis. Scenarios 1a,  
1013 3a, 4a, 4b, and 5 are recommended by the LHC Dark Matter Working Group and appeared  
1014 in previous ATLAS analyses [45]. This work considers in addition scenarios 1b, 2, 3b, and  
1015 6, which are motivated by the studies in references [12, 48, 46]. In particular, the choice  
1016 of  $\sin \theta = 0.7$  or  $\theta \approx \pi/4$  corresponds to maximal mixing in the pseudo-scalar sector and  
1017 is relevant for the  $E_T^{\text{miss}} + tW$  search, which was designed specifically for 2HDM+ $a$  signal  
1018 processes [48]. Scenario 6 is included for the first time in this work to showcase the rich  
1019 phenomenology of the model.

1020 This work also covers more production modes of the Higgs bosons and the pseudo-scalar  
1021 mediator. In the previous summary of dark matter searches by ATLAS [45], only  $gg$ -initiated  
1022 production was considered for the  $E_T^{\text{miss}} + Z$  signatures, and for the  $E_T^{\text{miss}} + h$  signatures,  
1023  $b\bar{b}$ -initiated production was considered only for  $\tan \beta > 10$ . In contrast, all  $E_T^{\text{miss}}$  signatures  
1024 take into account  $b\bar{b}$ -initiated production, which is relevant for the  $E_T^{\text{miss}} + Z$  and  $E_T^{\text{miss}} + h$   
1025 signatures not only at large  $\tan \beta$ , where it is more important, but also at more intermediate  
1026 values[40].

### 1027 4.3 Data and simulated event samples

1028 Proton–proton collision data collected with the ATLAS detector during the period 2015–  
1029 2018 at center-of-mass energy  $\sqrt{s} = 13$  TeV are used in the majority of analyses considered  
1030 in this summary. The data sample is equivalent to an integrated luminosity of  $139 \text{ fb}^{-1}$  after  
1031 ensuring good operational conditions of all detector sub-systems and high-quality data [49].

Scenario		Fixed parameter values			Varied parameters	
		$\sin \theta$	$m_A$ [GeV]	$m_a$ [GeV]	$m_\chi$ [GeV]	$\tan \beta$
1	a	0.35	—	—	10	1.0
	b	0.70	—	—	10	1.0
2	a	0.35	—	250	10	—
	b	0.70	—	250	10	—
3	a	0.35	600	—	10	—
	b	0.70	600	—	10	—
4	a	—	600	200	10	1.0
	b	—	1000	350	10	1.0
5		0.35	1000	400	—	1.0
6		0.35	1200	—	—	1.0
						$(m_a, m_\chi)$

**Table 4.1:** Summary of the parameter settings for the different 2HDM+ $a$  benchmark scenarios explored in this summary.

Monte Carlo simulation is used to model relevant background processes and predictions of the 2HDM+ $a$ . Details on MC generation of various background processes considered in this analysis can be found in the individual studies referenced in Section 4.4. The 2HDM+ $a$  benchmark is implemented in the Universal FeynRules Output (UFO) format [50] and is referred to as `Pseudoscalar_2HDM` throughout this discussion.

With the exception of the  $t b H^\pm(t b)$  process (Table 4.2), all signal processes are generated at leading order (LO) in the strong coupling constant. In this context, LO corresponds to loop-induced gluon-gluon fusion for the  $E_T^{\text{miss}} + X$  signatures, demonstrated for instance in figures 4.1a and 4.1b [40].

Event generation is performed using this UFO implementation with the `MADGRAPH5_AMC@NLO` [52] MC generator, which is interfaced with `PYTHIA 8`[53] to simulate the parton shower and

Analysis	Generator and Parton Shower	Cross-section	Further details
$E_T^{\text{miss}} + Z(\ell\ell)$	MADGRAPH5_AMC@NLO 2.4.3 (LO) + PYTHIA	LO 8.212	
$E_T^{\text{miss}} + h(b\bar{b})$	MADGRAPH5_AMC@NLO 2.6.0 (LO) + PYTHIA	LO 8.212	
$E_T^{\text{miss}} + h(\gamma\gamma)$	MADGRAPH5_AMC@NLO 2.7.3 (LO) + PYTHIA	LO 8.244	
$E_T^{\text{miss}} + h(\tau\tau)$	MADGRAPH5_AMC@NLO 2.7.3 (LO) + PYTHIA	LO 8.244	
$E_T^{\text{miss}} + j$	MADGRAPH5_AMC@NLO 2.7.3 (LO) + PYTHIA	LO 8.244	Section 4.4.6
$E_T^{\text{miss}} + tW$	MADGRAPH5_AMC@NLO 2.7.3 (LO) + PYTHIA	LO 8.244	
$t\bar{t}t\bar{t}$	MADGRAPH5_AMC@NLO 2.9.5 (LO) + PYTHIA	LO 8.245	Reference [11]
$tbH^\pm(tb)$	MADGRAPH5_AMC@NLO 2.2.2 (NLO) + PYTHIA 8.212	NLO, 4FS	Section 4.4.9

**Table 4.2:** Details of the MADGRAPH5\_AMC@NLO generation set-up used for the 2HDM+ $a$  signal samples, for the signatures considered in this publication. The `Pseudoscalar_2HDM` UFO model is used for all simulated samples except those for the  $tbH^\pm(tb)$  search, which relies on the UFO of reference [51]. The  $h \rightarrow$  invisible and  $h \rightarrow aa \rightarrow f\bar{f}f'\bar{f}'$  signatures are not listed here as no signal samples are required for the re-interpretation, which in those cases relies on the branching ratio limits [40].

hadronization. The parameter settings follow the ATLAS tune A14 [54]. Depending on the specific analysis, different versions of MADGRAPH5\_AMC@NLO (ranging from 2.6.0 to 2.9.5) and PYTHIA (from 8.212 to 8.245) were used, as summarized in Table 4.2. These version differences are not expected to impact the signal simulations. The NNPDF3.0NLO [55] parton distribution function (PDF) set, based on next-to-leading-order calculations in the five-flavor scheme, was used, assuming a massless  $b$ -quark and  $\alpha_s(m_Z) = 0.118$  [55].

1049 To maintain consistency, the five-flavor scheme with  $m_b = 0$  GeV was adopted for the  
 1050 matrix element (ME) computation in `MADGRAPH5_AMC@NLO` for  $b\bar{b}$ -initiated produc-  
 1051 tion. In contrast, the four-flavor scheme was used for  $gg$ -initiated production to incorporate  
 1052 top and bottom quark contributions in the production loop. These modelling choices align  
 1053 with the recommendations of the LHC Dark Matter Working Group [12].

1054 To account for pile-up effects, a number of interactions appropriate to the expected pile-  
 1055 up level of the data taking period were simulated using soft QCD processes in `PYTHIA 8.186`  
 1056 with the A3 tune[56] and the MSTW2008LO PDF [57]. These interactions were overlaid onto  
 1057 each simulated hard-scattering event. The generated samples were reweighted to match the  
 1058 instantaneous luminosity distribution observed in data. The simulations also incorporate  
 1059 the expected bunch train structure and include corrections to address related effects.

1060 Simulated events were processed using either a full detector simulation based on `GEANT4` [58,  
 1061 59] or a fast simulation[60] that parametrizes the calorimeter response while relying on  
 1062 `GEANT4` for the rest of the detector. Physics objects in all simulated data samples were  
 1063 reconstructed from detector response following identical procedures as those applied on real  
 1064 data. Additionally, corrections derived from data control samples were applied to the sim-  
 1065 ulations to account for differences between simulation and data in reconstruction efficiency,  
 1066 energy/momentum scale, and resolution of reconstructed electrons and muons. Analogous  
 1067 corrections were also made to account for differences in efficiency and false positive rate in  
 1068 the identification of jets containing  $b$ -hadrons. The energy scale and resolution of hadronic  
 1069 jets were adjusted to ensure consistency between data and simulation.

1070 To efficiently generate signal events across the extensive multi-dimensional parameter  
 1071 space of the 2HDM+ $a$ , the `MADGRAPH` reweighting module [61] was used to obtain predic-  
 1072 tions for various signal model parameters from a minimal set of generated events by assigning  
 1073 new event weights based on the ratio of matrix elements of the generated and target parame-  
 1074 ter points. These weights were computed dynamically during event simulation. The validity

1075 of this approach was confirmed by comparing weighted distributions with directly generated  
1076 ones for select sample cases. This reweighting method significantly reduces computational  
1077 costs, as detector simulation only needs to be performed once.

1078 **4.4 Experimental signatures**

1079 A total of 13 searches in different final states targeting invisible or visible mediator  
1080 decays are included in this summary. No significant deviation from the SM predictions was  
1081 observed in all searches, and instead they are used to derive constraints on the 2HDM+ $a$  for  
1082 the benchmark scenarios introduced in section 4.2. Because the sensitivity of these searches  
1083 varies across different regions of the 2HDM+ $a$  parameter space, most of them are interpreted  
1084 in a subset of the current benchmark scenarios. Table 4.3 summarizes the scenarios in which  
1085 each search is interpreted, and some details are provided in this section. The searches using  
1086  $E_T^{\text{miss}} + h(b\bar{b})$ ,  $E_T^{\text{miss}} + Z(\ell\ell)$  and  $tbH^\pm(tb)$  signatures enter a statistical combination described  
1087 in section 4.6; limit contours from other relevant searches are overlaid on summary plots.

1088 Each analysis targets a different signature and therefore relies on a different set of key  
1089 physics objects identified by various subsystems of ATLAS. Jets are reconstructed from  
1090 particle-flow objects using the anti- $k_t$  algorithm [76, 77, 78]. The radius parameters are  $R =$   
1091 0.4 for small- $R$  jets and  $R = 1.0$  for large- $R$  jets [79]. Small- $R$  jets with  $|\eta| < 2.5$  containing  
1092  $b$ -hadrons are identified with multivariate algorithms [80, 81]. Photons and electrons are  
1093 reconstructed from topologically connected clusters of energy deposits in the electromagnetic  
1094 (EM) calorimeters, with electron showers additionally matched to a charged-particle track  
1095 in the Inner Detector (ID) [82, 83]. Muons are reconstructed by matching tracks in the ID  
1096 and the muon spectrometer (MS), and refining through a global fit using hits from both sub-  
1097 detectors[84]. Different lepton and photon selection criteria, and kinematic requirements are  
1098 employed for particle identification and isolation in the analyses.  $\tau$ -lepton reconstruction  
1099 relies on leptonic or hadronic  $\tau$ -lepton decay targeted by each analysis depending on the

Analysis/Scenario	1a	1b	2a	2b	3a	3b	4a	4b	5	6
$E_T^{\text{miss}} + Z(\ell\ell)$ [14]	x	x	x	x	x	x	x	x	x	x
$E_T^{\text{miss}} + h(b\bar{b})$ [13]	x	x	x	x	x	x	x	x	x	x
$E_T^{\text{miss}} + h(\gamma\gamma)$ [62]	x	x			x	x	x	x		
$E_T^{\text{miss}} + h(\tau\tau)$ [63]	x				x					
$E_T^{\text{miss}} + tW$ [64]	x	x	x	x	x	x	x	x		
$E_T^{\text{miss}} + j$ [65]	x	x			x	x	x	x		
$h \rightarrow \text{invisible}$ [66]	x	x			x				x	
$E_T^{\text{miss}} + Z(q\bar{q})$ [67]	x						x	x		
$E_T^{\text{miss}} + b\bar{b}$ [68]							x	x		
$E_T^{\text{miss}} + t\bar{t}$ [68, 69]							x	x		
$t\bar{t}t\bar{t}$ [70]	x	x	x	x	x	x	x	x	x	x
$tbH^\pm(tb)$ [15]	x	x	x	x	x	x	x	x	x	x
$h \rightarrow aa \rightarrow f\bar{f}f'\bar{f}'$ [71, 72, 73, 74, 75]									x	

**Table 4.3:** Summary of input analyses used in the different benchmark scenarios [40].

given signature [85, 86]. The visible part of hadronically decaying  $\tau$ -leptons is seeded by small- $R$  jets reconstructed from topological clusters, calibrated with a hadronic weighting scheme [87]. The missing transverse momentum  $p_T^{\text{miss}}$  is calculated from the negative vector sum of the transverse momenta  $p_T$  of electrons, muons, jet candidates, and an additional soft term which includes activity in the tracking system originating from the primary vertex but not matched with any reconstructed particle [88]. Some analyses may also consider photons and  $\tau$ -leptons in the  $E_T^{\text{miss}}$  reconstruction.

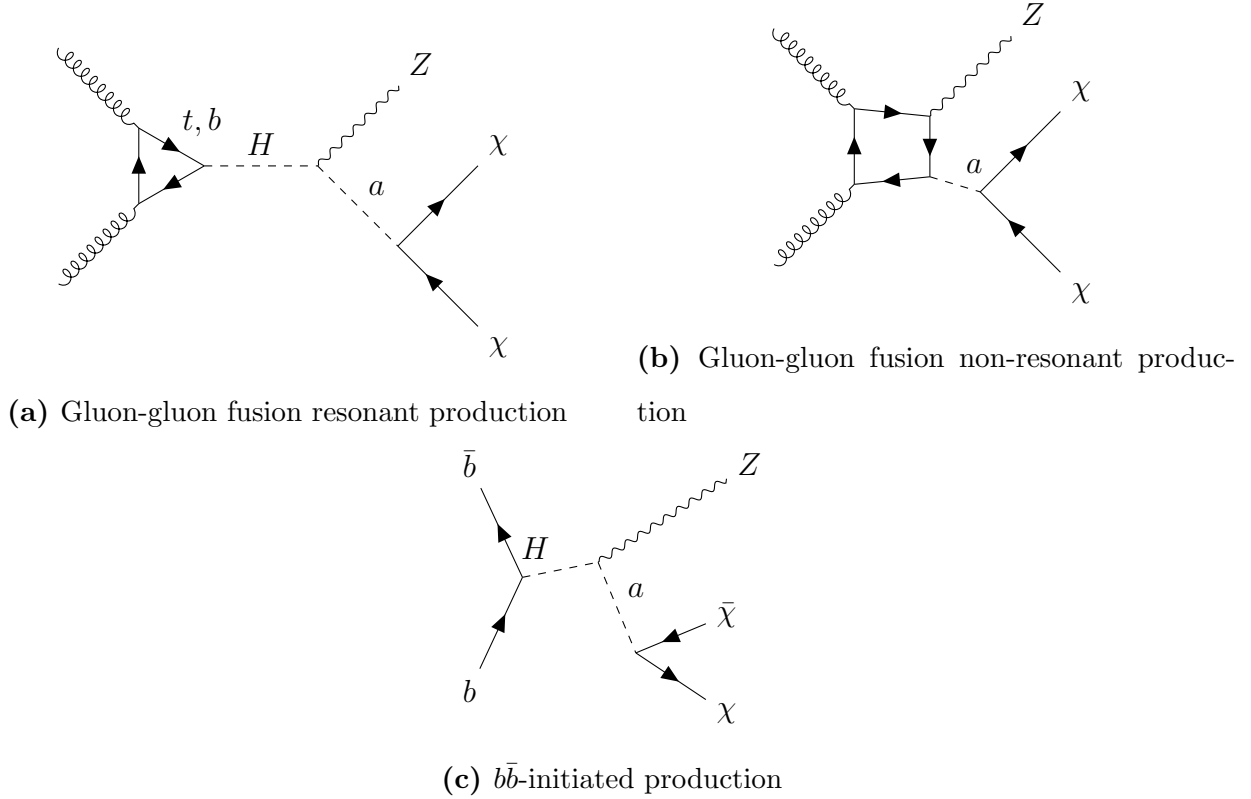


**Figure 4.1:** Representative production mechanisms and final state of the  $E_T^{\text{miss}} + Z(\ell\ell)$  signature, including gluon-gluon fusion resonant (a) and non-resonant production, and (c)  $b$ -initiated production.

#### <sup>1107</sup> 4.4.1 $E_T^{\text{miss}} + Z(\ell\ell)$ signature

<sup>1108</sup> The final state of this signature, shown on figure 4.1, is characterized by the presence of a  
<sup>1109</sup> large  $E_T^{\text{miss}}$  and a pair of high- $p_T$  electrons or muons [14]. Signal events must contain exactly  
<sup>1110</sup> a pair of oppositely charged electrons or muon, with an invariant mass consistent with the  
<sup>1111</sup>  $Z$ -boson mass. The leptons are order in increasing  $p_T$ . The leading lepton is required to  
<sup>1112</sup> have  $p_T > 30$  GeV, and the sub-leading lepton  $p_T > 20$  GeV. The dilepton system must  
<sup>1113</sup> have an invariant mass  $m_{ll}$  in the range  $76 < m_{ll} < 106$  GeV, in accordance with the mass of  
<sup>1114</sup> the  $Z$  boson. The missing transverse momentum is required to have  $E_T^{\text{miss}} > 90$  GeV, and a  
<sup>1115</sup>  $E_T^{\text{miss}}$  significance  $S_{E_T^{\text{miss}}} = \frac{E_T^{\text{miss}}}{\sigma_L \sqrt{1 - \rho_{LT}^2}} > 0$ , in which  $\sigma_L$  denotes the resolution of the  $pT$  of the

system and  $\rho_{LT}$  a correlation factor between the resolutions of the parallel and perpendicular momentum components of the  $E_T^{\text{miss}}$  vector [89]. These quantities are calculated from MC simulation and shown to well describe the data. The requirements of  $E_T^{\text{miss}}$ , in addition to the constraints that the angular separation between the leptons  $\Delta R_{ll} < 1.8$  ensure consistence with invisible particles recoiling against the  $Z$  boson.

The most abundant background is diboson production  $ZZ$ , followed by  $WZ$ ,  $Z + j$ , and non-resonant backgrounds ( $WW$ ,  $t\bar{t}$ , single top-quark,  $Z \rightarrow \tau\tau$ ). Additional backgrounds come from triboson production,  $t\bar{t} + V$ , and  $ZZ \rightarrow 4l$ , where a pair of leptons is not reconstructed.

The  $ZZ$  background is estimated from MC simulation using a 4-lepton control region (CR), which is almost 100% pure in  $ZZ$  events. Events are required to contain two lepton pairs of the same flavour, opposite charge, and  $p_T > 7, 15, 15, 27$  GeV in increasing order of  $p_T$ . If all leptons in the final state are of the same flavour, they are grouped in pair by minimizing the quantity  $|m_{ll1} - m_Z| + |m_{ll2} - m_Z|$ , where the indices 1 and 2 denote the lepton pairs and  $m_Z = 91.19$  GeV. Similar to the signal region (SR), both lepton pairs must have  $76 < m_{ll} < 106$  GeV. The quantities  $E_T^{\text{miss}}$  and  $S_{E_T^{\text{miss}}}$  are calculated similarly as in the SR by treating a random pair of leptons as invisible and excluded from the calculation.

The  $WZ$  background is constrained by a 3-lepton CR, in which two of the leptons have the same flavour and opposite charge to ensure their origin from a  $Z$  boson. This dilepton system, when ordered by increasing  $p_T$  must satisfy  $p_T^1 > 20$  GeV and  $p_T^2 > 30$  GeV, and  $76 < m_{ll} < 106$  GeV. If there is ambiguity in selecting a dilepton pair, the pair closest to the  $Z$  boson in invariant mass is selected. The select events consistent with a  $W$  boson decay, the third lepton is required to have  $p_T > 20$  GeV, the event to have  $E_T^{\text{miss}} > 30$  GeV and  $S_{E_T^{\text{miss}}} > 3$ , and the transverse mass of the  $W$  boson candidate  $m_T^W = \sqrt{2p_T^l E_T^{\text{miss}}(1 - \cos \Delta\phi(l, E_R^{\text{miss}}))} > 60$  GeV, where  $\Delta\phi(l, E_T^{\text{miss}})$  is the azimuthal angle between the third lepton and the  $E_T^{\text{miss}}$  momentum.

1142 Finally, the non-resonant background is constrained primarily by a  $e\mu$  CR, defined simi-  
1143 larly to the SR, with the exception of the lepton flavour requirement. This CR includes  $t\bar{t}$ ,  
1144 single top quark,  $WW$  and  $Z \rightarrow \tau\tau$  events. The remaining backgrounds are estimated from  
1145 MC simulation.

1146 A profile likelihood fit in the  $ee$  and  $\mu\mu$  signal regions and the control regions is used to  
1147 estimate the signal strength. In the SRs and the  $e\mu$  CR, the observable of interest is the  
1148 transverse mass

$$m_T^{lep} = \sqrt{\left[ \sqrt{m_Z^2 + (p_T^{ll})^2} + \sqrt{m_Z^2 + (E_T^{\text{miss}})^2} \right]^2 - [\mathbf{p}_T^{ll} + \mathbf{p}_T^{\text{miss}}]^2}, \quad m_T^{lep} > 200 \text{ GeV} \quad (4.9)$$

1149 while the  $E_T^{\text{miss}}$  is used in the  $4l$ - and  $3l$ -CR. The transverse mass provides a good separation  
1150 between the 2DHM+a signal and the  $ZZ$  background.

#### 1151 4.4.2 $E_T^{\text{miss}} + h(b\bar{b})$ signature

1152 The final state of this signature, shown on figure 4.2, is characterized by a SM Higgs  
1153 boson decaying into two  $b$ -jets and a significant  $E_T^{\text{miss}}$  from the decay of the pseudo-scalar  $a$   
1154 [13]. Hence, selected events must contain at least two jets identified as  $b$ -jets and  $E_T^{\text{miss}} >$   
1155 150 GeV. The angular separation between the two  $b$ -jets is inversely proportional to the  
1156 transverse momentum of the Higgs boson, which is highly correlated to  $E_T^{\text{miss}}$ ; as such, at  
1157  $E_T^{\text{miss}} > 500$  GeV, the dijet system is reconstructed as a single large-radius jet. This motivates  
1158 splitting the events into merged regions and resolved regions, according to the decay topology  
1159 represented by the  $E_T^{\text{miss}}$ .

1160 In  $b$ -associated production (Figure 4.2c), an extra pair of  $b$ -jets is present in the final state  
1161 from gluon splitting. Therefore, the resolved and merged regions are split into a topology  
1162 containing two  $b$ -jets and one containing  $> 3$   $b$ -jets to enhance the sensitivity to both  
1163 production mechanisms, which are significant at different values of  $\tan\beta$ .

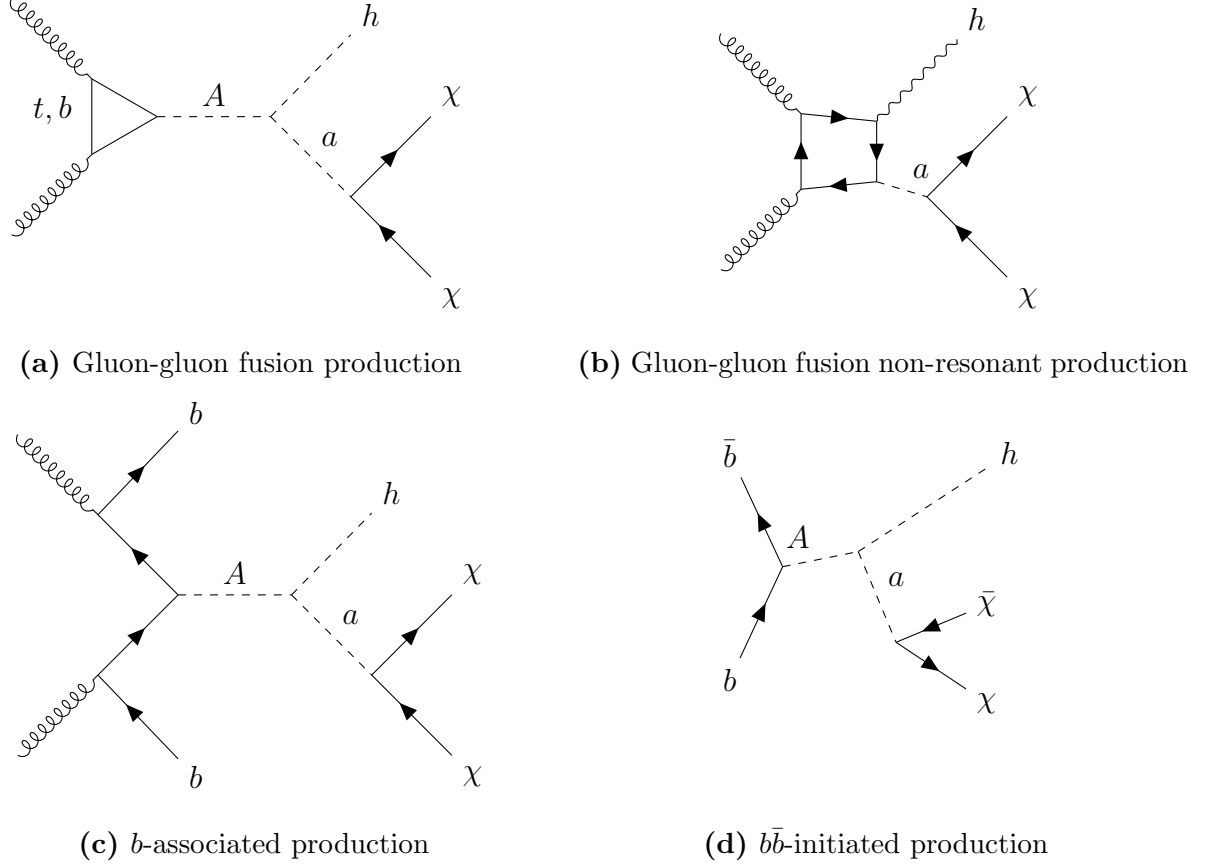


**Figure 4.2:** Production mechanisms and final state of the  $E_T^{\text{miss}} + h(b\bar{b})$  signature including gluon-gluon fusion resonant (a) and non-resonant production,  $b\bar{b}$ -associated production (c) and  $b\bar{b}$ -initiated production (d).

Table 4.4 summarizes the criteria used to select events in the signal regions. Owing to the complex topologies of the final state, event selection is carried out under several sets of selection criteria. First, all events are subjected to an “extended  $\tau$ -lepton veto” which consists of a baseline  $\tau$ -lepton veto, and a veto on small- $R$  jets whose multiplicity is within  $[1, 4]$  with  $\Delta\phi(\text{jet}, E_T^{\text{miss}}) < 22.5 \text{ deg}$ . Events in which any of the leading small- $R$  jets have  $\Delta\phi(\text{jet}, E_T^{\text{miss}}) < 20 \text{ deg}$  are also rejected. A loose selection on the Higgs mass  $m_h$ , defined from primary reconstructed object in each region, is applied.

Resolved	Merged
Primary $E_T^{\text{miss}}$ trigger	
Data quality selections	
$E_T^{\text{miss}} > 150 \text{ GeV}$	
Lepton and extended lepton vetos	
$\Delta\phi(jet_{1,2,3}, E_T^{\text{miss}}) > 20 \text{ deg}$	
$E_T^{\text{miss}} < 500 \text{ GeV}$	$E_T^{\text{miss}} > 500$
$\geq 2$ small- $R$ $b$ -tagged jets	$\geq 1$ large- $R$ jets, $\geq 2$ variable- $R$ $b$ -tagged jets
$p_{T_h} > 100 \text{ GeV}$ if $E_T^{\text{miss}} < 350$ , else $p_{T_h} > 300 \text{ GeV}$	
$m_T^{b,\min} > 170 \text{ GeV}$ , $m_T^{b,\max} > 200 \text{ GeV}$	
$S_{E_T^{\text{miss}}} > 12$	
$\leq 4$ small- $R$ jets (2 $b$ -tag)	
$\leq 5$ small- $R$ jets (3 $b$ -tag)	
$50 < m_h < 280 \text{ GeV}$	$50 < m_h < 270 \text{ GeV}$

**Table 4.4:** Selection criteria used to defined resolved and merged signal regions for the  $E_T^{\text{miss}} + h(b\bar{b})$  signature [13].

In the resolved SRs, events required to have  $E_T^{\text{miss}} < 500 \text{ GeV}$ , and at least 2  $b$ -tagged small- $R$  jets, of which the 2 highest- $p_T$  jets reconstruct the Higgs boson candidate, whose  $p_T$  must exceed 100 GeV. The dominant background in the resolved region is  $t\bar{t}$  production where one top quark decays leptonically but the lepton is misidentified or outright not reconstructed. To suppress this background, the transverse masses of the  $E_T^{\text{miss}}$ , defined for the  $b$ -jet closest to the  $E_T^{\text{miss}}$  in  $\phi$  (denoted  $m_T^{b,\min}$ ), and one furthest from it (denoted  $m_T^{b,\max}$ ) as

$$m_T^{b,\min/\max} = \sqrt{2p_T^{b,\min/\max} E_T^{\text{miss}} (1 - \cos \Delta\phi(p_T^{b,\min/\max}, E_T^{\text{miss}}))} \quad (4.10)$$

must satisfy  $m_T^{b,\min} > 170 \text{ GeV}$  and  $m_T^{b,\max} > 200 \text{ GeV}$ . The 2  $b$ -tag and  $\geq 3$   $b$ -tag regions are split into three bins according to  $E_T^{\text{miss}}$ , namely  $150 < E_T^{\text{miss}} < 200 \text{ GeV}$ ,  $200 < E_T^{\text{miss}} < 350$

<sub>1180</sub> GeV, and  $350 < E_T^{\text{miss}} < 500$  GeV, among which the highest  $E_T^{\text{miss}}$  bin is required to have  
<sub>1181</sub>  $p_{T_h} > 300$  GeV.

<sub>1182</sub> In the merge SRs, defined by  $E_T^{\text{miss}} > 500$  GeV, at least one large- $R$  jet is required and  
<sub>1183</sub> defined as the Higgs boson candidate, and 2 leading variable- $R$  track-jets must be  $b$ -tagged.  
<sub>1184</sub> Events are separated into those having no additional variable- $R$  track jets that are  $b$ -tagged,  
<sub>1185</sub> denoted 2  $b$ -tagged region, and those with at least one not associated with the Higgs boson  
<sub>1186</sub> candidate, denoted  $\geq 3$   $b$ -tagged region, the former of which is split into two  $E_T^{\text{miss}}$  bins,  
<sub>1187</sub> namely  $500 < E_T^{\text{miss}} < 750$  GeV and  $E_T^{\text{miss}} \geq 750$  GeV.

<sub>1188</sub> The most dominant backgrounds are  $t\bar{t}$  and  $W/Z$  boson production with jets from heavy  
<sub>1189</sub> flavour (HF) quarks. The the 2  $b$ -tag regions are dominated by  $t\bar{t}$  and  $Z + HF$  background,  
<sub>1190</sub> the latter of which becomes more important with increasing  $E_T^{\text{miss}}$ . In the 3  $b$ -tag regions,  
<sub>1191</sub> the main background is  $t\bar{t}$ , where the third jet, originating from a hadronic  $W$  decay, is  
<sub>1192</sub> mis-tagged as a  $b$ -jet. These backgrounds are modelled using MC simulation and corrections  
<sub>1193</sub> from data. Smaller backgrounds including single-top, diboson, and SM  $Vh$  production are  
<sub>1194</sub> modelled solely by simulation.

#### <sub>1195</sub> 4.4.3 $E_T^{\text{miss}} + h(\gamma\gamma)$ signature

<sub>1196</sub> The  $E_T^{\text{miss}} + h(\gamma\gamma)$  the  $E_T^{\text{miss}} + h(b\bar{b})$ , and the  $E_T^{\text{miss}} + h(\tau\tau)$  signatures in the next subsection  
<sub>1197</sub> share the same production mechanisms, shown in figure 4.2, differing only in the decay  
<sub>1198</sub> products of the SM Higgs boson. The  $h \rightarrow \gamma\gamma$  decay, despite a small branching ratio,  
<sub>1199</sub> benefits from excellent photon resolution and a clean Higgs signal [62]. The final state  
<sub>1200</sub> contains two photons and significant  $E_T^{\text{miss}}$ . Events must therefore pass a diphoton trigger  
<sub>1201</sub> with two reconstructed photon candidates having  $E_T^{\gamma,\text{lead}} \geq 35$  GeV and  $E_T^{\gamma,\text{sublead}} \geq 25$  GeV,  
<sub>1202</sub> and have  $E_T^{\text{miss}} > 90$  GeV. The Higgs boson candidate is constructed from the two photons  
<sub>1203</sub> with the largest  $E_T$ , if they satisfy  $E_T^{\gamma,\text{lead}}/m_{\gamma\gamma} > 0.35$  and  $E_T^{\gamma,\text{sublead}}/m_{\gamma\gamma} > 0.25$ . The  
<sub>1204</sub> invariant mass of the diphoton system must be compatible with the Higgs mass, such that

1205     $105 < m_{\gamma\gamma} < 160$  GeV. Events are separated into two categories, i.e. a low- $E_T^{\text{miss}}$  region with  
 1206     $E_T^{\text{miss}} < 150$  GeV, and a high- $E_T^{\text{miss}}$  region with  $E_T^{\text{miss}} > 150$  GeV. A machine learning classifier  
 1207    based on Boosted Decision Trees (BDT) is trained to distinguish the 2HDM+ $a$  signal from  
 1208    non-resonant background. In each  $E_T^{\text{miss}}$  region, the BDT score spectrum is divided into two  
 1209    categories, whose boundary is optimized for the combined signal sensitivity.

1210    SM Higgs boson production, QCD-induced non-resonant diphoton production, and re-  
 1211    ducible contributions from misidentified electrons or jets as photons and  $E_T^{\text{miss}}$  generated by  
 1212    particles outside of detector acceptance or by neutrinos constitute the primary background.  
 1213    In the low  $E_T^{\text{miss}}$  region, significant background arises from inaccurate  $E_T^{\text{miss}}$  reconstruction  
 1214    from high-energy objects and soft interactions in the ID. The photon invariant mass serves  
 1215    as the observable of interest to estimate various background contributions in each category  
 1216    using an analytic function.

#### 1217    4.4.4    $E_T^{\text{miss}} + h(\tau\tau)$ signature

1218    This search target a final state consisting of a Higgs boson decaying into a pair of  $\tau$ -  
 1219    leptons, which then decay hadronically, and a large  $E_T^{\text{miss}}$  [63]. The production mechanisms,  
 1220    similar to those of the  $E_T^{\text{miss}} + h(b\bar{b})$  and  $E_T^{\text{miss}} + h(\gamma\gamma)$ , are shown in figure 4.2. Selected  
 1221    events contain exactly two  $\tau$ -lepton objects of opposite charge that activate the di- $\tau_{had-vis}$   
 1222    trigger [90]. Event containing an electron or a muon are vetoed. Two SRs are defined to  
 1223    enhance the sensitivity to the 2HDM+ $a$  signal. Events are required to pass a set of common  
 1224    selections, shown in table 4.5, to reduce the dominant SM background processes. The limit  
 1225    on angular distance between the  $\tau$ -leptons suppresses the backgrounds involving  $\tau$ -leptons  
 1226    that do not come from a resonant decay (such as  $t\bar{t}$  and  $W+jets$ ). The event-level transverse  
 1227    mass is defined as

$$m_T^{tot} = \sqrt{(p_T^{\tau_1} + p_T^{\tau_2} + p_T^{\text{miss}})^2 - (p_{T,x}^{\tau_1} + p_{T,x}^{\tau_2} + p_{T,x}^{\text{miss}})^2 - (p_{T,y}^{\tau_1} + p_{T,y}^{\tau_2} + p_{T,y}^{\text{miss}})^2}, \quad (4.11)$$

1228 and the transverse mass of a  $\tau$ -lepton as

$$m_T^{\tau_i} = \sqrt{2p_T^{\tau_i} E_T^{\text{miss}} (1 - \cos \Delta\phi(\tau_1, p_T^{\text{miss}}))}. \quad (4.12)$$

1229 The sum of the  $\tau$  transverse mass is required to be larger than 100 GeV to reduce  $Z$  boson  
1230 decay background. The low- $m_A$  region is defined with  $m_A < 800$  GeV, in which the  
1231 angular distance between the  $\tau$ -leptons is limited to [0.6, 1.9], their visible invariant mass  
1232  $m_{\text{vis}}(\tau_1, \tau_2)$  to  $[75, \infty]$  GeV, and the individual transverse mass  $m_T^{\tau_1}, m_T^{\tau_2}$  to  $> 50$  GeV and  
1233  $> 25$  GeV, respectively. The high- $m_A$  corresponds to signal events with higher  $E_T^{\text{miss}}$  and  
1234 boosted Higgs boson, improving the sensitivity to 2HDM+ $a$  signal at high  $m_A$  masses. It  
1235 requires  $m_T^{\text{tot}} > 400$  GeV, and  $m_T^{\tau_1} + m_T^{\tau_2} > 400$  GeV. Both regions are binned according to  
1236 table 4.5

1237 Primary backgrounds include  $Z$  boson and multiboson production, and  $t\bar{t}$  production  
1238 decaying into two true  $\tau$ -leptons. Other background contributions arise from  $W$  boson and  
1239 multijet production, in which at least one reconstructed  $\tau$ -lepton is fake. These backgrounds  
1240 are estimated using both simulation and data-driven methods.

#### 1241 4.4.5 $E_T^{\text{miss}} + tW$ signature

1242 This search targets a final state with a  $W$  boson produced in association with a top  
1243 quark and a large  $E_T^{\text{miss}}$  resulting from invisible decay of the pseudo-scalar mediator  $a$  (figure  
1244 4.3) [64]. The primary top quark overwhelmingly to a  $W$  boson and a bottom quark, and  
1245 thus the final state is characterized by the decay channel of the two  $W$  bosons. The  $tW_{0L}$   
1246 channel target events in which both boson decay hadronically, and the  $tW_{1L}$  targets one  
1247 boson decaying leptonically and the other hadronically. The result from a previous search  
1248 targeting two charged leptons [91] in the final state is also included in the interpretation.  
1249 Zero-lepton and one-lepton signal regions enter the statistical combination.

Low $m_A$ SR	High $m_A$ SR
$\Delta R(\tau_1, \tau_2) < 2$	
$m_T^{tot} > 50$ GeV	
$40 < m_{vis}(\tau_1, \tau_2) < 125$ GeV	
$m_T^{\tau_1} + m_T^{\tau_2} > 100$ GeV	
$q(\tau_1)q(\tau_2) = -1$	
$N_{b-jet} = 0$	
$0.6 < \Delta R(\tau_1, \tau_2) < 1.9$	
	$m_T^{tot} > 400$ GeV
$m_T^{\tau_1} > 50$ GeV	
$m_T^{\tau_2} > 25$ GeV	
$m_{vis}(\tau_1, \tau_2) > 75$ GeV	$40 < m_{vis}(\tau_1, \tau_2) < 125$ GeV
$m_T^{\tau_1} + m_T^{\tau_2}$ bins $[100, 125, 400, 550, \infty]$ GeV	$[400, 750, \infty]$ GeV

**Table 4.5:** Selection criteria used to define low- and high- $m_R$  signal regions for the  $E_T^{\text{miss}} + h(\tau\tau)$  signature [63].

The search is sensitive to on-shell production of the charged Higgs bosons and their semi-visible decay. In both  $tW_{0L}$  and  $tW_{1L}$  channels, the hadronically decaying  $W$  boson is reconstructed as a single  $W$ -tagged large- $R$  jet due to its high  $p_T$ . Important background processes vary across different channels, but usually arise from genuine  $E_T^{\text{miss}}$  associated with neutrinos, or  $E_T^{\text{miss}}$  produced by particles which are misidentified, mismeasured, or outside of the detector's kinematic acceptance. For example,  $Z+jet$  in the  $tW_{0L}$  channel and  $W+jet$  in the  $tW_{1L}$  channel are both genuine  $E_T^{\text{miss}}$  background.  $t\bar{t}$  production and  $W+jet$  production in  $tW_{0L}$  are dominant background containing fake  $E_T^{\text{miss}}$ . Other significant contributions originate from  $t\bar{t}Z$  and single top quark production. These backgrounds are estimated from MC simulation via 6 dedicated control regions.

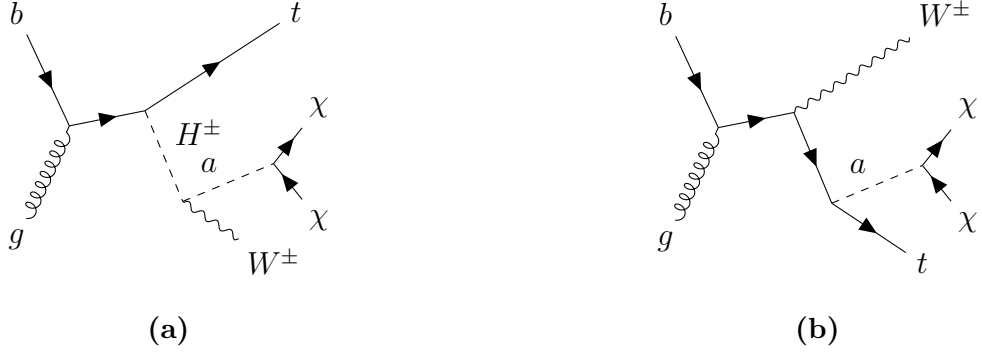


**Figure 4.3:** Production mechanisms and final state of the  $E_T^{\text{miss}} + tW$  signature.

#### 1260 4.4.6 $E_T^{\text{miss}} + j$ signature

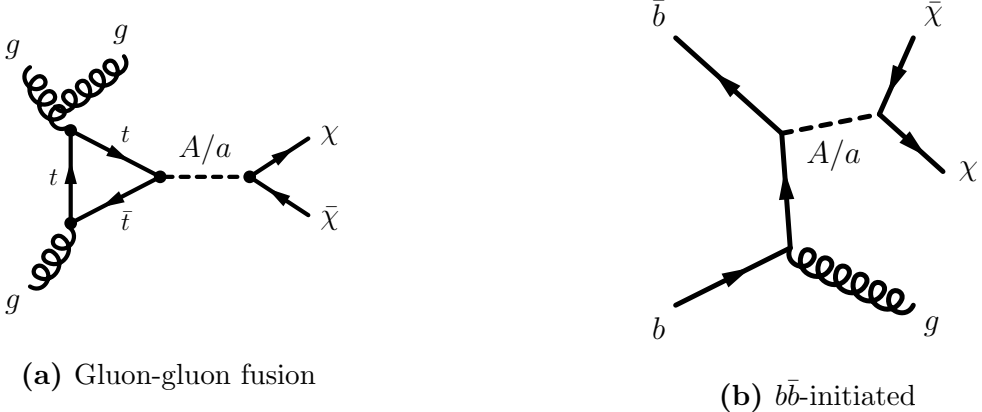


**Figure 4.4:** Production mechanisms and final state of the  $E_T^{\text{miss}} + j$  signature, including gluon-gluon fusion production (a) and  $b\bar{b}$ -initiated production (b).

1261 This search targets final states containing a single jet and a large  $E_T^{\text{miss}}$ , which must  
 1262 satisfy  $E_T^{\text{miss}} > 200$  GeV to guarantee full  $E_T^{\text{miss}}$  trigger efficiency for all selected events [65].  
 1263 Events must contain a leading jet with  $p_T > 150$  GeV,  $|\eta| < 2.4$ , up to three additional jets  
 1264 with  $p_T > 30$  GeV,  $|\eta| < 2.8$ , and no leptons or photons. The azimuthal angular separation  
 1265 between the  $E_T^{\text{miss}}$  vector and each jet is required to meet  $\Delta\phi(E_T^{\text{miss}}, \text{jet}) > 0.6$  for events  
 1266 with  $200 < E_T^{\text{miss}} < 250$  GeV, and  $\Delta\phi(E_T^{\text{miss}}, \text{jet}) > 0.4$  for those with  $E_T^{\text{miss}} > 250$  GeV to  
 1267 reduce multijet backgrounds.

Dominant SM backgrounds include  $Z(\nu\nu)$  and  $W(l\nu)$  production, in which the  $W$  decays into a  $\tau$ -lepton which later decays hadronically, or other leptons that are undetected. Other contributions arise from  $t\bar{t}$ , single top quark, and diboson production, as well as non-collision and multijet backgrounds. These background contributions are estimated using a profile likelihood fit to the  $p_T$  distribution of the system recoiling against the reconstructed jets in both signal and control regions.

In this combination, the search is reinterpreted in the context of 2HDM+ $a$ , which is not considered in the original search. Several signal contributions to this signature are considered. In the low- $E_T^{\text{miss}}$  region, the production of a pair of DM particles with a jet is the primary contribution at  $E_T^{\text{miss}} < 500 \text{ GeV}$   $m_a \leq 150 \text{ GeV}$ . Both  $gg$ -initiated and  $bb$ -initiated productions are considered, the latter of which is relevant at large  $\tan\beta$ . For larger  $E_T^{\text{miss}}$  and smaller  $m_a$ , the production of two pairs of DM particles via  $h \rightarrow aa \rightarrow \chi\bar{\chi}\chi\bar{\chi}$  (figure 4.7) is the dominant process. Smaller contributions come from  $E_T^{\text{miss}} + Z(q\bar{q})$  and  $E_T^{\text{miss}} + h(b\bar{b})$  productions which the invisible decays of the SM Higgs boson are kinematically forbidden. Finally, minor contributions from  $pp \rightarrow t\bar{t} + a$ , and  $pp \rightarrow tW + a$  are also present.

#### 4.4.7 $h \rightarrow$ invisible signature

The invisible decays of the SM Higgs boson represented by a  $E_T^{\text{miss}}$  associated to other visible signatures have been investigated in previous ATLAS publications and statistically combined in reference [66]. The main production mechanisms include vector-boson fusion (VBF) [92], VBF with an emitted photon [93], gluon-gluon fusion [65], associated production with a vector boson [14], and associated production with a pair of top quarks [94]. The results from Run 2 searches are combined statistically with constraints on invisible Higgs decays obtained from searches with up to  $4.7 \text{ fb}^{-1}$  of  $pp$  collision data at  $\sqrt{s} = 7 \text{ TeV}$  and  $20.3 \text{ fb}^{-1}$  at  $\sqrt{s} = 8 \text{ TeV}$  [95].

1292 Among these searches,  $h \rightarrow$  invisible from VBF production from Run 2 is the most  
 1293 sensitive and sets an observed limit of 0.145 and an expected limit of 0.103 at 95% confidence  
 1294 level on the invisible branching ratio. Selected events are required to pass the  $E_T^{\text{miss}}$  trigger  
 1295 and have  $E_T^{\text{miss}} > 160$  GeV. They must also contain from two to four jets with  $p_T > 25$  GeV,  
 1296 among which the leading and sub-leading jets must have  $p_T^{\text{lead}} > 80$  GeV and  $p_T^{\text{sub-lead}} > 50$   
 1297 GeV and be well separated in  $\eta$ . In addition, lepton and  $b$ -jet vetoes are applied to reduce  $W +$   
 1298 *jets* and top quark backgrounds. By partitioning the  $E_T^{\text{miss}}$  spectrum, the jet multiplicity, and  
 1299 jet-invariant masses, sixteen orthogonal signal regions are defined. Dominant background  
 1300 processes include  $Z(\nu\nu) + \text{jet}$  and  $W(l\nu) + \text{jet}$  production, the latter of which the charged  
 1301 lepton is undetected or misidentified. The backgrounds are estimated from control regions  
 1302 in the one-lepton and two-lepton channels. The multijet background is directly estimated  
 1303 from data. An upper limit on the  $h \rightarrow$  invisible of  $0.113 (0.080^{+0.031}_{-0.022})$  is observed (expected)  
 1304 at 95% confidence level.

1305 **4.4.8 Additional searches using  $36 \text{ fb}^{-1}$  of  $\sqrt{s} = 13 \text{ TeV}$   $pp$  collision  
 1306 data**

1307 Three searches using  $36 \text{ fb}^{-1}$  of  $\sqrt{s} = 13 \text{ TeV}$  data are shown in this combination, the  
 1308 first of which targets  $E_T^{\text{miss}} + Z(q\bar{q})$  signature [67]. The final state contains a  $E_T^{\text{miss}} > 150$   
 1309 GeV and a hadronically decaying vector boson reconstructed as a single large- $R$  jet with  
 1310  $p_T > 250$  GeV in a boosted topology and two small- $R$  jets with  $p_T > 20$  GeV in a resolved  
 1311 topology. A lepton veto is applied in both cases. Signal regions are defined using the number  
 1312 of  $b$ -jets in the final state. The dominant backgrounds of  $t\bar{t}$  and  $W/Z + \text{jets}$  are estimated  
 1313 using a simultaneous fit to the  $E_T^{\text{miss}}$  distribution in the signal and control regions.

1314 The second search targets a  $E_T^{\text{miss}} + b\bar{b}$  signature. The final state contains at least two  $b$ -  
 1315 jets and  $E_T^{\text{miss}} > 180$  GeV [68]. The irreducible background from  $Z(\nu\nu) + b\bar{b}$  events separated  
 1316 from the signal events using the azimuthal separation between the  $b$ -jets and the  $E_T^{\text{miss}}$ . The

1317 results are extracted from a likelihood fit to the angular observable  $\cos\theta_{b\bar{b}} = |\tanh\Delta\eta_{n\bar{b}}/2|$ ,  
1318 in which  $\Delta\eta_{n\bar{b}}$  is the difference in pseudorapidity between the  $b$ -jets.

1319 The last group of searches targeting  $E_T^{\text{miss}} + t\bar{t}$  and differing the the number of final-state  
1320 leptons are included [68]. A search in the final state where both  $W$  bosons decay hadronically  
1321 selects events with at least four energetic jets, of which at least two are  $b$ -jets, and a large  
1322  $E_T^{\text{miss}}$ . Several requirements on the invariant mass of the large- $R$  jets are applied to identify  
1323 events with a boosted  $W$  boson or top quark decay. The main backgrounds are  $Z + \text{jets}$ ,  
1324  $t\bar{t}$ , and  $t\bar{t} + Z$  production, constrained using dedicated control regions. A search in the  
1325 one-lepton final state, resulting from a leptonically decaying  $W$  boson, selects events with at  
1326 least four energetic jets, at least one of which is a  $b$ -jet, an isolated lepton, and a large  $E_T^{\text{miss}}$   
1327 [69]. They must also have at least one hadronic top candidate with invariant mass close  
1328 to the top quark mass. The azimuthal separation between the lepton and  $E_T^{\text{miss}}$  and that  
1329 between the jets and  $E_T^{\text{miss}}$  are used to suppress the background contamination in the signal  
1330 regions. Dedicated control regions are used to estimate background processes involving top  
1331 quarks.

#### 1332 4.4.9 $tbH^\pm(tb)$ signature

1333 The leading-order Feynman diagram for the target signature of this search is shown in  
1334 figure 4.5 [15]. The charged Higgs boson is produced together with a top and a bottom  
1335 quark, and subsequently decays into a top and a bottom quark, in which one top quark  
1336 decays semi-leptonically. Events are preselected to contain exactly one electron or muon  
1337 with  $p_T > 27$  GeV and at least five jets with  $p_T > 25$  GeV. At least three jets must be  
1338  $b$ -tagged to reduce large backgrounds from multijet production. Selected events are divided  
1339 into four separate regions, namely  $5j3b$ ,  $5j \geq 4b$ ,  $\geq 6j3b$ , and  $\geq 6j \geq 4b$ , where  $j$  and  $b$   
1340 respectively stand for jets and  $b$ -jets. A neural network is trained to discriminate between  
1341 signal and background, whose output distributions are used to extract the signal in data.

1342 Dominant backgrounds include  $t\bar{t} + jets$ , and single top quark production in the  $Wt$   
1343 channel. The former is divided into  $t\bar{t} + \text{light}$ ,  $t\bar{t}+ \geq 1b$ , and  $t\bar{t}+ \geq 1c$ . These along with  
1344 other minor backgrounds are model using MC simulation and corrections obtained from an  
1345 additional  $\geq 5j2b$  region via a reweighting procedure [96, 97]. After the reweighting, the  
1346  $t\bar{t}+ \geq 1b$  and  $t\bar{t}+ \geq 1c$  normalizations factors are extracted from the fit to data.

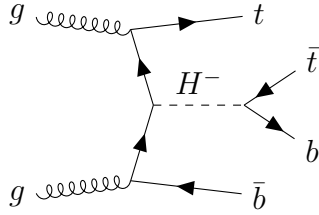


**Figure 4.5:** Production mechanisms and final state of the  $tbH^\pm(tb)$  signature.

#### 1347 4.4.10 $t\bar{t}t\bar{t}$ signature

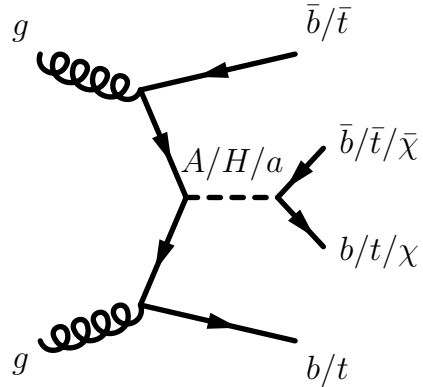


**Figure 4.6:** Production mechanisms and final state of the  $t\bar{t}t\bar{t}$ ,  $E_T^{\text{miss}} + b\bar{b}$ , and  $E_T^{\text{miss}} + t\bar{t}$  signatures.

1348 The targeted signature of this search, shown in figure 4.6, is a  $t\bar{t}$ -associated production  
1349 of a heavy scalar or pseudo-scalar Higgs boson in the 2HDM+ $a$ , which then decays into a  
1350 pair of top quarks[70]. The final state contains 2 pairs of top quarks, decaying into either  
1351 two leptons with the same-sign electric charge or at least three leptons, both with high  
1352 jet multiplicity. These leptons include electrons or muons from leptonic  $\tau$  decay, and are  
1353 required to have  $p_T > 28$  GeV. A baseline signal region is defined by requiring six jets with

<sup>1354</sup>  $p_T > 25$  GeV, among which at least two are  $b$ -tagged, and a scalar sum of the all transverse  
<sup>1355</sup> momenta of jets and leptons  $H_T > 500$  GeV. First, a BDT is trained to separate SM  $t\bar{t}t\bar{t}$   
<sup>1356</sup> production and background processes using event-level inputs. A second BDT, designated  
<sup>1357</sup> BSM mass-parametrised BDT (BSM pBDT), is then trained to discriminate between BSM  
<sup>1358</sup>  $t\bar{t}t\bar{t}$  events and all background. It is parametrised as a function of the mass of the heavy  
<sup>1359</sup> Higgs boson by introducing the mass as an input in the training [98].

<sup>1360</sup> The major irreducible backgrounds arise from the top quark pair production with a boson  
<sup>1361</sup> and jets ( $t\bar{t} + W + \text{jets}$ ,  $t\bar{t} + Z + \text{jets}$ , and  $t\bar{t} + h + \text{jets}$ ). These contributions are estimated  
<sup>1362</sup> using MC simulations with data-driven corrections for  $t\bar{t} + W + \text{jets}$ . Minor, irreducible  
<sup>1363</sup> backgrounds originate mostly from  $t\bar{t} + \text{jets}$  and  $tW + \text{jets}$  production with misidentified  
<sup>1364</sup> charge, fake and non-prompt leptons, which are estimated from data using dedicated control  
<sup>1365</sup> regions.

<sup>1366</sup> **4.4.11 Exotic Higgs boson decays  $h \rightarrow aa \rightarrow f\bar{f}f'\bar{f}'$**

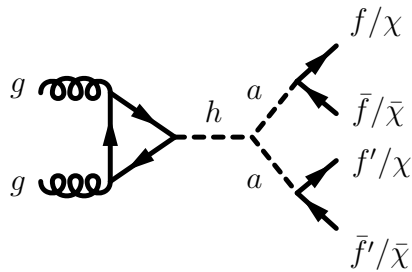


**Figure 4.7:** Production mechanisms and final state of the  $h \rightarrow aa \rightarrow f\bar{f}f'\bar{f}'$  signature.

<sup>1367</sup> This set of searches target the decays of the SM Higgs boson into a pair of light pseudo-  
<sup>1368</sup> scalar particles  $aa$ , which then decay into four fermions, as illustrated in figure 4.7. De-  
<sup>1369</sup> pending on the type of fermion present in the final state, the searches provide sensitivity to  
<sup>1370</sup> different pseudo-scalar mass ranges.

1371        The first search uses  $139 \text{ fb}^{-1}$  of  $\sqrt{s} = 13 \text{ TeV}$   $pp$  collision data, and targets the  $b\bar{b}\mu^+\mu^-$   
 1372        final state [71]. It is sensitive to pseudo-scalar mass in the range  $16 < m_a < 62 \text{ GeV}$ . The  
 1373        variable of interest is the dimuon invariant mass, chosen to probe for a resonant enhance-  
 1374        ment over the SM expectation. The dominant background is the Drell-Yan dimuon process  
 1375        together with  $b$  quarks and SM  $t\bar{t}$  production where both  $W$  bosons from the top quarks  
 1376        decay into a muon and a neutrino.

1377        A second search using  $36 \text{ fb}^{-1}$  of  $\sqrt{s} = 13 \text{ TeV}$   $pp$  collision data targeting  $b\bar{b}b\bar{b}$  final  
 1378        state provides sensitivity in the mass range  $20 < m_a < 60 \text{ GeV}$  [72]. The Higgs boson  
 1379        is produced in association with a leptonically decaying  $W$  boson (one-lepton channel) or  $Z$   
 1380        boson (two-lepton channel). Signal-background separation is performed with a BDT trained  
 1381        using event-level kinematic variables, notably the reconstructed pseudo-scalar masses. The  
 1382        dominant background process in the one-lepton channel is  $t\bar{t}$  production with additional  
 1383        jets, and  $Z + jet$  in the two-lepton channel. The BDT output distribution is used as the  
 1384        observable of interest in the final likelihood fit. This search is optimized for the resolved  
 1385        topology of the  $b\bar{b}$  dijet system, i.e. they are reconstructed as two small- $R$  jets.

1386        A third search on  $20.3 \text{ fb}^{-1}$  of  $\sqrt{s} = 8 \text{ TeV}$   $pp$  collision targeting  $\mu^+\mu^-\tau^+\tau^-$  probes the  
 1387        mass range  $3.7 < m_a < 50 \text{ GeV}$ . It probes resonant enhancement in the dimuon invariant  
 1388        mass spectrum [73].

1389        The last searches considered in this combination target final states with four charged  
 1390        leptons ( $l = e, \mu$ ) on  $36 \text{ fb}^{-1}$  and  $139 \text{ fb}^{-1}$  of  $\sqrt{s} = 13 \text{ TeV}$  [74, 75]. They probe two  
 1391        orthogonal pseudo-scalar mass regions, namely a low-mass region covering  $1 < m_a < 15$   
 1392        GeV range, excluding the mass ranges around the  $J/\psi$  and the  $\Upsilon$  resonances, and a high-mass  
 1393        region covering  $15 < m_a < 60 \text{ GeV}$ . The high-mass range is insensitive to 2HDM+ $a$  and  
 1394        therefore excluded from this combination. The final states containing at least four muons are  
 1395        exclusively considered thanks to their large branching ratio and the large selection efficiency  
 1396        of isolated muons relative to that of isolated electrons. The dominant background process is

<sup>1397</sup>  $ZZ^* \rightarrow \mu^+\mu^-\mu^+\mu^-$  and  $h \rightarrow ZZ^* \rightarrow \mu^+\mu^-\mu^+\mu^-$ . The observable of interest is the average  
<sup>1398</sup> dimuon invariant mass  $\langle m_{\mu^+\mu^-} \rangle = (m_{12} + m_{34})/2$ , in which the pairing is done to minimize  
<sup>1399</sup> the dimuon invariant mass difference.

<sup>1400</sup> Model-independent upper limit on the branching ratio of the  $h \rightarrow aa \rightarrow 4f$  are obtained.  
<sup>1401</sup> The upper limit is used directly to exclude parameter regions in the 2HDM+ $a$  based on  
<sup>1402</sup> the predicted  $h \rightarrow aa \rightarrow 4f$  branching ratio for each point considered in the benchmark  
<sup>1403</sup> scenarios in the previous section.

## <sup>1404</sup> 4.5 Systematic uncertainties

<sup>1405</sup> Systematic and statistical uncertainties depend on event selection, the considered phase  
<sup>1406</sup> space, and the background estimation strategy. Systematic uncertainties may be of experi-  
<sup>1407</sup> mental or theoretical origin. In general, experimental uncertainties may include uncertainties  
<sup>1408</sup> in the absolute jet energy scales and resolutions, jet quality requirements, pile-up corrections,  
<sup>1409</sup>  $b$ -jet identification efficiencies, and the soft contributions to  $E_T^{\text{miss}}$ . Uncertainties in lepton  
<sup>1410</sup> identification and reconstruction efficiencies, energy/momentum scale and resolution are con-  
<sup>1411</sup> sidered from events with selected or vetoed leptons. Uncertainties due to the finite size of the  
<sup>1412</sup> background MC samples and others related to the modelling of the background processes are  
<sup>1413</sup> also included in the analyses. A luminosity uncertainty of 1.7% is applied to backgrounds  
<sup>1414</sup> derived purely from MC simulation [99].

<sup>1415</sup> Theoretical uncertainties on the production cross-section or on the signal acceptance  
<sup>1416</sup> affect signal modelling. They include uncertainties related to the PDF and are evaluated  
<sup>1417</sup> following the PDF4LHC recommendations [100]. Other uncertainties pertain to the choice  
<sup>1418</sup> of renormalization and factorization scales. They are derived by varying independently such  
<sup>1419</sup> scales by a factor of 2.0 and 0.5 relative to the nominal values used for MC generation. In  
<sup>1420</sup> addition, for signatures entering the statistical combination, uncertainties in the modelling  
<sup>1421</sup> of initial- and final-state radiation and multi-parton interactions are taken into account.

## 1422 4.6 Statistical combination of results

1423 Three 2HDM+ $a$  signatures are selected to enter a statistical combination, namely  $E_T^{\text{miss}} +$   
1424  $h(b\bar{b})$ ,  $E_T^{\text{miss}} + Z(\ell\ell)$ , and  $tbH^\pm tb$ . They cover complementary regions of the model parameter  
1425 space, and are the most constraining signatures of those described in 4.4. These factors  
1426 simplify the statistical treatment and enhance the sensitivity to the 2HDM+ $a$  signal.

1427 These input analyses are statistically independent, due to their event selection. The  
1428  $E_T^{\text{miss}} + Z(\ell\ell)$  analysis vetoes events with  $b$ -jets, whereas the other analyses require the  
1429 presence of at least two jets. The  $tbH^\pm(tb)$  targets final states with a charged lepton, while  
1430  $E_T^{\text{miss}} + h(b\bar{b})$  vetoes the presence thereof. Therefore, the signal region of these analyses are  
1431 completely separated. A small event overlap ( $< 1\%$ ) is observed between  $tbH^\pm(tb)$  signal  
1432 region and the leptonic control region of the  $E_T^{\text{miss}} + h(b\bar{b})$  analysis, but has no impact on  
1433 the combination.

### 1434 4.6.1 Statistical analysis

1435 To statistically combine the results of these analyses, a combined likelihood function is  
1436 constructed and the corresponding profile likelihood ratio maximized [101]. The common  
1437 parameter of interest (POI) is the signal strength of a 2HDM+ $a$  signal at a particular point  
1438 in the parameter space, defined as the ratio of the observed number of signal event to  
1439 the signal cross-section times branching ratio. Systematic uncertainties are introduced to  
1440 the likelihood as constrained nuisance parameters (NPs), denoted by  $\theta_\mu$ , and modelled by  
1441 Gaussian, Poisson, or Log-normal probability density function. Background normalization  
1442 factors, denoted by  $\lambda_\mu$ , are floated without constraints in the fit to estimate the background  
1443 components in their corresponding control regions. The subscript  $\mu$  on these parameter is  
1444 in anticipation of their dependence on the best-fit signal strength.

1445 The combined likelihood is given by

$$L(\text{data}|\mu, \lambda_\mu, \theta_\mu) = \prod_{c=1}^{N_{cats}} L_c(\text{data}|\mu, \lambda_\mu, \theta_\mu) \prod_{k=1}^{N_{cons}} F(\tilde{\theta}_{\mu,k}|\theta_{\mu,k}), \quad (4.13)$$

1446 where  $N_{cats}$  is the number of categories,  $c$  the index of the event category,  $N_{cons}$  the number  
1447 of constrained NPs,  $k$  the index of the NP,  $\tilde{\theta}_{\mu,k}$  the global observable corresponding to  $\theta_k$ , and  
1448  $F$  the constraining probability distribution function corresponding to the type of uncertainty.

1449 The likelihood of observing  $m_c$  events in category  $c$  is

$$L_c(\text{data}|\mu, \lambda_\mu, \theta_\mu) = \frac{n_c^{m_c} e^{-n_c}}{m_c!}, \quad n_c = \mu s_c(\theta_\mu) + \lambda_\mu b_c(\theta_\mu), \quad (4.14)$$

1450 in which  $s_c$  and  $b_c$  are expected signal and background yields. The likelihood can be globally  
1451 maximized or conditional on a particular value of  $\mu$ .

1452 The 95% confidence level (CL) limits are obtained by the CLs frequentist formalism [102]  
1453 using the profile likelihood ratio test statistics ( $q_\mu$ )[101], defined as

$$q_\mu = \begin{cases} -2 \ln \frac{L(\text{data}|\mu, \hat{\lambda}_\mu, \hat{\theta}_\mu)}{L(\text{data}|0, \hat{\lambda}_0, \hat{\theta}_0)} & \hat{\mu} < 0, \\ -2 \ln \frac{L(\text{data}|\mu, \hat{\lambda}_\mu, \hat{\theta}_\mu)}{L(\text{data}|\hat{\mu}, \hat{\lambda}_\mu, \hat{\theta}_\mu)} & 0 \leq \hat{\mu} < \mu, \\ 0 & \hat{\mu} > \mu \end{cases} \quad (4.15)$$

1454 where the numerator is the likelihood maximized for a given fixed value of  $\mu$ , and the  
1455 denominator is the globally maximized likelihood. The single-hat quantities denote the global  
1456 optimum values, while the double-hat quantities denote the optima at  $\mu$ , i.e. a function of  
1457  $\mu$ . The confidence level is determined from the  $p$ -values of the  $b$ -only hypothesis and the  
1458 different  $s + b$  hypotheses,

$$\text{CL}_s = \frac{p_{s+b}}{1 - p_b}. \quad (4.16)$$

1459 Each signal hypothesis corresponds to a particular point in the parameter space. The  $p$ -  
1460 value of the null hypothesis  $p_b$  and the signal hypothesis is obtained by setting  $q_0 = 0$  and  
1461 evaluating  $q_1$  in equation (4.15) respectively and integrating over the corresponding sampling  
1462 distribution [101]. A signal model, i.e. a parameter point, is said to be excluded at 95% CL  
1463 when  $\text{CL}_s < 0.05$ .

### <sup>1464</sup> 4.6.2 Uncertainties and their correlations

<sup>1465</sup> Each of the three analyses treats a particular set of uncertainties. Often times, more  
<sup>1466</sup> than one analysis estimate the same systematic uncertainty, in which case it is correlated in  
<sup>1467</sup> the combination. This section describes this treatment. Most experimental uncertainties are  
<sup>1468</sup> correlated across search channels, namely they are modelled using the same observable in the  
<sup>1469</sup> combined likelihood. They include uncertainties related to the reconstruction of physics ob-  
<sup>1470</sup> jects, the integrated luminosity, and pile-up modelling. Physics object uncertainties include  
<sup>1471</sup> those from electrons, muons, and the jet energy response. Uncertainties from  $b$ -jet identi-  
<sup>1472</sup> fication depend on  $b$ -tagging algorithm and working point, which vary across the analyses.  
<sup>1473</sup> As a result, they are not correlated. Finally, several experimental systematic uncertainties  
<sup>1474</sup> are moderately constrained in a particular analysis, and hence not correlated to avoid phase-  
<sup>1475</sup> space biases. Different assumptions on the correlation of uncertainties related to jet,  $E_T^{\text{miss}}$ ,  
<sup>1476</sup> and  $b$ -jet identification, and other moderately constrained uncertainties are tested to gauge  
<sup>1477</sup> their impact on the observed exclusions, and found to have negligible impact.

<sup>1478</sup> Uncertainties on signal simulation and background modelling are assessed for each analy-  
<sup>1479</sup> sis. To each final state is dedicated a separate signal simulation, as they often probe different  
<sup>1480</sup> kinematic regions of the phase space. The theoretical uncertainties are found to be small  
<sup>1481</sup> and are considered to be uncorrelated. Uncertainties pertaining to background modelling  
<sup>1482</sup> are considered correlated amongst the analyses, motivated by their different sources of lead-  
<sup>1483</sup> ing background, different probed kinematic phase space, as well as different methods of  
<sup>1484</sup> background estimation.

### <sup>1485</sup> 4.6.3 The impact of uncertainties

<sup>1486</sup> Different 2HDM+ $a$  parameter values correspond to different signal kinematics and sen-  
<sup>1487</sup> sitivity delivered by each analysis, and thus see different levels of impact from uncertainties  
<sup>1488</sup> on the combined signal strength. As an example, the contributions to the uncertainty of the

best fit signal strength from statistical and systematic uncertainties are shown in table 4.6  
 for a parameter point at  $m_a = 450$  GeV,  $m_H = 800$  GeV,  $\tan \beta = 1.0$ , and  $\sin \theta = 0.35$ .  
 This signal is not excluded by any single input analysis, but is excluded by the combination.  
 The statistical uncertainty is slightly smaller than the systematic counterpart, which is bro-  
 ken into three categories: theoretical, experimental, and MC statistical uncertainties. The  
 impact of each category is estimated by fixing the uncertainties in that category in a fit, and  
 subtracting the resulting uncertainty in the signal strength from the total in quadrature.  
 Theoretical uncertainties arise mainly from uncertainties in background modelling and are  
 slight smaller than experimental ones. Among the experimental uncertainties originating  
 from reconstructed physics objects, those from jet and  $E_T^{\text{miss}}$  make the largest contributions.

For each input analysis, the most important uncertainties also make the largest con-  
 tribution to the combined uncertainty. For background modelling, the largest components  
 are  $ZZ$  modelling from  $E_T^{\text{miss}} + Z(\ell\ell)$ ,  $t\bar{t}$  uncertainties from  $E_T^{\text{miss}} + h(bb)$ , and uncertainties  
 from  $t\bar{t}$  production with additional  $b$  quarks from  $tbH^\pm(tb)$ . Among experimental systematic  
 uncertainties, the largest sources are lepton systematic uncertainties from  $E_T^{\text{miss}} + Z(\ell\ell)$ , un-  
 certainties related to jets and  $E_T^{\text{miss}}$  from  $E_T^{\text{miss}} + h(bb)$ , and those related to  $b$ -jet identification  
 from  $tbH^\pm(tb)$ .

## 4.7 Results on combined constraints on the 2HDM+ $a$

A summary of combined constraints on 2HDM+ $a$  across all benchmark scenarios intro-  
 duced in section 4.2 is presented in this section.

### 4.7.1 Scenario 1: $m_a - m_A$ planes

Figure 4.8 shows the exclusion contours from the  $m_a - m_A$  scans with the 2HDM mixing  
 angle fixed to  $\sin \theta = 0.35$  in 4.8a and 4.8c, and  $\sin \theta = 0.7$  in 4.8b and 4.8d. These choices

Uncertainty source	$\Delta\mu \cdot 100$
Statistical uncertainty	25.0
Systematic uncertainty	27.6
Theory uncertainties	16.2
Signal modelling	2.8
Background modelling	15.9
Experimental uncertainties (excl. MC stat.)	18.8
Luminosity, pile-up	3.9
Jets, $E_T^{\text{miss}}$	12.3
Identification of $b$ -jets	9.1
Electrons, muons	6.1
MC statistical uncertainty	9.3
Total uncertainty	37.2

**Table 4.6:** Impact from different sources of uncertainties on the best-fit signal strength express in  $\Delta\mu$  on the signal at ( $m_A = 800 \text{ GeV}$ ,  $m_a = 450 \text{ GeV}$ ,  $\tan\beta = 1$ ,  $\sin\theta = 0.35$ ), estimated by fixing the corresponding NPs to their best-fit values, and subtracting the resulting uncertainty from the total uncertainty in quadrature. The statistical uncertainty component is obtained by fixing all NPs except the floating background normalization factors, and quantifies the impact of the limit data yields in the signal and control regions. The total uncertainty is not the quadratic sum of the individual contribution due to correlations between systematic uncertainties [40].

1512 of parameters correspond to benchmark scenarios 1a and 1b in section 4.2. The combined  
 1513 exclusion contours are shown along with those of the three individual channels entering the  
 1514 statistical combination in 4.8a and 4.8b, and with the remaining channels in 4.8b and 4.8d.  
 1515 Over the two benchmark parameter planes, the  $E_T^{\text{miss}} + Z(\ell\ell)$  and  $E_T^{\text{miss}} + h(b\bar{b})$  drive the  
 1516 sensitivity across a large region, due primarily to the resonant production of the scalar and  
 1517 pseudo-scalar according to the diagram in figures 4.1a and 4.2a. Their sensitivity varies  
 1518 widely with the pseudo-scalar Higgs boson and the mediator masses. At  $\sin \theta = 0.35$  and in  
 1519 the region where  $E_T^{\text{miss}} + Z(\ell\ell)$  and  $E_T^{\text{miss}} + h(b\bar{b})$  dominate, all pseudo-scalar mass is excluded  
 1520 up to a maximum  $m_a = 560$  GeV for  $m_A = 1.2$  TeV, while for  $m_a = 1.5$  GeV, all pseudo-  
 1521 scalar Higgs mass is excluded up to  $m_A = 1.55$  TeV. At  $\sin \theta = 0.7$ , all pseudo-scalar mass  
 1522 is excluded up to a maximum  $m_a = 550$  GeV for  $m_A = 1$  TeV, while for  $m_a = 400$  GeV,  
 1523 all pseudo-scalar Higgs mass is excluded up to  $m_A = 1.2$  TeV. For both choices of  $\sin \theta$ , the  
 1524  $E_T^{\text{miss}} + Z(\ell\ell)$  contour reaches closer to the  $m_A = m_a$  limit than that of  $E_T^{\text{miss}} + h(b\bar{b})$ , because  
 1525 the former can probe lower  $E_T^{\text{miss}}$  values, whereas the latter is sensitive at higher  $E_T^{\text{miss}}$  due  
 1526 to the presence of a  $E_T^{\text{miss}}$  trigger in its selection and the mass difference between the  $Z$  and  
 1527 the Higgs bosons. In addition, the exclusion power of  $E_T^{\text{miss}} + h(b\bar{b})$  is increased relative to  
 1528  $E_T^{\text{miss}} + Z(\ell\ell)$  at high  $m_A$  and low  $m_a$ , because of an increase in the cross-section of the  
 1529 non-resonant  $a^* \rightarrow ah$  process, without resonant  $A$  production, which has no equivalence in  
 1530 the latter's signature.

1531 For both values of  $\sin \theta$ , the  $tbH^\pm(tb)$  channel excludes complementary regions where  
 1532 the other channels provide less exclusion power. For  $\sin \theta = 0.35$  all pseudo-scalar Higgs  
 1533 mass up to  $m_A \leq 700$  GeV is excluded, and for  $\sin \theta = 0.7$ , the upper bound of the  
 1534 excluded  $m_A$  ranges from 600 GeV to 700 GeV. The weak dependence on the mediator  
 1535 mass  $m_a$  is due to the absence of the mediator in its signature, such that its sensitivity  
 1536 is only indirectly affected by  $m_a$  via the competition from other possible decay modes,  
 1537 for instance  $H^\pm \rightarrow aW^\pm$ . The reduction in branching ratio is observed at  $\sin \theta = 0.7$ ,  
 1538 where the limits from this channel weakens at lower  $m_a$ , where the aforementioned decay

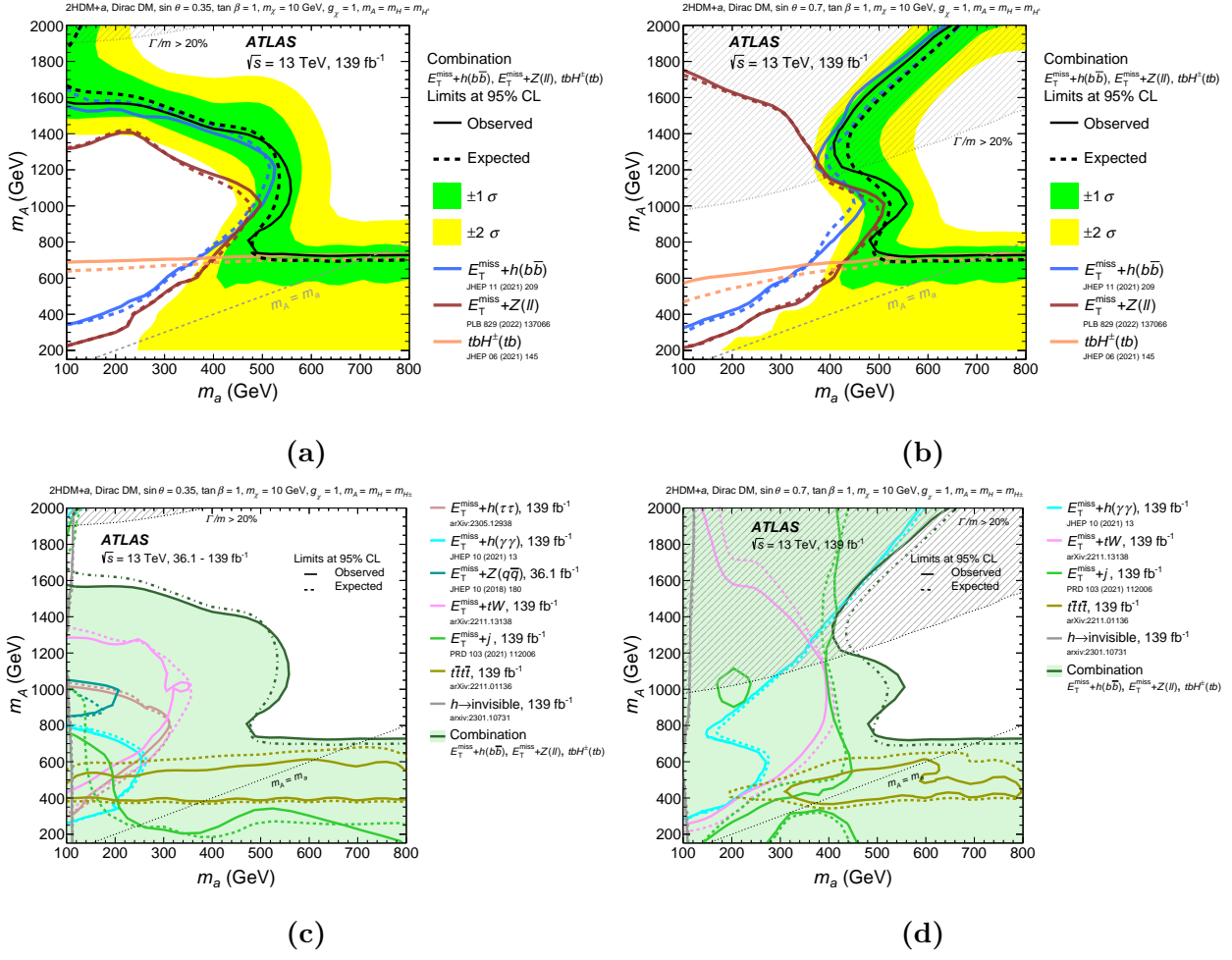


**Figure 4.8:** Observed and expected exclusion regions at 95% CL over the  $(m_a, m_A)$  plane evaluated at 2HDM+a mixing angles  $\sin \theta = 0.35$  (subfigures (a), (c)), and  $\sin \theta = 0.7$  (subfigures (b), (d)). The observed and expected contours are respectively shown in solid and dashed lines in all subsequent figures. In (a) and (b), the observed and expected exclusion limits from each of the three statistically combined signatures are shown along with the combined limits. The green and yellow shaded bands respectively correspond to the  $\pm 1$  and  $\pm 2$  standard deviation uncertainty in the combined expected limits. In (c) and (d), the combined exclusion contours are overlaid along those of additional channels not included in the statistical combination. In all subfigures, a dashed grey region indicates the region where the width of any of the Higgs boson exceeds 20% of its mass [40].

1539 is kinematically possible. The statistical combination with  $tbH^\pm(tb)$  augments the excluded  
 1540 parameter space above  $m_a = 500$  GeV and below  $m_A = 700$  GeV for both scenarios.

1541 The exclusion power of other channels not entering the statistical combination varies  
 1542 widely and is demonstrated on figures 4.8c and 4.8d. The  $E_T^{\text{miss}} + h(\gamma\gamma)$  search probes a  
 1543 region in the parameter space that is similar in shape to that of the  $E_T^{\text{miss}} + h(b\bar{b})$  search,  
 1544 only smaller due to the smaller branching ratio of the  $h \rightarrow \gamma\gamma$  decay relative to the  $h \rightarrow b\bar{b}$   
 1545 decay. At lower values of  $m_A$  however, it becomes more sensitive than  $E_T^{\text{miss}} + h(b\bar{b})$ , as it  
 1546 does not rely on the  $E_T^{\text{miss}}$  trigger and is capable of probing smaller values of  $E_T^{\text{miss}}$ , similar to  
 1547 the better sensitivity of  $E_T^{\text{miss}} + Z(\ell\ell)$  relative to  $E_T^{\text{miss}} + h(b\bar{b})$  in the same region. Similar to  
 1548 the  $E_T^{\text{miss}} + h(b\bar{b})$  search, the  $E_T^{\text{miss}} + h(\gamma\gamma)$  shows a significant boost in sensitivity at higher  
 1549  $m_A$  for  $\sin\theta = 0.7$ , due to an increase in the cross-section of the  $a \rightarrow ah$  process.

1550 The  $E_T^{\text{miss}} + h(\tau\tau)$  search is only interpreted at  $\sin\theta = 0.35$ , and its exclusion contour  
 1551 has a similar shape to that of other  $E_T^{\text{miss}} + h$  signatures, but is even smaller in coverage due  
 1552 to a small branching ratio relative to the  $h \rightarrow b\bar{b}$  final state.

1553 The exclusion contours of the  $E_T^{\text{miss}} + tW$  search have a similar shape to those of the  
 1554  $E_T^{\text{miss}} + Z(\ell\ell)$  search for both values of  $\sin\theta$ , albeit smaller in exclusion area. The observed  
 1555 exclusion consistently covers a smaller area of the phase space than the expected sensitivity,  
 1556 due to a small excess in the 2-lepton channel of less than  $2\sigma$  significance [91].

1557 The sensitivity of the  $E_T^{\text{miss}} + j$  search shows interesting features on the  $m_a - m_A$  plane.  
 1558 The signature does not contain resonant production as in the case of the  $Z/h$  boson in figures  
 1559 4.1a and 4.2a. Therefore, the exclusion contour differ significantly from the  $E_T^{\text{miss}} + Z$  and  
 1560  $E_T^{\text{miss}} + h$  signatures. In addition, the signal cross-section is affected by the inference between  
 1561 non-resonant contributions from the pseudo-scalars  $a$  and  $A$ , which depends on both  $m_a$   
 1562 and  $m_A$ , especially at the larger value of the mixing angle  $\sin\theta$  [11]. A small difference in  
 1563 pseudo-scalar mass ( $m_a \approx m_A$ ) leads to destructive interference, reducing the signal cross-  
 1564 section and thus the sensitivity to the 2HDM+ $a$ . This effect is observed for both values

of  $\sin \theta$ . At  $\sin \theta = 0.35$ , the  $E_T^{\text{miss}} + j$  search excludes values of  $m_a$  up to 600 GeV for  $m_A \approx 200$  GeV, and values of  $m_A$  up to 800 GeV for  $m_a \approx 100$  GeV. At  $\sin \theta = 0.7$ , stronger mixing leads to higher cross-sections for signal hypotheses with  $m_A > m_a$ . For  $m_A \approx 1300$  GeV, all values of  $m_a$  up to  $\approx 400$  GeV are excluded, comparable to the exclusion power of the  $E_T^{\text{miss}} + Z(\ell\ell)$  and  $E_T^{\text{miss}} + h(b\bar{b})$  searches.

The  $t\bar{t}t\bar{t}$  search is sensitive in regions where the  $E_T^{\text{miss}} + Z(\ell\ell)$  and  $E_T^{\text{miss}} + h(b\bar{b})$  searches have lower sensitivity, similar to the  $tbH^\pm(tb)$  search. However, unlike the latter, it is only sensitive to the 2HDM+ $a$  when either of the pseudo-scalar masses is above the production threshold of a top quark pair ( $m_{A/a} \geq 2m_t$ ). For  $\sin \theta = 0.35$ , the contour is almost independent of  $m_a$ , driven largely by the resonant production of the heavy Higgs bosons  $A/H$ . For  $\sin \theta = 0.7$ , the sensitivity is lowered for small  $m_a$  compared to the scenario with  $\sin \theta = 0.35$  due to a larger  $a/A$  and a forbidden  $a \rightarrow t\bar{t}$  decay.

The exclusion contours from the  $E_T^{\text{miss}} + Z(q\bar{q})$  search on 36  $\text{fb}^{-1}$  data are shown for scenario 1a [45]. The search provides the smallest sensitivity because it suffers from larger multijet production backgrounds and smaller data sample.

#### 4.7.2 Scenario 2: $m_A - \tan \beta$ planes

Figure 4.9 summarizes the exclusion limits over the  $m_A - \tan \beta$  parameter plane evaluated with  $\sin \theta = 0.35$  and  $\sin \theta = 0.7$ . In both scenarios, a large portion of the parameter plane is excluded by the combined contours. At  $\sin \theta = 0.35$  the combined sensitivity is driven primarily by the  $E_T^{\text{miss}} + Z(\ell\ell)$  search, which is also observed at lower pseudo-scalar mass at  $\sin \theta = 0.7$ . At higher values of  $m_A$ , the  $E_T^{\text{miss}} + h(b\bar{b})$  provides stronger constraints. In general, the sensitivity of these channels is influenced by the transition from  $gg$ - to  $bb$ -initiated production of the  $Z/h$  boson, and finds its minimum in the region around  $\tan \beta = 5$ .

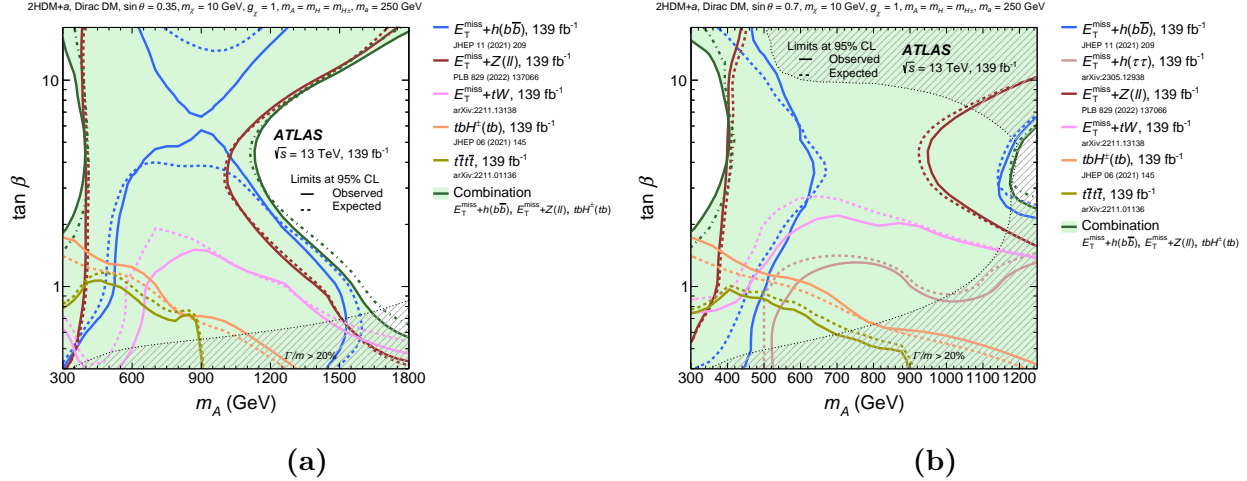


**Figure 4.9:** Observed and expected exclusion regions at 95% CL over the  $(m_A, \tan \beta)$  plane evaluated at 2HDM+ $a$  mixing angles  $\sin \theta = 0.35$  (a), and  $\sin \theta = 0.7$  (b). The statistical combined contours are shown along with those from individual searches. In both subfigures, a dashed grey region indicates the region where the width of any of the Higgs boson exceeds 20% of its mass [40].

The  $E_T^{\text{miss}} + tW$  search excludes regions of the parameter space up to  $\tan \beta = 1.5$  for  $\theta = 0.35$  and  $\tan \beta = 2$  for  $\sin \theta = 0.7$ . The observed sensitivity in both scenarios is weaker than the expected counterpart because of a small excess in the two-lepton signal region of the search [91]. The larger mixing angle again shows better sensitivity to the  $E_T^{\text{miss}} + tW$  signature [48].

The exclusion contour from the  $E_T^{\text{miss}} + h(\tau\tau)$  search is evaluated as a function of  $m_A$  and  $\tan\beta$  only at  $\sin\theta = 0.7$ . Because of the small branching ratio of the  $h \rightarrow \tau\tau$  decay, it has low sensitivity for the 2HDM+ $a$  signal.

The  $t\bar{t}t\bar{t}$  and  $tbH^\pm(tb)$  searches provide sensitivity at low values of  $m_A$  and  $\tan\beta$ , due to enhanced production cross-section for smaller resonance masses and a preference for coupling third generation quarks in this region.

### 1599 4.7.3 Scenario 3: $m_a$ – $\tan \beta$ planes

1600 Figure 4.10 summarizes the exclusion limits as a function of the  $m_a$  and  $\tan \beta$  evaluated  
 1601 at  $\sin \theta = 0.35$  (scenario 3a) and  $\sin \theta = 0.7$  (scenario 3b). In both scenarios, the  $E_T^{\text{miss}} +$   
 1602  $Z(\ell\ell)$  search drives the sensitivity over a large portion of the parameter plane. The  $E_T^{\text{miss}} +$   
 1603  $h(b\bar{b})$  and  $E_T^{\text{miss}} + h(\gamma\gamma)$  searches exclude analogous regions, albeit the latter covers a smaller  
 1604 area, due to the smaller  $h \rightarrow \gamma\gamma$  branching ratio. Both channels observe decreased sensitivity  
 1605 at  $\tan \beta \approx 5$  as the  $gg$ -initiated production transitions to the  $bb$ -initiated counterpart.

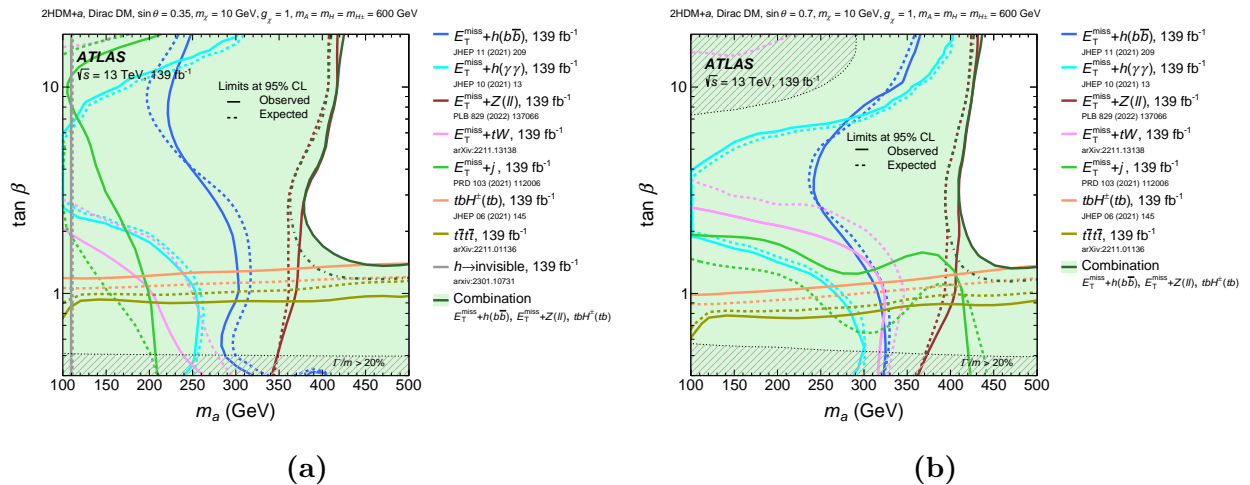


Figure 4.10: Observed and expected exclusion regions at 95% CL over the  $(m_a, \tan \beta)$  plane evaluated at 2HDM+ $a$  mixing angles  $\sin \theta = 0.35$  (a), and  $\sin \theta = 0.7$  (b). The statistical combined contours are shown along with those from individual searches. In both subfigures, a dashed grey region indicates the region where the width of any of the Higgs boson exceeds 20% of its mass [40].

1606 The  $E_T^{\text{miss}} + tW$  search excludes regions of the parameter space at low  $\tan \beta$  and low  
 1607  $m_a$ . Better sensitivity is observed for the larger  $A/a$  mixing angle.

1608 The  $E_T^{\text{miss}} + j$  search excludes signal hypotheses characterized by low values of  $m_a$  and  
 1609  $\tan \beta$ , and its sensitivity is enhanced at  $\sin \theta = 0.7$  due to more significant  $a/A$  mixing,  
 1610 enlarging the signal cross-sections for  $m_A > m_a$ .

1611 The  $h \rightarrow$  invisible decay suffers from small branching ratio and thus provides sensitivity

1612 at low values of  $m_a$ , independent of  $\tan\beta$ .

1613 The  $t\bar{t}t\bar{t}$  and  $tbH^\pm(t)$  searches constrain regions complementary to the  $E_T^{\text{miss}} + X$  signa-

1614 tures. It is sensitive at low  $\tan\beta$  and almost independent of  $m_a$ .

#### 1615 4.7.4 Scenario 4: Variation of $\sin\theta$

1616 Figure 4.11 summarizes the exclusion limits as a function of  $\sin\theta$  for the 2HDM+ $a$  under

1617 both low- and high-mass mediator hypotheses. The upper row shows the results for the

1618 baseline parameter choice of Scenario 4, in which  $\tan\beta = 1.0$ , and the lower row additional

1619 results obtained for alternative values of  $\tan\beta$ , namely  $\tan\beta = 0.5$  and  $\tan\beta = 50$ .

1620 Exclusion limits shown in the subfigures on the left are derived at  $m_A = 600$  GeV,  $m_a = 200$

1621 GeV, corresponding to scenario 4a and the low-mass hypothesis, and those on the right at

1622  $m_A = 1.0$  TeV,  $m_a = 350$  GeV, corresponding to scenario 4b and the high-mass hypothesis.

1623 The exclusion limits are represented by the ratio of the excluded cross-section to the nominal

1624 cross-section of the signal model.

1625 For the low-mass hypothesis at  $\tan\beta = 1.0$ , the most stringent limits in the region of

1626 medium to high values of  $\sin\theta$  are set by the  $E_T^{\text{miss}} + Z(\ell\ell)$  and  $E_T^{\text{miss}} + h(b\bar{b})$  searches. The

1627 sensitivity of the former increases monotonically with  $\sin\theta$ , as the cross-section of both non-

1628 resonant and resonant production mechanisms, illustrated in figures 4.2 and 4.1, grows with

1629  $\sin\theta$ . On the other hand, the production diagrams contributing to the  $E_T^{\text{miss}} + h$  signature

1630 show a different dependence on  $\sin\theta$ , as discussed in references [11, 45]. The relative

1631 contributions of each diagram are further affected by the different selections employed by

1632 the  $E_T^{\text{miss}} + h(b\bar{b})$  and  $E_T^{\text{miss}} + h(\gamma\gamma)$  analyses, both of which reach a the maximum sensitivity

1633 around  $\sin\theta = 0.5$ .

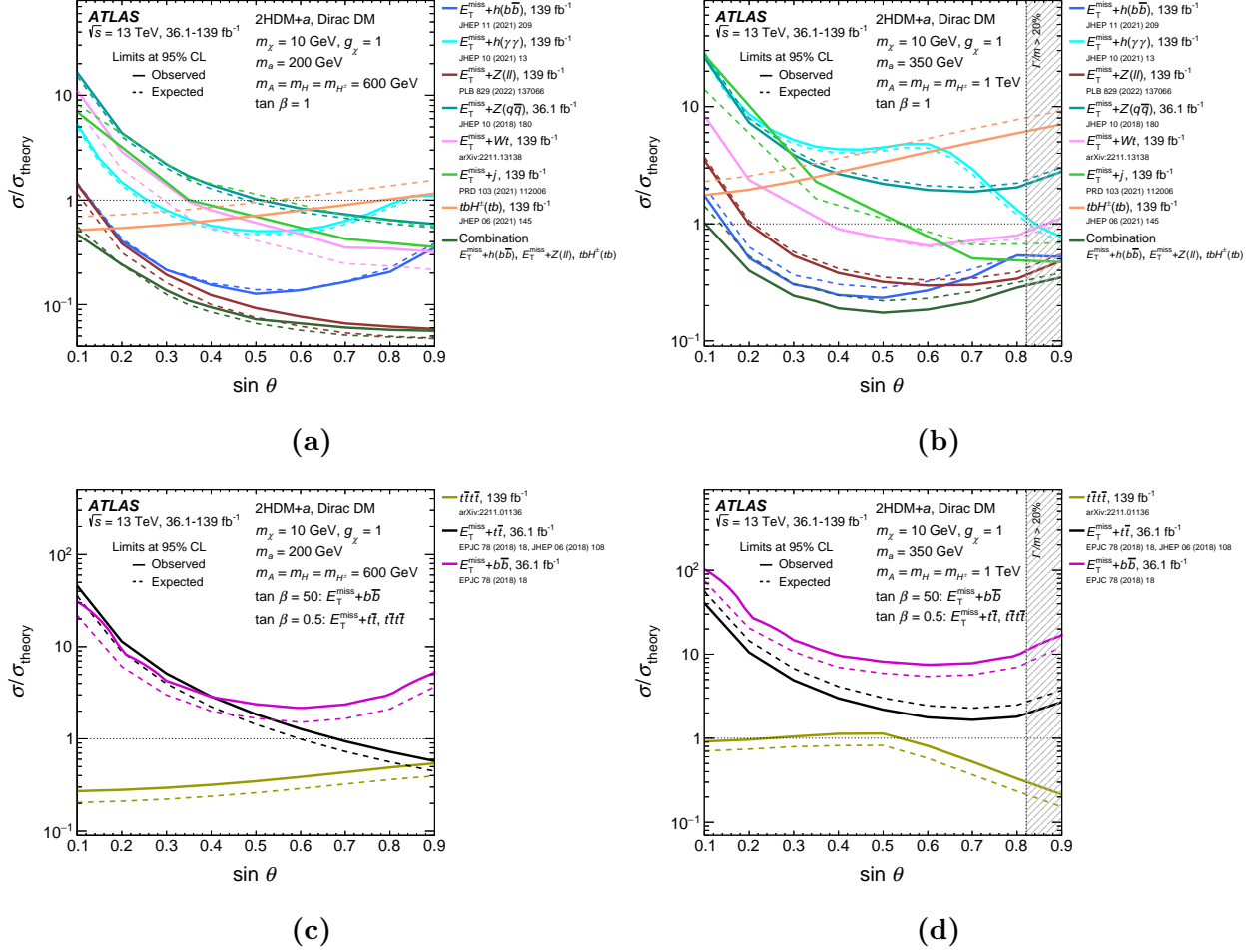


**Figure 4.11:** Observed and expected exclusion limits at 95% CL for the 2HDM+a as a function of  $\sin \theta$  plane evaluated under benchmark scenarios 4. In subfigures (a) and (b), the results are derived at  $\tan \beta = 1$ , while in (c) and (d) they are derived at  $\tan \beta = 0.5$  or  $\tan \beta = 50$ . (a) and (c) represent the sensitivity at low pseudo-scalar mass, in particular  $m_A = 600$  GeV and  $m_a = 200$  GeV, and (b) and (d) the high-mass regime, namely  $m_A = 1.0$  TeV and  $m_a = 350$  GeV. The combined exclusion is shown along with individual searches. In all subfigures, a dashed grey region indicates the region where the width of any of the Higgs boson exceeds 20% of its mass [40].

The sensitivity of both  $E_T^{\text{miss}} + j$  and  $E_T^{\text{miss}} + tW$  searches also monotonically increases with  $\sin \theta$ , similar to that of the  $E_T^{\text{miss}} + Z(\ell\ell)$  signature, albeit an order of magnitude lower than the latter. This is due to the smaller cross-sections of these processes. Meanwhile, the

1637  $tbH^\pm(tb)$  and  $t\bar{t}t\bar{t}$  signatures see a dependence on  $\sin\theta$  compared to other signatures, since  
1638 they are not directly sensitive to neutral boson production. They are particularly sensitive  
1639 at small mixing angle, with the sensitivity of  $tbH^\pm(tb)$  exceeding that of the  $E_T^{\text{miss}} + Z/h$   
1640 searches at  $\sin\theta < 0.2$ .

1641 For the high-mass hypothesis at  $\tan\beta = 1.0$ , the light pseudo-scalar mass is sufficiently  
1642 large to kinematically allow the  $a \rightarrow t\bar{t}$  decay, introducing an additional  $\sin\theta$  dependence  
1643 in the interpretation of the  $E_T^{\text{miss}} + Z/h$  searches. Consequently, the highest sensitivity for  
1644 these analyses is observed near or just below the maximal mixing condition  $\theta = \pi/4$ .

1645 In the case of the  $E_T^{\text{miss}} + h$  searches, there is a more complex dependence on  $\sin\theta$ , owing to  
1646 different contributions from the resonant and non-resonant productions of the Higgs boson  
1647 to the final selection of each analysis. In particular, the  $E_T^{\text{miss}} + h(b\bar{b})$  signature displays  
1648 in a broad peak at values of  $\sin\theta$  slightly below the maximal mixing. In contrast, the  
1649  $E_T^{\text{miss}} + h(\gamma\gamma)$  shows a local sensitivity minimum around  $\sin\theta \approx 0.6$ .

1650 The  $E_T^{\text{miss}} + tW$  search follows a similar  $\sin\theta$  dependence as the  $E_T^{\text{miss}} + Z(\ell\ell)$  and  
1651  $E_T^{\text{miss}} + h(b\bar{b})$  searches, but remains approximately an order of magnitude below the combined  
1652 sensitivity. On the other hand, the  $E_T^{\text{miss}} + j$  demonstrates a monotonic increase in sensitivity  
1653 and reaches a level similar to that of the  $E_T^{\text{miss}} + Z(\ell\ell)$  and  $E_T^{\text{miss}} + h(b\bar{b})$  searches at large  
1654  $\sin\theta$ . Results from the  $E_T^{\text{miss}} + V(q\bar{q})$  search are shown for completeness [45].

1655 Alternative values  $\tan\beta = 0.5$   $\tan\beta = 50$  are considered for Scenario 4 to illustrate the  
1656 strong dependence of the exclusion limits on  $\tan\beta$ , particularly in searches that are sensitive  
1657 to the Yukawa couplings of the neutral Higgs bosons and the mediator to fermions in a Type-II 2HDM.  
1658 At low  $\tan\beta$ , the scalar and pseudo-scalar states couple primarily to top quarks,  
1659 whereas at high  $\tan\beta$ , they predominantly couple to bottom quarks. Therefore, the results  
1660 of the  $t\bar{t}t\bar{t}$  search are shown for  $\tan\beta = 0.5$ . The sensitivity of this search is generally  
1661 higher in the low-mass scenario relative to the high-mass counterpart, mainly due to the  
1662 reduced production cross-section of the heavy Higgs bosons  $A/H$  at higher  $m_{A/H}$ . However,

in the high-mass scenario, an enhancement in sensitivity is observed for  $\sin \theta > 0.5$ , and attributed to the increased  $a/A$  mixing and the fact that the mediator mass is sufficiently large to kinematically allow a decay into a pair of top quarks. At the same time, the mediator mass remains significantly below the masses of the heavy Higgs bosons, leading to the  $t\bar{t}t\bar{t}$  signal cross-section being dominated entirely by  $t\bar{t} + a(t\bar{t})$  production.

For completeness, results from the  $E_T^{\text{miss}} + t\bar{t}$  and  $E_T^{\text{miss}} + b\bar{b}$  searches reported in reference [45] are included for  $\tan \beta = 0.5$  and  $\tan \beta = 50$ , respectively.

#### 4.7.5 Scenario 5: Variation of $m_\chi$

In Figure 4.12, the sensitivity of various searches as a function of the fermion dark matter mass  $m_\chi$ , which has the strongest impact on the relic density predicted by the 2HDM+ $a$ , is shown. The sensitivity is evaluated as the observed exclusion limit on the ratio of the excluded cross-section to the nominal cross-section of the signal model. The relic density is overlaid on the plot as a long-dashed line. A notable feature of the relic density occurs around  $m_\chi = m_a/2 = 200$  GeV, known as the  $a$ -funnel region, where the predicted density is depleted by the resonant enhancement of the process  $\chi\bar{\chi} \rightarrow a \rightarrow \text{SM}$  [103, 104, 12]. A second resonant, occurring at  $m_\chi = m_A/2 = 500$  GeV, corresponding to a second funnel region, is not fully covered within the probed  $m_\chi$  range but nevertheless visible as a decrease in the predicted relic density for  $m_\chi > 400$  GeV. For  $m_\chi > 200$  GeV, the relic density reaches a plateau due to the increase in annihilation cross-section of the DM particles near the kinematic threshold of the processes  $\chi\bar{\chi} \rightarrow t\bar{t}$  (if  $m_\chi > m_t$ ) and  $\chi\bar{\chi} \rightarrow ah$  (if  $m_\chi > (m_a + m_h)/2$ ).

For all considered signatures, the sensitivity becomes independent of  $m_\chi$  as long as the pseudo-scalar mediator, whose mass is fixed at 400 GeV in this benchmark scenario, can decay into a pair of DM particles. The most stringent constraints in the region where  $m_\chi < 200$  GeV are provided by the  $E_T^{\text{miss}} + Z(\ell\ell)$  search. Together with the  $E_T^{\text{miss}} + h(b\bar{b})$ ,

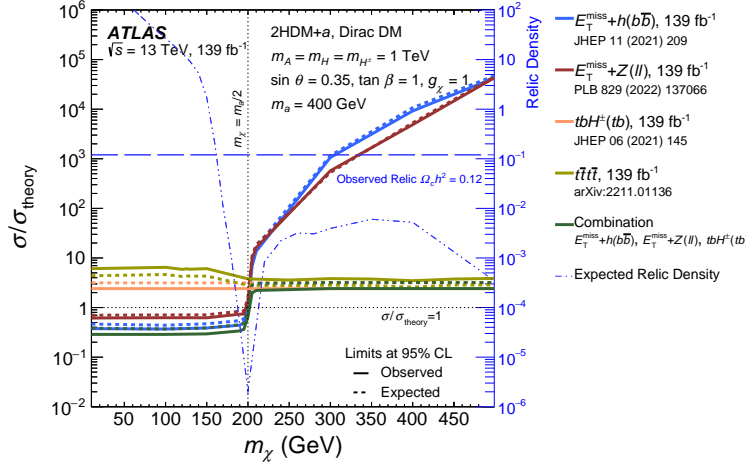


**Figure 4.12:** Observed and expected exclusion limits at 95% CL for the 2HDM+ $a$  as a function of the dark matter particle mass  $m_\chi$  evaluated under benchmark scenario 5 following  $m_A = 1.0$  TeV,  $m_a = 400$  GeV,  $\tan \beta = 1.0$ , and  $\sin \theta = 0.35$ . The limits are expressed in terms of the ratio of the excluded cross-section to the nominal cross-section of the signal model. The results from several individual searches are shown along with the combined limits. The relic density for each  $m_\chi$  assumption, calculated with MADDM [105], is superimposed on the plot in dashed line [40].

it excludes this part of the parameter space. However, at higher DM masses, the sensitivity of the  $E_T^{\text{miss}} + Z/h$  searches rapidly decreases, while that of the  $tbH^\pm(tb)$  and  $t\bar{t}t\bar{t}$  searches remains largely constant. This is because the corresponding leading-order signal processes do not involve the DM particle  $\chi$ , rendering their signal cross-sections independent of  $m_\chi$ .

For  $m_\chi > m_a/2$ , the  $tbH^\pm(tb)$  search provides the strongest constraints, probing cross-sections as low as  $\sigma = 2\sigma_{\text{theory}} - 3\sigma_{\text{theory}}$ . None of the searches exclude the 2HDM+ $a$  in this mass range under the chosen benchmark scenario. It is possible to match the observed relic density for  $m_\chi = 170$  GeV without changing the collider phenomenology, though this mass value is disfavored by the considered analyses.

It is important to emphasize that the relic density considerations primarily serve as a tool to assess 2HDM+ $a$  model predictions in the context of cosmological observations. They should not be interpreted as strict constraints on the model parameters, as the values of the

1700 parameters producing the correct relic density could shift if the model is modified to include  
1701 additional physics at high-energy scales or if an alternative cosmological history is assumed.

1702 **4.7.6 Scenario 6:  $m_a - m_\chi$  plane**

1703 Figure 4.13 presents exclusion limits as a function of  $m_a$  and  $m_\chi$  for Scenario 6. The  
1704  $h \rightarrow aa \rightarrow f\bar{f}f'\bar{f}'$  searches target the region characterized by  $m_a < m_h/2$  and  $m_a <$   
1705  $2m_\chi$ , which kinematically allows the  $h \rightarrow aa$  decay and forbids the  $a \rightarrow \chi\bar{\chi}$  decay. This  
1706 region is excluded almost entirely by these searches, except for two narrow bands where  $m_a$   
1707 approaches the masses of the  $J/\psi$  and  $\Upsilon$  mesons. Searches for dimuon final states near the  
1708  $J/\psi$  mass are experimentally challenging, as are searches for  $h \rightarrow aa \rightarrow 4g$ . The  $\mu^+\mu^-\tau^+\tau^-$   
1709 final state provides some sensitivity but is not sufficient to exclude the higher mass range  
1710 around  $m_a = 10$  GeV [73]. Similarly, searches for hadronic final states are complicated by  
1711 the collimation of the quark pairs, often necessitating dedicated techniques to enhance the  
1712 sensitivity of signatures such as  $b\bar{b}\gamma\gamma$  and  $b\bar{b}b\bar{b}$ . The  $h \rightarrow aa \rightarrow f\bar{f}f'\bar{f}'$  searches lose sensitivity  
1713 when  $m_a > m_A/2$ , as invisible mediator decays become dominant. For  $m_a < m_h/2$ , this  
1714 region is excluded by the  $h \rightarrow$  invisible search. For larger values of  $m_a$ , the region where  
1715  $m_a > m_\chi$  is excluded by the  $E_T^{\text{miss}} + h(b\bar{b})$  search up to  $m_a \approx 600$  GeV.

1716 The remaining high-mass region is not excluded, and can be probed by searches targeting  
1717 the mediator or heavy Higgs boson final states in  $t\bar{t}t\bar{t}$  and  $tbH^\pm(tb)$  signatures, which are  
1718 currently unable to exclude  $m_A = 1200$  GeV.

1719 The relic density contour for the case  $\Omega_c h^2 = 0.12$  is overlaid on figure 4.13 as a long-  
1720 dashed line. Regions above this line at low  $m_\chi$  and below it at high  $m_\chi$ , with an  
1721 exception of an island around  $(m_\chi \approx 100, m_a \approx 100)$  GeV, have a predicted relic density  
1722  $\Omega_c h^2 < 0.12$ .

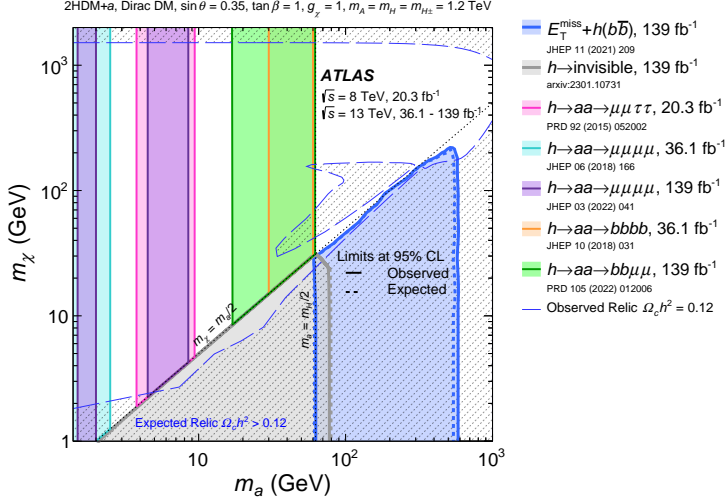


**Figure 4.13:** Observed and expected exclusion limits at 95% CL for the 2HDM+ $a$  as a function of  $m_a$  and  $m_\chi$  evaluated under benchmark scenario 6 following  $m_A = 1.2$  TeV,  $\tan\beta = 1.0$ , and  $\sin\theta = 0.35$ . The relic density contour for the case  $\Omega_c h^2 = 0.12$ , calculated with MADDM [105], is superimposed on the plot in dashed line. The shaded regions mark the region where the model predicts a relic density greater than the observed value  $\Omega_c h^2 = 0.12$ . The island around  $(m_\chi \approx 100, m_a \approx 100)$  GeV corresponds to the resonant enhancement of the process  $\chi\bar{\chi} \rightarrow ah \rightarrow \text{SM}$  that depletes the relic density [40].

1723 Due to the strong Yukawa coupling, the annihilation  $\chi\bar{\chi} \rightarrow t\bar{t}$  is highly efficient. However,  
 1724 in regions of small DM mass ( $m_\chi < m_t$ , the decay is kinematically forbidden, often leading  
 1725 to an overabundance of relic density unless alternative annihilation mechanisms are available.  
 1726 Key processes that help deplete the relic density include resonant annihilation when  $m_\chi \approx$   
 1727  $m_a/2$ , as well as other decay channels such as  $\chi\bar{\chi} \rightarrow aa$ , or  $\chi\bar{\chi} \rightarrow ah$  when they are allowed  
 1728 or kinematically enhanced. For small mediator mass, annihilation into fermions, such as  $b\bar{b}$ ,  
 1729  $c\bar{c}$ , and  $\tau\tau$  can be sufficiently efficient to compensate for their smaller couplings and deplete  
 1730 the relic density. Larger values of  $m_\chi$  can also satisfy the observed relic density, as these  
 1731 annihilations are suppressed.

## 1732 4.8 Conclusion

1733 A wide range of searches for new phenomena performed by the ATLAS Collaboration  
 1734 are summarized and interpreted in the context of a Two-Higgs-Doublet model extended by  
 1735 a pseudo-scalar mediator  $a$ , designated 2HDM+ $a$ . The model extends the Standard Model  
 1736 by introducing two Higgs doublets and an additional pseudo-scalar particle, which mediates  
 1737 interactions between dark matter and the SM particles. It predicts a wide variety of final  
 1738 states, of which the most relevant to DM searches consist of a large missing transverse energy  
 1739 originating from the decay of the mediator  $a$  into DM particles and a mono- $X$ , ( $X = Z, h$ )  
 1740 visible signatures. The majority of searches considered in this summary are based on up to  
 1741  $139 \text{ fb}^{-1}$  of proton-proton collision data at center-of-mass energy of  $\sqrt{s} = 13 \text{ TeV}$  collected  
 1742 by the ATLAS detector during the second run of the Large Hadron Collider. The results are  
 1743 in accordance with Standard Model predictions, as no significant excess is found. They are  
 1744 used to derive constraints on the 2HDM+ $a$  for a diverse selection of benchmark scenarios  
 1745 recommended by the LHC Dark Matter Working Group previously explored, as well as  
 1746 several benchmark scenarios which provide insights into the rich phenomenology of the model.  
 1747 Three searches targeting  $E_T^{\text{miss}} + Z(\ell\ell)$ ,  $E_T^{\text{miss}} + b(b\bar{b})$ , and  $t b H^\pm (tb)$  examine complementary  
 1748 regions of the parameter space, provide the most stringent constraints in many benchmark  
 1749 scenarios, and thus enter a statistical combination to derive an enhanced set of limits on the  
 1750 2HDM+ $a$ .

1751 All benchmark scenarios are simplified by assuming the mass degeneracy of the addi-  
 1752 tional Higgs bosons, namely  $m_A = m_{H^\pm} = m_H$ . The combined result excludes masses of  
 1753 the pseudo-scalar mediator  $a$  up to 560 GeV for  $m_{A/H/H^\pm} = 1.2 \text{ TeV}$ ,  $\sin \theta = 0.35$ , and  
 1754  $\tan \beta = 1.0$  (scenario 1a), and up to 640 GeV for  $m_{A/H/H^\pm} = 2.0 \text{ TeV}$ ,  $\sin \theta = 0.7$ , and  
 1755  $\tan \beta = 1.0$  (scenario 1b). In regions of large heavy Higgs mass ( $m_A$ ), the  $E_T^{\text{miss}} + Z(\ell\ell)$   
 1756 and  $E_T^{\text{miss}} + b(b\bar{b})$  searches are the most sensitive. The results from this benchmark see a

significant improvement over the same scan performed on  $36\text{ fb}^{-1}$  of  $\sqrt{s} = 13\text{ TeV}$  proton-proton collision data, which excludes values of  $m_a$  up to 340 GeV for  $m_{A/H/H^\pm} = 1.0\text{ TeV}$ ,  $\sin\theta = 0.35$ , and  $\tan\beta = 1.0$ . The improvement can be attributed to the full Run 2 dataset, as well as various improvements in the analysis strategies employed by individual searches, and a statistical combination of the most sensitive results.

The interpretation of the  $tbH^\pm(tb)$  in the combined limits represents a novel strategy previously not considered. This signature is the most sensitive of the three combined searches in the low- $m_A$  region where  $m_a > 400\text{ GeV}$ . It allows values of  $m_A$  up to 650 GeV to be excluded across the entire range of examined  $m_a$ , highlighting the importance of searches not classically interpreted in the context of DM in constraining more complex models such as the 2HDM+ $a$ . The statistical combination the  $E_T^{\text{miss}} + Z(\ell\ell)$ ,  $E_T^{\text{miss}} + h(b\bar{b})$ , and  $tbH^\pm(tb)$  searches extends the sensitivity to the 2HDM+ $a$  compared to that of individual analyses across different regions of the parameter space. In addition, the results of searches targeting  $h \rightarrow aa \rightarrow f\bar{f}f'\bar{f}'$  are used for the first time to constrain a part of the parameter space not previously probed. Overall, these results represent the most comprehensive set of constraints on the 2HDM+ $a$  obtained by the ATLAS collaboration to date.

1773

## Part II

1774

Track reconstruction with geometric

1775

deep learning using graph neural

1776

networks in the ATLAS Inner Tracker

1777 **Chapter 5**

1778 **The High Luminosity Large Hadron Collider**

1779 At the time of writing this thesis in 2025, the LHC has been in operation for over 13  
1780 years and delivered to each of its general-purpose detectors, ATLAS and CMS, approximately  
1781  $350 \text{ fb}^{-1}$  of proton–proton collision data at a peak center-of-mass energy of  $\sqrt{s} = 13 \text{ TeV}$ .  
1782 Table 5.1 illustrates the energy and quantity of data collected over the LHC runs. An  
1783 instantaneous luminosity of  $2 \times 10^{34} \text{ cm}^{-1} \text{s}^{-1}$  was achieved in 2018 and has been maintained  
1784 until now, furnishing an integrated luminosity well above the initial goal of  $300 \text{ fb}^{-1}$ .

Run	Period	Integrated luminosity [ $\text{fb}^{-1}$ ]
1	2010 – 2012	29.2
2	2015 – 2018	159.8
3	2022 – 2025	160.4
Total		349.4

**Table 5.1:** The integrated luminosity delivered to the ATLAS detector by the LHC as of September 2, 2024.

1785 Even before the nominal LHC operation, the High-Luminosity LHC (HL-LHC) project  
1786 was established to fully exploit the collider’s discovery potential. The aim is to increase the  
1787 instantaneous luminosity to  $5 \times 10^{34} \text{ cm}^{-1} \text{s}^{-1}$ , reaching up to  $7.5 \times 10^{34} \text{ cm}^{-1} \text{s}^{-1}$ , 3.75 times  
1788 higher than the current rate. As such, the total integrated luminosity at the end of the  
1789 HL-LHC will attain  $3000 \text{ fb}^{-1}$ , 10 times the data planned for the baseline LHC. Increasing

<sub>1790</sub> luminosity proportionately increases the rate of event production  $\langle N \rangle$ , since

$$\langle N_{pp \rightarrow X} \rangle = \mathcal{L} \sigma_{pp \rightarrow X} \quad (5.1)$$

<sub>1791</sub> where  $\mathcal{L}$  and  $\sigma_{pp \rightarrow X}$  are respectively the instantaneous luminosity and the production cross-  
<sub>1792</sub> section of the final state  $X$ . For example, the production cross-section of a Higgs boson  
<sub>1793</sub> is  $\sigma_{pp \rightarrow H} = 50 \text{ pb}$ , so the average Higgs production rate at the current luminosity  $\mathcal{L} =$   
<sub>1794</sub>  $2 \times 10^{34} \text{ cm}^{-1} \text{s}^{-1}$  is

$$\langle N_{pp \rightarrow H} \rangle = [2 \times 10^{34} \text{ cm}^{-1} \text{s}^{-1}] \times [50 \times 10^{-36} \text{ cm}^{-2}] = 1 \text{ Hz}, \quad (5.2)$$

<sub>1795</sub> i.e. one Higgs boson produced every second.

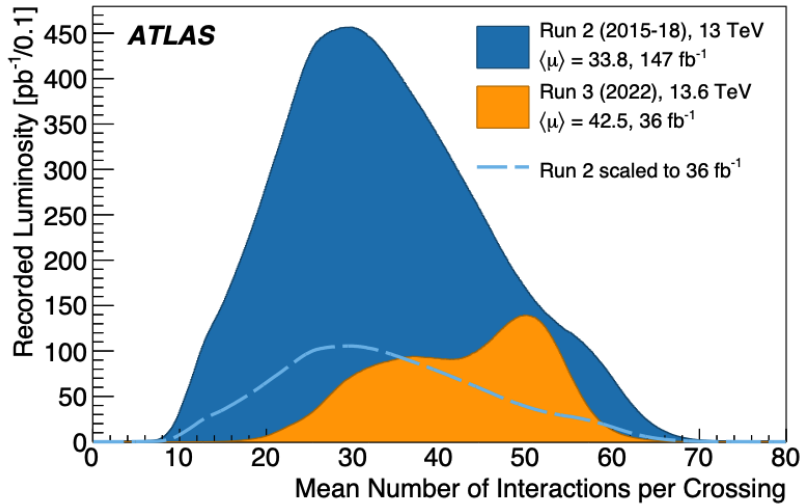


**Figure 5.1:** Distribution of pile-up multiplicity ( $\mu$ ) in proton–proton collision at the ATLAS interaction point during Run 2 and the data taking period in 2022 of Run 3. The dashed line represents a rescaled Run 2 distribution such that its integral is the same as that of the Run 3 distribution.  $\langle \mu \rangle$  denotes the distribution mean. Figure taken from reference [106].

<sub>1796</sub> All interactions that can occur in  $pp$  collision are boosted by higher luminosity. The  
<sub>1797</sub> rate not only of interesting collision events, but also of soft background events increases.  
<sub>1798</sub> The gross number of proton–proton interactions per bunch crossing, called the **pile-up**  
<sub>1799</sub> **multiplicity** and denoted  $\mu$ , can be estimated using equation (5.1) by noting that the total

1800  $pp$  cross-section is of order 100 mb. Figure 5.1 shows the distribution of the average pile-up  
1801 at the ATLAS interaction point during Run 2 and the first year of Run 3. While pile-up  
1802 primarily ranged from 20-40 in Run 2, it peaks around  $\mu = 50$  in a large fraction of events  
1803 recorded by ATLAS in Run 3. The HL-LHC is designed to achieve a peak luminosity of  
1804  $7.5 \times 10^{34} \text{ cm}^{-1} \text{s}^{-1}$ , corresponding to an average pile-up of  $\langle \mu \rangle = 200$ .

1805 To prepare for this major change in operating conditions, the accelerator as well as all  
1806 experiments at the LHC will undergo significant upgrades during the Long Shutdown after  
1807 Run 3, between 2026 and 2029. In the ATLAS Collaboration, both hardware and software  
1808 upgrades will take place, among which the most relevant to this thesis is the replacement  
1809 of the current Inner Detector described in section 3.1.1 by a new all-silicon **Inner Tracker**,  
1810 commonly known as the **ITk**. Chapter 6 describes the design and simulation of the ITk, and  
1811 chapter 7 the current track reconstruction chain, concluding with the challenges associated  
1812 with this process at high pile-up. This difficulty motivates the development of a novel,  
1813 accelerated tracking algorithm which constitutes the rest of this thesis.

## 1814 Chapter 6

### 1815 The ATLAS Inner Tracker

1816 The Inner Tracker (ITk) is the successor to the current Inner Detector (ID) in the High-  
1817 Luminosity era. It inherits many design features from the Pixel and SCT components of the  
1818 ID, but with significant improvements in granularity, geometry coverage, material budget  
1819 and expected parameter resolution. Understanding of its geometry and interaction with  
1820 charged particles is crucial to fully simulate its detector response, extract useful information  
1821 from track candidates, and interpret tracking results. This chapter describes aspects of the  
1822 ITk design and simulation, providing a foundation for the discussion in subsequent chapters.

#### 1823 6.1 Overview of the Inner Tracker

1824 The Inner Tracker consists of two silicon-based sub-detectors, a Pixel Detector close to  
1825 the interaction point (IP) and a Strip Detector at a larger radius, and, unlike the Inner  
1826 Detector, without the Transition Radiation Tracker. They feature a total area of  $180\text{ m}^2$   
1827 with more than 5 billion readout channels, in comparison to  $63\text{ m}^2$  and 100 million channels  
1828 in the ID, translating to a significant increase in granularity. In the barrel region, the pixel  
1829 subsystem comprises five layers and the strip subsystem four layers. Each of the endcaps is  
1830 equipped with six strip rings featuring a petal design and many thin pixel rings. The layout  
1831 of the ITk, demonstrated in figure 6.1, is optimized to provide maximal hit coverage across  
1832 the pseudorapidity range.

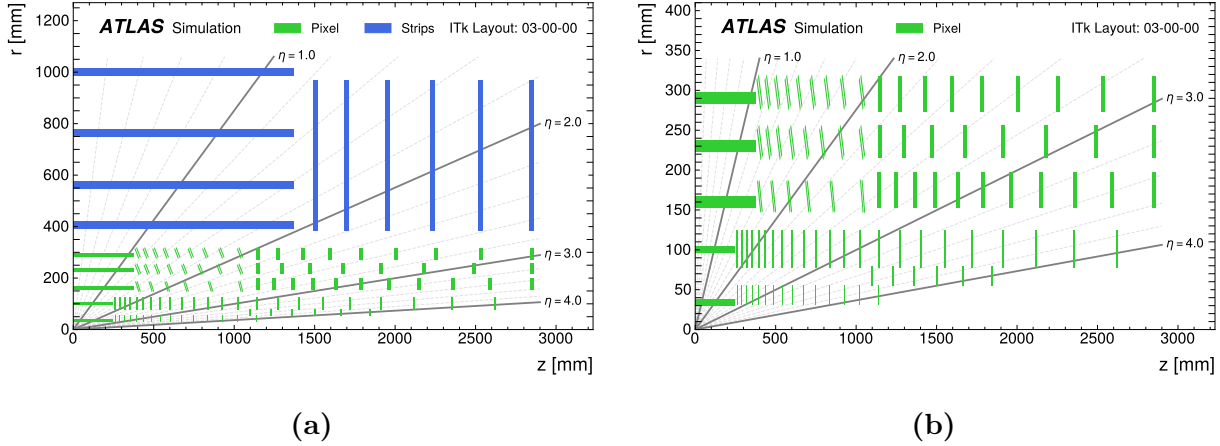


**Figure 6.1:** A schematic view of the ITk layout (a), and of the pixel detector layout (b), both in one quadrant. Only active elements are visible in both figures. Pixel and strip elements are respectively shown in green and blue. The IP is located at the origin. The horizontal axis is parallel to the beam line, and the vertical axis is the radius measured from the IP [107].

1833        The ITk is immersed in a solenoidal magnetic field of 2T, whose principal component  
 1834        lies largely along the  $z$ -axis. The bending power of the magnetic field creates a curvature in  
 1835        the trajectory of a charged particle, from which its transverse momentum  $p_T$  is deduced. In  
 1836        addition, the ITk produces tracking measurements in close proximity to the IP, which plays  
 1837        an important role in impact parameter estimation, vertex fitting and subsequent pile-up  
 1838        mitigation. In addition, the detector is designed to measure at least 9 hits per track in the  
 1839        barrel region and 13 in the endcaps, which provide strong constraints on the curvature of the  
 1840        track. Finally, pseudorapidity coverage is extended up to  $|\eta| = 4$ , in comparison to  $|\eta| < 2.5$   
 1841        in the ID.

1842        The ITk layout plays an important role in simulation and event reconstruction. It has  
 1843        undergone numerous refinements and evolutions since the first layout detailed in the technical  
 1844        design reports [108, 109], with the current edition designated 03-00-00. All subsequent results  
 1845        in this document are evaluated on data simulated using this version.

1846        The pixel system is divided into three subsystems: the Inner System, the Outer Barrel,  
 1847        and the Outer Endcap. The Inner System (IS) encompasses the two innermost layers of the  
 1848        pixel detector, the first of which is located at a radius of 34 mm from the beam pipe. Because  
 1849        of its proximity to the luminous region, the IS is exposed to the highest radiation damage of  
 1850        the entire ITk, and is thus designed to be replaced after  $2000 \text{ fb}^{-1}$  of data has been recorded,  
 1851        when its modules are anticipated to deteriorate. The Outer Barrel (OB) radially covers the  
 1852        IS in the central region at larger radii, and consists of three layers of modules and three  
 1853        sets of endcap rings. As seen on figure 6.1b, the inner rings of the OB are mounted at an  
 1854        incline angle to maximize the angular coverage while using less silicon, and to minimize the  
 1855        material length traversed by a particle having  $1.0 < |\eta| < 2.8$ . The third subsystem, the  
 1856        Outer End-cap (OE), contains three sets of double-sided rings located on each side of the  
 1857        OB at  $|z| \approx 3000 \text{ mm}$ .

1858        The pixel detector uses two different types of silicon sensors, namely 3D and planar  
 1859        sensors, depending on the radiation dose expected at different layers. The former is installed  
 1860        on the innermost layer and rings of the IS due to its radiation hardness, which is improved  
 1861        with respect to the 3D sensors employed in the ID. The rest of the pixel layers and rings  
 1862        uses planar sensors. The dimension of a pixel featured on the 3D sensor is  $25 \mu\text{m}$  in  $R\phi$   
 1863        direction and  $100 \mu\text{m}$  in the longitudinal direction, while the rest of the detector uses  $50 \times 50$   
 1864         $\mu\text{m}^2$  pixels. The small pixel size implies a better resolved cluster shape, and subsequently  
 1865        improves impact parameter resolution. The pixel detector layout in the barrel and endcaps is  
 1866        summarized in tables 6.1 and 6.2. In both tables, the triplet module features three connected  
 1867        read-out chips each processing electronic signals from a  $2 \times 2 \text{ cm}^2$  sensor, and the quad module  
 1868        features 4 connected chips processing signals from a single  $4 \times 4 \text{ cm}^2$  sensor.

1869        The strip detector is divided into two subsystems: the barrel region and two endcap  
 1870        regions with different arrangements of sensor modules. Figure 6.2 shows an overview of the  
 1871        support structure and the arrangement of strip modules in each subsystem. In the barrel  
 1872        region, four cylindrical barrel layers surround the beam line and cover  $|z| < 1.4 \text{ m}$ . Each

Barrel layer	Radius [mm]	Rows of sensors	Flat barrel $ z $ [mm]	Incl. rings per row	Incl. $ z $ [mm]	Module ring	Sensor type	Sensor dim. [ $\mu\text{m}^2$ ]
0	34	12	0-245	24			triplets	$25 \times 100$
1	99	20	0-245	12			quads	$50 \times 50$
2	160	32	0-372	18	380-1035	$2 \times 6$	quads	$50 \times 50$
3	228	44	0-372	18	380-1035	$2 \times 8$	quads	$50 \times 50$
4	291	56	0-372	18	380-1035	$2 \times 9$	quads	$50 \times 50$

**Table 6.1:** Representative parameters of the pixel flat barrel and inclined rings in the ITk layout 03-00-00. Note that while all pixel layers have rings, only the OB features inclined rings. The fifth column provides the number of flat sensors mounted on a complete stave in the central barrel of each layer. The number of inclined rings is given by  $2 \times$  the number of rings on each of the barrel [107].

1873 layer consists of staves running parallel to the  $z$ -axis, on each side of which 14 modules are  
 1874 mounted. The strips on each side of the stave are rotated with respect to the  $z$ -axis by  $\pm 26$   
 1875 mrad to form a stereo angle of 52 mrad between the microstrip on the two sides. Since each  
 1876 microstrip provides a one-dimensional measurement, the stereo angle allows an estimate of  
 1877 a second coordinate from combining the measurements on both side of the stave. The strips  
 1878 on the two inner cylinders are 24.1 mm long and those on the outer two are 48.2 mm long,  
 1879 designated respectively as short- and long-strips. The barrel sensors are tilted in the  $R\phi$   
 1880 plane to allow for an overlap between neighbouring sensors which ensures detection coverage  
 1881 over the entire azimuthal range ( $\phi$ -hermeticity). Table 6.3 shows the number of staves, tilt  
 1882 angle, and strip length on each barrel strip layer.

1883 The endcap region features six disks on each side, the outermost of which is located at  
 1884  $|z| = 3$  m. Each endcap disk is partitioned into 32 identical wedge-shaped petals, and each  
 1885 petal contains nine modules on each side organized into six subsegments referred to as rings  
 1886 (figure 6.2). The strips on each side are constructed with a stereo angle of  $\pm 20$  mrad with  
 1887 respect to the radial line that bisects the petal, achieving a total stereo angle of 40 mrad

Ring layer	Radius [mm]	$ z $ [mm]	Rings	Sensors per ring	Module type	Sensor dim. [ $\mu\text{m}^2$ ]
0	33.20	263-1142	$2 \times 15$	18	triplets	$50 \times 50$
0.5	58.70	1103-1846	$2 \times 6$	30	triplets	$50 \times 50$
1	80.00	263-2621	$2 \times 23$	20	quads	$50 \times 50$
2	154.50	1145.5-2850	$2 \times 11$	32	quads	$50 \times 50$
3	214.50	1145.5-2850	$2 \times 8$	44	quads	$50 \times 50$
4	274.60	1145.5-2850	$2 \times 9$	52	quads	$50 \times 50$

**Table 6.2:** Representative parameters of the pixel endcaps in the ITk layout 03-00-00. The radius in the second column refers to the radius of the circle formed by the innermost point of the sensors on each ring. The number of rings is twice the number of rings on each of the barrel [107].

1888 between the two sides. Because of the increasing circumferences of the petal rings, each of  
1889 them has a distinct sensor geometry and electronic arrangement. These features are detailed  
1890 in the Technical Design Report [108].

## 1891 6.2 Simulation of the Inner Tracker

1892 The production of data samples used to study track reconstruction in the ITk proceeds  
1893 through several steps: event generation, detector simulation using GEANT4 [58], and digitiza-  
1894 tion of simulated energy deposits. Detector simulation is the costliest and the most difficult  
1895 step, having to account for complex detector effects on the particle's trajectory. Charged par-  
1896 ticles interact with the material through which they travel via several mechanisms. Because  
1897 material interactions can change both the magnitude and direction of particle momentum,  
1898 an accurate description of the material distribution in the detector is crucial to the modelling  
1899 of particle trajectories as well as the extraction of track parameters from track candidates.  
1900 Particular care was taken to describe the material at a high level of detail. The dimensions,

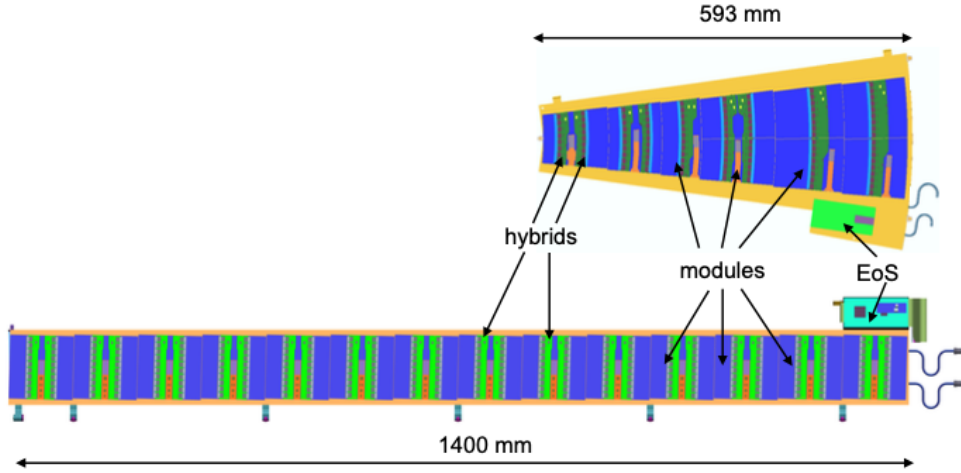


**Figure 6.2:** Overview of the endcap petal (upper) and barrel stave (lower) in the strip detector. Sensor modules shown in blue are mounted directly on a rigid carbon-fiber sandwich structure. Only one half of a stave is shown [108].

1901 location, and material of all detector elements are implemented in the simulation framework.  
 1902 The location of the material is shown in figure 6.3. The materials are defined in GEANT4 in  
 1903 terms of their chemical composition and density.

### 1904 6.2.1 Simulation of the Pixel Detector

1905 The Pixel Detector is divided into a barrel region and two identical endcaps. The outer  
 1906 barrel support structure is modelled using the longeron support structure, shown in figure  
 1907 6.4. The longeron truss structures are approximated as thin sheets of carbon fiber, and the  
 1908 main rails supporting the truss, accounting for 80% of the mass, are modelled by denser  
 1909 materials.

1910 The inner barrel support structure is modelled as truss double shells, with one shell per  
 1911 layer. The shells are modelled as a sheet of carbon fiber behind each row of modules. The  
 1912 total mass of each shell in the support structure is adjusted to match the corresponding

Barrel layer	Number of staves	Radius [mm]	Tilt angle [degree]	Strip length [mm]
0	56	399	13	2.5
1	80	562	12	2.5
2	112	762	12	5
3	144	1000	11	5

**Table 6.3:** Characterization of the strip barrel, including the number of staves, radius, tilt angle, and strip length in the ITk layout 03-00-00 [107].

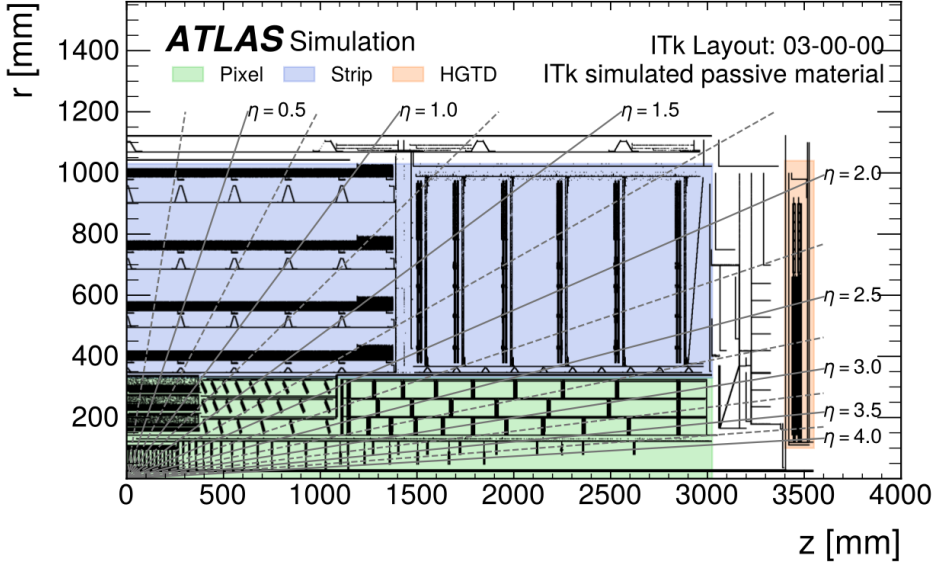


**Figure 6.3:** Location of the materials for one quadrant of the ITk layout 03-00-00. The pixel subsystem is shown in green and surrounded by the strip subsystem shown in blue. The location of the materials are indicated by black regions [12].

<sup>1913</sup> engineering estimate. The outer pixel endcaps are modelled as rings. Each layer of rings is  
<sup>1914</sup> also supported by a cylindrical carbon-fiber shell.

<sup>1915</sup> Pixel modules are modelled as an active sensor volume and a front-end (FE) chip. Layer  
<sup>1916</sup> 0 of both the barrel in the endcaps features 3D pixel sensors. The active part of the sensor

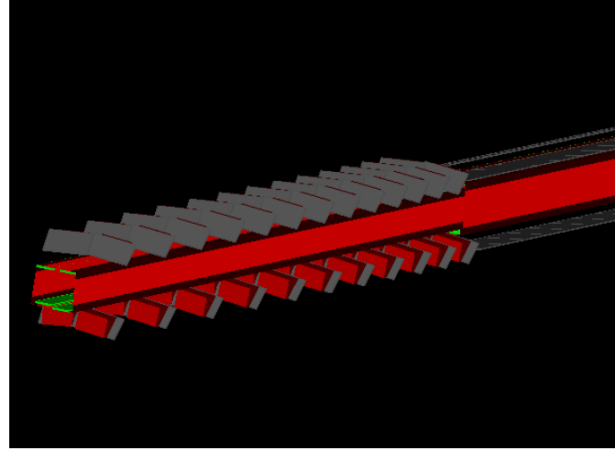


**Figure 6.4:** An illustration of the GEANT4 geometry model of the outer barrel longeron stave with mounted inclined and flat modules. Figure taken from reference [109].

is implemented as a  $150\text{-}\mu\text{m}$  thick layer of silicon and the support wafer as a  $100\text{-}\mu\text{m}$  thick layer of inactive silicon. Other layers feature planar pixel sensors, modelled as  $100\text{-}\mu\text{m}$  and  $150\text{-}\mu\text{m}$  thick active silicon respectively in layer 1 and layers 2-4.

Front-end chips are modelled as a  $150\text{-}\mu\text{m}$  thick silicon wafer, with a  $1\text{-}\mu\text{m}$  thick copper layer to model its circuitry, and a Sn-Ag bump bond of  $20\text{-}\mu\text{m}$  in diameter per pixel channel. The material of each component in the FE chips is homogeneously distributed throughout its corresponding volume.

### 6.2.2 Simulation of the Strip Detector

In the strip barrel detector, each individual part is modelled separately, with masses and material compositions reflecting the mechanical designs. In the strip endcaps, materials and objects in close proximity with each other are not individually modelled, but instead as one homogeneous block of material adjusted to have the same radiation length as calculated based on engineering designs. Figure 6.5 displays the GEANT4 geometry model of barrel staves and endcap petals in the Strip detector.

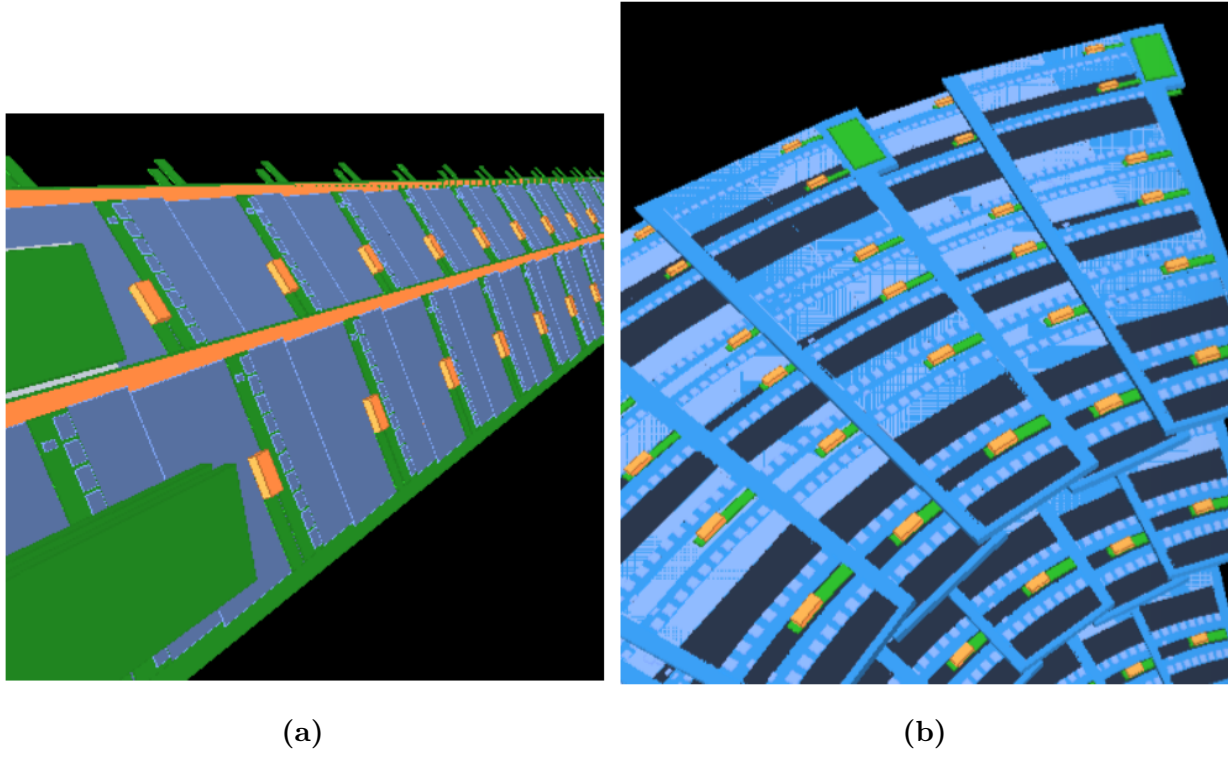


**Figure 6.5:** Displays of the GEANT4 geometry model of the strip barrel staves (left) and the endcap petals (right). Figure taken from reference [109].

1931        The global support of the detector in both the barrel and the endcaps is modelled in detail.  
 1932        Components include stave cooling pipes, carbon-foam, facesheets, cable bus, hybrids, and  
 1933        FE ASICs. Endcap sensors are individually modelled, while other components are modelled  
 1934        as a single edge-shaped object sandwiched between two silicon layers and uniformly filled  
 1935        with a generic material. The density of the material is adjusted to provide a radiation length  
 1936        of 0.02  $X_0$  per substructure.

### 1937        6.3 Particle interaction with detector material

1938        An important aspect of realistic detector simulation as well as track reconstruction is  
 1939        the treatment of interactions between high-energy particles and the materials they traverse.

1940 For charged particles at the energy range relevant to the Inner Tracker, these interactions  
 1941 are dominated by two processes: (i) inelastic collisions with atomic electrons, and (ii) elastic  
 1942 scattering against atomic nuclei. In turn, they result in two primary effects: (1) a loss in  
 1943 energy by the particle, and (2) a deflection from the original direction of incident. Of the  
 1944 two electromagnetic processes, inelastic collisions are responsible for the greater part of the  
 1945 energy loss from heavy particles in matter. Each collision transfers but a tiny fraction of  
 1946 the particle's energy to the incident atom, causing an ionization or excitation of the latter<sup>1</sup>.  
 1947 However, the number of collisions encountered by a particle per unit path length in dense  
 1948 materials is typically large enough that a non-negligible amount of its energy is lost to the  
 1949 environment.

### 1950 6.3.1 Energy loss of heavy particles

1951 The probability of an inelastic collision is described by the quantum mechanical scattering  
 1952 amplitude calculated for the corresponding process. In a macroscopic path length, a particle  
 1953 undergoes so many collisions that the distribution of total energy loss sharply peaks around  
 1954 an average value. Therefore, it is sufficient to compute the average energy loss per unit  
 1955 length, also called the stopping power or  $\frac{dE}{dx}$ . The stopping power of a material on an  
 1956 incident particle in the momentum range relevant to the ITk is given by the Bethe-Bloch  
 1957 formula [22]

$$-\frac{dE}{dx} = 2\pi N_a r_e^2 m_e c^2 \frac{Z}{A} \left( \frac{z^2}{\beta^2} \right) \left[ \log \left( \frac{2m_e \gamma^2 v^2 W_{max}}{I^2} \right) - 2\beta^2 - \delta \right], \quad (6.1)$$

1958 in which  $r_e = 2.817 \times 10^{-13}$  cm is the classical electron radius,  $m_e$  the electron mass,  $N_a$   
 1959 the Avogadro's number,  $I$  the mean excitation potential,  $Z$  and  $A$  the atomic number and  
 1960 atomic weight of the absorbing material,  $z$  the charge of the incident particle in units of  $e$ ,  
 1961  $\beta$  the  $\frac{v}{c}$  ratio,  $\gamma = (1 - \beta^2)^{-1/2}$  the relativistic  $\gamma$  factor,  $\delta$  the density correction, and  $W_{max}$   
 1962 the maximum energy transfer in a single collision. The maximum energy transfer depends

---

<sup>1</sup>To demonstrate the scale of each energy loss, note that atomic excitations are often measured in eV, while particle energy is often given in MeV or GeV.

1963 on the ratio of the electron mass and the particle mass

$$W_{max} = \frac{2m_e c^2 \beta^2 \gamma^2}{1 + 2\gamma(m_e/M) + (m_e/M)^2}. \quad (6.2)$$

1964 The left hand side of equation (6.1) is called the mass stopping power, which varies slowly  
 1965 with different materials. The average energy loss per unit length is simply given by  $\rho \left( \frac{dE}{dx} \right)$ .  
 1966 Shown in figure 6.6 is the mass stopping power computed for a positive muon in copper over  
 1967 12 order of magnitude in muon momentum. The region corresponding to  $10 \text{ MeV} < p_{\mu^+} <$   
 1968  $100 \text{ GeV}$ , most relevant in high-energy physics, is called the Bethe region where the stopping  
 1969 power is a function of  $\beta$  alone. At non-relativistic energies,  $\frac{dE}{dx}$  is dominated by the overall  
 1970  $1/\beta^2$  factor (note the logarithmic scale in the vertical axis of 6.6). The stopping power  
 1971 reaches a minimum at  $\beta\gamma \approx 3$ , and slowly rises thanks to the logarithmic dependence up  
 1972 to  $\beta\gamma = 1000$ , a range equivalent to a muon momentum of  $1 - 100 \text{ GeV}$ . This minimum is  
 1973 broad and almost the same for all particles of the same charge. For this reason, particles at  
 1974 this point are called “minimum-ionizing”.

1975 The stopping power in equation (6.1) is computed for pure elements. A non-elemental  
 1976 material can be considered as a mixture of elements, whose stopping power is approximated  
 1977 by a weighted mean of  $\frac{dE}{dx}$  over the elements in the compound. The weight is given by the  
 1978 fraction of electrons contributed by each element. In particular, the average mass stopping  
 1979 power is

$$\frac{dE}{dx} = \sum_i w_i \left( \frac{dE}{dx} \right)_i, \quad w_i = \frac{a_i A_i}{\sum_j a_j A_j} \quad (6.3)$$

1980 where  $a_i$  is the number of atoms in the  $i$ -th element, and  $A_i$  the atomic weight. Knowing  
 1981 the stopping power of each element in a material and the molecular composition, one can  
 1982 easily compute the mean energy loss of an incident particle given its momentum.

1983 Because of the statistical nature of inelastic collisions, the amount of energy deposited  
 1984 by a particle fluctuates around the mean calculated in equation (6.1). In a relatively thick  
 1985 absorber, the number of collisions is large, and, assuming each collision results in a small en-  
 1986 ergy loss  $\delta E$ , such that the particle velocity stays constant, the stopping power  $\frac{dE}{dx}$  negligibly

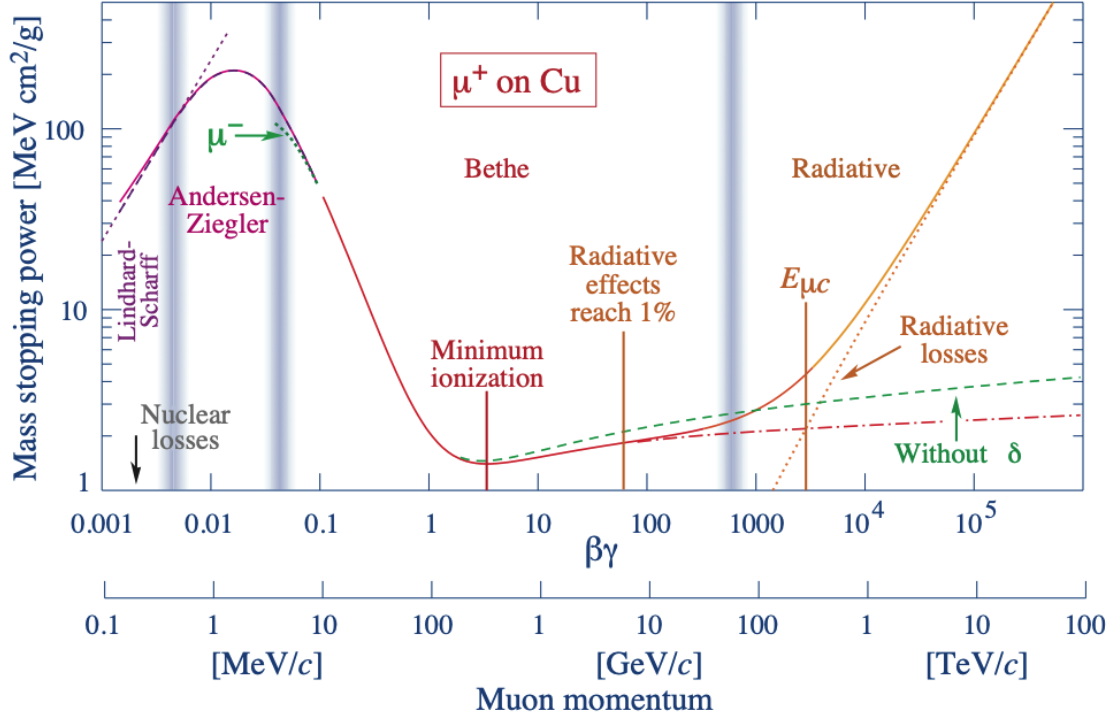


**Figure 6.6:** The mass stopping power of positive muons in copper as a function of the muon momentum spanning nine orders of magnitude. The solid curves indicate the total stopping power of all dissipative effects. The region of interest in HEP ranges from 100 MeV to 100 GeV, well within the so-called Bethe region, in which the stopping power is strongly dependent on  $\beta$  (see text for definition). Figure taken from reference [22].

1987 varies throughout the particle's path. The total energy loss is thus the sum of a large number  
 1988 of independent identically distributed random energy losses, which approaches a Gaussian  
 1989 as  $N \rightarrow \infty$

$$f(\Delta E; x) = \frac{1}{\sqrt{2\pi}\sigma} \exp \left[ \frac{-(\Delta E - \langle \Delta E \rangle)^2}{2\sigma^2} \right], \quad \langle \Delta E \rangle = \int_0^x \left( \frac{dE}{dx'} \right) dx'. \quad (6.4)$$

1990 with variance

$$\sigma = 0.1569\rho \left( \frac{Z}{A} \right) \frac{1 - \beta^2/2}{1 - \beta^2} x. \quad (6.5)$$

### 1991 6.3.2 Energy loss of electrons and positrons

1992 Light charged particles such as electrons and positrons undergo collisional energy loss  
 1993 in matter, just like heavy particles. However, because of their small mass, electromagnetic  
 1994 radiation in the electric field of atomic nuclei becomes a significant contribution to their  
 1995 overall rate of energy loss

$$\left( \frac{dE}{dx} \right) = \left( \frac{dE}{dx} \right)_{rad} + \left( \frac{dE}{dx} \right)_{col}, \quad (6.6)$$

1996 in which  $\left( \frac{dE}{dx} \right)_{rad}$  is the radiative component and  $\left( \frac{dE}{dx} \right)_{col}$  the collisional component already  
 1997 described.

1998 Even though the mechanism of collisional loss remains the same, because their mass is  
 1999 small, light particles could get deflected significantly from the original direction of incident.  
 2000 In addition, the collision occurs between identical particles, so several modifications to the  
 2001 Bethe equation are needed, starting with the maximum energy transfer  $W_{max} = T/2$  where  
 2002  $T$  is the kinetic energy of the incident particle. The collisional stopping potential becomes

$$-\left( \frac{dE}{dx} \right)_{col} = 2\pi N_a r_e^2 m_e c^2 \frac{Z}{A} \left( \frac{1}{\beta^2} \right) \left[ \log \frac{\tau^2(\tau+2)}{2(I/m_e c^2)^2} + F(\tau) - \delta \right], \quad \tau = \frac{T}{m_e c^2} \quad (6.7)$$

where the function  $F(\tau)$  modifies the  $\beta^2$  term in equation (6.1) to account for the interaction  
 between identical particles, resulting from crossing Feynman diagrams:

$$F_{e^-}(\tau) = 1 - \beta^2 + \frac{\tau^2/8 - (2\tau+1)\ln 2}{(\tau+1)^2},$$

and

$$F_{e^+}(\tau) = 2\ln 2 - \frac{\beta^2}{12} \left( 23 + \frac{14}{\tau+2} + \frac{10}{(\tau+2)^2} + \frac{4}{(\tau+2)^3} \right).$$

2003 Qualitatively, the radiative cross-section of bremsstrahlung is proportional to the inverse  
 2004 square of particle mass. Therefore, being far lighter than any other particle, electrons and,  
 2005 to a much lesser extent, muons lose a significant portion of their energy to this phenomenon.  
 2006 The radiative contribution to the mass stopping power can be written as

$$-\left( \frac{dE}{dx} \right)_{rad} = \frac{N_a}{A} E \Phi_{rad}, \quad (6.8)$$

2007 where  $\Phi_{rad}$  is the total radiative cross section, approximated by

$$\Phi_{rad} = 4Z^2(e^2/m_e c^2)^2 \alpha^2 \left[ \ln(183Z^{-1/3}) + \frac{1}{18} - f(Z) \right], \quad (6.9)$$

2008 where  $f(Z)$  is a small correction to the Born approximation accounting for the Coulomb  
2009 interaction between the electron and the nucleus.

2010 It is straightforward to compare the two contributions of the total stopping power. Figure  
2011 6.7 demonstrates the the radiation and collisional energy losses for electron in copper as  
2012 functions of the electron energy. Bremsstrahlung takes effect starting at 15 MeV, and at  
2013 energy above a critical value of  $\approx 25$  MeV, its contribution quickly dominates the total  
2014 energy loss. This observation is due to the fact that collisional loss rises logarithmically with  
2015 energy, whereas radiative loss scales linearly, evidenced by equations (6.7) and (6.8). In the  
2016 energy range from 1 – 100 GeV relevant to the ITk, the electron stopping power is composed  
2017 almost entirely of radiative loss.

2018 The critical energy at which the both components contribute equality to the total energy  
2019 loss for a material is approximated by

$$E_c (\text{MeV}) = \frac{800}{Z + 1.2} \quad (6.10)$$

2020 It is evident that the material energy loss of electrons and positrons is characterized  
2021 by the Bremsstrahlung cross section. In practice, it is more convenient to characterize a  
2022 material by its radiation length  $X_0$ , defined as the distance over which the average electron  
2023 energy is reduced by a factor of  $1/e$  due to radiation loss. Equation (6.8) can be rewritten  
2024 as

$$-\rho \left( \frac{dE}{dx} \right)_{rad} \frac{1}{E} = \frac{N_a \rho}{A} \Phi_{rad} = N \Phi_{rad} = \frac{1}{X_0} \quad (6.11)$$

2025 or

$$E = E_0 \exp \left( -\frac{x}{X_0} \right), \quad (6.12)$$

2026 where  $N$  is the volumetric density of atomic nuclei in the material.

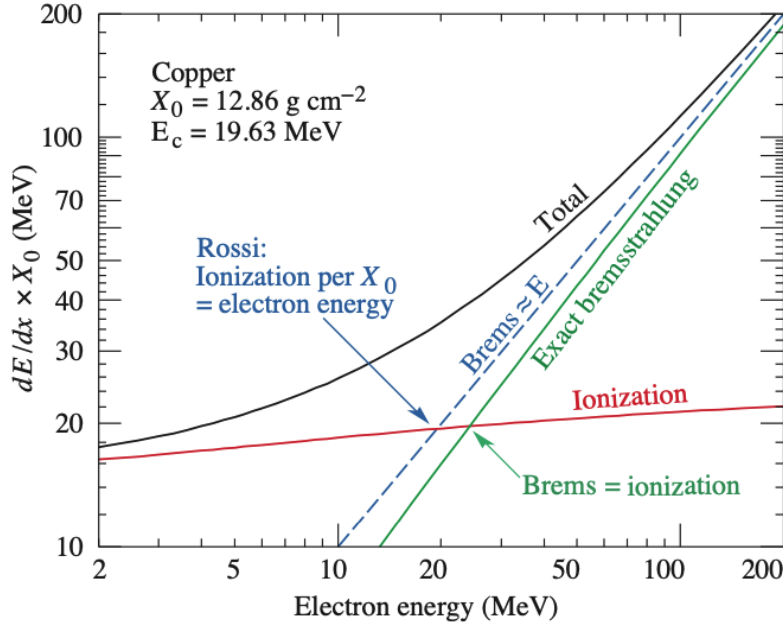


**Figure 6.7:** Contribution of radiative and collisional components in the total energy loss of electrons in copper as functions of electron energy. At a critical value  $E_c = 19.63 \text{ MeV}$ , radiative loss becomes the dominant mechanism. The energy range of electrons in HEP detectors is well within the Bremsstrahlung regime [22].

2027 In the ITk, material thickness is described in units of radiation length. Figure 6.8a shows  
 2028 the material thickness traversed by a straight track as a function of its pseudorapidity.  
 2029 Obviously, charged particles move in mostly helical orbits, whose curvature depends on the  
 2030 transverse momentum, because of the magnetic field, and thus the actual material length  
 2031 traversed by the particle is obtained by numerical integration. The central region has very  
 2032 little material, resulting from the light design of the sensor support. At higher  $\eta$ , a particle  
 2033 travels through progressively more layers and thus experiences almost linearly increasing  
 2034 material thickness. The largest contribution to the total radiation length comes from pixel  
 2035 services and cooling.

2036 For comparison, the material depth of the ID in Run 2, including the Pixel, SCT and  
 2037 TRT, is shown in figure 6.8b, and expected material thickness traversed by a particle until

it reaches the minimum number of hits required for track reconstruction in figure 6.8c. The linear ITk material budget is significantly smaller than that of the ID in the forward region, despite having more layers and better eta coverage. This is due to the adoption of serial powering in the ITk, among other design optimizations. A realistic particle experiences up to 50% more material before reaching the minimum number of hits for  $\eta < 1.5$  in the ITk than in the ID. Note, however that ID tracks are required to have only 8 hits in this region, compared to 9 hits for an ITk track. Beyond this point, the ITk becomes more transparent than the ID, by up to 50%.

### 6.3.3 Multiple Coulomb scattering

In addition to inelastic collision and radiation, charged particles undergo a large number of small-angle elastic scattering due to Coulomb interaction with atomic nuclei. Coulomb scatterings are governed by the Rutherford formula for non-relativistic collision, and the Mott formula for the relativistic counterpart. In both formulae, the scattering cross-section follows

$$\frac{d\sigma}{d\Omega} \propto \frac{1}{\sin^4(\theta/2)} \quad (6.13)$$

which favours a small scattering angle  $\theta$ . Assuming the material is sufficiently thick and the energy transfer to the nuclei is negligible, the particle suffers a large number of small deflections. The net effect can therefore be statistically represented by a probability distribution function of the total deflection which depends on the material thickness. A rigorous treatment of multiple scattering is complicated. Among the most commonly used approximations is the theory of Molière [110, 111], valid for the scattering of fast charged particles. The theory was expanded by Bethe [112] and later Scott [113] to account for Coulomb interactions with atomic electrons. Although it agrees well with data, especially at small angles and large target nuclear numbers, it relies on an unwieldy series expansion and is therefore inconvenient to use. Rossi and Greisen [114] developed a simple estimate of the root-mean-square scattering angle, which was improved by Highland [115] and Lynch and Dahl [116]

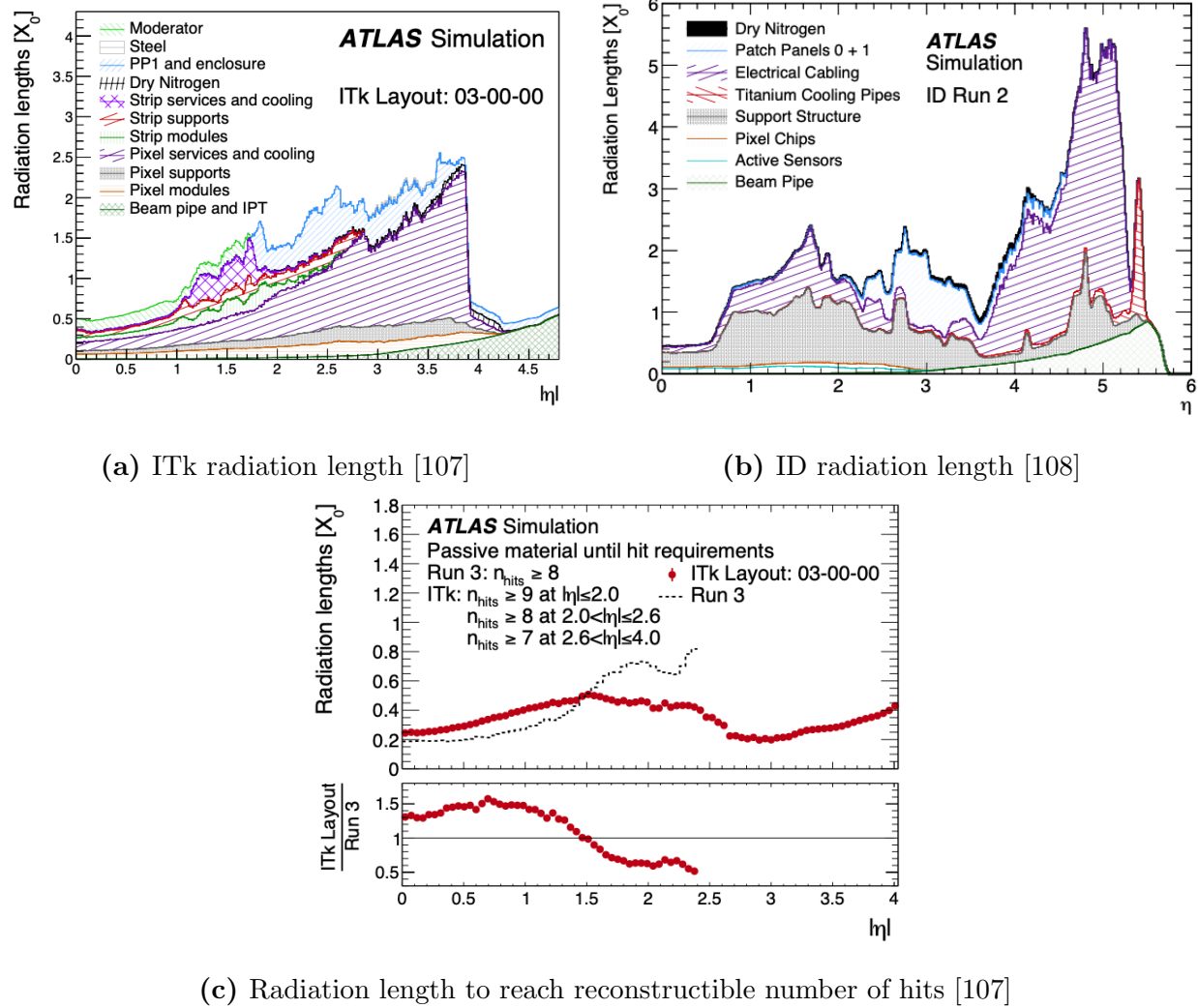


**Figure 6.8:** Integrated material budget encountered on a particle's path in unit of radiation length as a function of pseudorapidity based on (a) the ITk and (b) the ID. The particle assumes a straight trajectory from the origin. (c) is a comparison between the amount of material that must be traverse before the particle accumulates enough hits to be deemed reconstructible.

2063 to obtain the RSM width of the projected scattering angle distribution on a plane

$$\theta_0 = \frac{13.6z \text{ MeV}}{pc\beta} \sqrt{\frac{x}{X_0}} \left[ 1 + 0.038 \ln \frac{z^2(x/X_0)}{\beta^2} \right], \quad (6.14)$$

2064 where  $p$ ,  $\beta c$ , and  $z$  are the momentum, the velocity, and the charge of the incident particle.

2065  $x/X_0$  is the material thickness in radiation lengths. The scattering angle projected on a

2066 plane  $\theta_{plane}$  can be approximated by a Gaussian centered at  $\theta_{plane} = 0$

$$dP(\theta_{plane}) = \frac{1}{\sqrt{2\pi}\theta_0} \exp\left[-\frac{\theta_{plane}^2}{2\theta_0^2}\right] d\theta_{plane} \quad (6.15)$$

2067 The total angle  $\vartheta$  can be approximated by the quadratic sum of two small projected angles  
2068 on orthogonal planes

$$\vartheta^2 = \theta_{plane,x}^2 + \theta_{plane,y}^2, \quad d\vartheta = d\theta_{plane,x} d\theta_{plane,y} \quad (6.16)$$

2069 and with the assumption that the two projected angles are independent,  $\vartheta_{tot}$  is

$$dP(\vartheta) = \frac{1}{2\pi\theta_0^2} \exp\left[-\frac{\vartheta^2}{2\theta_0^2}\right] d\vartheta \quad (6.17)$$

2070 Figure 6.9 illustrates the quantities used to describe the effect of multiple scattering. The  
2071 total scattering angle is projected on a plane

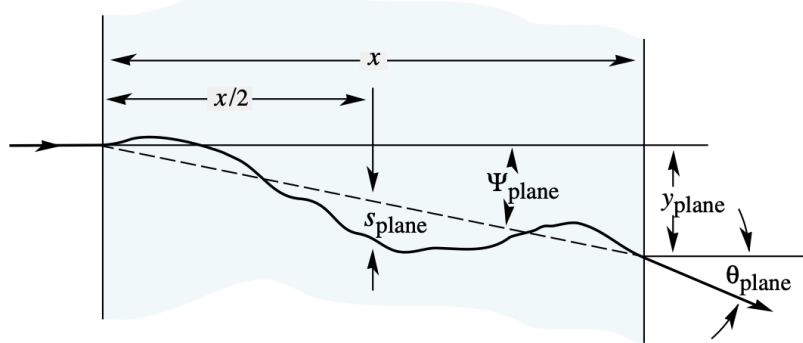


**Figure 6.9:** Schematic of the calculation of macroscopic mean deflection angle caused by multiple scattering [22].

2072 The material effects described in this section, sections 6.3.1 and 6.3.2, are sufficient for  
2073 Monte-Carlo simulations of the particle passage through material in the ITk. The overall  
2074 trajectory can be discretized into small segments. The mean energy loss and Coulomb  
2075 scattering angle over each segment can be estimated using equations (6.1), (6.12), (6.15) and  
2076 (6.17), along with the material distribution as shown in figure 6.8a. The actual energy loss  
2077 and scattering angle are then sampled from the corresponding distribution.

2078 **6.4 Simulated samples**

2079 The development and evaluation of the new tracking algorithm in this thesis is carried  
2080 out using a sample of simulated  $pp \rightarrow t\bar{t}$  events at center-of-mass energy  $\sqrt{s} = 14$  TeV,  
2081 with average pile-up ranging from 190 to 210. The actual number of pile-up interactions  
2082 in each event is randomly sampled from a Poisson distribution centred at the average pile-  
2083 up. The hard-scattering event is generated using the POWHEG Box v2 [117, 118, 119, 120]  
2084 generator at next-to-leading order in QCD with the NNPDF3.0NLO [55] Parton Distribution  
2085 Functions (PDFs). The  $h_{\text{damp}}$  parameter<sup>II</sup> is fixed to  $1.5m_{\text{top}}$  [121] and the top quark mass to  
2086  $m_{\text{top}} = 172.5$  GeV. Parton shower and hadronization are modeled using PYTHIA 8.230[53],  
2087 with the A14 set of tuned parameters [54] and using the NNPDF2.3LO [122] set of PDFs. A  
2088 semi-leptonic final state, in which one of the two  $W$ -bosons descending from the top quarks  
2089 decays to an electron or a muon, is enforced. The decay of bottom and charm hadrons are  
2090 performed by EVTGEN 1.6.0[123]. The simulation described here follows the procedure  
2091 detailed in reference [107].

2092 To simulate the pile-up background, a large pool of soft minimum-bias interactions is  
2093 generated. Each event is created by overlaying a number of min-bias sub-events on the hard-  
2094 scattering sub-event, and then digitizing the detector response. A feature of MC simulation  
2095 in ATLAS is that the pile-up sub-events are not uniquely generated for each events but ran-  
2096 domly sampled from the common pool, resulting in a dataset whose events are guaranteed to  
2097 feature different hard-scattering events, but may share a portion of their pile-up background.  
2098 A dataset of 100000  $t\bar{t}$  events are simulated, from which a subset of 10000 events is identified  
2099 to share no pile-up particles with the remaining 90000. This subset is dedicated to machine  
2100 learning training and performance evaluation. The hard-scattering particles of the 90000 are  
2101 used to train an algorithm to construct graphs from detector hits.

---

<sup>II</sup> $h_{\text{damp}}$  is a resummation damping factor and one of the parameters that controls the matching of POWHEG matrix elements to the parton shower and regulates the high- $p_T$  radiation against which the  $t\bar{t}$  system recoils.

2102 **Chapter 7**

2103 **The ATLAS track reconstruction chain**

2104 The High Luminosity era brings many challenges to event reconstruction in general and  
2105 charged-particle tracking in particular, due to increased pile-up level and detector granu-  
2106 larity. The current algorithm used in offline tracking scales super-linearly with pile-up and  
2107 struggles to meet the future operational requirements. This motivates the development of  
2108 an alternative algorithm that leverages modern hardware accelerators, such as the Graphic  
2109 Processing Unit (GPU) or the Field-Programmable Gate Array (FPGA), to boost the re-  
2110 construction speed. In this context, an understanding of the existing algorithm is necessary  
2111 to adequately compare its performance to that of the proposed algorithm. This chapter  
2112 describes the working principle of the Combinatorial Kalman Filter—the engine of charged-  
2113 particle tracking, and the challenges facing it in the High-Luminosity era. The Kalman  
2114 mechanism stems naturally from the least-square fit, which is also the basis of the discussion  
2115 in chapter 11.

2116 **7.1 Clusterization and space point formation**

2117 The first step of track reconstruction is the clusterization of the energy deposit on indi-  
2118 vidual sensor cells recorded by the detector. Figure 7.1 illustrates a particle passing through  
2119 a planar pixel sensor and depositing a small amount of its energy. Each sensor cell inde-  
2120 pendently measures this energy and, when the energy exceeds a certain threshold, records a  
2121 signal. Throughout an event, a sensor may experience multiple passages of different particle

2122 trajectories, as shown on figure 7.2, so its collection of cell read-outs must then be sorted into  
 2123 groups of neighbouring cells likely to originate from the same particle. This process, called  
 2124 clusterization, transforms low-level information from individual sensor cells to a higher-level  
 2125 and more compact objects, called **clusters**.

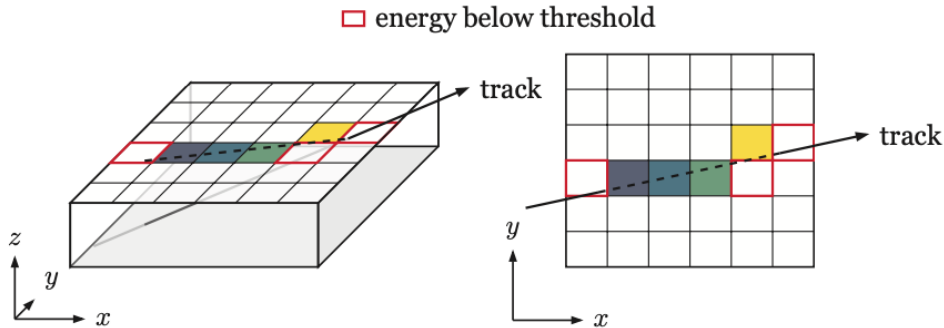


**Figure 7.1:** Formation of a pixel clusters from multiple cells. The particle deposits its energy in 7 cells, 5 of which receive charges exceeding the detection threshold and enter the clusterization [124].

2126 ATLAS traditionally uses a connected component analysis (CCA) [125], and more re-  
 2127 cently a neural network-based approach to clusterize cell read-outs[126]. The intersection  
 2128 point  $\mathbf{l}$  between the track and the sensor is estimated from the local coordinates  $\mathbf{l}_i$  of each  
 2129 cells in the clusters

$$\mathbf{l} = \begin{cases} \frac{1}{N} \sum_i \mathbf{l}_i \\ \frac{1}{\sum_i q_i} \sum_i q_i \mathbf{l}_i \end{cases}, \quad (7.1)$$

2130 where  $q_i$  is the charge deposit on cell  $i$ . The first formula computes a simple vector mean of  
 2131 the cell location, and the second a charge-weighted mean. In the neural network approach,  
 2132 the cluster position and uncertainty are both predicted by the network and found to be more  
 2133 accurate than the (weighted) mean approach.

2134 A cluster can be regarded as a measurement made in the local coordinate of the measuring  
 2135 surface<sup>I</sup>. From a cluster, the location of the hit in global coordinate, called the space point,

---

<sup>I</sup>For rest of this thesis, the terms “measurement” and “cluster” are interchangeable and refer to the same objects

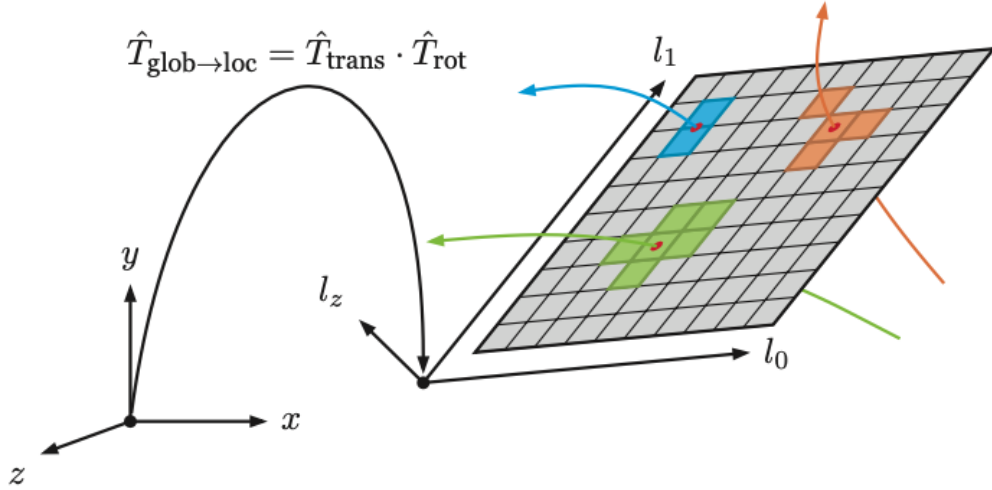


**Figure 7.2:** The passage of a particle through a pixel sensor segmented in two dimensions. The energy deposit in each sensor cell is measured as a signal when it exceeds a measurement threshold. The true intersection point is estimated from the signal cells grouped together, called a cluster [124].

can be derived. Figure 7.2 illustrates three particle tracks traversing a pixel sensor and inducing separate clusters. The true intersections are shown as red dots. An estimate of each of the true intersections between the trajectory and the sensor plane shown as red dots, is made in the clusterization step, and combined with the location and rotation of the sensor surface to obtain the space points. In this sense, pixel space point formation is obtained from a change in reference frame of the cluster coordinates via a series of translational and rotational transformations.

While there is a one-to-one correspondence between a pixel cluster and a pixel space point, the space point formation in the strip detector is more complicated. Strip modules are finely segmented in only one direction, rendering each measurement one-dimensional, in contrast to the two-dimensional measurements on a pixel module. To obtain a three-dimensional position estimate, two strip clusters from the same layer are combined, as shown in fig. 7.3. The local position of the hit along the thinly segmented dimension is estimated with high resolution. Thanks to the stereo angle between the modules, an estimate of the second

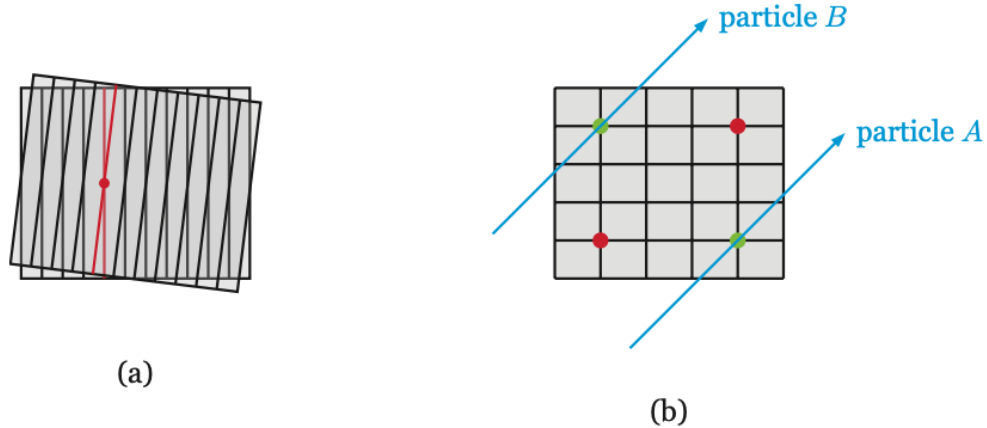


**Figure 7.3:** A pair of strip sensors are used to reconstruct a 3-dimensional estimate of the particle’s true impact point (a). Ambiguity arises when more than one particle hit a strip module, leading to more combinations than particles (b) [124].

2150 coordinate is made from the intersection of the strip cells, albeit with lower resolution. These  
2151 measurements are then transformed to a global position estimate, as described above.

2152 In the current track reconstruction chain, space points are used to build track seeds, which  
2153 are small groups of hits likely to originate from the same particle. A dedicated seeding stage  
2154 creates large number of seeds each containing three space points and subsequently feeds them  
2155 to a track building algorithm. The latter extends the seed by iteratively adding clusters that  
2156 are compatible with the corresponding track state. A small number of clusters in the final  
2157 track candidate come from the seed space points, and the rest from individually incorporated  
2158 clusters on the track path.

2159 Finally, we note an important consequence of the 2-cluster composition of the strip space  
2160 point. Despite meticulous optimization of the detector layout, a particle does not always  
2161 leave two hits on a strip layer. Silicon sensors have inherent inefficiency, which means that a  
2162 particle may traverse a detector module without inducing a signal. This phenomenon occurs  
2163 in both sub-detectors of the ITk, but is very unlikely. A more important inefficiency comes  
2164 from the the strip detector, in which a particle may approach a layer in a direction such that

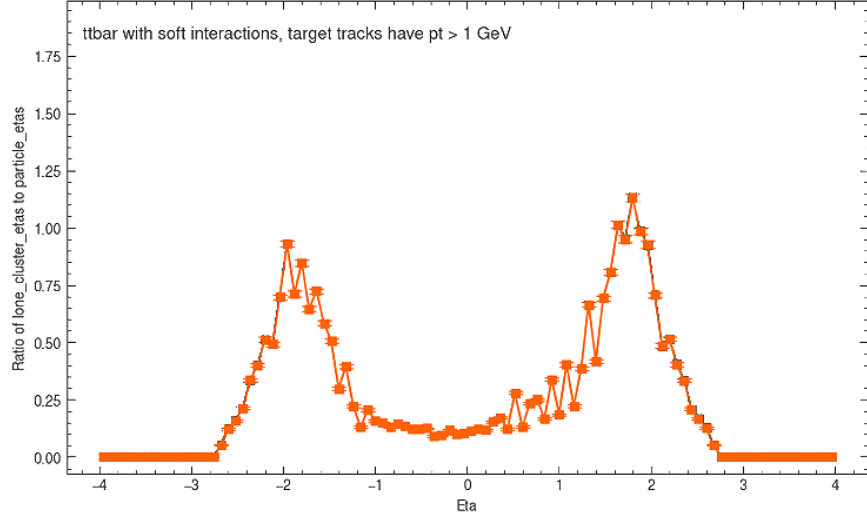


**Figure 7.4:** Average number of lone strip clusters per track as a function of the particle pseudo-rapidity  $\eta$ .

it intersects only one of two physical strip modules (see section 6.1 for a description of the strip detector). For any reason, when a strip layer records a *lone* cluster, it is ignored by the space point formation algorithm, resulting in its absence from the space point collection. On figure 7.4, we observe that particles leave lone clusters when their pseudorapidity falls under the coverage of the strip detector at  $|\eta| < 2.8$ , reaching up to one lone cluster per particle at  $|\eta| \simeq 1.8$ . This means that if we look at the space point record, every particle in this region effectively skips a strip layer. This hit inefficiency is inconsequential in the current ATLAS reconstruction chain, because space points are only used for track seeding, and there is enough redundancy to cover all true particle seeds. However, an algorithm that builds tracks from space points would not see lone clusters in the input, which may cause potential impacts on its performance. This issue will become important for the new algorithm and be described in chapter 11.

## 2177 7.2 The least-square fit

2178 A track candidate is a set of measurements made by sensitive detector elements on  
2179 the particle's trajectory. The latter is mathematically represented by a set of parameters  
2180 describing its position and momentum as it traverses the detector. Although in idealized  
2181 situations, the track may be parametrized by constants of motion, in a realistic detector,  
2182 even these constants vary over time, due to random material effects. Therefore, a necessary  
2183 ingredient to describe the trajectory is the solution to the equation of motion given the  
2184 detector setup. From an initial value and the precise magnetic field on a dense grid of  
2185 sampling points, the equation of motion is numerically integrated to obtain the a description  
2186 of that particle state as it evolves along the trajectory.

2187 Let  $\mathbf{x} \in \mathbb{R}^d$  represent the state of the particle and vary as a function of the arc length  $s$   
2188 along the trajectory<sup>II</sup>, so that

$$\mathbf{x} = \mathbf{x}(s) \tag{7.2}$$

2189 We will keep the discussion here general and note that any set of parameters from which the  
2190 instantaneous position and momentum of the particle can be derived is usable. The choice  
2191 of parametrization in ATLAS is discussed in section 11.1. In general, track parameters can  
2192 be regarded as the internal state of the particle, which is not directly measurable. Instead  
2193 the measurements are made at discrete points on the trajectory where a sensitive module  
2194 is present. Each measurement  $\mathbf{m}_i$  can then be modelled as a deterministic function of the  
2195 track state at that the measuring surface  $\mathbf{x}_i$  superimposed by a random experimental noise  
2196  $\epsilon_i$ .

$$\mathbf{m}_i = h_i(\mathbf{x}_i) + \epsilon_i. \tag{7.3}$$

2197 The function  $h_i : \mathbb{R}^d \rightarrow \mathbb{R}^n$ , called the *measurement model*, projects the  $d$ -dimensional state  
2198 vector  $\mathbf{x}_i$  on the  $i$ -th surface to an  $n$ -dimensional measurement vector. Its functional form  
2199 depends on the type of measuring surface, hence the subscript. For example, a measurement

---

<sup>II</sup>Since  $s = vt$ , this is equivalent to parametrization in time.

2200 on a pixel module is intrinsically different from one on a strip module<sup>III</sup>, so their measurement  
2201 models naturally differ.

2202 The experimental noise  $\epsilon_i$  also depends on the type of measuring surface. However, it is  
2203 generally assumed to be unbiased with finite variance, namely

$$E[\epsilon_i] = \mathbf{0}, \quad 0 < \sigma(\epsilon_i^{(j)}) < +\infty, \forall j \in [n], \quad (7.4)$$

2204 where the superscript denotes the  $j$ -th component of the  $n$ -dimensional error vector. The  
2205 covariance matrix of  $\epsilon$  is an important ingredient of the least-square fit, denoted by

$$\mathbf{V}_i = E[\epsilon_i \epsilon_i^T] \quad (7.5)$$

2206 As mentioned above, the state vector evolves along the trajectory, governed by the Equa-  
2207 tion of Motion (EOM), the solution to which is called the track model. The system evolution  
2208 can be written as a recursive process

$$\mathbf{x}_i = \mathbf{x}(s_i) = f_{i-1}(\mathbf{x}_{i-1}). \quad (7.6)$$

2209 The extrapolation function  $f_{i-1} : \mathbb{R}^d \rightarrow \mathbb{R}^d$  projects the track state from the previous  
2210 measuring surface  $\mathbf{x}_{i-1}$  to the current surface. Its functional form depends on the equation  
2211 of motion, which in turns depends on detector characteristics, such as its magnetic field  
2212 and layouts. As the EOM is in general a second-order non-linear differential equation, a  
2213 close-form solution, if it exists, is likely non-linear. However, in practice, the EOM is often  
2214 linearized and numerically integrated by, for example, Euler's method, allowing a linear,  
2215 albeit recursive and potentially expensive solution

$$\mathbf{x}(s_{i-1} + \Delta s) \approx \mathbf{x}(s_{i-1}) + \frac{\partial \mathbf{x}'}{\partial s'} \Big|_{s'=s_{i-1}} \Delta s + \mathcal{O}((\Delta s)^2), \quad (7.7)$$

2216 where the derivative is calculated from the dynamical equation of the system. More sophis-  
2217 ticated numerical methods can be used, but in principle, it is possible to approximate the

---

<sup>III</sup>A pixel cluster is a 2D measurement, while a strip cluster is 1D.

2218 transport equation (7.6) as a linear recursive relation. The benefit of such linearization is  
2219 that we can write the track state on any surface  $\mathbf{x}_i$  as a simple linear function of some initial  
2220 value on a reference surface  $\mathbf{x}_0$ ,

$$\mathbf{x}_i = f_{i-1}(x_{i-1}) = f_{i-1}(f_{i-2}(\mathbf{x}_{i-2})) = f_{i-1} \circ f_{i-2} \circ \dots \circ f_0(\mathbf{x}_0) = f_i(\mathbf{x}_0), \quad (7.8)$$

2221 and take  $\mathbf{x}_0$  as *the* estimated track parameters.

2222 Track fitting is now reduced to finding an estimator  $F$  from the set of measurements  
2223  $M = \{\mathbf{m}_1, \dots, \mathbf{m}_N\}$  to the parameter space, such that (1) the estimate  $\hat{\mathbf{x}}_0 = F(M)$  is  
2224 unbiased

$$E[\hat{\mathbf{x}}_0] = \mathbf{x}_0 \quad (7.9)$$

2225 and (2) of minimum variance

$$E[(F(M) - \mathbf{x}_0)^2] = \min_{F'} E[(F'(M) - \mathbf{x}_0)^2] \quad (7.10)$$

2226 The Gauss-Markov theorem [127] states that among the class of linear and unbiased esti-  
2227 mators, the Least Squares Estimator (LSE) has minimum variance, provided a linear track  
2228 model, purely statistical<sup>IV</sup>, unbiased and uncorrelated errors  $\epsilon_i$ . The LSE is obtained by  
2229 minimizing the  $\chi^2$ -function, defined as

$$\chi^2 = \sum_{i=1}^N [\mathbf{m}_i - h_i(f_i(\mathbf{x}_0))]^T \mathbf{V}_i^{-1} [\mathbf{m}_i - h_i(f_i(\mathbf{x}_0))], \quad (7.11)$$

2230 where both  $h_i$  and  $f_i$  are now assumed to be linear. The linearity of  $h_i$  can be achieved by a  
2231 careful choice of parametrization, such as the one used by ATLAS, discussed in section 11.1.  
2232 The estimator is simply the solution to

$$\nabla \chi^2(\mathbf{x}_0) = 0 \quad (7.12)$$

---

<sup>IV</sup>i.e. independent of  $\mathbf{x}$

2233 **7.3 Iterative track fit**

2234 Because the LSM considers all measurements at the same time, it is a global fitting  
2235 method. It can be shown that in situations where the material effects described in section  
2236 6.3 cannot be ignored, the minimization of the  $\chi^2$ -function translates to the inversion of a  
2237 non-diagonal covariance matrix whose dimension grows with the number of measurements  
2238  $N$ . This computation can become a significant bottleneck in complex and granular detectors  
2239 (see chapter 3 of reference [128] for more details).

2240 The Kalman formalism [129, 130, 131] offers a faster alternative to global fit that, cru-  
2241 cially, yields optimal estimates for Gaussian measurement uncertainties. The track state still  
2242 evolves as a linear dynamical system. Multiple scattering and energy loss due to material  
2243 interactions are modelled as random process noise  $\mathbf{w}$  added to the transport equation

$$\mathbf{x}_i = \mathbf{F}_{i-1} \mathbf{x}_{i-1} + \mathbf{w}_{i-1}, \quad (7.13)$$

2244 where the matrix  $\mathbf{F}_{i-1}$  is the track model given in equation (7.6) now written in the explicitly  
2245 linear form. The process noise  $\mathbf{w}$  has a covariance denoted by

$$\mathbf{Q} = E[(\mathbf{w} - E[\mathbf{w}])(\mathbf{w} - E[\mathbf{w}])^T] \quad (7.14)$$

2246 Instead of minimizing a  $\chi^2$ -function over all measurements, the Kalman procedure iteratively  
2247 incorporates measurements into an existing estimate of the track parameters. Each iteration  
2248 inverts a single  $n \times n$  matrix, so in total,  $N$  inversions of  $n \times n$ -matrices are needed, where  $n$   
2249 is the number of measurement coordinates<sup>V</sup> and  $N$  the number of measurements, as opposed  
2250 to inverting an  $(nN) \times (nN)$  matrix in the LSM. The information from the measurement  
2251 is used to constrain the estimate and reduce the error. The procedure is carried out in the  
2252 following 3-step recipe.

2253 **Step 1: Prediction.** Suppose the measurement  $\mathbf{m}_i \in M$  is being incorporated. Let  $\mathbf{x}_{i-1}$   
2254 and  $x_i^{i-1}$  denote the track state before the inclusion of  $\mathbf{m}_i$ , and its projection to the measuring

---

<sup>V</sup>In typical ATLAS parametrization,  $n = 2$

2255 surface of  $\mathbf{m}_i$  by the transport equation. In addition, denote the covariance of the estimate  
 2256 as  $\mathbf{C}$ ,

$$\mathbf{C} = E[(\mathbf{x} - E[\mathbf{x}])(\mathbf{x} - E[\mathbf{x}])^T], \quad (7.15)$$

2257 so that the covariance before inclusion is  $\mathbf{C}_{i-1}$ . Neither of  $\mathbf{x}_{i-1}$  nor  $\mathbf{x}_i^{i-1}$  contains information  
 2258 from  $\mathbf{m}_i$ , nor any material effect during the propagation,

$$\mathbf{x}_i^{i-1} = \mathbf{F}_{i-1}\mathbf{x}_{i-1}. \quad (7.16)$$

2259 The stochastic noise due multiple Coulomb scattering and energy loss corrections is instead  
 2260 superimposed on the projected covariance,

$$\mathbf{C}_i^{i-1} = \mathbf{F}_{i-1}\mathbf{C}_{i-1}\mathbf{F}_{i-1}^T + \mathbf{Q}_{i-1}. \quad (7.17)$$

2261 **Step 2: Filtering.** The predicted track state in (7.16) is combined with the present mea-  
 2262 surement  $\mathbf{m}_i$  to yield the updated estimate  $\mathbf{x}_i$

$$\mathbf{x}_i = \mathbf{x}_i^{i-1} + \mathbf{K}_i(\mathbf{m}_i - \mathbf{H}_i\mathbf{x}_i^{i-1}). \quad (7.18)$$

2263  $\mathbf{K}_i$  is called the Kalman gain matrix

$$\mathbf{K}_i = \mathbf{C}_i^{i-1}\mathbf{H}_i^T(\mathbf{V}_i + \mathbf{H}_i\mathbf{C}_i^{i-1}\mathbf{H}_i^T)^{-1}. \quad (7.19)$$

2264 Intuitively,  $(\mathbf{m}_i - \mathbf{H}_i\mathbf{x}_i^{i-1})$  represents the difference between the actual measurement and  
 2265 the expected measurement given the predicted track state. If the measurement exactly  
 2266 equals its predicted value, it supports the predicted track state, so the update track state  
 2267 equals its predicted value. No new information is added to the filtered estimate in such a  
 2268 case. Therefore, we can think of the Kalman matrix as the information gained from any  
 2269 disagreement between the predicted and the actual measurement, hence its denomination.

2270 The covariance of the estimate is updated from its prediction as

$$\mathbf{C}_i = (\mathbf{I} - \mathbf{K}_i\mathbf{H}_i)\mathbf{C}_i^{i-1}. \quad (7.20)$$

2271 The uncertainty from stochastic noise and the measurement uncertainty are respectively  
2272 encoded in  $\mathbf{C}_i^{i-1}$  and  $\mathbf{K}_i$ . Both sources of uncertainty thus contribute to the filtered covari-  
2273 ance, as expected. Both the state vector and its covariance are updated by incorporating a  
2274 new measurement and the material effects from propagating the particle from its last known  
2275 position.

2276 Repeated applications of prediction and filtering incorporate all measurements to refine  
2277 the track state from its initial value  $\mathbf{x}_0$

2278 **3. Smoothing.** The prediction and filtering sequence refines the track state in the forward  
2279 direction. This means that an estimate at the end of the trajectory is better than one  
2280 at the beginning. It is, however, desirable that all estimates receive information from all  
2281 measurements, rather than those preceding them. The smoothing step achieves this goal by  
2282 working backward from the outermost measurement and updating a state vector at step  $i$   
2283 using the state vector at step  $i + 1$

$$\mathbf{x}_i^N = \mathbf{x}_i + \mathbf{A}_i(\mathbf{x}_{i+1}^N - \mathbf{x}_{i+1}^i), \quad (7.21)$$

2284 in which the superscript  $N$  signifies an estimate incorporating all  $N$  measurements.  $\mathbf{A}_i$  is  
2285 called the smoothing gain matrix, defined as

$$\mathbf{A}_i = \mathbf{C}_i \mathbf{F}_i^T (\mathbf{C}_{i+1}^i)^{-1}. \quad (7.22)$$

2286 Only after filtering through all measurements on track can the smoothing be effected. In  
2287 ATLAS terminology, the former is therefore referred to as the forward filter, while the latter  
2288 backward smoothing. The initial track state  $\mathbf{x}_0$ , or the state on any other surface, real or  
2289 imaginary, can be refined or extrapolated using the entire measurement set.

## 2290 7.4 Combinatorial Kalman Filter

2291 Thanks to its iterative mechanism, the Kalman formalism can be extended from track  
2292 fitting to track finding, called the Combinatorial Kalman Filter (CKF). From a track seed

2293 containing  $k$  measurements, it estimates the initial value  $\mathbf{x}_k$  and projects it to the next surface  
 2294 using equation (7.13). In the filtering stage, instead of incorporating a given measurement,  
 2295 as in the case of track fitting, it considers all measurements on the target surface falling  
 2296 into a search window defined by the projected measurement covariance. By filtering each  
 2297 candidate measurement  $l$ , it computes a filtered track state and measurement residual

$$\mathbf{r}_{k+1,l} = \mathbf{m}_{k+1,l} - \mathbf{H}_{k+1}\mathbf{x}_{k+1,l}. \quad (7.23)$$

2298 The increment in  $\chi^2$  is computed from the residual

$$\chi_{+,l}^2 = \mathbf{r}_{k+1,l}^T [(\mathbf{I} - \mathbf{H}_{k+1}\mathbf{K}_{k+1})\mathbf{V}_{k+1,l}]^{-1} \mathbf{r}_{k+1,l}. \quad (7.24)$$

2299 All candidate measurements  $l$  whose contribution to the global  $\chi^2$  falls before a certain  
 2300 threshold are admitted, creating the same number of branches from the track seeds. The  
 2301 procedure is repeated till no more measurements can be incorporated. The output from a  
 2302 given track seed is usually a large set of track candidates each originating from a combination  
 2303 of branching connections, hence the *combinatorial* denomination.

2304 The track candidate is characterized by a global  $\chi^2$  equal to the sum of the contributions  
 2305 from individual measurements in equation (7.24). Several candidates might be ruled out  
 2306 based on the mean  $\chi_{track}^2/|M_{track}|$ , as well as other quality cuts. To guarantee tracking  
 2307 efficiency, a large number of track seeds are produced and considered by the CKF. The  
 2308 number of considered track seeds combined with the number of combinations per seed results  
 2309 in significant track redundancy and overlapping measurements. An ambiguity resolution step  
 2310 globally sorts through the track candidates and assigns each measurement to mostly a unique  
 2311 track, effectively reducing them to a set of tracks of highest quality and compatibility to real  
 2312 particles.

## 2313 7.5 Computational cost of track reconstruction

2314 Inner tracking is one of the most expensive tasks of event reconstruction. For instance,  
2315 table 7.1 illustrates the CPU consumption in  $\text{HS06} \times \text{seconds}$  of each reconstruction stage  
2316 under Run 2 conditions but scaled to  $\langle \mu \rangle = 90$  [132]. Track reconstruction dominates the  
2317 computing budget, consuming 67% of the total reconstruction time. This contribution will  
2318 only get worse at pile-up 200, due to the strong scaling behaviour of the Combinatorial  
2319 Kalman Filter and the Ambiguity Resolution step which necessarily follows.

Detector	$\langle \mu \rangle$	Tracking	Calo and M.S	Combined Reco.	Monitoring	Total
Run 2	90	1137	149	301	106	1693

**Table 7.1:** The CPU required in  $\text{HS06} \times \text{seconds}$  to reconstruct a Run 2 data event using the corresponding software release at average pile-up 90 using. The total reconstruction time is broken down into inner tracking, Calorimeter and Muon Spectrometer reconstruction, and Monitoring. Numerical figures taken from reference [132].

2320 Within Inner Tracking, the tracking finding step described in this chapter consumes the  
2321 largest CPU resource. Listed in table 7.2 are the cost of each step in the tracking stage,  
2322 assuming the pile-up levels of 140 and 200. In the default tracking chain, the tracking finding  
2323 and ambiguity resolution steps dominate the total CPU consumption. Although listed as  
2324 separate items, the former's performance is severely degraded without the latter, so they  
2325 should be considered together as one item, which occupies 83% of the overall computing  
2326 consumption for inner tracking at pile-up 200.

2327 ATLAS has carried out major optimizations of the default CKF chain to improve its CPU  
2328 performance, shown in table 7.2 as Fast tracking. Track seeds used to initialize the CKF are  
2329 created exclusively from pixel space points, enabled by the increased number of expected  
2330 pixel hits thanks to an additional layer and the full  $\eta$ -coverage of the ITk compared to the  
2331 ID. A tighter track selection and precise cluster calibrations are used to remove duplicate and

$\langle \mu \rangle$	Algorithm	Decoding	Clustering	S.P. Formation	CKF	Am. Reso.	Total
140	Default	1.2	17.1	6.0	41.1	58.2	124
140	Fast	1.2	4.5	0.9	12.4		19.0
200	Default	1.6	26.3	8.6	85.8	92.0	214
200	Fast	1.6	6.3	1.2	22.6		31.7

**Table 7.2:** The CPU required in HS06×seconds to reconstruct a  $t\bar{t}$  MC event with  $\langle \mu \rangle = 140$  and 200 in the ITk. The total track reconstruction time, evaluated for both the default and an optimized CKF-based chains, is broken down into individual steps, most significant of which are clustering, space point formation, CKF-based track finding and ambiguity resolution. An Intel Xeon E5-2620v2 processor with 2.1 GHz and six physical cores per CPU was used. The CPU time is multiplied by an HS06 factor of 17.8 for single-thread running. Numerical figures taken from reference [133].

fake tracks after the track finding step, in lieu of the costly ambiguity resolution step. These changes, along with other incremental improvements, allows running the track reconstruction pass approximately 8 times faster than the default chain, as illustrated in table 7.2, but with a loss in physics performance, as shown in figure 7.5 [133]. Despite the impressive acceleration, the fast track chain still is far from ready for production due to both latency and tracking performance.

Along with optimizing the traditional event reconstruction algorithm, ATLAS is actively pursuing significant modernization of its analysis software, both online and offline. As outlined in reference [134], the primary challenge of the HL-LHC era will be the effective use of General Purpose Graphics Processing Units (GP-GPUs), which are becoming ubiquitous in large High-Performance Computing (HPC) facilities and data centers. They can accelerate suitable applications by orders of magnitude, many of which have already been deployed in ATLAS. Examples include Fast Simulation [135], Particle Flow [136], and  $b$ -tagging graph

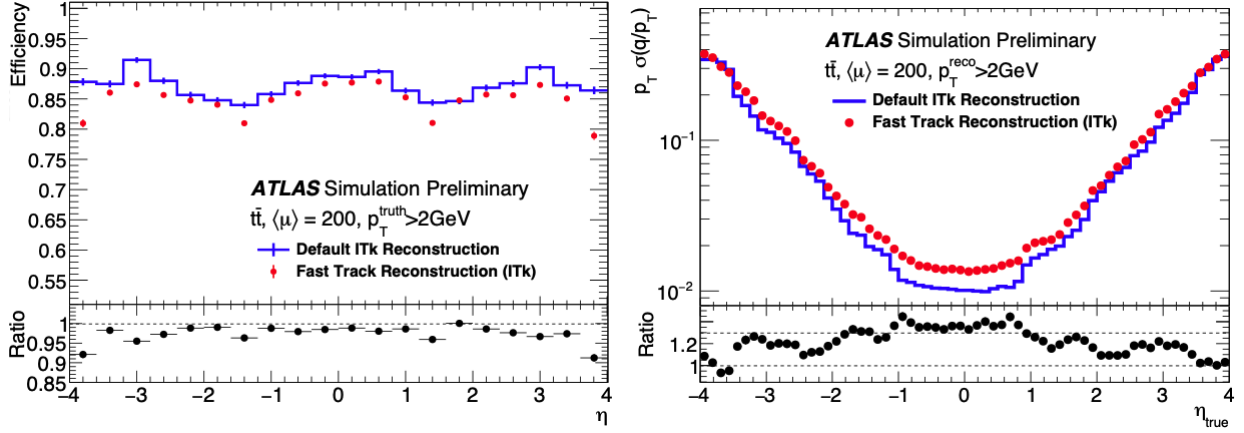


**Figure 7.5:** Tracking efficiency (left) and track parameter resolution (right) as functions of the truth particle’s pseudorapidity, evaluated at  $\langle \mu \rangle = 200$ . The bottom plots show the ratio of the corresponding metric observed in the fast chain to that in the default chain [133].

neural networks [137]. Exploiting this computing resource requires recasting current software on the hardware accelerators, for instance the TRACKCC project [138], or designing new algorithms inherently compatible with them. In addition, because of the increased track multiplicity in HL-LHC, online applications such as trigger and data acquisition will likely be migrated to accelerators, and thus, new hardware-accelerated algorithms are further incentivized for offline software to maintain synergies between the two computing domains. In this context, the next big component in event reconstruction to be modernized is inner tracking, attracting substantial interest and investment in person power within ATLAS. The work done in this thesis plays a significant role in this effort, resulting in a competitive candidate for an end-to-end, machine learning-based and fully GPU-compatible algorithm for track reconstruction. The remaining chapters of this thesis describe its development and latest results.

2357 **Chapter 8**

2358 **Track reconstruction with Graph Neural Networks**

2359 Graph Neural Networks (GNNs) were first proposed in 2018 as an alternative track finder  
2360 to the Combinatorial Kalman Filter (CKF) [139]. Developed and tested on the TRACKML  
2361 dataset [140], they demonstrated excellent physics performance and favourable scaling be-  
2362 haviour [141, 142]. Fundamentally, GNN-based algorithms represent a shift from the local  
2363 track finding approach of the CKF to a global approach. Instead of extending a track seed  
2364 with compatible hits in sequence, as described in chapter 7, global track finding considers  
2365 simultaneously a set of connections between detector hits and finds those that are most  
2366 likely to belong to true particle tracks. This set should contain most of the true connections  
2367 and can be quite large, but the ability to parallelize the computation on GPUs makes this  
2368 approach an attractive alternative to the sequential mechanism and redundancy of the CKF.  
2369 The shift from hit finding to connection finding necessitates a change in representation of  
2370 the collision event from a point cloud to a collection of nodes and edges, the very definition  
2371 of a **graph**. This approach therefore relies on graph data structure.

2372 The work documented in this thesis builds upon that of reference [141], which examined  
2373 the physics and computing performance of the GNN on the TrackML dataset [140], and of  
2374 reference [143], which made initial strides in applying the GNN to data from full detector  
2375 simulation using ITk geometry. It contributes numerous developments that bring the new  
2376 approach closer to the state-of-the-art performance. Neural network architectures undergo  
2377 significant refinements. The algorithm is fully integrated into the official ATLAS software

2378 framework [144], thus enabling direct performance comparison to the CKF. Finally, many  
2379 components are computationally optimized, resulting in competitive reconstruction speed.  
2380 This chapter commences the discussion with an overview of the algorithm and the construc-  
2381 tion of graphs from detector data. Subsequent stages of the algorithm, especially the graph  
2382 neural network, are detailed in chapters 9 and 10, and finally the results are presented in  
2383 chapters 11 and 12.

## 2384 8.1 Overview

2385 The GNN-based approach, illustrated in figure 8.1 and hereafter referred to as the  
2386 **GNN4ITk** algorithm, creates track candidates by segmenting a graph constructed from  
2387 the collection of space points in each event. A graph  $G(V, E)$  is a mathematical structure  
2388 consisting of a set of nodes  $V$ , and a set of pairwise connections  $E$  between these nodes. Each  
2389 node  $v_i \in V$  represents a space point, and an edge  $e_{ij} \in E$  a hypothesis that the space points  
2390 represented by  $v_i$  and  $v_j$  are created from successive energy deposits by the same particle.  
2391 In addition, a ground truth graph  $G_{truth} = (V, E_{truth})$  is defined from the same set  $V$  and  
2392 the connections between successive space points on the trajectories of all particles in the  
2393 event, denoted by  $E_{truth}$ , oriented in the direction of increasing distance from the particle's  
2394 production vertex. An edge  $e_{ij} \in E$  is true if it is also in the truth graph, i.e.

$$y_{ij} = 1_{[e_{ij} \in E_{truth}]}, \quad (8.1)$$

2395 and fake otherwise. A graph neural network is used to assign to every edge  $e_{ij}$  a score  
2396  $s_{ij} = P[y_{ij} = 1]$ , representing a continuous function of the probability that the edge in  
2397 question is true. To obtain the probability, a calibration step is sometimes needed [145]. For  
2398 our purpose, a score threshold is selected to satisfy certain requirements on the edge efficiency  
2399 evaluated on the validation set. Edges with scores under the threshold are eliminated, and  
2400 the remaining graph is segmented into **track candidates**, collections of nodes believed to  
2401 originate from the same particle.

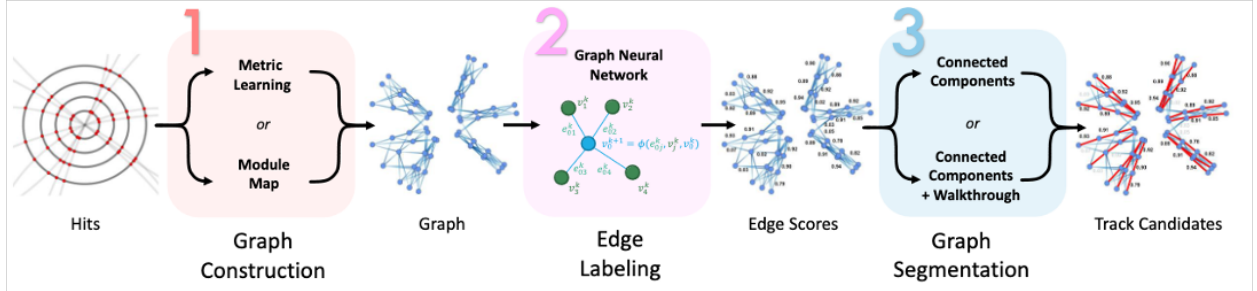


**Figure 8.1:** The GNN4ITk algorithm consists of three distinct stages. The first stage constructs a graph from the set of space points in an event, each acting as a node. The second stage identifies edges connecting consecutive nodes on a particle tracks from other edges. The last stage construct track candidates by segmenting the graph using the output of the second stage. The algorithm’s output consists of individual track candidates each as a set of space points believed to belong to the same particle.

## 2402 8.2 Target, non-target particles and evaluation metrics

2403 At  $\langle \mu \rangle = 200$ , each collision event produces  $\langle N \rangle \approx 10000$  final-state stable particles, the  
 2404 majority of which are of little interest to the physics program in ATLAS. They include, for  
 2405 example, low-momentum particles from background processes or particles which leave too few  
 2406 hits to be considered reconstructible. The remaining particles can be broadly categorized by  
 2407 the interaction from which they emerge. Primary particles are produced in the luminous area  
 2408 directly from proton-proton interactions. Only particles that are stable enough to traverse  
 2409 the detector, including protons, electrons, muons, pions, etc can be reconstructed. Secondary  
 2410 particles arise from the interaction of stable primary particles with detector material, such as  
 2411  $\delta$ -ray electrons and nuclear interaction products. The CKF chain does not target secondary  
 2412 particles for reconstruction, due to the high computational cost to simultaneously consider  
 2413 them. In the same spirit, throughout the GNN4ITk chain, we identify these particles prior to  
 2414 model training and exclude them from the loss function, as well as performance evaluation.

2415 Since a secondary interaction occurs when the primary particle has travelled a distance  
 2416 from the luminous region, their vertices are often considerably further from the origin than  
 2417 the primary counterpart. Shown on figure 8.2, the majority of primary vertex positions are  
 2418 located at  $v_r < 2$  cm and  $v_z < 20$  cm, in contrast to secondary vertices, whose distributions  
 2419 of  $v_r$  and  $v_z$  are more spread-out and with longer tails. This distinction allows us to select  
 2420 primary particles in training by requiring the production vertex to be within 26 cm from the  
 2421 origin. As we will see in chapter 11, the ATLAS reconstruction chain eliminates secondary  
 2422 particle tracks by applying selection cuts on the impact parameters, which are good estimates  
 2423 of the vertex point, of  $|z_0| \leq 20$  cm and  $|d_0| \leq 10$  cm.

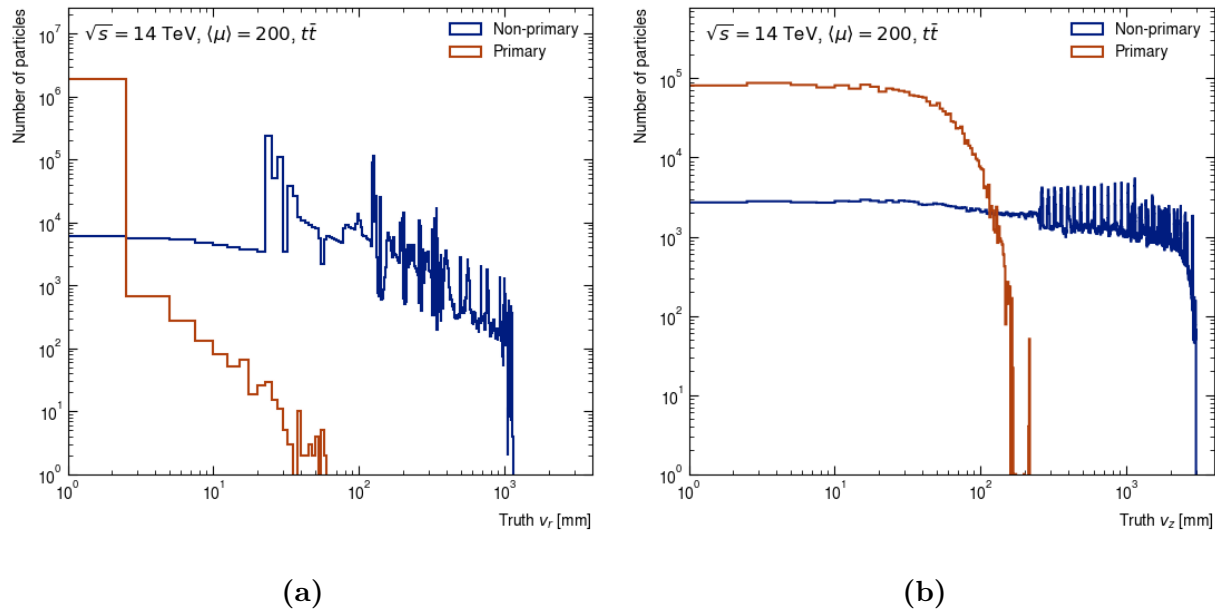


**Figure 8.2:** Distributions of the production vertex position on the transverse plane (a) and along the  $z$ -axis (b) of simulated particles in  $t\bar{t}$ -events at  $\langle \mu \rangle = 200$  for non-primary and primary particles. Primary vertices are restricted to a small region around the interaction point, whereas non-primary vertices can occur throughout the detector.

2424 As we have seen in section 6.3.2, electrons and positrons uniquely undergo significant  
 2425 energy loss due to Bremsstrahlung, and often follow trajectories that deviate from a helix.  
 2426 To guarantee good electron efficiency without compromising that of other particles, the

2427 ATLAS chain reconstructs electron tracks in a separate pass with a specialized parameter  
2428 estimation technique. Similarly, we avoid training models on “irregular” electron tracks by  
2429 excluding their contribution from the loss function.

2430 Because each simulated event is generated from one hard-scattering (HS) collision and  
2431 on average 200 pile-up collisions (section 6.4), particles originating from soft interactions  
2432 outnumber HS particles by about two orders of magnitude, (figure 8.3b). HS particles are  
2433 generally more energetic; their  $p_T$  spectrum stretches up to 100 GeV, whereas that of pile-up  
2434 particles strongly peaks at  $p_T < 1$  GeV and terminates at 20 GeV, as shown in figure 8.3a.  
2435 As a consequence, a loss function calculated from all edges in the event is dominated by  
2436 examples from low- $p_T$  tracks and bias the model at the expense of high- $p_T$  HS particles that  
2437 represent the interesting physics. This data imbalance largely impacts the performance, since  
2438 in the presence of the magnetic field, low- $p_T$  particles have larger curvature and therefore  
2439 different track pattern than do high- $p_T$  particles. In addition, the CKF chain also targets  
2440 high- $p_T$  particle in the primary pass. Therefore, we neglect the contribution to the loss  
2441 function from particles of  $p_T < 1$  GeV.

2442 In light of this discussion, we sort truth particles into two subsets by the following criteria

- 2443 1. **Target** particles: primary particles from both hard-scattering and pile-up interactions,  
2444 which have  $p_T > 1$  GeV and  $|\eta| < 4$ , leave at least 3 hits in the tracker, are produced  
2445 at a transverse radius  $R < 26$  cm, and are not electron nor positrons.
- 2446 2. **Non-target** particles: The rest of truth particles, including electrons and other par-  
2447 ticles not satisfying the kinematic selection.

2448 In the same manner, the subset of  $E_{truth}$  comprising exclusively connections from target  
2449 particles is called the target truth edges and denoted as  $E_{truth,target}$ . A subset of non-target  
2450 truth edges is defined as  $E_{truth,non-target} = E_{truth} - E_{truth,target}$ . The objective of global track  
2451 finding then is to identify as many target truth edges and to misidentify as few fake edges

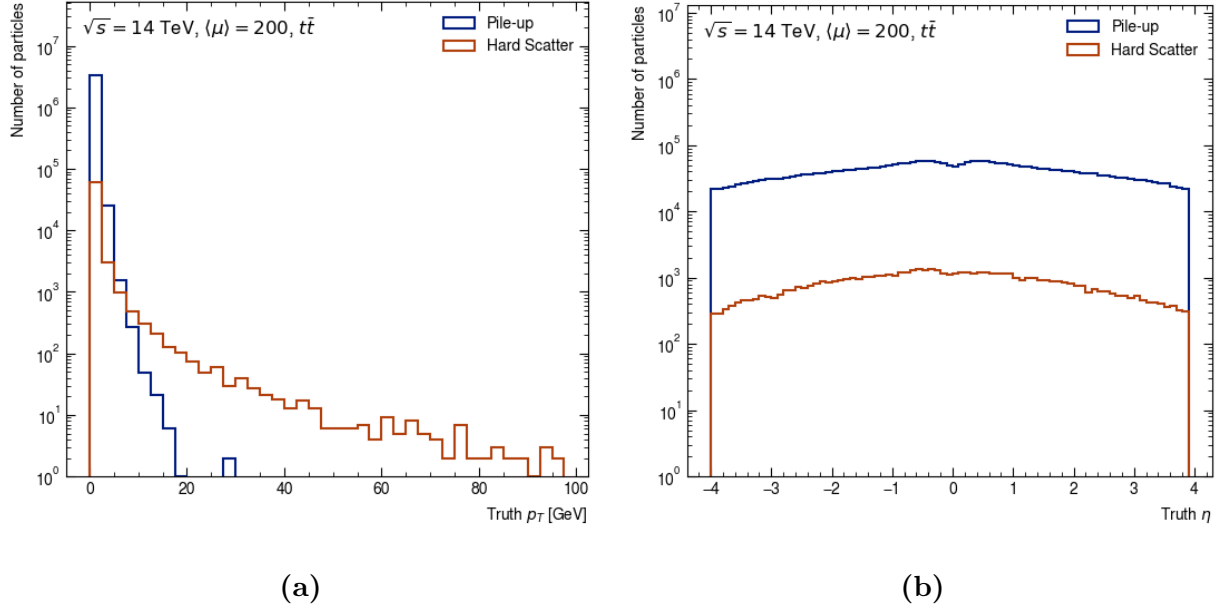


**Figure 8.3:** Distributions of transverse momentum  $p_T$  (a) and pseudorapidity (b) of simulated particles in  $t\bar{t}$ -events at  $\langle \mu \rangle = 200$  separated according into hard-scattering and pile-up particles. Soft pile-up particles have low  $p_T$ , whereas hard-scattering particles have a wider  $p_T$  distribution. The former is two orders of magnitude more abundant than the latter.

as possible. Two metrics are defined from the edge sets to quantify these criteria. The first is the **edge efficiency**  $\epsilon$ : the fraction of target true edges present in a given edge set  $E$

$$\epsilon = \frac{|E \cap E_{truth,target}|}{|E_{truth,target}|}, \quad (8.2)$$

and the second is the **edge purity**  $\rho$ : the fraction of target true edges in  $E$ , excluding non-target true edges

$$\rho = \frac{|E_{truth,target} \cap E|}{|E - E_{truth,non-target}|}. \quad (8.3)$$

<sup>2456</sup> High edge efficiency indicates that  $E$  contains a large proportion of target edges in the event,  
<sup>2457</sup> while high purity means that a small proportion of  $E$  is fake edges. These definitions also  
<sup>2458</sup> explicitly exclude non-target particles from the evaluation of model performance.

## 2459 8.3 Graph construction methods

2460 The first step of the GNN4ITk chain constructs a graph from the collision event. After  
2461 the space point formation stage, discussed in section 7.1, an event is a set of space points,  
2462 which can be considered as a graph with an empty edge set  $G_0 = (V, E = \emptyset)$ . The graph  
2463 construction stage populates  $E$  with edges, with an objective of including as many target  
2464 edges as possible, and at the same time control the total number of edges such that the  
2465 resulting graph can fit on GPU memory to train the GNN. At  $\langle\mu\rangle = 200$ , a  $t\bar{t}$  event has  
2466  $\mathcal{O}(10^5)$  space points, and a fully-connected graph, though simple, would have  $\mathcal{O}(10^{10})$  edges,  
2467 most of which are unphysical and a too expensive to process. Such a sizeable graph would  
2468 also be unable to fit on the GPU memory. Therefore, more clever methods are needed to  
2469 construct the graph. We investigate two approaches to construct graphs: Module Map and  
2470 Metric Learning.

### 2471 8.3.1 The Module Map Method

2472 The module map is a data-driven approach to construct a graph. It is based on the  
2473 observation that a small fraction of edges in a fully-connected graph is physical, and an even  
2474 smaller fraction comes from target particles. It is therefore possible to create a list of all  
2475 pairs of detector modules connected by target particles in a large number of  $t\bar{t}$  events. By  
2476 following the path of each target particle and recording pairs of modules that it sequentially  
2477 traverses, we build up this list and call it the **Module Map**. To maximize the coverage of  
2478 possible module connections, 90000  $t\bar{t}$  simulated events described in section 6.4 are used

2479 Illustrated on the left-hand side of figure 8.4 is an example of module map learning, in  
2480 which two particles are observed to sequentially hit modules  $1 \rightarrow 2 \rightarrow 3 \rightarrow 4 \rightarrow 5 \rightarrow 6$   
2481 and  $3 \rightarrow 4 \rightarrow 7 \rightarrow 8 \rightarrow 9$ . From these particles, connections between the following pairs  
2482 of modules (1,2), (2,3), (3,4), (4,5), (5,6), (4,7), (7,8), and (8,9) are registered to the

module map (note the presence of two connections sharing module number 4). As more particles are observed, the set of recorded connections grows, covering a wider range of module connectivity. The idea is that once the number of observed events is large enough, the map is saturated and becomes a “dictionary” of all possible module connections.

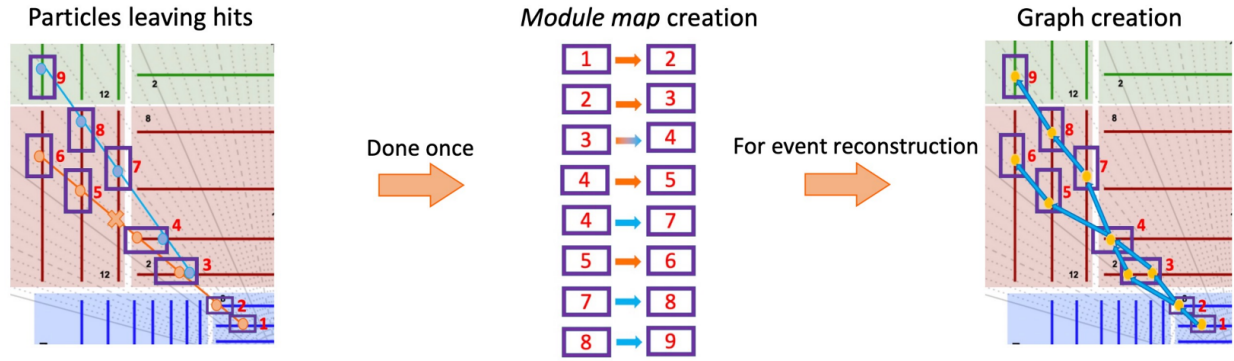


**Figure 8.4:** Principle of the Module Map method for graph construction. On the left, hits from target particles on 9 detector modules in a  $t\bar{t}$  event is observed and module connections are recorded. By observing the trajectory of target particles in 90000  $t\bar{t}$  events, a list of all pairs of detector modules sequentially traversed by a particle is built. During reconstruction of a new unobserved event on the right, the space points residing on the pairs of modules which appear in the module map are connected by an edge. A set of selections are applied to reduce the number of edges and eliminate outliers.

When building a graph from an event *which has not been seen* by the Module Map, out of all possible connections between space points, only those linking pairs of modules present in the Module Map are admitted to become graph edges. On the right-hand side of figure 8.4, for example, 10 space points on 9 modules are recorded in the new event, with 2 space points present on module 3. The module map therefore admits connections between space points residing on the following module pairs: (1,2), (2,3<sub>1</sub>), (2,3<sub>2</sub>), (3<sub>1</sub>,4), (3<sub>2</sub>,4), (4,5), (4,7), (5,6), (7,8), (8,9), with subscripts indicating different space points on the same module where necessary. The module map thus allows to select a small subset of the 90 possible connections, based on our previous observations.

2496     The same principle can be extended from pairs of modules to triplets of modules, so that  
 2497     the module map is built from a list of three modules sequentially hit by a particle, and on  
 2498     inference, pairs of possible connections appearing in the module map are admitted. Since  
 2499     the requirement of three consecutive hits is stricter than that on two hits, the *triplet* module  
 2500     map helps reduce the number of edges in the reconstructed graph compared to the simple  
 2501     *doublet* module map. Nevertheless, the average number of edges in graphs constructed from  
 2502     the triplet module map is still too large to process on available hardware, averaging  $\mathcal{O}(10^8)$ .

2503     On the chosen GNN architecture, we found that a GPU with 80GB memory is capable  
 2504     of running the forward pass with gradient tracking on  $\sim 2 \times 10^6$  edges/graph, which is the  
 2505     target of graph construction. The number of edges per event acts as a batch size which can  
 2506     limit the number of trainable parameters in a neural network and its expressive power. In  
 2507     addition, processing a massive graph of mostly fake edges is a computing a bottleneck and a  
 2508     waste of computing resource for the powerful GNN, when most of them can be filtered out  
 2509     by simpler techniques. To build leaner graphs, additional selection requirements are imposed  
 2510     on doublets and triplets in the “crude” module map graphs.

2511     Edge selections are based on geometric features derived from the connected space points.  
 2512     Denoting the nodes in a doublet ordered by increasing distance from the origin by  $(v_1, v_2)$ ,  
 2513     and in a triplet in the same order by  $(v_1, v_2, v_3)$ , we define two categories of geometric features.

2514     1. **Doublet features** are calculated from the doublet hits connected by an edge. They  
 2515     include:

- 2516       •  $z_0 = z_1 - r_1 \frac{z_2 - z_1}{r_2 - r_1}$ .
- 2517       •  $\Delta\phi = \phi_2 - \phi_1$
- 2518       •  $\Delta\eta = \eta_2 - \eta_1$
- 2519       •  $\phi_{slope} = \frac{\phi_2 - \phi_1}{r_2 - r_1}$ .

2520 These features represent several basic assumptions about the trajectory of a charged  
 2521 particle in a magnetic field. For example, the pseudorapidity  $\eta$  depends only on the  
 2522 polar angle  $\theta$  and is constant if the particle does not interact with materials. The  
 2523 distribution of  $\Delta\theta$  of two consecutive hits on a particle's path should therefore peak  
 2524 at 0 with some width  $\sigma$  resulting from detector effects.

2525 2. **Triplet features** are calculated from the doublet features of the pair of edges, resem-  
 2526 bling a second-order derivative.

$$\begin{aligned} 2527 \bullet \Delta\text{slope}_{xy} &= \left( \frac{\Delta y}{\Delta x} \right)_{12} - \left( \frac{\Delta y}{\Delta x} \right)_{23} \\ 2528 \bullet \Delta\text{slope}_{rz} &= \left( \frac{\Delta z}{\Delta r} \right)_{12} - \left( \frac{\Delta z}{\Delta r} \right)_{23} \end{aligned}$$

2529 where  $\Delta u$  is the difference in variable  $u$  between the nodes indicated by the numerical  
 2530 subscript.  $\Delta\text{slope}_{xy}$  is related to the curvature of the orbit and  $\Delta\text{slope}_{rz}$  the deviation  
 2531 from a straight line over the two triplet connections.

2532 The empirical distributions of these features are established from events dedicated to the  
 2533 construction of the module map, along with a set of thresholds that defines the acceptance  
 2534 region. These thresholds are selected to eliminate as many fake edges as possible without  
 2535 rejecting true edges in the observed 90000 events. In inference, any edge failing to meet  
 2536 these thresholds is rejected. A simple choice for the acceptance region of a feature  $\xi$  is the  
 2537 whole range  $[\xi_{min}, \xi_{max}]$ , such that an inferred edge is rejected if  $\xi < \xi_{min}$  or  $\xi > \xi_{max}$ . This  
 2538 is called the **MinMax** selection. Another choice is the interval of  $[\bar{\xi} - 5\sigma_\xi, \bar{\xi} + 5\sigma_\xi]$ , where  
 2539  $\bar{\xi}$  and  $\sigma_\xi$  are respectively the sample mean and standard deviation of the feature, denoted  
 2540 the **MeanRMS** selection. Both selections are examined, and the graph construction result  
 2541 is discussed in section 8.4.

### 2542 8.3.2 The Metric Learning approach

2543 Metric Learning [146, 147, 148] is a semi-supervised machine learning technique which  
 2544 models the difference between a pair of data points. Given a sample  $X$  and corresponding  
 2545 labels  $Y$ , we seek a transformation  $f_\theta : \mathbb{R}^d \rightarrow \mathbb{R}^n$ , where  $d$  is the dimension of  $\mathbf{x} \in X$ ,  $n$   
 2546 the dimension of an embedding space and  $\theta$  a set of learnable weights. A distance metric  
 2547  $\mathcal{D} : \mathbb{R}^n \otimes \mathbb{R}^n \rightarrow [0, \infty)$  is selected to measure the difference between two data points in  
 2548 the embedding space. The objective is that for two examples  $\mathbf{x}_i, \mathbf{x}_j \in X$  and their labels  
 2549  $y_j, y_j \in Y$ , the distance  $\mathcal{D}(f_\theta(\mathbf{x}_i), f_\theta(\mathbf{x}_j))$  is small if  $y_i = y_j$  and large otherwise. After  
 2550 training, the transformation  $f$  sends data points of the same class labels to the same region in  
 2551 the embedding space, and separate those having different labels (figure 8.5). For conciseness,  
 2552 we define

$$d_\theta(\mathbf{x}_i, \mathbf{x}_j) = \mathcal{D}(f_\theta(\mathbf{x}_i), f_\theta(\mathbf{x}_j)), \quad (8.4)$$

2553 The distance metric can be any mapping that satisfies the following criteria, defined for all  
 2554  $\mathbf{z}_i, \mathbf{z}_j, \mathbf{z}_k \in \mathbb{R}^n$

- 2555 1. non-negativity:  $\mathcal{D}(\mathbf{z}_i, \mathbf{z}_j) \geq 0$
- 2556 2. symmetry:  $\mathcal{D}(\mathbf{z}_i, \mathbf{z}_j) = \mathcal{D}(\mathbf{z}_j, \mathbf{z}_i)$
- 2557 3. identity:  $\mathcal{D}(\mathbf{z}_i, \mathbf{z}_i) = 0$
- 2558 4. triangle inequality:  $\mathcal{D}(\mathbf{z}_i, \mathbf{z}_j) \leq \mathcal{D}(\mathbf{z}_i, \mathbf{z}_k) + \mathcal{D}(\mathbf{z}_k, \mathbf{z}_j)$

2559 To construct a graph using metric learning, we assume that two nodes belonging to  
 2560 different tracks differ from each other in some sense. Taking  $X$  as the set of node feature  
 2561 vector, and  $Y$  the set of the particle label, we can write  $y_{ij} = 1_{[y_i=y_j]}$ ,  $y_i \in Y$ . Through  
 2562 metric learning, the transformation weights  $\theta$  are adjusted to minimize  $d_\theta(\mathbf{x}_i, \mathbf{x}_j)$  if  $y_{ij} = 1$   
 2563 and maximize it if  $y_{ij} = 0$ .

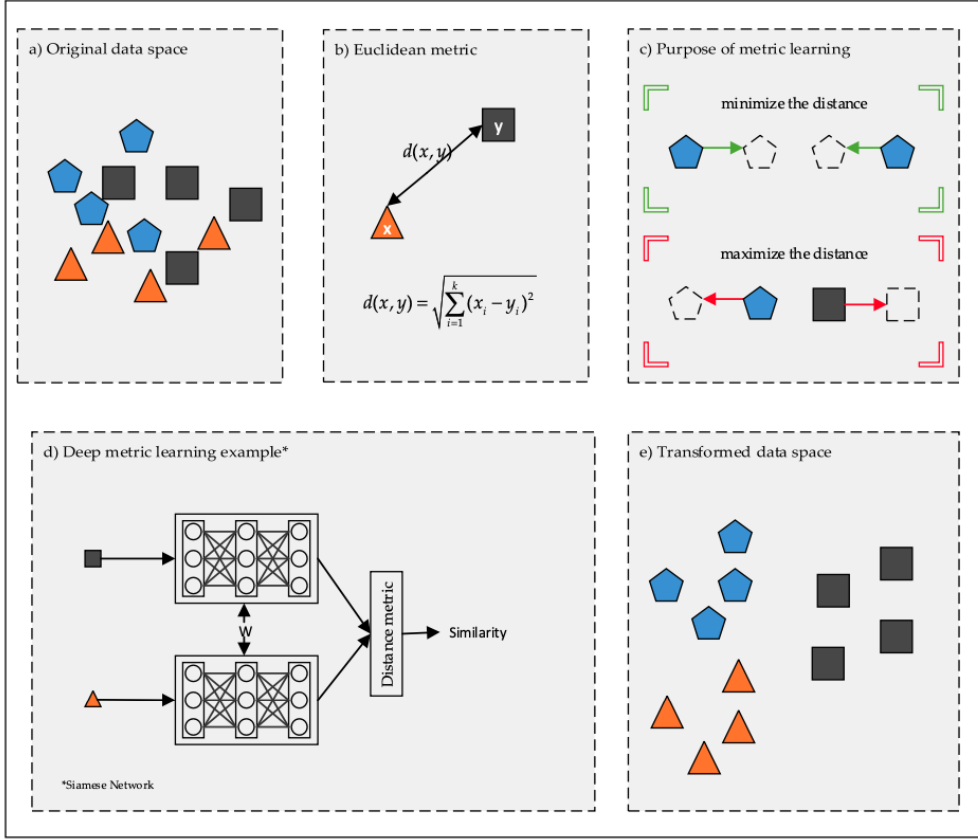


**Figure 8.5:** Principle of deep metric learning. Starting from (a) labelled data which are difficult to separate in real space, (b) a distance metric is defined to measure the similarity between data points in an embedding space, in this case a simple Euclidean distance. (c) A transformation from real to embedding space is learned, such that examples of the same class are close together, whereas those of different classes are pushed away from each other. (d) The transformation is a simple feed-forward network applied to all instances of the dataset. (e) After training, examples of different classes are well-separated, and clusterizable [147].

2564 The Euclidean distance is chosen as distance metric

$$\mathcal{D}(\mathbf{p}, \mathbf{q}) = \|\mathbf{p} - \mathbf{q}\|_2 = \sqrt{(\mathbf{p} - \mathbf{q})^2}, \quad \mathbf{p}, \mathbf{q} \in \mathbb{R}^n, \quad (8.5)$$

2565 and a simple Multi-Layer Perceptron (MLP) as the transformation  $f_\theta$ . The last ingredient  
2566 is the loss function  $\mathcal{L}(\theta)$ . There are many choices of loss function for metric learning, each

targeting a slightly different learning objective. A comprehensive summary is given in references [147, 149]. In this thesis, the simplest and most intuitive choice, called **Contrastive Loss**, is employed. Over a set of edges  $E$ , we define

$$\mathcal{L}_E(\theta) = \frac{1}{|E|} \sum_{e_{ij} \in E} l_\theta(\mathbf{x}_i, \mathbf{x}_j), \quad l_\theta(\mathbf{x}_i, \mathbf{x}_j) = y_{ij} d_\theta(\mathbf{x}_i, \mathbf{x}_j) + (1 - y_{ij}) \max\{0, r - d_\theta(\mathbf{x}_i, \mathbf{x}_j)\}. \quad (8.6)$$

For a positive pair ( $y_{ij} = 1$ ), the loss function is minimized if the distance between  $f_\theta(\mathbf{x}_i)$  and  $f_\theta(\mathbf{x}_j)$  is 0, effectively pulling together  $(\mathbf{x}_i, \mathbf{x}_j)$ . For a negative pair ( $y_{ij} = 0$ ), the loss is minimized if their distance is increased up to a margin  $r$ .  $l_\theta(\mathbf{x}_i, \mathbf{x}_j)$  becomes 0 if  $d_\theta > r$ . This margin prevents the model from enlarging the distance when the pair of nodes is sufficiently separated, focusing the attention on those that are not. The contrastive loss defined with a margin is also called the contrastive hinge loss.

Note that the loss is computed from pairs of nodes, which can be regarded as edges, but we do not have edges at this point. A training sample  $E$  must therefore be generated from the input nodes. Again, a simple choice of all  $N(N - 1)$  possible unordered pairs of node is far too many to fit on memory and would overwhelmingly contain fake edges. Instead, we construct  $E$  using a technique called hard negative mining [150]

$$E = E_{truth,target} \cup E_{hnm} \cup E_{random}, \quad (8.7)$$

where  $E_{truth,target}$  is the set of target true edges as defined in 8.2. This is truth information that comes from the training data. To generate training fake edges, a training graph is constructed in the latent space by connecting each node  $v_i \in V$  to a maximum of  $k$  closest nodes within a sphere centered at  $v_i$  of radius  $r$  using a k-Nearest-Neighbor algorithm (kNN). Note that the radius is equal to the margin. A set of edges, denoted  $E_{hnm}$ , is constructed from the training graph by finding  $n_{hnm}$  fake edges with the smallest distance in the transformed space.  $E_{hnm}$  represents the negative pairs that most resemble true pairs, so maximizing their distance is equivalent to lower-bounding the separation between all fake pairs of nodes. Finally, a set of randomly sampled edges  $E_{random}$  is added to stabilise the loss.

Hit input	Description
$r$	Global transverse radius of space point
$\phi$	Global azimuthal angle of space point
$z$	Global $z$ -coordinate of space point
$x_{CL,i}$	Global $x$ -coordinate of cluster $i$
$y_{CL,i}$	Global $y$ -coordinate of cluster $i$
$z_{CL,i}$	Global $z$ -coordinate of cluster $i$
$n_{cell}$	Number of pixels cells contained in a cluster
$q_{tot}$	Total charge deposit on a pixel cluster, 0 for strip
$\eta_{shape,loc,i}$	Cluster shape $\eta$ in local coordinate system
$\phi_{shape,loc,i}$	Cluster shape $\phi$ in local coordinate system
$x_{shape,loc,i}$	Cluster shape $x$ in local coordinate system
$y_{shape,loc,i}$	Cluster shape $y$ in local coordinate system
$z_{shape,loc,i}$	Cluster shape $z$ in local coordinate system
$\eta_{shape,glob,i}$	Cluster shape $\eta$ in global coordinate system
$\phi_{shape,glob,i}$	Cluster shape $\phi$ in global coordinate system
$\theta_{shape,glob \rightarrow loc,i}$	$\theta$ angle of the global cluster shape projected on local coordinate system
$\phi_{shape,glob \rightarrow loc,i}$	$\phi$ angle of the global cluster shape projected on local coordinate system

**Table 8.1:** Input features into the Metric Learning model include the global coordinates of the reconstructed space point ( $r, \phi, z$ ) and features describing the number of cells, the total charge deposit in the clusters from which the space point is reconstructed. A pixel space point is formed from a single cluster, and a strip space point from two clusters. The subscript  $i \in \{1, 2\}$  of the cluster features denote the cluster index. The cluster shape is a vector pointing from the cell where the particle enters the detector element to one where it exits. To preserve the same input vector shape, pixel cluster features of are duplicated at each node.

Hyperparameter	Value
Hidden layers	4
Hidden dimension	1024
Embedding dimension	12
KNN	50
Margin	0.1
Weighting ratio	1.0 : 4.0

**Table 8.2:** Hyperparameters used to train the Metric Learning model.

2590        The model was trained on an NVIDIA A100 GPU with 80 GB in memory. The train  
 2591    set contains 7800 simulated  $t\bar{t}$  events, each treated as a batch. An iteration over the train  
 2592    set (epoch) takes approximately 1 hour, and the model is trained over approximately 200  
 2593    epochs.

## 2594    8.4    Result

2595        Shown in figure 8.6 is the averaged edge efficiency of graphs constructed with the **Min-**  
 2596    **Max** and **MeanRMS** selections as a function of the pseudorapidity  $\eta^I$  and transverse mo-  
 2597    mentum  $p_T$ . The Module Map method under both choices of edge cuts produces efficiency  
 2598     $\epsilon \geq 99.5\%$  across  $\eta$ . Averaged across test events, the **MeanRMS** selection is slightly less  
 2599    efficient than the **MinMax** counterpart by 0.2%, due to tighter thresholds on geometric  
 2600    observables. The former's inefficiency is observed in the barrel region ( $|\eta| < 2$ ) and the very  
 2601    forward region ( $|\eta| \approx 4$ ). The slight efficiency loss comes with the benefit of building smaller  
 2602    graphs. The **MeanRMS** selection produces graphs having  $\langle |V| \rangle = (8.55 \pm 2.26) \times 10^5$  edges,  
 2603    30% fewer than those from the latter, averaging at  $(1.22 \pm 0.31) \times 10^6$  edges.

---

<sup>I</sup>Here the pseudorapidity of an edge is defined as that of the inner node.

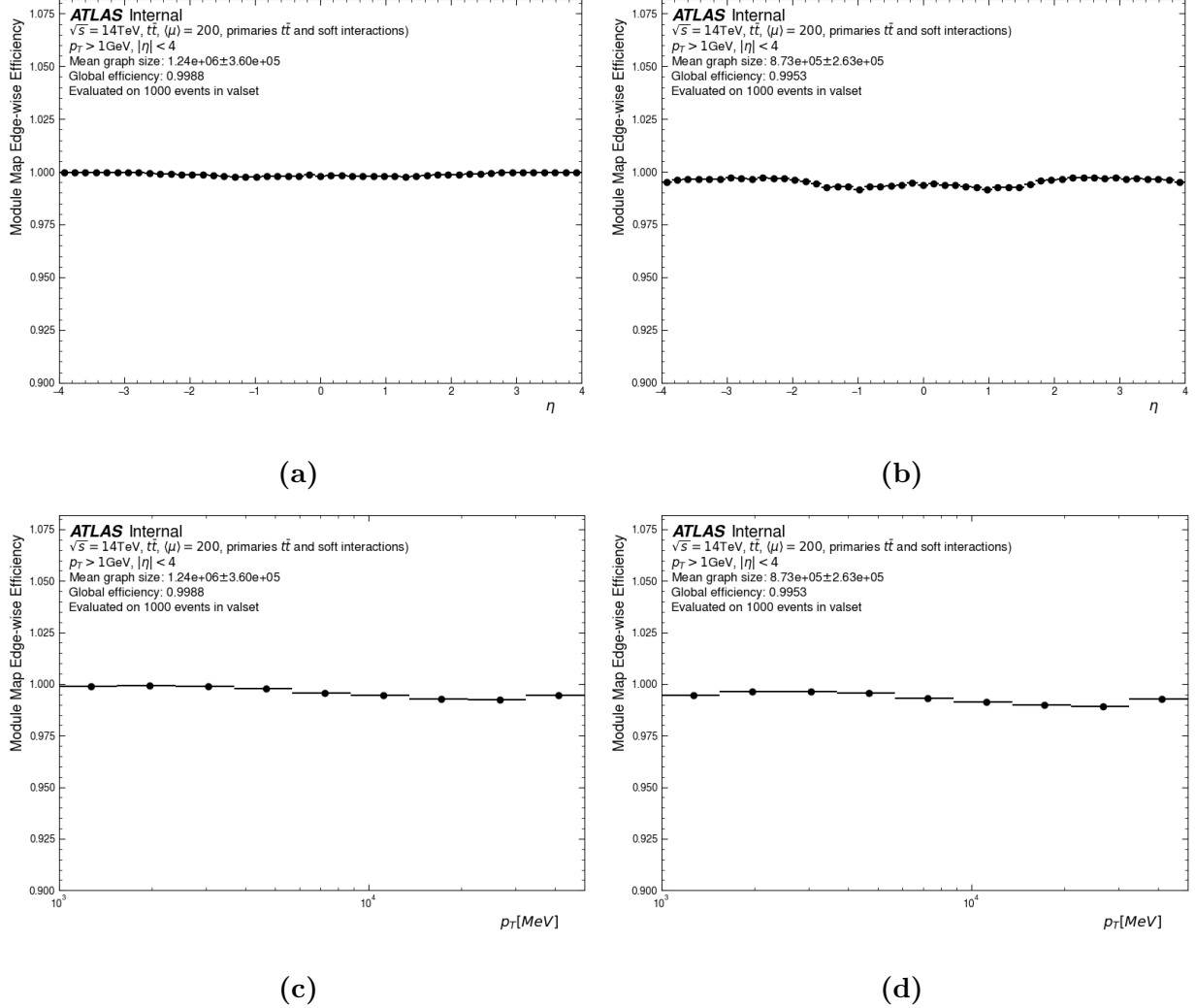


**Figure 8.6:** Graph construction efficiency of the Module Map approach as a function of  $\eta$  (upper) and  $p_T$  (lower), using the MinMax selection (left) and MeanRMS selection (right).

The reduced number of edges at negligible efficiency cost is a strong advantage of the **MeanRMS** method. It allows the GNN to be trained with better class balance, because the majority of additional eliminated edges are fake or non-target, evidenced by almost identical efficiency values. In addition, a smaller graph leads to better latency and smaller memory footprint, which are important factors in inference. Therefore, graphs produced by both selections are examined in later stages of the reconstruction chain.

Both of the module map selections show good edge efficiency over the  $p_T$  range, reaching  $\epsilon \geq 99\%$  (figures 8.6c and 8.6d). A slight decrease is observed at the high- $p_T$  region, above  $p_T \geq 5$  GeV, which, as we will see in the next chapters, is a common occurrence in the GNN4ITk chain. It can be attributed to the rarity of high- $p_T$  particles in the training data, as discussed in section 8.2, which affects the coverage of possible module connections produced by high- $p_T$  particles. The Module Map can only create an edge in the inferred event if it has seen the same edge during its construction. In other words, in order for a true connection to appear in the inferred graph, the corresponding pair of modules must have been consecutively traversed by a particle in the training events. However, high- $p_T$  particles constitute but a small portion of final-state particles (figure 8.3a), and those observed from the training event might not cover all possible trajectories through the detector's modules. As a result, it is more likely that a high- $p_T$  connection from a target particle in an inferred event was not seen in the training events, leading to inefficiency.

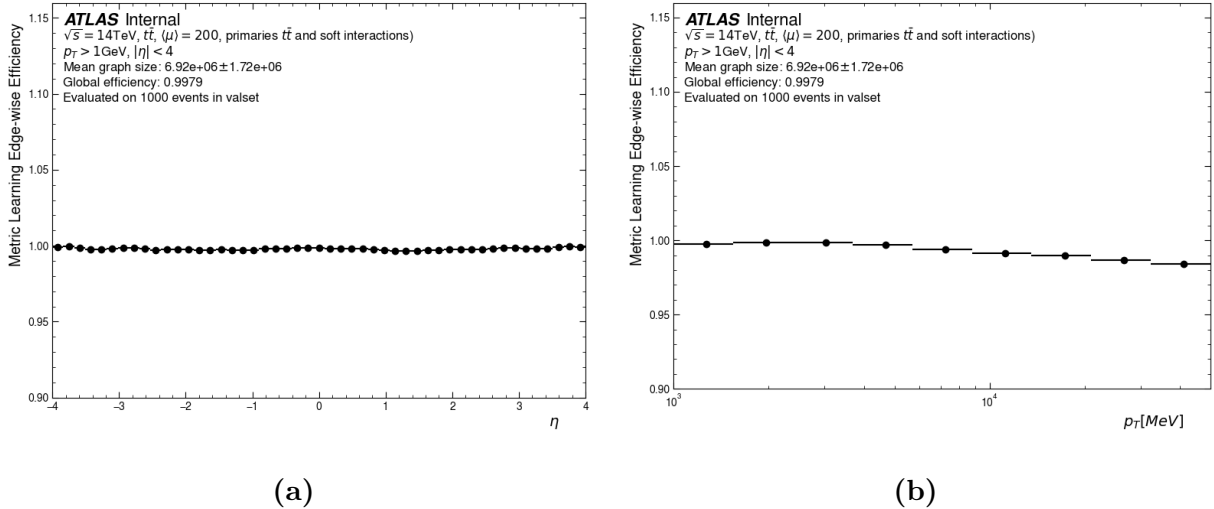


**Figure 8.7:** Graph construction efficiency of the Metric learning approach as a function of  $\eta$  (a) and  $p_T$  (b), averaged over 1000  $t\bar{t}$  events.

The efficiency of graphs constructed with the Metric Learning method as a function of  $\eta$  and  $p_T$  is shown in figure 8.7. Good edge efficiency is observed across the  $\eta$  range, averaging at 99.79%, on par with those from the Module Map under the **MinMax** selection, but with a

2626 considerably larger edge set,  $|V| = (6.92 \pm 1.72) \times 10^6$ , compared to just  $(1.24 \pm 0.36) \times 10^6$ . As  
 2627 already discussed, the increased graph size will pose a problem for the edge-classifying GNN,  
 2628 so the graph is pruned using a light-weight neural network, which will be discussed in section  
 2629 9.2. Although good efficiency is observed throughout the  $p_T$  range, a slight decrease appears  
 2630 at  $p_T > 5$  GeV, which, similar to what that of the Module Map method, can be attributed  
 2631 to small training statistics at high  $p_T$ . The metric learning model learns to minimize the  
 2632 distance between space points belonging to the same particle via an attractive term in the  
 2633 loss function (equation (8.6)), which can be rewritten as

$$\mathcal{L}_\theta = E[d_\theta] = \left( \sum_{p_T} E[d_\theta | p_T, \text{target}] P[p_T | \text{target}] P[\text{target}] \right) + E[r - d_\theta | \text{fake}] P[\text{fake}], \quad (8.8)$$

2634 where  $E[X]$  and  $P[A]$  denote unconditional expectation value and probability, and  $E[X|A]$   
 2635 and  $P[X|A]$  the conditional counterpart. The first term on the right-hand size, representing  
 2636 the attractive loss, is a sum over the  $p_T$ -dependant mean distance between nodes connected  
 2637 by a target edge, weighted by  $P[p_T | \text{target}]$ , the probability that the edge comes from a  
 2638 particle having transverse momentum  $p_T$ . As seen on figure 8.3a,  $P[p_T | \text{target}]$  decreases  
 2639 monotonically with  $p_T$ , down-weighing the loss contribution, and thus directing the attention  
 2640 away from high-momentum particles. As the curvature, which highly depends on  $p_T$ , is an  
 2641 important track pattern, the lack of high- $p_T$  examples impacts the performance of not only  
 2642 the metric learning, but also throughout the GNN4ITk algorithm.

2643 **Chapter 9**

2644 **Edge classification**

2645 Graphs constructed by both methods introduced in the last chapter contain many fake  
2646 edges. The second stage of the GNN4ITk chain labels the graph connections, so that fake  
2647 ones are removed and track candidates are built from exclusively true connections. We carry  
2648 out this task using a Graph Neural Network (GNN), which leverages the graph connectivity  
2649 to compute a score for each edge that represents the probability of being a true edge. This  
2650 chapter describes the edge classification stage, starting with a general introduction to GNNs.  
2651 Sections 9.2 and 9.3 respectively detail the filter network and the interaction network, two  
2652 edge-classifying GNN architectures investigated in this thesis, and their results.

2653 **9.1 Introduction to graph neural networks**

2654 The last 15 years have seen an explosion of deep neural networks into a major domain  
2655 of machine learning, achieving unprecedented performance on complicated tasks thanks to  
2656 increasingly available training data and computing power. An ecosystem of different network  
2657 architectures has been explored targeting different data representations. For example, Feed-  
2658 forward Neural Networks (FNNs) for tabular data, Convolutional Neural Networks (CNNs)  
2659 for 2-dimensional images, Recurrent Neural Networks (RNNs) for sequences. These archi-  
2660 tectures are effective on Euclidean, or grid-like data, but not sufficiently flexible to model  
2661 irregular non-Euclidean data structures such as graphs, which comprise entities (nodes) and

2662 their relationships (edges). In this context, **Graph Neural Networks** enable representation learning on graph-structured data by leveraging the underlying patterns in features associated with nodes and edges.

2665 Graph neural networks operate on a graph by iteratively propagating information via the edges. The representation of a node is updated based on its features and those of its direct neighbours through a learnable aggregation mechanism. The general formulation of the  $k$ -th iteration at can be written as

$$\mathbf{h}_i^k = \text{UPDATE}_k(\mathbf{h}_i^{k-1}, \text{AGGREGATE}_k(\{\mathbf{h}_j^{k-1} : j \in \mathcal{N}(v_i)\})) \quad (9.1)$$

2669 where  $\mathbf{h}_i^k$  denotes the embedding of node  $v_i$  after the  $k$ -th iteration, and  $\mathcal{N}(v_i)$  the set of 2670 neighbouring nodes of  $v_i$ . Numerous GNN architectures have been proposed, from the simple 2671 Graph Convolutional Networks (GCNs) [151], which leverage spectral graph theory to define 2672 convolution-like operations on graphs, Graph Attention Networks (GATs) [152], which introduce 2673 attention mechanisms for adaptive neighbourhood weighting, to GraphSAGE [153], and 2674 Graph Isomorphism Networks (GINs) [154], which improved expressiveness in distinguishing 2675 graph structures.

## 2676 9.2 The filter network

2677 In the previous section, we have motivated and introduced graph neural networks as 2678 the deep learning method for non-Euclidean data represented as graphs. The GNN4ITk 2679 algorithm uses graph networks to identify fake edges in the graphs built from the methods 2680 described in chapter 8.

### 2681 9.2.1 Method

2682 As discussed in 8.3.2 and shown on figure 8.7, the number of edges in a graph produced 2683 by the **Metric Learning** method is on average  $|E| = (6.92 \pm 0.17) \times 10^6$ , most of which are

2684 fake. For comparison, the number of true target edges are of  $\mathcal{O}(10^4)$ , two orders of magnitude  
 2685 fewer. Among the fake edges, we can categorize *hard* fake edges as those resembling true  
 2686 edges, for example, a connection from a source node  $i$  to a false destination node  $j'$  on  
 2687 the same detector module as the true destination node  $j$ , so that  $|\mathbf{r}_j - \mathbf{r}_{j'}| \approx 0$ . The true  
 2688 edge  $e_{ij}$  is therefore difficult to distinguish from the fake edge  $e_{ij'}$ . In contrast, *easy* fakes  
 2689 are recognizable from target true edges, such as unphysical edges randomly selected by the  
 2690 kNN.

2691 Because hard fakes are difficult to identify, it is necessary to train a deep network to  
 2692 guarantee good performance. A large graph coupled with a large network creates a bottleneck  
 2693 in inference time and resource consumption. In addition, training on both hard and easy  
 2694 fake edges directs the classifier's attention away from hard fakes and affects the performance.  
 2695 A better strategy, therefore, is to train a shallow network on the output graphs of the Metric  
 2696 Learning to eliminate easy fakes and subsequently a deeper, more sophisticated network to  
 2697 eliminate hard fakes. The first network, designated the **Filter Network**, is described in  
 2698 this section, and the second, called the **Interaction Network**, in section 9.3.

2699 The architecture of the Filter Network is based on the GRAPH SAGE convolution pro-  
 2700 posed by reference [153], which facilitates the efficient learning of large complex graphs. The  
 2701 idea is to train a set of functions which aggregate and propagate information between dif-  
 2702 ferent depths of a node's neighborhood. We define a  $k$ -hop neighborhood of a node as the  
 2703 subset of nodes whose shortest path to the center node proceeds through exactly  $k$  edges.  
 2704 Figure 9.1 shows an example of a **central node** and its neighborhoods with  $k = 1$  and  $k = 2$ .  
 2705 At each depth, a trainable function aggregates the features of the nodes residing within, and  
 2706 passes the aggregated features to the next depth. In the figure, the messages from nodes  
 2707 at  $k = 2$  gathered by the **green aggregator** are used to evolve the features of **nodes** at  
 2708  $k = 1$ , which are then aggregated by the **blue aggregator** and passed to the **central node**.

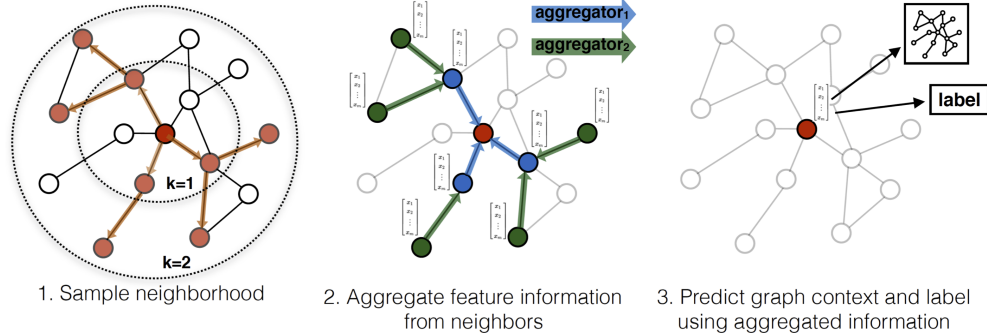


**Figure 9.1:** GRAPHSAGE sampling and aggregation mechanism. [153]

This mechanism is expressed more concretely in the pseudocode shown in algorithm 1. Each GRAPHSAGE is defined by  $K$  aggregator functions, denoted  $\text{AGGREGATE}_k$ ,  $k \in \{1, \dots, K\}$ , and a set of weight matrices  $\mathbf{W}^k$ ,  $k \in \{1, \dots, K\}$ , which propagate the aggregated information between different search depths. The aggregators must be differentiable to allow back-propagation through the search depths. Recall that the graph is defined by a set of nodes  $V$  and a set of edges  $E$ . To each node  $i \in V$  is associated a node feature vector  $\mathbf{x}_i \in \mathbb{R}^d$ . A neighbourhood function  $\mathcal{N} : v \rightarrow V$  finds other nodes directly connected to a given node  $v$ . In each step  $k$ , to each node  $v_i \in \mathcal{V}$  are aggregated the representations of other nodes in its local neighborhood  $\{\mathbf{h}_j^{k-1}\}$ , found by  $\mathcal{N}(v_i)$ , into a single vector  $\mathbf{h}_{\mathcal{N}(v_i)}^k$ . The current representation of  $v_i$  namely  $\mathbf{h}_v^{k-1}$  is concatenated with  $\mathbf{h}_{\mathcal{N}(v_i)}^k$ , and fed through an MLP represented by  $W^k$ , followed by a non-linear activation function  $\sigma$ . As this process iterates, nodes incrementally receive more information from further reaches of the graph, and their features become more expressive.

Any element-wise function is a good aggregator. However, for simplicity the **Filter** uses the mean aggregator, i.e.

$$\text{AGGREGATE}(\{\mathbf{h}_1, \dots, \mathbf{h}_N\}) = \frac{1}{N} \sum_{i=1}^N \mathbf{h}_i \quad (9.2)$$

---

**Algorithm 1:** Calculation of node embedding  $\mathbf{z}_i$  with GRAPHsAGE [153]

---

```

 $h_i^0 \leftarrow \mathbf{x}_i;$ 
for  $k \in \{1, \dots, K\}$  do
  for  $i \in \{1, \dots, |V|\}$  do
     $\mathbf{h}_{\mathcal{N}(v_i)}^k \leftarrow \text{AGGREGATE}_k(\{\mathbf{h}_j^{k-1} \forall v_j \in \mathcal{N}(v_i)\}) ;$ 
     $\mathbf{h}_i^k \leftarrow \sigma \left( \mathbf{W}^k \cdot [\mathbf{h}_v^{k-1} | \mathbf{h}_{\mathcal{N}(v_i)}^k] \right)$ 
  end
   $\mathbf{h}_i^k \leftarrow \frac{\mathbf{h}_i^k}{\|\mathbf{h}_i^k\|_2}, \forall v_i \in \mathcal{V}$ 
end

```

$\mathbf{z}_i \leftarrow \mathbf{h}_i^K \forall v_j \in \mathcal{V},$

where  $\sigma(\cdot)$  is an activation function,  $[\mathbf{x}|\mathbf{y}]$  a vector concatenation.

---

2724        The neighbourhood function  $\mathcal{N}(v)$  uniformly draws a fixed number of edges from the set  
 2725         $\{(u, v) \in \mathcal{V}\}$ , instead of using the entire 1-hop neighbourhood. Sampling limits the mem-  
 2726        ory footprint of a GRAPH SAGE operation on large graphs. Without it, the consumption  
 2727        becomes unpredictable and grows with  $|\mathcal{V}|$ . It is found in reference [153] that  $K = 2$  and  
 2728        sample sizes  $S_1 = 25$ ,  $S_2 = 10$  produce a good balance between memory and performance,  
 2729        which are used in the **Filter**.

2730        With the GRAPH SAGE mechanism defined, we can now describe the network architec-  
 2731        ture. First, the node embedding is evolved over  $L$  iterations of GRAPH SAGE to encode local  
 2732        context from a search depth at most  $K \times L$ . The embedding of two nodes  $(v_i, v_j)$  connected  
 2733        by an edge  $e_{ij} \in E$  are concatenated and fed to a decoder  $\phi : \mathbb{R}^n \times \mathbb{R}^n \rightarrow (0, 1)$  to obtain  
 2734        a score representing the probability of being a true edge. The corresponding pseudo-code is  
 2735        shown in algorithm 2.

---

**Algorithm 2:** The **Filter** network
 

---

```

 $\mathbf{z}_i^0 \leftarrow \mathbf{x}_i;$ 
for  $l \in \{1, \dots, L\}$  do
|  $z_i^l \leftarrow \text{GRAPH SAGE } (\mathbf{z}_i^{l-1}, \mathcal{V})$ 
end
 $\forall e_{ij} \in E : \hat{y}_{ij} \leftarrow \sigma(\mathbf{W} \cdot [\mathbf{z}_i^L | \mathbf{z}_j^L] + \mathbf{b}) \equiv \phi(\mathbf{z}_i^L, \mathbf{z}_j^L)$ 
  
```

---

2736        Each event is treated as a minibatch. The model weights  $\theta$  is optimized via the loss  
 2737        function  $\mathcal{L}_E(\theta)$ , defined over a set of edges  $E$  as

$$\mathcal{L}_E(\theta) = \frac{1}{|E|} \sum_{e_{ij} \in E} w_{ij} l(y_{ij}, \hat{y}_{ij}), \quad l(y, \hat{y}) = (y \log \hat{y} + (1 - y) \log(1 - \hat{y})), \quad (9.3)$$

2738        in which the edge score  $\hat{y}_{ij}$  is obtained according to algorithm 2, and the label  $y_{ij}$  is the truth  
 2739        edge label. The cost function  $l(y, \hat{y})$  is simply the cross-entropy of a binary label  $y \in \{0, 1\}$   
 2740        and a score prediction  $\hat{y} \in (0, 1)$ .

2741 Due to the large graph size, the loss function is computed from a subset of edges  $E_{train} \subset$   
2742  $E$  to avoid GPU memory overflow. The edge list is constructed in a manner similar to  
2743 equation (8.7), such that

$$E_{train} = E_{\text{truth,target}} \cup E_{\text{hnm}} \cup E_{\text{random}}. \quad (9.4)$$

2744 The difference between the training edge set of the **Metric Learning** network and that  
2745 of the **Filter** network is that the former is created on-the-fly from a kNN graph, whereas  
2746 the latter from an existing graph. In addition, the hard negatively-mined edges in this case  
2747 are defined as fake edges whose score exceeds a threshold  $Y_t = 0.5$ . This implies that  $E_{\text{hnm}}$   
2748 component of the loss punishes the network for false positive edges and ignores true negative  
2749 edges, assuming threshold  $Y_t$  is used to make predictions. In practice, we observe that the  
2750 **GRAPH SAGE** convolutions have relatively modest memory footprint even with gradient  
2751 tracking, thanks to the sampling mechanism. In contrast, the decoder consumes larger GPU  
2752 memory and can cause overflow in large graphs. Therefore, the loss function is calculated  
2753 with a memory-saving trick illustrated in algorithm 3. First, the **GRAPH SAGE** convolutions  
2754 are applied on the input graph with gradient tracking, yielding the node embedding vectors  
2755  $\mathbf{z}_i^L$  attached to a gradient compute graph. Then, the node vectors are fed to the decoder  
2756  $\phi$  **without** gradient tracking to calculate the score of **all** edges in  $E$ , which are then used  
2757 to create the training edge set  $E_{train}$  through hard-negative mining. Finally, the decoder is  
2758 invoked again, this time **with** gradient tracking and **exclusively** over  $E$ .

2759 The last ingredient is the weight  $w_{ij}$ , defined as

$$w_{ij} = \begin{cases} 1, & y_{ij} = 0 \\ 10, & (y_{ij} = 1) \wedge (e_{ij} \in E_{\text{truth,target}}) \\ 0 & (y_{ij} = 1) \wedge (e_{ij} \notin E_{\text{truth,target}}) \end{cases} \quad (9.5)$$

2760 To deal with class imbalance, true target edges are given a weight of 10 to amplify their  
2761 importance in the loss. On the other hand, the more abundant non-target edges are ignored  
2762 by giving them 0 weight.

---

**Algorithm 3:** Computation of the loss function of the **Filter** network
 

---

```

 $\mathbf{z}_i^0 \leftarrow \mathbf{x}_i;$ 
for  $l \in \{1, \dots, L\}$  do
   $//$  with gradient tracking
   $\mathbf{z}_i^l \leftarrow \text{GRAPHsAGE}(\mathbf{z}_i^{l-1}, \mathcal{V})$ 
end

begin torch.no_grad():
   $//$  Compute edge score for the whole graph without gradient tracking
   $\forall e_{ij} \in \mathcal{E} : \hat{y}_{ij} \leftarrow \phi(\mathbf{z}_i^L, \mathbf{z}_j^L);$ 
   $E_{\text{hnm}} \leftarrow \{e_{ij} \in \mathcal{E} : (\hat{y}_{ij} > Y_t) \wedge (y_{ij} = 0)\};$ 
end

 $E_{\text{train}} \leftarrow E_{\text{truth,target}} \cup E_{\text{hnm}} \cup E_{\text{random}};$ 
// Compute scores for edges in  $E$  with gradient tracking
 $\forall e_{ij} \in E_{\text{train}} : \hat{y}_{ij} \leftarrow \phi(\mathbf{z}_i^L, \mathbf{z}_j^L);$ 
 $\mathcal{L}_E(\theta) \leftarrow \frac{1}{|E|} \sum_{e_{ij} \in E} w_{ij} l(y_{ij}, \hat{y}_{ij})$ 
  
```

---

Hyperparameter	Value
GRAPHSAGE search depths (K)	2
GRAPHSAGE sample size ( $S_1, S_2$ )	(25, 10)
Number of GRAPHsAGE layers	3
Decoder hidden layers	6
Decoder hidden dimension	1024
Decoder activation function	ReLU
Learning rate	0.001
Epochs	$\approx 200$

**Table 9.1:** Hyperparameters used to train the Filter network.

2763        The Filter network takes the same input node vector as described in table 8.1, totalling 37  
 2764        features. The embedding is gradually enlarged to 1024 dimensions over 3 GRAPHsAGE con-  
 2765        volutions, and then fed to the decoder  $\phi$ . The latter is a simple MLP taking as input a con-  
 2766        catenated vector in 2048D and consisting of 6 layers of 1024 neurons with ReLU nonlinearity  
 2767        [155], and a final single-neuron output layer. The network is trained with the hyperparam-  
 2768        eters listed in table 9.1. The training set contains 7785 events. Each full iteration over the  
 2769        training set (epoch) is followed by an evaluation epoch on a validation set of 1000 events.  
 2770        The model with the best area under the Receiver Operating Curve (ROC-AUC) is selected  
 2771        for inference.

### 2772        9.2.2 Results

2773        We evaluate the performance of the Filter network as described in section 8.4. By re-  
 2774        jecting edges whose score falls under a threshold, we create a filtered edge list  $E_f \subseteq \mathcal{E}$ .  
 2775        Substituting  $E_f$  for  $E$  in equations (8.2) and (8.3), we evaluate the edge efficiency and  
 2776        purity yielded by the model.

Figures 9.2a 9.2b respectively show the edge efficiency as functions of the pseudorapidity  $\eta$  and transverse momentum  $p_T$ . To maximize the efficiency, a loose score cut of 0.05 is applied. The model efficiency is almost flat at  $\epsilon = 1$  the entire  $\eta$  range. As a function of the transverse momentum, the edge efficiency slightly decreases at high  $p_T$ , when compared to the lower range. This might be due to the imbalance over  $p_T$  in training data. The majority of generated particles in each event have low  $p_T$  and follow curved trajectories, i.e. small radius, large curvature. High- $p_T$  tracks, on the other hand, follow more straight tracks. Such difference in geometry, coupled with the data imbalance, might bias the model towards low- $p_T$ , high-curvature tracks, and degrade the efficiency at high transverse momentum.

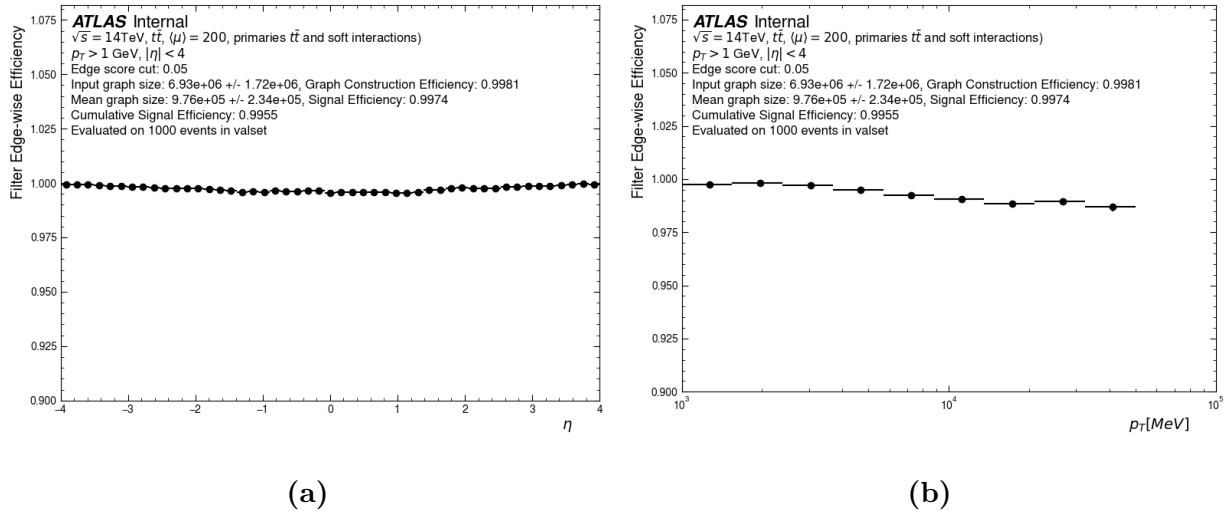


**Figure 9.2:** Edge efficiency of the Filter network on graphs constructed by the Metric Learning method as a function of  $\eta$  (a) and  $p_T$  (b).

Figures 9.3a 9.3b respectively show the edge efficiency and purity as functions of the spherical coordinates  $(r, z)$  of the source node. These plots illustrate the variation in  $\epsilon$  and  $\rho$  over the detector volume. 9.3a show excellent efficiency throughout the detector. Slight efficiency loss is observed in the outermost pixel layer and inner two layers of the strip barrel, where a track transitions between two sensor technologies. Overall, the edge efficiency over target particles is 0.996, i.e. on average 0.4 is lost per 100 target edges.

2792        The average edge purity after filtering is  $\rho = 1.48\%$ , which is not uniform throughout the  
 2793      detector. Two regions of low purity are identified. The first region with  $\rho \approx 0.4\%$  is located  
 2794      in the innermost pixel layer, closest to the interaction point. This proximity leads to a high  
 2795      density of space points, as shown in figure 9.4, and consequently a large number of possible  
 2796      random connections. This increases the chance of a misidentified fake edge and leads to low  
 2797      purity. The second region is located in the transition region between the pixel detector and  
 2798      the strip detector, and between the strip barrel and end-caps. Multiple factors play a role  
 2799      in the lowered purity, including (1) changing detector geometry, (2) accumulated material  
 2800      effects, and (3) the presence of single-cluster strip hits. A similar performance decrease is  
 2801      observed with the **Interaction Network** in the same detector region, of which a detailed  
 2802      discussion accounting for both networks will be given in section 9.3.2.

2803        Although the edge purity remains low, of  $\mathcal{O}(1\%)$ , the Filter network reduces the average  
 2804      number of edges to  $9.76 \times 10^5$ , 86% smaller than the input graph size of  $6.93 \times 10^6$ , while  
 2805      preserving the high edge efficiency from the graph construction stage. Recall that the Filter  
 2806      network aims to bring the number of edges down to a reasonable level, so it is more important  
 2807      to avoid falsely rejecting target edges than to eliminate *all* fake edges. This mission is  
 2808      reserved for a larger, more sophisticated INTERACTIONGNN introduced in the next section.

Graph Construction Method	Edge efficiency [%]	Edge Purity [%]	Number of edges
Module Map MINMAX	99.69		$1.22 \times 10^6$
Module Map MEANRMS	99.51		$8.55 \times 10^5$
Metric Learning + Filter	99.53	1.48	$9.76 \times 10^5$

**Table 9.2:** Comparison of the three graph construction methods: Module Map MINMAX, Module Map MEANRMS and Metric Learning. The constructed graphs become input to the INTERACTIONGNN.

2809        Table 9.2 compares properties of graphs produced by Metric Learning and Filter networks  
 2810      to those produced by the Module Map method. They all have high edge efficiency, with

2811  $\epsilon > 99.5\%$ . The Module Map with MINMAX selection creates edges with 1.2 million edges,  
2812 while the other methods yield fewer than 1 million edges.

### 2813 9.3 The Interaction Network

2814 In the section, a graph neural network is used to identify the majority of fake edges in  
2815 graphs constructed from either the Module Map technique, or the Metric Learning network.  
2816 Graphs from the former are directly subjected to the GNN, whereas those from the latter  
2817 are passed through a Filter network to reduce “easy” fake edges beforehand.

#### 2818 9.3.1 Methods

2819 The INTERACTIONGNN architecture, proposed by Google DeepMind in 2016, is used  
2820 in this thesis [156]. It was first successfully applied to the problem of track reconstruction  
2821 by the EXATRX project [141], delivering good tracking performance when tested on the  
2822 Particle Tracking Challenge, or commonly known as the TrackML, dataset [140]. Compared  
2823 to TrackML, our dataset represents a more realistic and complex detector geometry and  
2824 thus a greater challenge. The INTERACTIONGNN model architecture has been carefully  
2825 optimized to deal with this complexity.

2826 The model can be divided into three components: a set of encoders, a set of convolution  
2827 modules, and a decoder. In the encoding phase, a node encoder, denoted by  $\phi_{enc} : \mathbb{R}^d \rightarrow \mathbb{R}^D$   
2828 maps the features  $\mathbf{x}_i$  of node  $v_i \in V$  to a D-dimensional latent representation  $\mathbf{h}_i^0$ , such that

$$\mathbf{h}_i^0 = \phi_{enc}(\mathbf{x}_i). \quad (9.6)$$

2829 Next, an edge encoder  $\phi_e : \mathbb{R}^{2 \times D+F} \rightarrow \mathbb{R}^D$  maps the latent space node features  $(\mathbf{h}_i^0, \mathbf{h}_j^0)$   
2830 of nodes  $(v_i, v_j)$  connected by an edge  $e_{ij} \in E$ , and a set of hand-engineered edge features

2831  $\mathbf{u}_{ij} \in \mathbb{R}^F$  to an edge feature vector  $\mathbf{k}_{ij}^0$ ,

$$\mathbf{k}_{ij}^0 = \psi_{enc}([\mathbf{h}_i^0 | \mathbf{h}_j^0 | \mathbf{u}_{ij}]) \quad (9.7)$$

2832 The custom edge features, listed in table 9.3, resemble the geometric observables defined for  
2833 the Module Map edge cuts, making  $\mathbf{u}_{ij}$  a 6-dimensional vector.

Feature	Formula
$\Delta r_{ij}$	$r_j - r_i$
$\Delta\phi_{ij}$	$\phi_j - \phi_i$
$\Delta z_{ij}$	$z_j - z_i$
$\Delta\eta_{ij}$	$\eta_j - \eta_i$
$\phi$ -slope	$\frac{\Delta\phi_{ij}}{\Delta r_{ij}}$
$r\phi$ -slope	$\frac{r_i + r_j}{2} \times \frac{\Delta\phi_{ij}}{\Delta r_{ij}}$

**Table 9.3:** Edge-level input features to the INTERACTIONGNN. The subscripts  $i$  and  $j$  respectively denote the source and destination nodes connected by an edge.

2834 The most important component of the INTERACTIONGNN is the graph convolution  
2835 modules  $\{\varphi^l\}_{l=1}^L$ . They evolve the encoded node and edge features over  $L$  iterations by  
2836 taking into account the graph connectivity. At each iteration  $l$ , the node feature  $\mathbf{h}_i^l$  of  
2837 node  $v_i$  is computed from its feature from the previous step  $\mathbf{h}_i^{l-1}$ , and a message vector  $\mathbf{m}_i^l$   
2838 containing information from other nodes directly connected to  $v_i$ . First, the latent feature  
2839 vectors  $k_{ij}^{l-1}$  of edges connecting to  $v_i$  are aggregated to generate a vector  $\mathbf{m}_{i\leftarrow}^l$

$$\mathbf{m}_{i\leftarrow}^l = \text{AGGREGATE}(\{\mathbf{k}_{ji}^{l-1} \forall e_{ji} \in E\}), \quad (9.8)$$

2840 and then the aggregation is repeated on edges connecting from  $v_i$  to create a vector  $\mathbf{m}_{i\rightarrow}^l$

$$\mathbf{m}_{i\rightarrow}^l = \text{AGGREGATE}(\{\mathbf{k}_{ij}^{l-1} \forall e_{ij} \in E\}). \quad (9.9)$$

2841 The message vector  $\mathbf{m}_i^l$ , simply

$$\mathbf{m}_i^l = [\mathbf{m}_{i\leftarrow}^l | \mathbf{m}_{i\rightarrow}^l], \quad (9.10)$$

2842 is used to update the node vector by

$$\mathbf{h}_i^l = \varphi_v^l(\mathbf{h}_i^{l-1}, \mathbf{m}_i^l), \quad (9.11)$$

2843 and the updated node vector is then used to update the edge vector

$$\mathbf{k}_{ij}^l = \varphi_e^l(\mathbf{k}_{ij}^{l-1}, \mathbf{h}_i^l, \mathbf{h}_j^l). \quad (9.12)$$

2844 Equations (9.8)-(9.12) describe the message passing mechanism of the INTERACTIONGNN,  
2845 which, analogous to the GRAPHSAGE mechanism of the Filter network, leverages the con-  
2846nectivity on which the graph is defined to evolve the node vectors.

---

**Algorithm 4:** Message passing mechanism of the INTERACTIONGNN

---

```

for  $l \in \{1, \dots, L\}$  do
     $\mathbf{m}_{i\leftarrow}^l \leftarrow \text{AGGREGATE}(\{\mathbf{k}_{ji}^{l-1} \forall e_{ji} \in E\});$ 
     $\mathbf{m}_{i\rightarrow}^l \leftarrow \text{AGGREGATE}(\{\mathbf{k}_{ij}^{l-1} \forall e_{ij} \in E\});$ 
     $\mathbf{m}_i^l \leftarrow [\mathbf{m}_{i\leftarrow}^l | \mathbf{m}_{i\rightarrow}^l];$ 
     $\mathbf{h}_i^l \leftarrow \varphi_v^l(\mathbf{h}_i^{l-1}, \mathbf{m}_i^l);$ 
     $\mathbf{k}_{ij}^l \leftarrow \varphi_e^l(\mathbf{k}_{ij}^{l-1}, \mathbf{h}_i^l, \mathbf{h}_j^l);$ 
end

```

---

2847 However, different from GRAPHSAGE, the message passing mechanism of the INTER-  
2848 ACTIONGNN tracks the edge vector and treats it as the message between nodes. Indeed,  
2849 very few other GNN architectures maintain edge-level intermediate vectors, since informa-  
2850tion exchange between nodes can be effectuated without an explicit edge state. Because the  
2851number of edges in a graph is generally much larger than the number of nodes, tracking the  
2852gradient of an edge-level network, such as the edge updater  $\varphi_e^j$ , consumes more memory than  
2853that of node-level networks. However, the increased computational cost is justified by better  
2854expressivity. Reference [156] proposed the INTERACTIONGNN to model a multi-body phys-  
2855ical system, in which each node represents an object and each edge the interaction between  
2856these objects. As such, the node vector represents the physical state of each object, and the

2857 edge vector quantifies the effect an object has on another’s hidden state. So naturally, the  
 2858 object state vector evolves with its previous state and the interaction as input, as seen on  
 2859 equation (9.11). This interaction itself depends not only on the current object state, but  
 2860 also on its history, so the edge updater uses its previous state, and the current object state,  
 2861 as seen in equation (9.12).

2862 The accuracy of the INTERACTIONGNN in modelling multi-body physical systems ob-  
 2863 served by reference [156] lends evidence to the effectiveness of explicitly tracking edge-level  
 2864 features following this physics intuition. In it unclear, however, how far this logic could be  
 2865 extended to other problems, or in reverse, how closely the track pattern recognition problem  
 2866 resembles an  $n$ -body system. For example, it is conceivable that since a track traces the  
 2867 evolution of a particle through the detector, hits from inner layers (the past) provide useful  
 2868 information to predict whether a hit in an outer layer (the future) belongs to the track, and  
 2869 vice versa. In this sense, the interaction between two hits, when evolved over multiple steps,  
 2870 encodes the properties of a track formed from themselves and other hits among which they  
 2871 exchange information. The network can then learn to distinguish true and fake edges by  
 2872 picking the most probable path given the hits on a particular search road. This intuition is  
 2873 in no way a *proof*. Deep neural networks are after all blackbox algorithms, whose explain-  
 2874 ability awaits further developments and lies outside the scope of this thesis. We contend  
 2875 with the assumption that the INTERACTIONGNN’s success on a simplified tracking problem  
 2876 (TrackML) [141] holds potentials for a more realistic counterpart (ATLAS ITk), if given  
 2877 sufficient training data and optimization.

2878 In the final stage, the edge vector  $\mathbf{k}_{ij}^L$  is fed to a decoder  $\psi_{dec} : \mathbb{R}^D \rightarrow [0, 1]$  to compute a  
 2879 single number interpreted as the probability of being a true edge.

$$\hat{y}_{ij} = \psi_{dec}(\mathbf{k}_{ij}^L) \quad (9.13)$$

2880 The INTERACTIONGNN architecture is summarized in algorithm 5. The hidden dimension  
 2881 of all latent-space vectors is set to  $D = 128$ . A simple element-wise average is used as the

2882 aggregation function

$$\text{AGGREGATE} \left( \{\mathbf{k}_{ij}\}_{j=1}^N \right) = \frac{1}{N} \sum_{i=1}^N \mathbf{k}_{ij}. \quad (9.14)$$

2883 The message passing mechanism is carried out over  $L = 8$  iterations, each with a distinct set  
2884 of node and edge updaters. All neural network submodules in the model are MLPs consisting  
2885 of 3 layers, each containing  $M = 128$  neurons.

**Algorithm 5:** The INTERACTIONGNN

Given input graph  $G(V, E)$ , input node feature  $\mathbf{x}_i \forall v_i \in V$ ,

```

 $\mathbf{h}_i^0 \leftarrow \phi_{enc}(\mathbf{x}_i);$ 
 $\mathbf{k}_{ij}^0 \leftarrow \psi_{enc}(\mathbf{h}_i^0, \mathbf{h}_j^0);$ 
for  $l \in \{1, \dots, L\}$  do
|  $(\mathbf{h}_i^l, \mathbf{k}_{ij}^l) \leftarrow \varphi(\mathbf{h}_i^{l-1}, \mathbf{k}_{ij}^{l-1}, \{\mathbf{k}_{ij}^{l-1} \forall e_{ij} \in E\}, \{\mathbf{k}_{ji}^{l-1} \forall e_{ji} \in E\})$ 
end
 $\hat{y}_{ij} = \psi_{dec}(\mathbf{k}_{ij}^L)$ 
```

2886 The model weights are optimized on the edge classification objective, using the weighted  
2887 binary cross-entropy loss described in equation (9.3). Other hyperparameters related to  
2888 model training are detailed in table 9.4.

Hyperparameter	Value
Number of message passing operations	8
Hidden dimension	128
Hidden activation functions	RELU
Optimizer	ADAM
Learning rate	0.001
Epochs	$\approx 200$

**Table 9.4:** Hyperparameters used to train the INTERACTIONGNN.

### 2889 9.3.2 Results

2890 Being both edge-classifying graph neural networks, the Filter and the Interaction network  
 2891 are evaluated using the same metrics. Figure 9.5 shows the edge efficiency of the INTERAC-  
 2892 TIONGNN as a function of the particle's pseudorapidity (left) and transverse momentum  
 2893 (right). Figures 9.5a and 9.5b describes the performance on graphs from the Module Map  
 2894 MeanRMS variant, whereas figures 9.5c and 9.5d those from the Metric Learning variant.  
 2895 The Module Map MinMax and MeanRMS variants have similar performance, so the former  
 2896 is omitted from all following figures in this chapter for brevity. The standard edge score cut  
 2897 0.5 is applied to make the binary prediction. Note, however, that this simple score cut will  
 2898 not be used to construct the final track candidate, as described in chapter 10.

2899 The INTERACTIONGNN achieves efficiency exceeding 99.5% on graphs constructed by  
 2900 both the Module Map and Metric Learning techniques. The performance is also consistently  
 2901 higher than 99% throughout the detector. Against the truth transverse momentum, a slight  
 2902 dip in efficiency is observed at high  $p_T$ . As we have seen from the discussion on the Filter  
 2903 network, the combination of low training statistics and different curvature means that edges  
 2904 from high- $p_T$  tracks receive less attention during training. As a result, the model favours the  
 2905 more abundant low- $p_T$  track edges and more often misidentifies high- $p_T$  ones. Since high- $p_T$   
 2906 tracks are more concentrated in the barrel region, a slight decrease in efficiency is observed  
 2907 in  $|\eta| < 1.5$ .

2908 It is worth noting that the GNN4ITk pipeline has been developed over several iterations  
 2909 of MC data, the most recent of which is described in reference [157], on a dataset of 1780  
 2910  $t\bar{t}$ -events. The cumulative edge efficiency achieved in this thesis is 99.04% for the **Mean-**  
 2911 **RMS** variant, higher than the previous result of 98.2%. The enhanced performance can be  
 2912 attributed to an optimized model architecture, and a larger training dataset, in particular  
 2913 7800 event versus 1600 in reference [157].

2914 The edge efficiency as a function of the  $(z, r)$ -coordinates of the inner hit, shown in figure  
 2915 9.6, illustrates the spatial distribution of misidentified true edges. Similar to the case of the  
 2916 Filter network, pockets of edge inefficiency as low as 96% are observed on the outermost pixel  
 2917 layer and near the edges of barrel strip layers, where a trajectory passes from one sensor  
 2918 technology or geometry to another. It is clear that both graph neural networks perform  
 2919 better in the pixel detector than in the the strip detector. The degraded performance can be  
 2920 attributed to a number of factors. First, accumulated material effects change the geometry of  
 2921 the orbit and increase the chance of an edge deviating from the pattern observed on the inner  
 2922 layers and being deemed incompatible with other true edges. Second, the transition between  
 2923 one sensor technology to another creates heterogeneity in both the geometric representation  
 2924 of the local coordinates, which is part of the input features and their resolution, as described  
 2925 in section 7.1. Yet despite the inherently heterogeneous data, all models employed in this  
 2926 thesis are homogeneous in architecture, which, though generally sufficient for their purpose,  
 2927 cannot predict well the cases where the heterogeneity can provide useful discrimination.  
 2928 Third, the hit inefficiency in space point formation, also described in section 7.1, means that  
 2929 true particle tracks are more likely to pass a strip layer without a hit when constructed from  
 2930 space points. Learning from these tracks, the GNNs may tolerate or even encourage layer-  
 2931 skipping edges in the strip detector, at the detriment of some true edges not well featured  
 2932 in the training data. We will return to the third issue in chapter 11, as it has an even  
 2933 larger implication on the tracking performance. In general, the training input data into the  
 2934 GNN4ITk contains shortcomings that are not optimal for learning and processing the output  
 2935 track candidates, to be addressed in future work.

2936 The edge purity as a function of the  $(z, r)$ -coordinates of the inner hit, shown in figure  
 2937 9.7, paints a similar picture as the efficiency distribution. On graphs from the MeanRMS  
 2938 variant, an average purity of 95.3% is achieved with noticeable variations over the detector  
 2939 regions. Model predictions are more pure in the pixel detector than in the strip detector,  
 2940 with pockets of impurity as high as 25% at the edges of the strip barrel. When compared

2941 to the input graphs, which average to  $\rho < 0.1\%$  and  $\mathcal{O}(10^6)$  edges in all variants (see table  
2942 9.2), a purity level of  $\sim 95\%$  in graphs of  $\mathcal{O}(10^4)$  edges represents a significant rate of fake  
2943 rejection. Nevertheless, the residual impurity creates challenges to the construction of track  
2944 candidates, which is the focus of chapter 10.

Graph Construction Method	Edge efficiency [%]	Edge Purity	Number of edges
Module Map <b>MinMax</b>	99.40	95.64	$2.53 \times 10^4$
Module Map <b>MeanRMS</b>	99.04	95.34	$2.48 \times 10^4$
Metric Learning + Filter	97.98	97.86	$2.54 \times 10^4$

**Table 9.5:** Performance of the GNN4ITk algorithm after the across three graph construction methods. Edges are classified using the INTERACTIONGNN with a threshold of 0.5 on the classification score. The edge efficiency is cumulative throughout the pipeline. The number of edges is the size of the remaining edge set after the score cut.

2945 The performance of the GNN4ITk algorithm through both graph construction and edge  
2946 classification steps is shown in table 9.5, including the cumulative efficiency, purity and the  
2947 graph size after rejecting edges with  $s < 0.5$ . Three variants corresponding to three graph  
2948 construction methods are contrasted. On graph constructed by the Module Map techniques,  
2949 the performance of the GNN is almost identical between the MINMAX and MEANRMS  
2950 variants, with the former having slightly better efficiency and purity. The Metric Learning  
2951 variant is 1.4% less efficient than the MinMax variant, but 3% more pure. The number  
2952 of remaining edges after the score cut is similar throughout the graph construction methods  
2953 and is significantly smaller than that of the input graphs.

2954 The edge-based metrics are useful in evaluating machine learning models, and a simple  
2955 score cut is typically sufficient in many applications. However, in order to build track  
2956 candidates, the scored graphs are subjected to a segmentation stage, which treats the edge  
2957 score in a procedure more sophisticated than a simple cut. In addition, the resulting track  
2958 candidates must fed into Athena [144], the main software analysis framework of ATLAS,

2959 so that they are properly processed and become input into subsequent steps of the event  
2960 reconstruction chain.

2961 As such, the next step of the GNN4ITk algorithm partitions a graph whose edges have  
2962 been scored by the GNN into track candidates. Track parameters are estimated and other  
2963 important metrics are computed in a unified framework for both the CKF- and the GNN-  
2964 based track finders. The graph segmentation step is presented in the next chapter, and the  
2965 tracking performance in chapter 11.

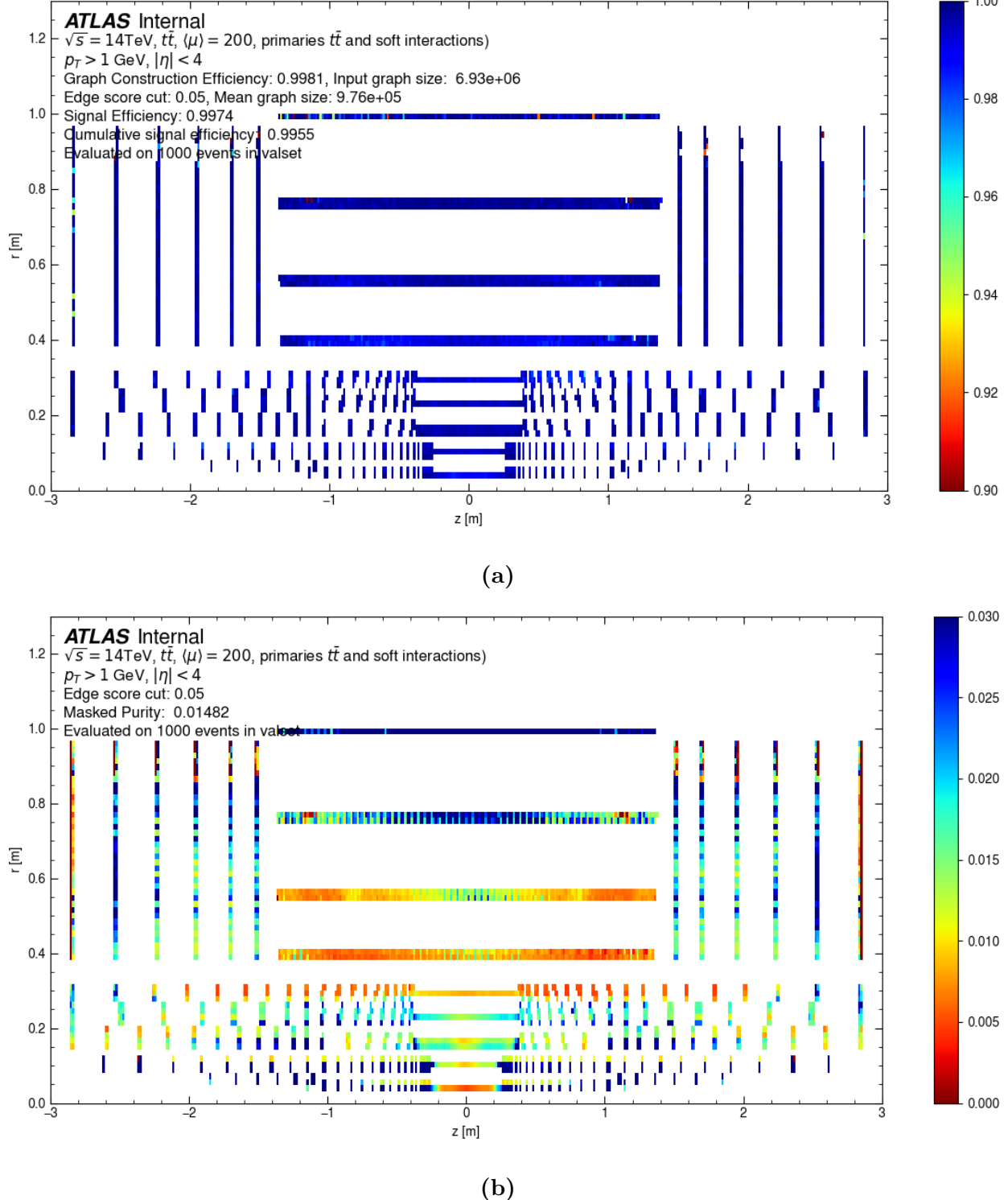


**Figure 9.3:** Edge efficiency (a) and purity (b) of the Filter network on graphs constructed by the Metric Learning method as functions of the  $(z, r)$ -coordinates of the inner hit.

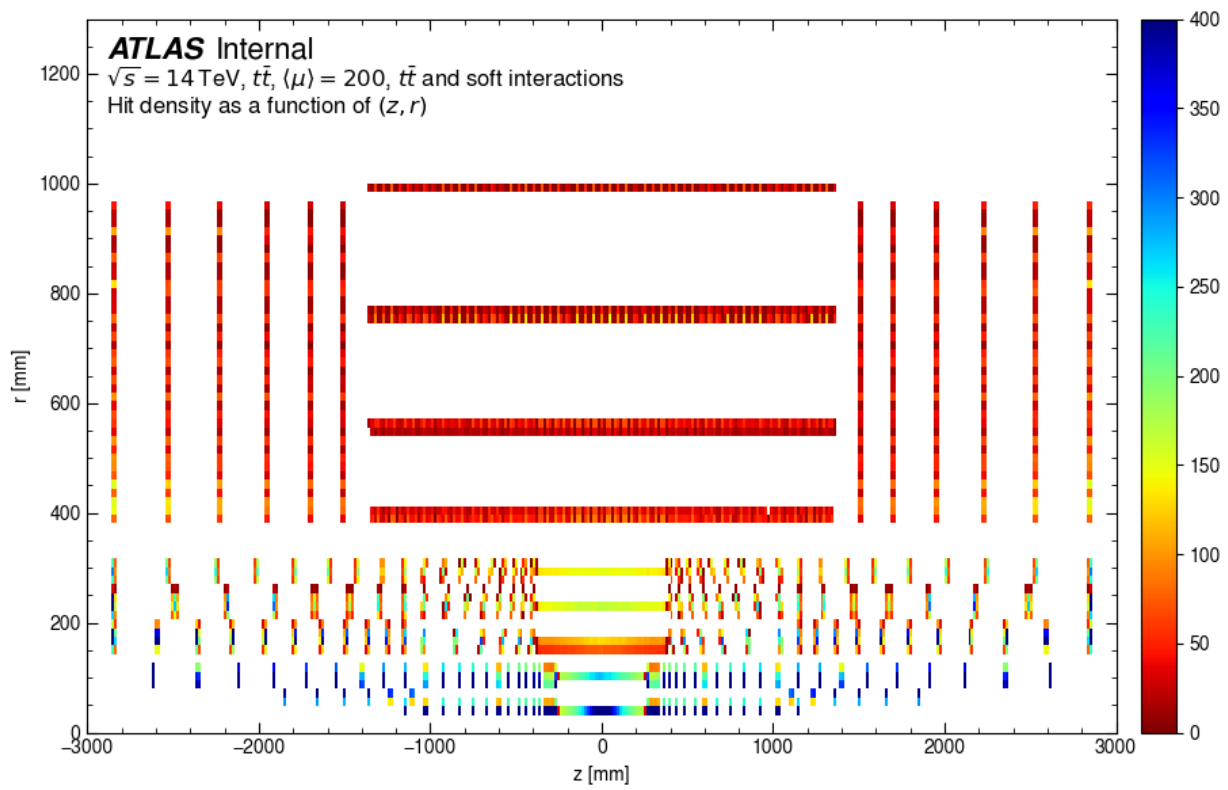


**Figure 9.4:** The number of space points per  $(z, r)$ -bin averaged over 50  $t\bar{t}$  events. The binwidth is 15 mm in both  $z$ - and  $r$ -direction.

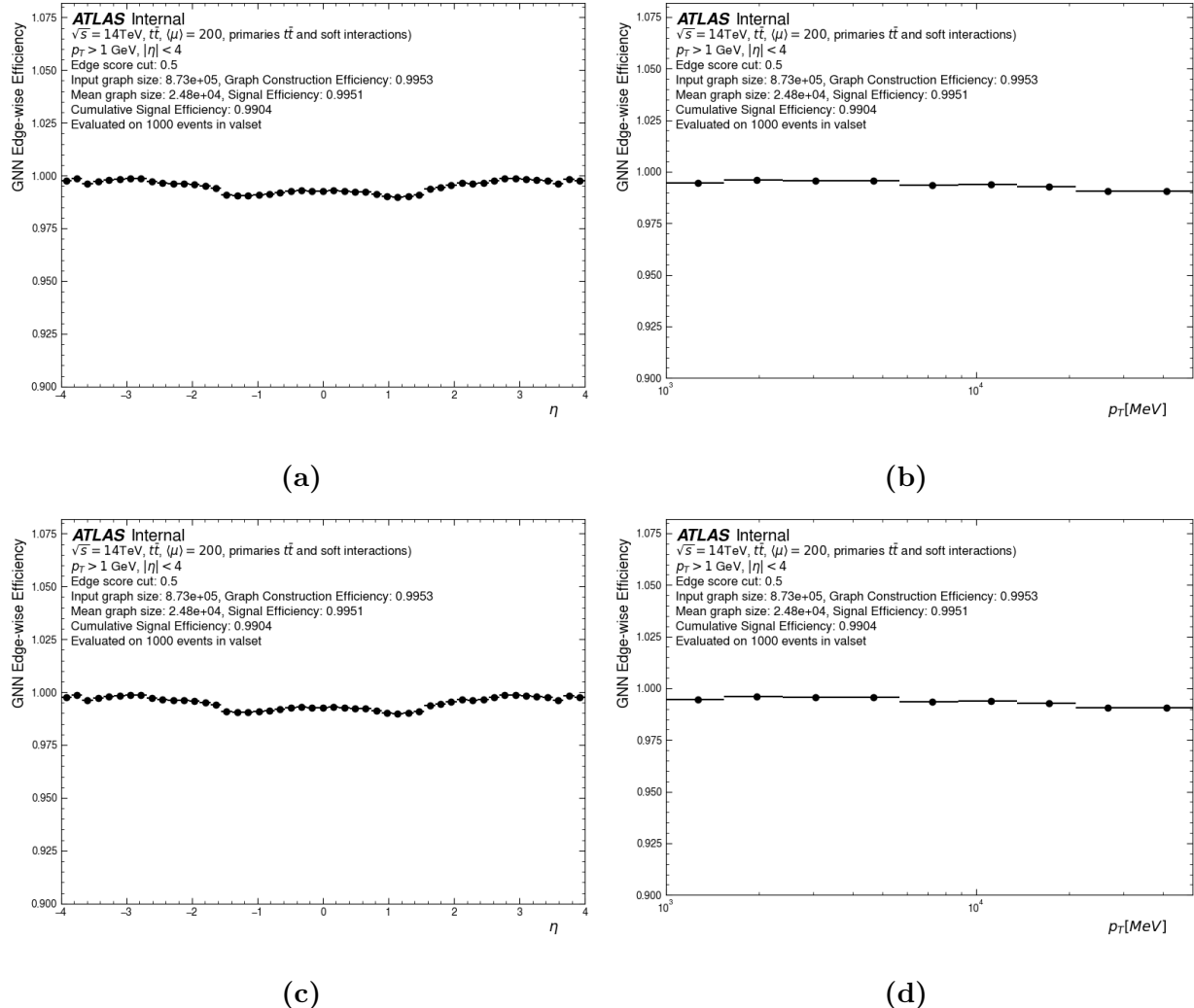


**Figure 9.5:** Edge efficiency of the INTERACTIONGNN as a function of  $\eta$  (left) and  $p_T$  (right), evaluated on graphs created using the Module Map method with MeanRMS (upper) and MinMax selections (lower).

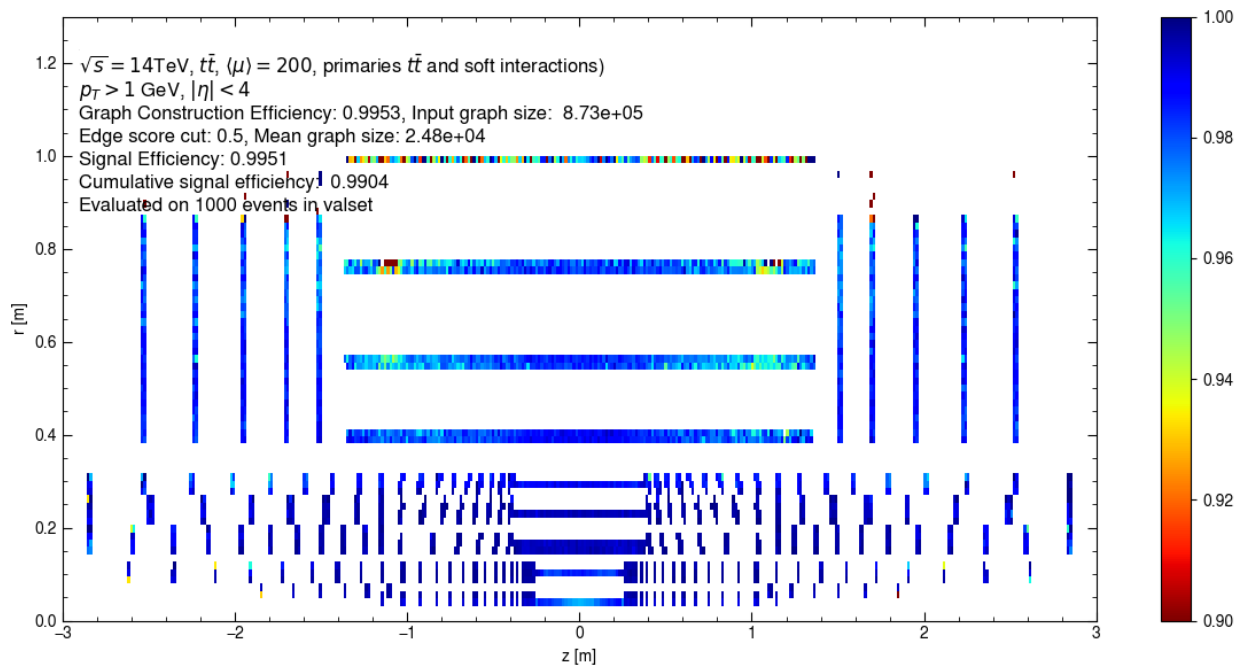


**Figure 9.6:** Edge efficiency of the INTERACTIONGNN on graphs constructed by the **Module Map MeanRMS** as a function of the  $(z, r)$ -coordinates of the inner hit.

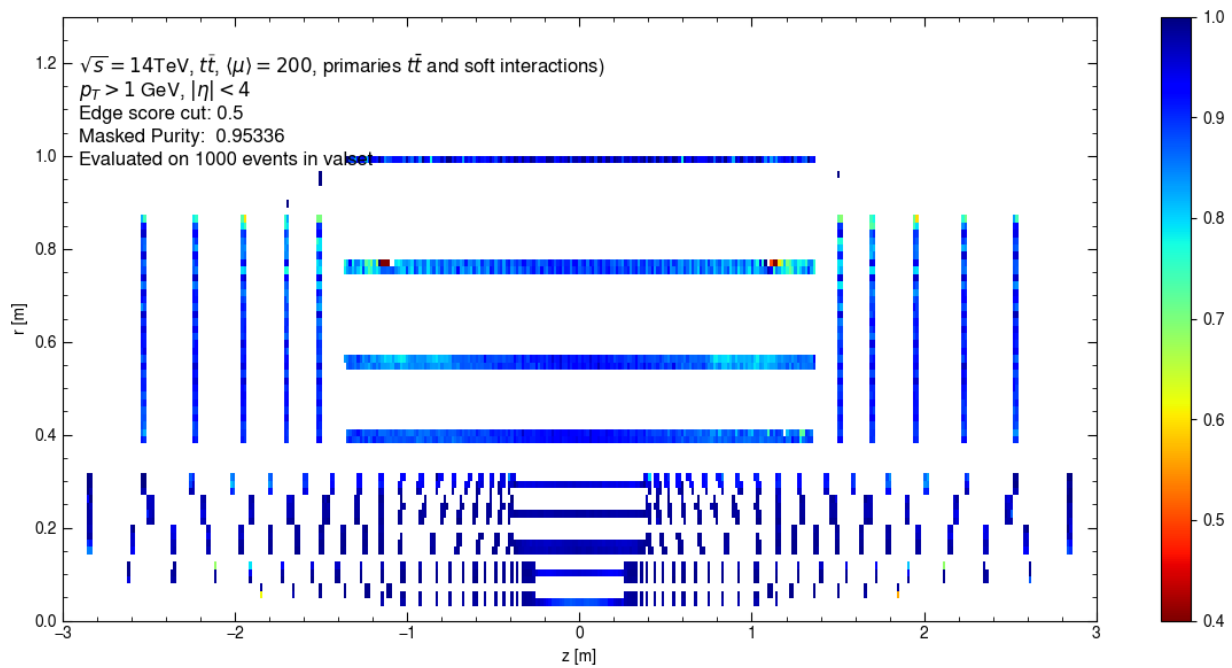


**Figure 9.7:** Edge purity of the INTERACTIONGNN on graphs constructed by the **Module Map MeanRMS** as a function of the  $(z, r)$ -coordinates of the inner hit.

## 2966 Chapter 10

### 2967 Graph segmentation

2968 Given a set of scored edges, the last stage of the pipeline segments them into individual  
2969 track candidates. There are several methods to carry out this task. The simplest case  
2970 applies a score threshold to eliminate edges believed to be fake, and treats the remaining  
2971 connected subgraphs as track candidates. This approach, called **Connected Component**,  
2972 ignores the directionality of graph edges. At the other edge of complexity, the edge direction  
2973 is retained and exploited to make heuristic segmentation decisions. A subgraph is traversed  
2974 outward from a source node—one with no incoming edges, selecting the longest path to form a  
2975 track candidate. This method is called **Walkthrough**. Both approaches are detailed in this  
2976 chapter, starting with the simple Connected Component. The track candidates constructed  
2977 by the Walkthrough algorithm are used to evaluate tracking performance in chapter 11.

#### 2978 10.1 Connected components

2979 The simplest and most intuitive method of track building involves pruning the graph  
2980 of edges that are deemed fake. Assigned to each edge by the GNN is a score  $s \in [0, 1]$   
2981 representing the probability that it is a true edge. A binary label is obtained from a threshold  
2982  $s_{cut}$ , which reflects the level of confidence one desires in a prediction of a positive edge

$$\hat{y}_{ij} = \mathbb{1}_{s_{ij} > s_{cut}}. \quad (10.1)$$

2983 The threshold is typically set to  $s_{cut} = 0.5$  in typical classification problems. However, the  
 2984 score cut in our problem needs not follow this convention. Figure 10.1 shows the score  
 2985 distribution of the GNN on graphs constructed with Metric Learning method, categorized  
 2986 by the true label. We observe an excellent separation between target and fake edges. 99.6%  
 2987 of fake edges have score lower than 0.01, with the highest among other bins contributing  
 2988 < 0.1%. On the other hand, 99.7% of target edges get score higher than 0.01. This means  
 2989 that even a loose  $s_{cut} = 0.01$  eliminates 99.6% fake edges and retains 99.7% target edges.  
 2990 The edge efficiency and fake reduction of several other cuts are shown in table 10.1. It is  
 2991 obvious that the edge efficiency decreases, while the fake reduction increases with tightening  
 2992 score cut. It is also clear that for our purpose, we lose too much efficiency at  $s_{cut} = 0.5$ ,  
 making it sub-optimal. A score cut of  $s_{cut} = 0.01$  is chosen to label the graph edges.

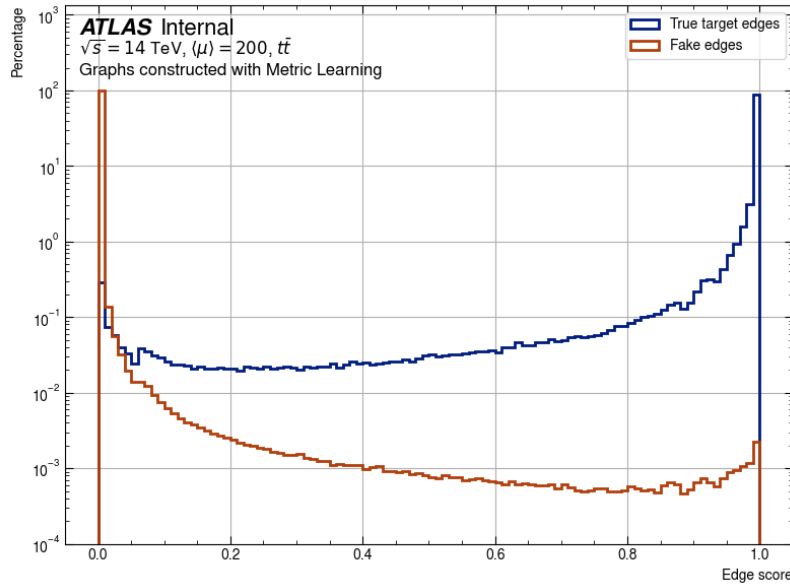


**Figure 10.1:** A distribution of the GNN edge classification scores. 200 graphs constructed using the Metric Learning approach are used.

2993

2994 Illustrated in figure 10.2, the elimination of fake edges results in the segmentation of the  
 2995 input graph into subgraphs which are not connected to the rest of the graph. Mathematically,

2996 the segmented graph can be written as

$$G(V, E) = \bigcup_{i=1}^M G(V_i, E_i) \quad (10.2)$$

2997 where for any pair  $i \neq j$ ,  $i \in [M]$ ,  $j \in [M]$ ,

$$V_i \cap V_j = \emptyset, \quad E_i \cap E_j = \emptyset \quad (10.3)$$

2998 figure 10.2a, shows a simplified input graph to the GNN, which contains two color-coded  
2999 tracks: a **green** track with 4 hits labelled  $\{1, 2, 3, 4\}$ , a **blue** track with 3 hits labelled  
3000  $\{5, 6, 7\}$ ; and a single **violet** hit labelled  $\{8\}$ . Hits and true edges from a track share the  
3001 same color. Fake edges are shown in **red**. Note that the colours represent truth information  
3002 available only for evaluation. During inference, the GNN **ideally** gives **fake** edges a low score,  
3003 and true edges a high score. After eliminating edges whose score falls belows  $s_{cut} = 0.01$ , we  
3004 are left with three correctly segmented subgraphs, each containing all hits from the parent  
3005 particle. Every node in each subgraph has at most 1 incoming and 1 outgoing edge, creating  
3006 a single path from the innermost to the outermost hit <sup>1</sup>. These graphs, designated simply  
3007 connected components, are labelled as track candidates.

Score cut	Edge efficiency [%]	Fake reduction [%]
0.01	99.71	99.58
0.02	99.63	99.72
0.05	99.50	99.82
0.1	99.35	99.89
0.2	99.12	99.93
0.5	98.42	99.97

**Table 10.1:** Edge efficiency and fake reduction rate at representative values of GNN edge score cut.

---

<sup>1</sup>Note that all input edges point in the direction of increasing distance from the IP

Because of its simplicity, **Connected Component** is fast and widely available in many Python libraries. We use the NETWORKX library[158] to implement the segmentation, which has a GPU backend called Nx-CUGRAPH. The latter allows the GNN-labelled graph which already resides on the GPU during inference to be segmented without being moved to the CPU, avoiding data transfer overheads.

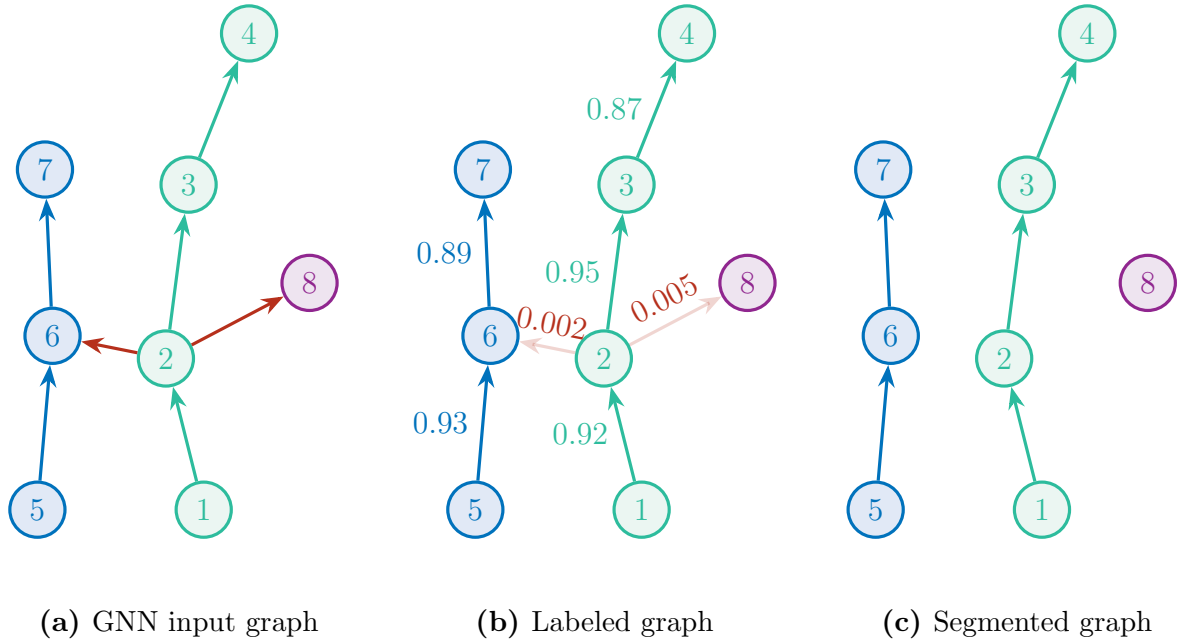


**Figure 10.2:** Illustration of the Connected Component method. (a) The input graph contains two particle tracks and a single hits, all color-coded. The three objects are merged by two fake edges in red. (b) Edges whose score falls under a threshold is eliminated. (c) The remaining connected components are considered as track candidates.

It is perhaps not surprising that connected component alone is not sufficient to build track candidates with sufficient reconstruction efficiency, which is why its description emphasizes on an ideal GNN labelling. We already see from figure 10.1 that this is not the case. Aside from the inefficiency associated with the rejection of true edges with  $\hat{y} < 0.01$ , 0.42% of the fake edges still remain after the edge cut. Despite their small population, residual fake edges create a non-negligible number of non-simple subgraphs, with whom the method is not equipped to deal. These non-simple subgraphs occur then true tracks are merged by

3020 a misclassified fake edge, creating an object that fails to represent any of the underlying  
 3021 particle. We will examine this problem in greater details and its treatment in the next  
 3022 section.

3023 **10.2 The Walkthrough algorithm**

3024 Non-simple subgraphs are a big drawback of the Connected Component approach. Their  
 3025 topology can range from a random hit being wrongly connected to an otherwise good track,  
 3026 to several tracks being merged together. With the only tuneable parameter being the GNN  
 3027 edge score cut, it undergoes a trade-off between the edge efficiency and the fake edge rate. A  
 3028 high score cut decreases the efficiency but also the number of fake edges, thus reducing the  
 3029 occurrence of non-simple subgraphs. This edge efficiency reduction, however, often results  
 3030 in strong impact on the tracking efficiency of high- $p_T$  particles due to their small proportion.  
 3031 To avoid compromising high- $p_T$  tracks, we must contend with a loose score cut and resolve  
 3032 the ensuing merged tracks.

3033 The Walkthrough algorithm is constructed as a solution to this issue. It still relies on the  
 3034 Connected Component method to quickly construct simple track candidates. On non-simple  
 3035 subgraphs, however, it considers both the directionality and the GNN edge score to isolate  
 3036 merged tracks. The main idea is to traverse all possible paths starting from the source nodes  
 3037 and to identify the longest paths which do not share any node with each other. The edge  
 3038 score is used to resolve ambiguity when multiple paths have the same lengths, and other  
 3039 subtle cases.

3040 First, all cycles in the form  $u \rightarrow \dots \rightarrow v \rightarrow \dots \rightarrow u$  are removed. Although by construc-  
 3041 tion graph edges always point in the direction of increasing distance from the interaction  
 3042 point, a loop can occur when three or more equidistant nodes are connected in a manner  
 3043 such as  $v_1 \rightarrow v_2 \rightarrow v_3 \rightarrow v_1$ , in which case one of the edge is randomly flipped to remove the  
 3044 loop. The removal of loops enables a topological sort  $f : V \rightarrow \mathbb{N}$  of nodes in the subgraph,

3045 such that for every directed edge  $u \rightarrow v$ ,  $f(u) < f(v)$ . The sorting places all nodes that have  
 3046 no incoming edges at the top, which are isolated into a set of starting nodes. Thanks to the  
 3047 loop removal and the edge orientation, this set is guaranteed non-empty. Each starting node  
 3048 becomes a seed for iterative track building.

3049 Space points are sequentially added to the seed path, guided by the GNN edge score.  
 3050 Two thresholds on edge score are defined. The first, denoted  $s_{min}$ , is the minimum score of  
 3051 an edge via which the path may be extended. The second, denoted  $s_{add}$  and always larger  
 3052 than  $s_{min}$ , is the minimum score to create an alternative path. With these thresholds, three  
 3053 distinct scenarios can be identified.

- 3054 1. A unique outgoing edge exists from the starting node. This is the trivial case. The  
 3055 receiving node is added to the path and becomes the next starting node (figure 10.3a),
- 3056 2. Multiple outgoing edges stem from the starting node, among which the highest score  
 3057  $s_{max} \leq s_{add}$ . The edge with the highest score is uniquely chosen and its receiving node  
 3058 becomes the next starting node (figure 10.3b),
- 3059 3. Multiple outgoing edges stem from the starting node, and  $s_{max} \geq s_{add}$ . All edges with  
 3060  $s > s_{add}$  are admitted to create multiple parallel paths, each now starting from the  
 3061 corresponding receiving node (figure 10.3c).

3062 In these scenarios, the scores of all considered edges must exceed  $s_{min}$ . This local procedure  
 3063 is repeated until all paths reach a terminal node, from which no outgoing edge stems. In  
 3064 the end, every encounter of scenario (3) creates at least two track paths. To resolve the  
 3065 ambiguity, we select the longest path. Thus, from a given starting node, we obtain a single  
 3066 track candidate, whose node are removed from the parent subgraph. This prevents space  
 3067 points from being shared among multiple track candidates. Nodes from the globally rejected  
 3068 paths, and locally rejected nodes can be reused to build track candidates from other starting  
 3069 nodes.

3070 Nevertheless, ambiguity may still arise when multiple globally longest paths are identified  
3071 from a starting node, as illustrated in figure 10.4. The path traversing via the edge of  
3072 highest score is then chosen as the track candidate in such case. In the figure, the path  
3073  $1 \rightarrow 2 \rightarrow 3 \rightarrow 4 \rightarrow 5$  is selected, since  $s_{23} > s_{26}$ . Nodes (5, 6, 7) are returned to the  
3074 subgraph to build subsequent paths. With the Walkthrough technique, the track finding  
3075 part of the GNN4ITk algorithm is concluded. The final product of graph segmentation is  
3076 simple a set of track candidates. Each candidate is a list of space points ordered by their  
3077 distance from the origin. Equivalently, the CKF also creates a collection of track candidates,  
3078 which are subjected to an ambiguity resolution step to reduce the number of shared hits  
3079 and fake tracks, as described in chapter 7. Different from GNN-built tracks, CKF tracks  
3080 by construction “live” in Athena as a link in the event reconstruction chain, and more  
3081 importantly, are equipped with the track parameters. From an engineering point of view,  
3082 it is crucial to treat GNN-built track candidates in Athena, so that they can rejoin the  
3083 chain and be ready for downstream tasks. This also enables an apple-to-apple performance  
3084 comparison of both track finders in the same environment, which is presented in the next  
3085 chapter.

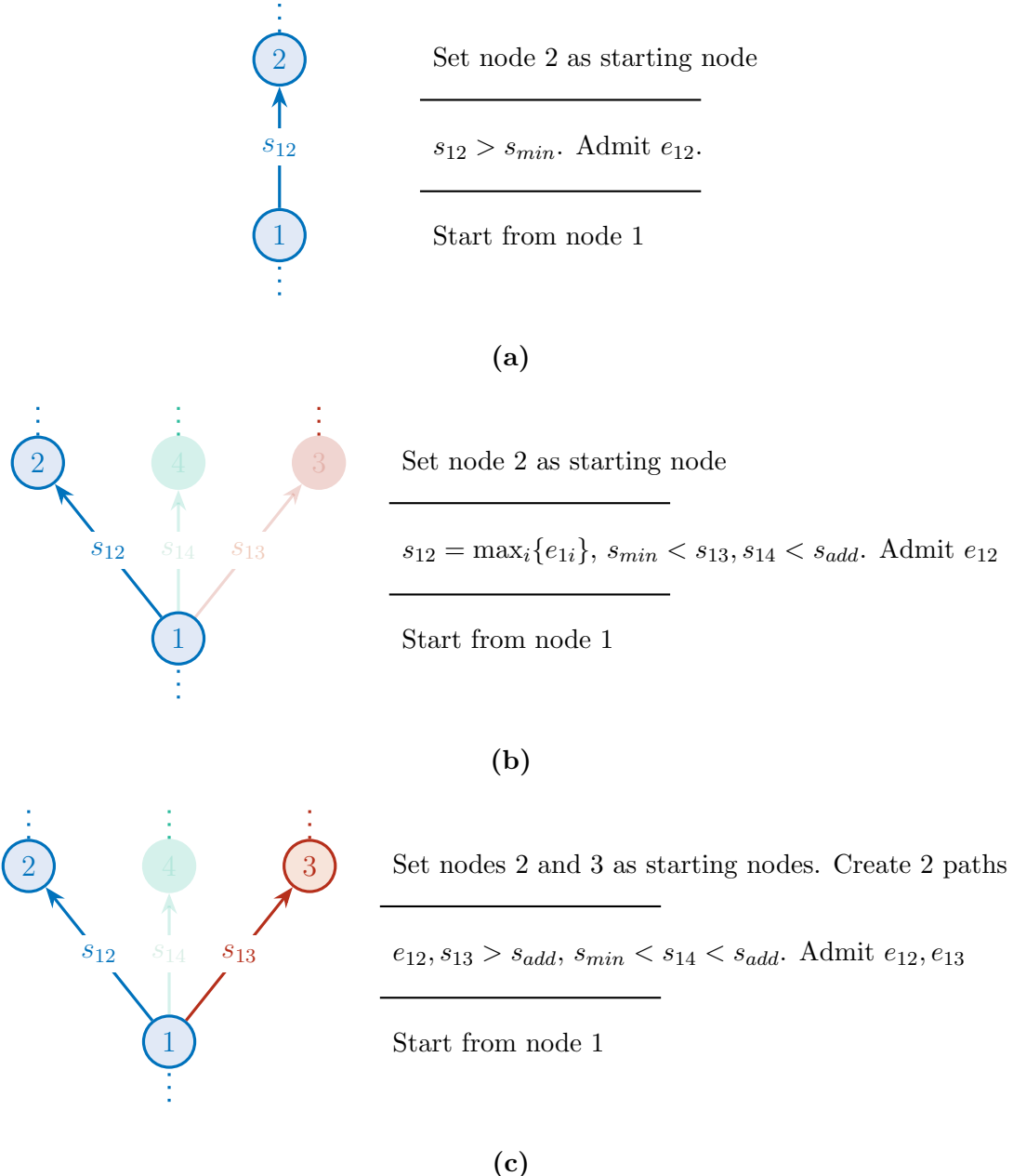


**Figure 10.3:** Different scenarios encountered by the Walkthrough algorithm. (a) A starting node as a single outgoing edge. (b) The starting node has several outgoing edges  $\{e_{12}, e_{13}, e_{14}\}$ . Edge  $e_{12}$  has the highest score, and neither lower-score edges exceed the minimum score  $s_{add}$  to create an alternative path. Only edge  $e_{12}$  is admitted. (c) The starting node has several outgoing edges  $\{e_{12}, e_{13}, e_{14}\}$ , in which  $e_{12}$  and  $e_{13}$  exceed  $s_{add}$ . Two candidate paths stemming from the junction are considered, the longer of which is admitted.

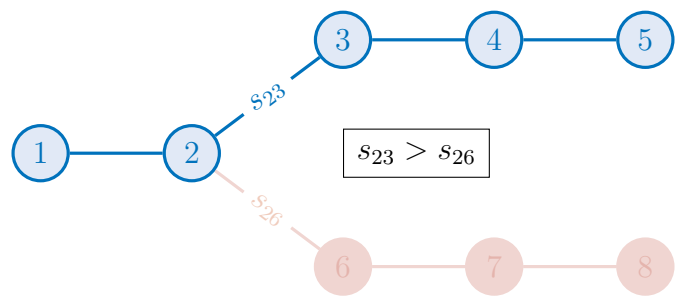


**Figure 10.4:** An ambiguity occurs when two candidate paths have equal lengths. The path stemming from the higher edge score at the junction is selected.

3086 **Chapter 11**

3087 **Track reconstruction performance**

3088 Track reconstruction identifies a track candidate as the digital realization of a particle  
3089 trajectory. In the GNN-based chain, after graph segmentation, a track candidate is a list of 3-  
3090 dimensional estimates of the intersections between a trajectory and different detector layers.  
3091 The analysis of tracking performance starts with the extraction of track parameters by a  
3092  $\chi^2$ -fit over on the measurements contained in the candidate. These parameters characterize  
3093 the impact parameters and the momentum of the particle, which are crucial information for  
3094 downstream tasks in event reconstruction. We have described the principles of track fitting  
3095 in section 7.2. The parameter extraction in this chapter closely follows this description, with  
3096 a small number of adaptations described in section 11.1.

3097 To evaluate the tracking efficiency, fake rate, and parameter resolution, fitted tracks  
3098 are matched to generator-level truth particles, which must satisfy a number of criteria on  
3099 reconstructibility and kinematics. Section 11.2 describes the matching procedure and the  
3100 metrics under which the performance is assessed.

3101 Finally, section 11.3 is an apple-to-apple comparison between GNN4ITk and CKF track-  
3102 ing performance.

### 3103 11.1 Extraction of track parameters

3104 As mentioned in section 7.2, the tracking model used in ATLAS considers the local  
 3105 coordinates of individual clusters as measurements. A GNN track candidate, however, is a  
 3106 list of space points reconstructed from these clusters, according to section 7.1. To carry out  
 3107 the fit, the space points are first matched to their corresponding clusters. A pixel space point  
 3108 is matched to a unique pixel cluster, while a strip space point is matched to two strip clusters,  
 3109 each from one side of a barrel stave or an endcap petal (see section 6.1). The building block  
 3110 of track candidates is a major difference between the GNN-based and the current tracking  
 3111 algorithm, which has implications in the interpretation of results.

3112 To fully characterize a charged particle’s trajectory in a magnetic field, the parametriza-  
 3113 tion must specify its global position, momentum and charge at any given point. Various  
 3114 conventions satisfy this requirement. In the offline analysis framework of ATLAS, the fol-  
 3115 lowing track parametrization convention is chosen as part of the Event Data Model (EDM)  
 3116 [159]

$$\mathbf{x} = (l^{(1)}, l^{(2)}, \phi, \theta, q/p)^T \quad (11.1)$$

3117 where  $(l^{(1)}, l^{(2)})$  denote the coordinates of the intersection between the measuring surface  
 3118 and the trajectory in the local frame of reference,  $\phi \in [-\pi, \pi]$  and  $\theta \in [0, \pi]$  respectively the  
 3119 azimuthal angle and the polar angle in the global frame of the current location, and  $q/p$  the  
 3120 inverse momentum signed by the particle charge. The track parameters vary continuously  
 3121 along the trajectory, and the measurements are “snapshots” taken at the active layers that it  
 3122 traverses. The local coordinates  $(l^{(1)}, l^{(2)})$  take different meaning depending on the measur-  
 3123 ing surface. For example, on a disk, they are the polar coordinates  $(l^{(1)}, l^{(2)}) = (R_{loc}, \phi_{loc})$  of  
 3124 the cluster, while on a plane, they are given in Cartesian coordinates  $(l^{(1)}, l^{(2)}) = (X_{loc}, Y_{loc})$ .  
 3125 The perigee parametrization, shown in figure 11.1, is an imaginary cylindrical surface par-  
 3126 allel to the global  $z$ -axis and passing through the point of closest approach to the origin<sup>I</sup>.

---

<sup>I</sup>This point is defined as the perigee, hence the designation.

3127 The local parameters  $(l^{(1)}, l^{(2)}) = (d_0, z_0)$  are respectively the transverse and longitudinal  
3128 impact parameters, which, along with other global parameters estimated at this position,  
3129 are reported as *the* track parameters of the corresponding hypothetical particle. The perigee  
3130 parameters are the quantity denoted by  $\mathbf{x}_0$  in the discussion in 7.2.

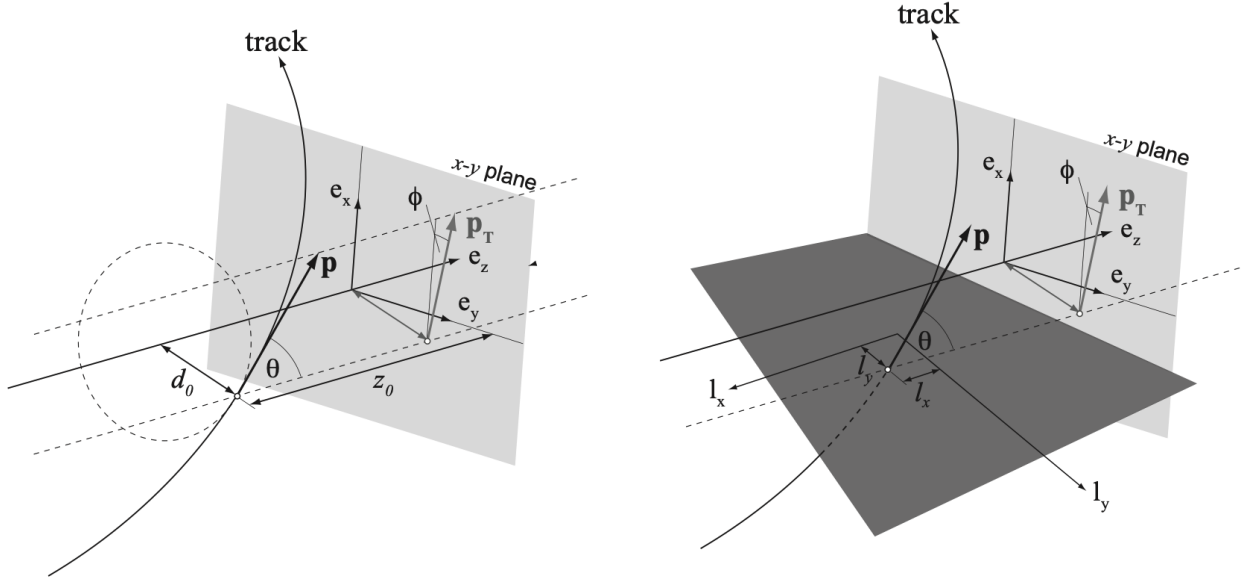


**Figure 11.1:** A track represented in two different parametrizations, both being particular instances of the general ATLAS parametrization in equation (11.1). The perigee parametrization (left) is defined with respect to the global  $z$ -axis, while the planar parametrization (right) is defined with respect to the coordinate axes of a local measuring surface [160].

3131 Thanks to this parametrization, the measurement model is a simple identity projection  
3132 of the first two track parameter parameters. The  $i$ -th measurement on track is given by

$$\mathbf{m}_i = \mathbf{H}_i \mathbf{x}_i = \begin{bmatrix} 1 & 0 & 0 & 0 & 0 \\ 0 & 1 & 0 & 0 & 0 \end{bmatrix} \begin{bmatrix} l^{(1)} \\ l^{(2)} \\ \phi \\ \theta \\ q/p \end{bmatrix} = \begin{bmatrix} l^{(1)} \\ l^{(2)} \\ \phi \\ \theta \\ q/p \end{bmatrix}. \quad (11.2)$$

3133 The measurement uncertainty is codified in the covariance matrix

$$[\mathbf{V}_i]_{jk} = \begin{cases} \sigma^2(l_i^{(j)}), & i = j \\ \rho(l_i^{(j)}, l_i^{(k)}), & j \neq k \end{cases} \quad (11.3)$$

3134 which is a block of the covariance matrix of the track parameters

$$[\mathbf{C}_i]_{jk} = \begin{cases} \sigma^2(\mathbf{x}_i^{(j)}), & j = k \\ \rho(\mathbf{x}_i^{(j)}, \mathbf{x}_i^{(k)}), & j \neq k \end{cases} \quad (11.4)$$

3135 where  $\mathbf{x}^{(i)}$  is the  $i$ -th component of the track parameters,  $\sigma^2(X)$  the variance of  $X$  and

3136  $\rho(X, Y)$  the covariance of  $X$  and  $Y$ .

3137 Given the track state  $\mathbf{x}$  and a covariance  $\mathbf{C}$  at any point on the trajectory, an estimate  
3138 of the state at another point  $\mathbf{x}'$  can be obtained by numerically integrating the EOM, as  
3139 described in section 11.1. If the position of  $\mathbf{x}'$  coincides with a sensitive element, an expected  
3140 value of the corresponding measurement could be derived using equation (11.2), allowing to  
3141 write the measurement error as a function of  $\mathbf{x}$ . Repeating this process, taking  $\mathbf{x}$  as the  
3142 initial value, we can define the measurement error of the entire track candidate and optimize  
3143 for  $\mathbf{x}$ .

3144 Let  $M = \{\mathbf{m}_1, \dots, \mathbf{m}_N\}$  be the set of all clusters matched to the track candidate. The  
3145 cost function can be written as a function of an initial state  $\mathbf{x}$  as

$$\mathcal{L}_M(\mathbf{x}, \vartheta) = \frac{1}{2} \sum_{i=1}^N [\mathbf{m}_i - \mathbf{H}_i f_i(\mathbf{x}, \vartheta)]^T \mathbf{V}_i^{-1} [\mathbf{m}_i - \mathbf{H}_i f_i(\mathbf{x}, \vartheta)] + \frac{1}{2} \sum_{j=1}^J \frac{\vartheta_j^2}{\sigma^2(\vartheta_j)}, \quad (11.5)$$

3146 in which, as discussed in section 7.2, the set of angles  $\{\vartheta_j\}$  is included to model small-  
3147 angle multiple scatterings due to interaction with the detector material. These angles are  
3148 assumed to be normally distributed with mean  $\langle \vartheta_j \rangle = 0$  and variance estimated by the  
3149 Highland formula (6.14). It is important to note that these scattering angles are floated as  
3150 fit parameters, but they are constrained by the variances  $\sigma^2(\vartheta_j)$  which are functions of the  
3151 trajectory and therefore the initial state  $\mathbf{x}$ .

3152 Since the cost function is no longer linear, an analytical solution to the equation

$$\nabla \mathcal{L}_M(\mathbf{x}, \vartheta) = 0 \quad (11.6)$$

3153 does not exist. Instead, it must be numerically minimized, starting from some initial value  
3154  $\tilde{\mathbf{x}}$ . To estimate  $\tilde{\mathbf{x}}$ , a circle fit using the conformal map method is performed over the  $(x, y)$   
3155 coordinates the first three space points of the track candidate. This procedure is described  
3156 in reference [161]. The crude estimate is fed into the optimizer, along with the cost function  
3157 to obtain a globally optimal estimate  $\hat{\mathbf{x}}$  of the track parameters.

$$\hat{\mathbf{x}} = \min_{\mathbf{x}} \mathcal{L}_M(\mathbf{x}, \vartheta) \quad (11.7)$$

## 3158 11.2 Track matching and performance metrics

3159 In simple terms, tracking performance is evaluated by answering the following questions

- 3160 1. **Efficiency:** How many *relevant* truth particles are reconstructed?
- 3161 2. **Fake rate:** How many tracks are created but represent no truth particles?
- 3162 3. **Track quality:** How well does a reconstructed track represent the corresponding truth  
3163 particle?

3164 Since all three items compare tracks to particles, it is necessary to match the reconstructed  
3165 track candidates and truth-level particles. It is for this reason that the evaluation can only  
3166 be done with Monte-Carlo simulation where truth information is available.

3167 **Definition 11.1** The tracking efficiency ( $\epsilon_{track}$ ) is the fraction of prompt particles associated  
3168 with track candidates passing some quality selection.

$$\epsilon_{track} = \frac{N_{reco}}{N_{truth}}, \quad (11.8)$$

3169 in which  $N_{truth}$  is the number of particle passing a set of reconstructibility criteria, and  $N_{reco}$   
3170 the number of those matched to a “good” track candidate.

3171 It is important to distinguish the tracking efficiency the edge efficiency defined in equation  
3172 (8.2). The former is defined on the set of truth particles, while the latter the set of edges  
3173 between space points reconstructed from truth particles. While the edge efficiency is useful in  
3174 machine learning development, only the tracking efficiency is meaningful in the performance  
3175 presented in this chapter, and, to a larger extent, in the ATLAS event reconstruction chain.

3176 A matched track candidate is required to have a high matching probability with the  
3177 particle in question, defined as follows.

3178 **Definition 11.2** Matching probability  $P_m(A, B)$ : Let  $A$  denote both a track candidate and  
3179 the set of clusters it contains, and  $B$  those of a particle. The matching probability between  
3180 track  $A$  and particle  $B$  is the weighted fraction of clusters contained in  $A$  that are in common  
3181 with  $B$ .

$$P_m(A, B) = \frac{2|(A \cap B)_{pix}| + |(A \cap B)_{strip}|}{2|A_{pix}| + |A_{strip}|}, \quad (11.9)$$

3182 where  $S_{pix}$  and  $S_{strip}$  respectively denote the subsets of pixel and strip clusters of set  $S$ .

Intuitively, a track candidate has a high probability of matching to a particle if the majority of its hits originate from that particle. The factor of 2 gives a doublet the weight to a pixel cluster, because it provides a 2D measurement of the track, whereas a strip cluster provides only 1<sup>II</sup>. A track  $A$  is said to be matched to a particle  $B$  if its matching probability

$$P_m(A, B) > 0.5.$$

3183 Tracks candidates that are not matched to any particle are said to be fake. The fake rate is  
3184 thus defined as follows.

---

<sup>II</sup>Remember that it takes 2 measurements (2 clusters) from a double-sided strip layer to form a 3D space point.

3185 **Definition 11.3** The fake rate  $F_{track}$  is the fraction of reconstructed track candidates having  
3186 the highest matching probability not exceeding 0.5

$$F_{track} = \frac{1}{N_{track}} \sum_{i=1}^{N_{track}} \mathbb{I}_{[\max_j P_m(A_i, B_j) \leq 0.5]} = \frac{N_{fake}}{N_{track}}, \quad (11.10)$$

3187 where  $\mathbb{I}$  is the indicator function.

3188 Definitions 11.1 and 11.3 thus answer questions (1) and (2).

3189 The track quality is a comparison between the properties of truth particles, including  
3190 momentum, cluster composition, and impact parameters, to those of the matched track  
3191 candidate. The track properties are estimated by the track fit described in 11.1. Most  
3192 important among them are the track parameter resolution, defined as

$$\sigma(\mathbf{x}^{(i)}) = \left| \mathbf{x}_{reco}^{(i)} - \mathbf{x}_{truth}^{(i)} \right|. \quad (11.11)$$

### 3193 11.3 Results

3194 The tracking performance of the GNN-based algorithm is presented in this section. Track  
3195 candidates constructed from 1000  $t\bar{t}$  events at  $\langle \mu \rangle = 200$  using the GNN4ITk algorithm are  
3196 processed in ATHENA<sup>III</sup>. These are the same events used to evaluate the individual stages of  
3197 the GNN-based pipeline presented in chapters 8 and 9. We implemented a new component,  
3198 denoted `InDetGNNTracking`, in ATHENA to interface between the GNN-based track builder  
3199 and the current event reconstruction chain [144]. The same events are fed to the Kalman  
3200 Filter under the configuration outlined in ref. [107]. Tracking performance is evaluated using  
3201 the standard `InDetPhysValMonitoring` tool in the software framework.

3202 As mentioned in definition 11.1, track candidates must pass a set of quality selections to  
3203 be considered for truth-particle matching. In production, the same selections are applied to

---

IIIThe ATLAS offline analysis framework

reconstructed tracks before submitting them to downstream reconstruction stages. Reference [107] studies the expected tracking performance of the ITk at  $\langle \mu \rangle = 200$  under the CKF, for which a set of such selection criteria is optimized. These  $\eta$ -dependent criteria, shown in table 11.1, are hereafter referred to as the **nominal cuts**. Among these requirements, a hole

Requirements	Pseudorapidity interval		
	$ \eta  \leq 2.0$	$2.0 <  \eta  \leq 2.6$	$2.6 <  \eta  < 4.0$
Number of clusters	$\geq 9$	$\geq 8$	$\geq 7$
Number of holes	$\leq 2$	$\leq 2$	$\leq 2$
Number of pixel clusters	$\geq 1$	$\geq 1$	$\geq 1$
$p_T$ [MeV]	$> 900$	$> 400$	$> 400$
$ d_0 $ [mm]	$< 2.0$	$< 2.0$	$< 10.0$
$ z_0 $ [cm]	$< 20.0$	$< 20.0$	$< 20.0$

**Table 11.1:** Nominal track selection criteria featured in reference [107].

is defined as the absence of a cluster between the first and the last hit on track, when the interpolated trajectory intersects a layer of active sensors.  $p_T$ ,  $d_0$  and  $z_0$  are respectively the transverse momentum, the transverse and longitudinal impact parameters, as described in section 11.1. The dependence on  $\eta$  accounts for the difference in detector layout and material distribution, and helps maintain uniform reconstruction efficiency throughout the detector.

It is important to note that the CKF and the GNN-based algorithm are two different techniques running on different event-level inputs, the former directly consuming the recorded clusters while the latter using space points formed from these clusters, adding an extra layer of abstraction. As mentioned in section 7.1, there exists by construction cluster inefficiency amongst the reconstructed space points. In other words, assuming a particle generates at least one lone cluster in the strip detector, even a track perfectly reconstructed<sup>IV</sup> from space points cannot recuperate the lone clusters. This issue also leads to an increase in the average

---

<sup>IV</sup>that is, containing all of the particle's space points and no space points from other particles

3220 number of holes on track, because every lone cluster that is not the outermost cluster of the  
 3221 particle contributes an additional hole, on top of those caused by detector or algorithmic  
 3222 inefficiency. Consequently, the first two criteria in table 11.1 on the number of clusters and  
 3223 holes would likely penalize an algorithm based on space point because of information lost in  
 3224 its input rather than its inherent inefficiency. We thus examine a second set of selections,  
 denoted **relaxed cuts** and shown in table 11.2. In particular, compare to the nominal

Requirements	Pseudorapidity interval		
	$ \eta  \leq 2.0$	$2.0 <  \eta  \leq 2.6$	$2.6 <  \eta  < 4.0$
<b>Number of clusters</b>	$\geq 7$	$\geq 7$	$\geq 7$
<b>Number of holes</b>	$\leq 4$	$\leq 4$	$\leq 4$
Number of pixel clusters	$\geq 1$	$\geq 1$	$\geq 1$
$p_T$ [MeV]	$> 900$	$> 400$	$> 400$
$ d_0 $ [mm]	$< 2.0$	$< 2.0$	$< 10.0$
$ z_0 $ [cm]	$< 20.0$	$< 20.0$	$< 20.0$

**Table 11.2:** Relaxed selections adapted to GNN-based tracks. Modified criteria with respect to those in table 11.1 are highlighted in boldface. The rest is identical to reference [107].

3225  
 3226 cuts, the minimum number of clusters is decreased to 7 and the maximum number of holes  
 3227 increased to 4 for pseudo rapidity range  $-2.6 \leq \eta \leq 2.6$ . All particle traversing this region  
 3228 intersect the strip detector and may produce lone clusters, as shown in figure 7.4. The  
 3229 selections on tracks having  $|\eta| > 2.6$  are identical to those in table 11.1, since this region  
 3230 features exclusively pixel sensors.

3231    **11.3.1 Reconstruction performance of the GNN-based algorithm**  
 3232    **under nominal and relaxed track selections**

3233    In this section, we compare the tracking performance of the GNN-based algorithm under  
 3234    the **nominal** and the **relaxed** selections. This discussion will shed light on the effect of  
 3235    cluster inefficiency and justify the relaxation in selection cuts.

3236    Shown in figure 11.2a is the tracking efficiency of the GNN4ITk chain in the **Module**  
 3237    **Map MeanRMS** variant. Other graph construction techniques slightly differ in numerical  
 3238    value but maintain the same trend. The efficiency under the relaxed selections selections  
 3239    is significantly higher than that under the nominal selections. It follows that the algorithm  
 3240    produces a number of track candidates which are matchable to a target truth particle but  
 3241    contain an insufficient number of cluster or an excess number of holes to pass the nominal  
 3242    selections. The relaxed selections allow these candidates to enter truth matching, so a larger  
 3243    proportion of particles are reconstructed, yielding better efficiency.

3244    The difference is clearly visible in the particle pseudorapidity range  $|\eta| < 2.6$ , whereas  
 3245    no difference in the range  $|\eta| > 2.6$  is observed. A strong correlation between the truth  
 3246    pseudorapidity, the number of lone clusters, and the efficiency gain with relaxed selection  
 3247    emerges when we consider together figures figure 7.4 and 11.2a. For  $|\eta| < 2.6$ , lone clusters  
 3248    appear in the particle's trajectory, reaching up to one lone cluster per track near  $|\eta| = 2.0$ .  
 3249    Correspondingly, the efficiency in this region benefits from allowing fewer hits and more  
 3250    holes in the track candidate. For  $|\eta| > 2.6$ , the particle stays entirely in the pixel detector,  
 3251    thus generating no lone cluster. No efficiency gain from relaxed selections is observed in  
 3252    this region, implying that without lone clusters, the reconstructed track candidate contains  
 3253    fewer missing hits than it would otherwise. Almost all pixel-only candidates passing other  
 3254    selection cuts have at most 2 holes, so they gain nothing from further increase in maximum  
 3255    hole count. The logical conclusion of these observation is that the excess holes and deficient

3256 clusters on tracks containing strip clusters are largely due to hit inefficiency in the put rather  
 3257 than algorithmic inefficiency of the GNN-based track maker.

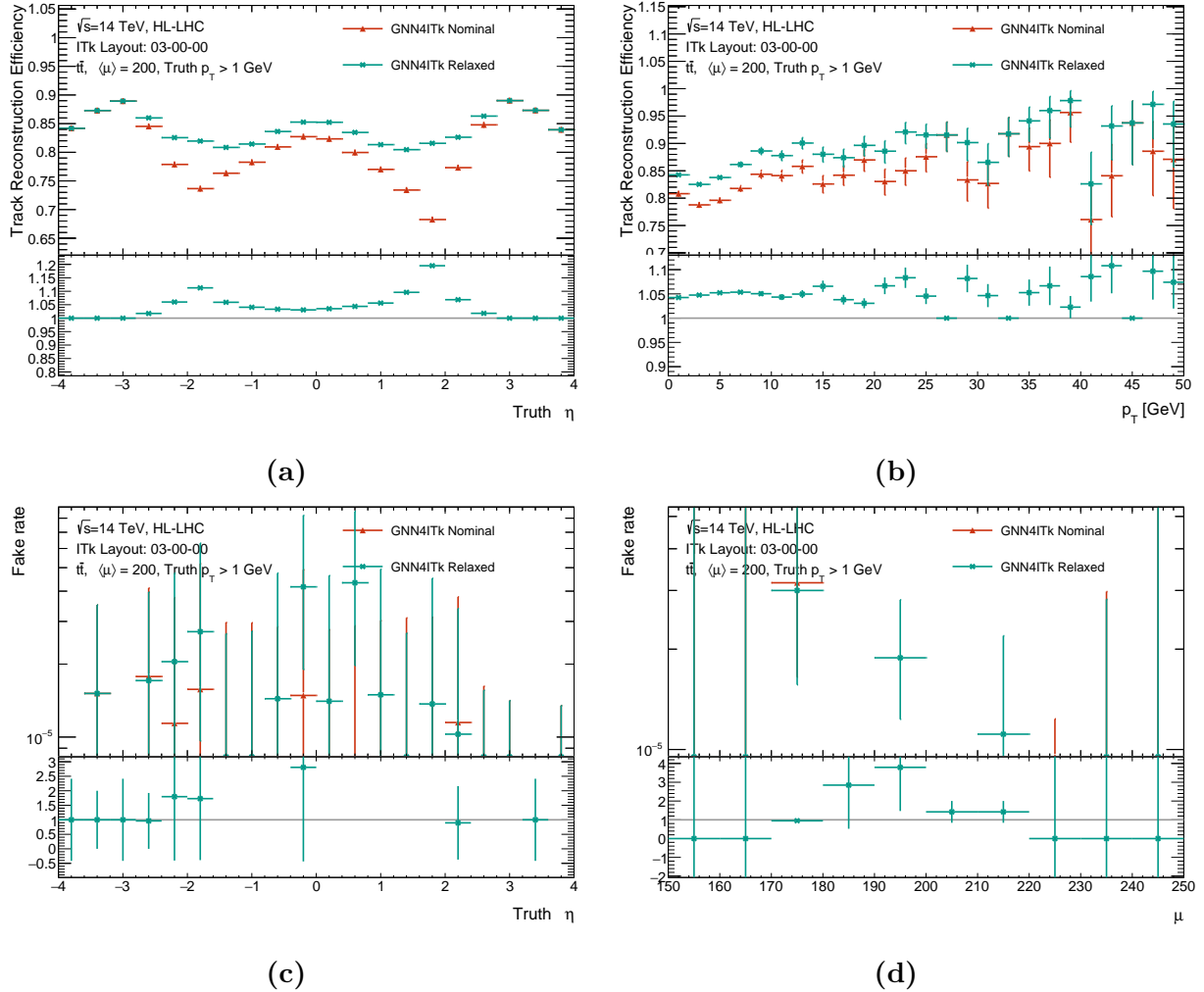


**Figure 11.2:** A comparison of the GNN-based track candidates selected by the nominal and the relaxed criteria in representative performance metrics. Top plots show the efficiency as functions of the truth pseudorapidity  $\eta$  (a) and transverse momentum  $p_T$  (b). Bottom plots show the rate of fake tracks as functions of  $\eta$  (c) and the pile-up level  $\mu$  (d).

3258 Efficiency and fake rate are typically in a trade-off relationship, such that to increase  
 3259 efficiency, one often admits more track candidates by loosening some selection criteria, poten-  
 3260 tially allowing those constructed from randomly associated hits. Fake tracks at best consume

extra computing resources and at worse introduce bias to event- and object-level parameters, such as the missing transverse momentum  $p_{T,miss}$  which is estimated as the compliment of the total visible transverse momentum. As parameter biases from the tracker accumulate throughout the reconstruction chain, it is particularly important to control the number of fake tracks. In fact, the nominal cuts in table 11.1 are optimized with a primary objective of limiting the fake rate [107].

Despite the increased efficiency, no explosion in the number fake tracks is observed with the relaxed cuts. Shown in figure 11.2c, the average fake rate under both the nominal and the relaxed selections is of  $\mathcal{O}(10^{-5})$ , i.e. every 10000 track candidates contain  $\mathcal{O}(1)$  fake track. Considering that the track builder produces about 2000 tracks per event, this fake rate implies that both sets of cuts can filter all fake candidates in the majority of events. Table 11.3 shows the total number of fake candidates among 1000 test  $t\bar{t}$ -events produced by the GNN- and CKF-based track builders under the two sets of selections. While the relaxed cuts increase the number of fake by a factor of 9 for the CKF, only a factor of 2 is observed for the GNN, in addition to its small absolute values. Therefore, for the CKF, requiring track candidates to satisfy the requirements in table 11.1 is *essential* to limit fake tracks and maintain good efficiency. On the other hand, for the GNN4ITk, a relaxation in the minimum number of hits and the maximum number of holes in the strip region ( $|\eta| < 2.6$ ) is necessary to cope with the input hit inefficiency, yet still guarantees low fake rate, thus achieving an optimal performance.

Track selection	GNN4ITk	CKF
Nominal	11	130
Relaxed	22	1205

**Table 11.3:** The total number of reconstructed tracks by the GNN4ITk and the CKF chains having matching probability less than 0.5 over 1000  $t\bar{t}$  events.

These factors when considered together justify the evaluation of GNN-based tracking performance at relaxed selections, and the CKF-based performance at the nominal selections. In light of this discussion, we propose to apply a minimally modified set of cuts, shown in table 11.4 to all tracks built by the GNN-based algorithm.

Requirements	Pseudorapidity interval		
	$ \eta  \leq 2.0$	$2.0 <  \eta  \leq 2.6$	$2.6 <  \eta  < 4.0$
Number of clusters	$\geq 7$	$\geq 7$	$\geq 7$
Number of holes	$\leq 4$	$\leq 4$	$\leq 2$
Number of pixel clusters	$\geq 1$	$\geq 1$	$\geq 1$
$p_T$ [MeV]	$> 900$	$> 400$	$> 400$
$ d_0 $ [mm]	$< 2.0$	$< 2.0$	$< 10.0$
$ z_0 $ [cm]	$< 20.0$	$< 20.0$	$< 20.0$

**Table 11.4:** Minimally modified selections adapted to GNN-based tracks. Modified criteria with respect to those in table 11.1 are highlighted in boldface. The rest is identical to reference [107].

### 11.3.2 Reconstruction efficiency

In this section, we compare the reconstruction efficiency of the three variants of the GNN-based algorithm to that of the CKF. Track candidates produced by the former are required to pass the quality cuts in table 11.4, and those produced by the latter are required to pass the cuts in table 11.1. The tracking efficiency as functions of the truth  $\eta$  and  $p_T$  are respectively shown in figures 11.3a and 11.3b. The bottom plot in each figure shows the ratio between each of the GNN-based curves to the CKF-based curve.

The tracking efficiency varies as a function of truth pseudorapidity. All reconstruction algorithms reach the maximum efficiency at  $|\eta| = 0$  and  $\eta = 3.0$ , and minimum at  $|\eta| = 1.8$ , symmetric around  $\eta = 0$ . These variations are strongly correlated to the detector material encountered by the particle on its path, illustrated on figure 6.8c. The total radiation length

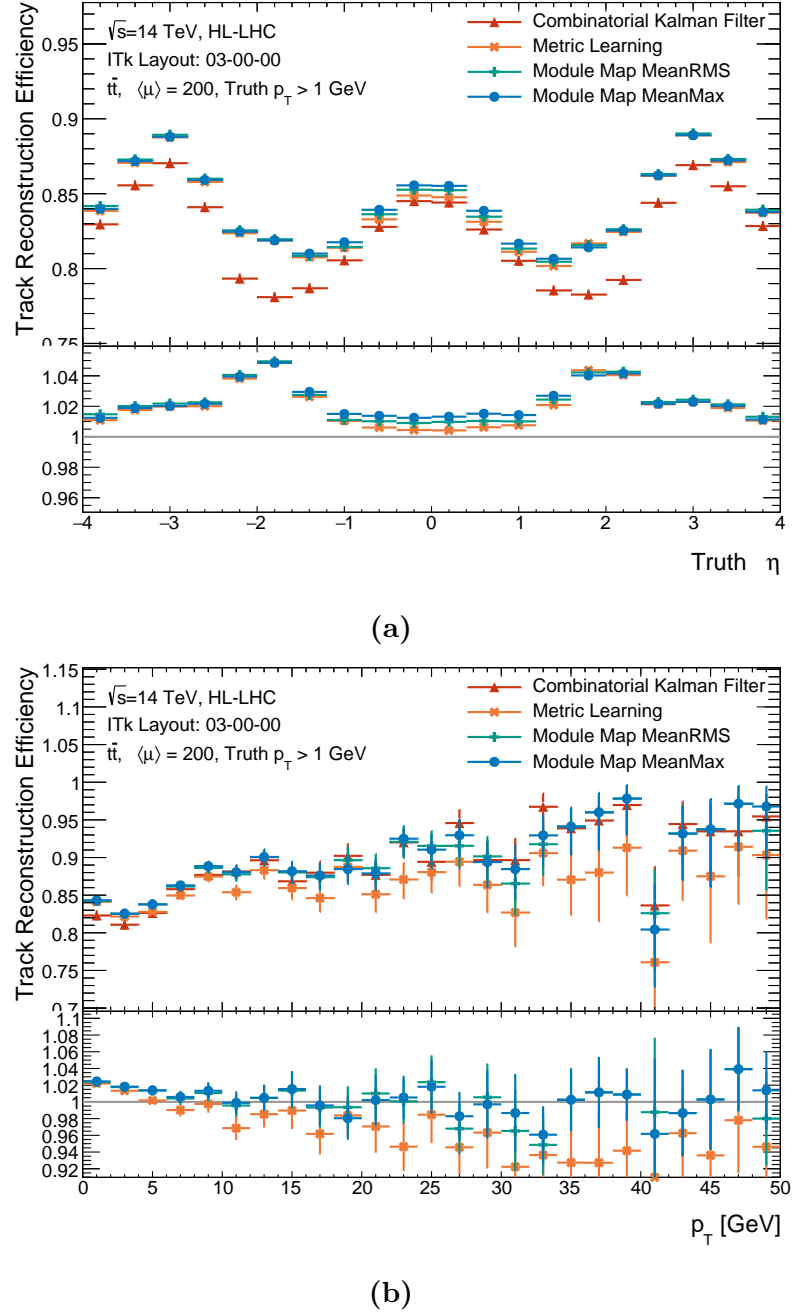


**Figure 11.3:** Tracking efficiency as functions of the truth pseudorapidity  $\eta$  (a) and transverse momentum  $p_T$  (b). The bottom plots show the ratio of the GNN-based curves to the CKF-based curve.

3296 traversed by a particle before reaching the minimum number of hits to be reconstructible is  
 3297 lowest at  $|\eta| = 0$  and  $|\eta| = 3.0$  and peaks at  $|\eta| = 1.5$ . Since material effects randomly direct  
 3298 the real trajectory away from an ideal helix, particles travelling through more material tend  
 3299 to have more hits deviating considerably from their expected position. For the CKF, this  
 3300 means that incorporating the correct hit could significantly increase the total  $\chi^2$ , leading to  
 3301 an early termination of the hit-finding sequence and subsequently the track candidate failing  
 3302 the selection cuts. On the other hand, trained on data which contain these “irregular”  
 3303 connections, the GNN is observed to tolerate large deviations, but the constructed track  
 3304 candidate could still be ruled out by the global  $\chi^2$  fit.

3305 Among the GNN-based trackers, the best efficiency is observed in the Module Map Min-  
 3306 Max variant, followed closely by the MeanRMS variant. All three variants yield similar  
 3307 efficiency at low transverse momentum ( $p_T < 5$  GeV), but start to diverge at high  $p_T$ . The  
 3308 Metric Learning variant is slightly less efficient than the Module Map variants for  $p_T > 5$   
 3309 GeV. On the pseudorapidity spectrum, it has lower efficiency in the strip barrel in the range  
 3310  $|\eta| < 1$ , but otherwise identical to the other GNN-based variants. These observations are  
 3311 explain by the fact that high- $p_T$  particles are more likely to have small pseudorapditiy and  
 3312 concentrate in the barrel region. Graph construction using the Metric Learning is less efficient  
 3313 than the Module Map at high  $p_T$ , as shown in figure 9.2a, and the inefficiency accumulates  
 3314 throughout the pipeline, leading to the observed degradation in tracking efficiency.

3315 All variants of the GNN4ITk algorithm produce tracking efficiency exceeding that of the  
 3316 CKF when plotted as a function of  $\eta$ , in which each bin is the conditional efficiency averaged  
 3317 over all particle momenta. On the  $p_T$  spectrum, however, it is clear that the improvement  
 3318 is not evenly distributed. All of the efficiency improvement occurs on particles with low  
 3319  $p_T$ , as seen on the ratio plot of figure 11.3b, the performance at high  $p_T$  is largely similar  
 3320 to that of the CKF. High- $p_T$  particles are rare, as they commonly originate from the hard-  
 3321 scattering collision, and concentrate around the barrel region. The absence of efficiency  
 3322 improvement at high  $p_T$  partially explains the comparatively smaller efficiency boost near

$\eta = 0$ . In contrast, low- $p_T$  particles constitute the majority of target particles, orders of magnitude more abundant than their high- $p_T$  counterparts, and are distributed quite evenly throughout the detector, which explains the excess efficiency in all  $\eta$  bins on figure 11.3a.

Though not simply related, tracking efficiency is determined by the edge-level efficiency encountered the results of previous chapters. The impact of the uneven  $p_T$  distribution in training data on edge-level performance was already seen in section 9.2.2. All models in the GNN4ITk are trained on data which predominantly features low- $p_T$  tracks. They learn to minimize the classification loss of true edges from these tracks, possibly at the expense of the other less abundant particles. As discussed in section 9.3.2, increasing the weight of high- $p_T$  edges in the loss function proves ineffective. For now, despite the degradation in the edge efficiency, the efficiency of the GNN-based tracker at high momentum matches that of the CKF in absolute terms. Increasing the per-edge performance of the pipeline at high  $p_T$  is a priority for future work.

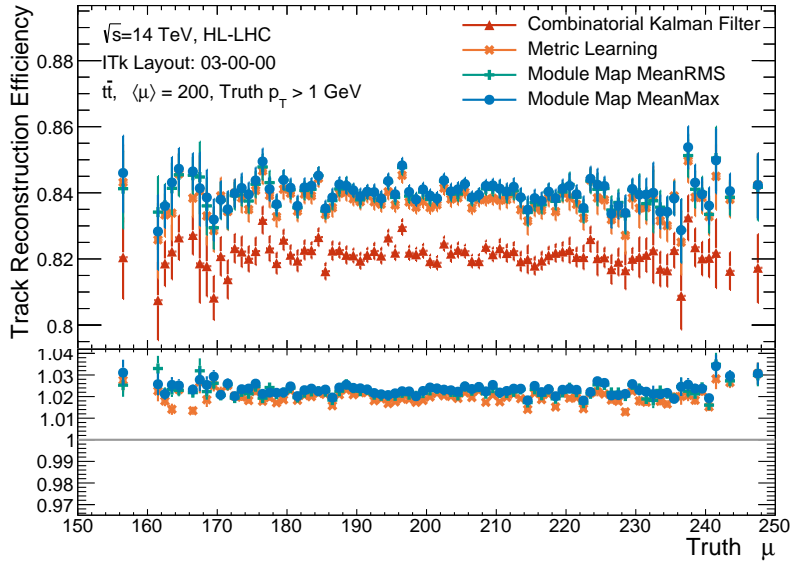


**Figure 11.4:** Tracking efficiency as a function of the pile-up level  $\langle \mu \rangle$ . The bottom plots show the ratio of the GNN-based curves to the CKF-based curve.

3336      Figure 11.4 shows the tracking efficiency as a function of truth pile-up level. The tracking  
3337      efficiency is found to be stable over a range of pile-up from  $\mu = 160$  to  $\mu = 240$ . The GNN-  
3338      based track builders are on average 84% efficiency, while the CKF is 82%. No degradation  
3339      is observed with increased pile-up.

3340      **11.3.3 Track fake rate**

3341      The proportion of track candidates without a matching truth particle as functions of  
3342      the truth pseudorapidity and pile-up is shown in figures 11.5a and 11.5b. While both the  
3343      GNN4ITk and the CKF have fake rate order  $\mathcal{O}(10^{-5})$ , the former produces fewer fake tracks  
3344      than the latter. As seen in table 11.3, the total number of fake tracks from the GNN is  
3345      approximately 1/6 of those from the CKF. Despite more truth particles are reconstructed  
3346      by the GNN than by the CKF, evidenced by the better efficiency, only track candidates  
3347      matched to these particles are created in excess. In other words, we achieve higher efficiency  
3348      without paying the cost of building more low-quality, unassociated tracks. It lends support  
3349      to the use of selection criteria that are adapted to a specific algorithm of interest, rather  
3350      than rigidly adopting a predetermined working point optimized for a different one.

3351      Given the small number of fake tracks, it is difficult to examine their spatial distribution  
3352      and variation with pile-up, the latter being of particular importance. This is due to the  
3353      small number of  $t\bar{t}$  events used in evaluation. Future work may address this problem with a  
3354      larger test sample.

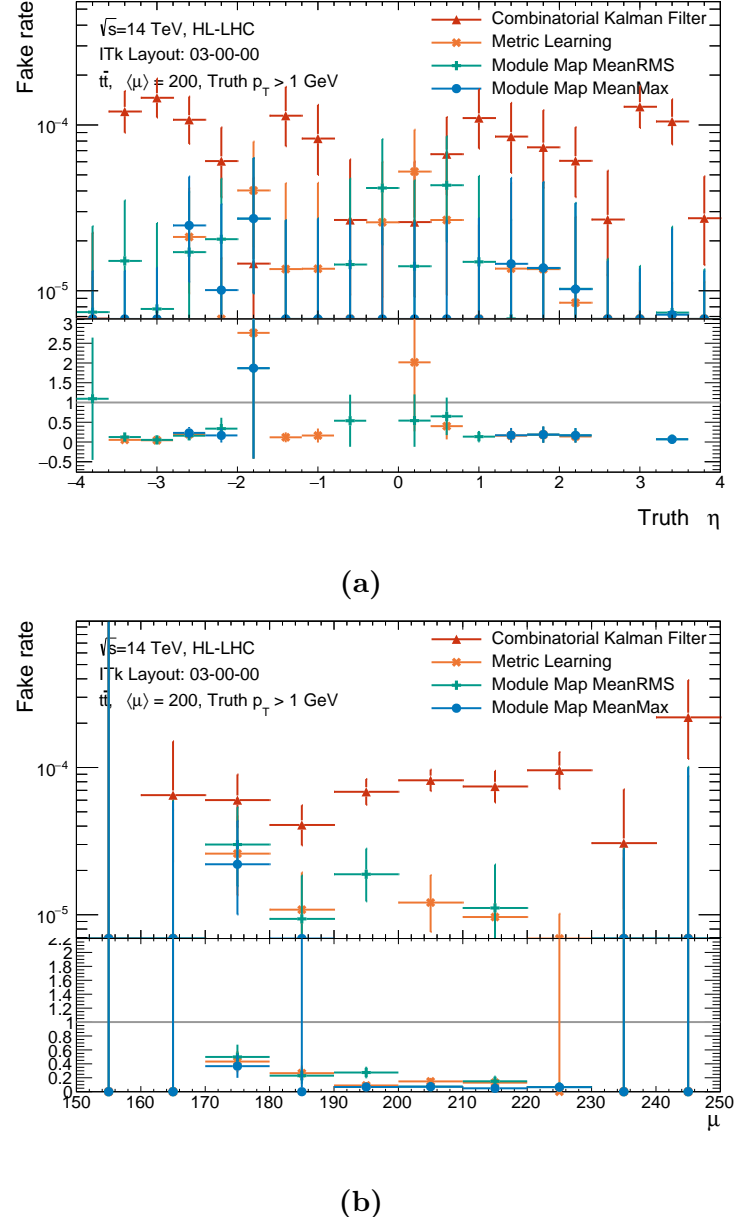


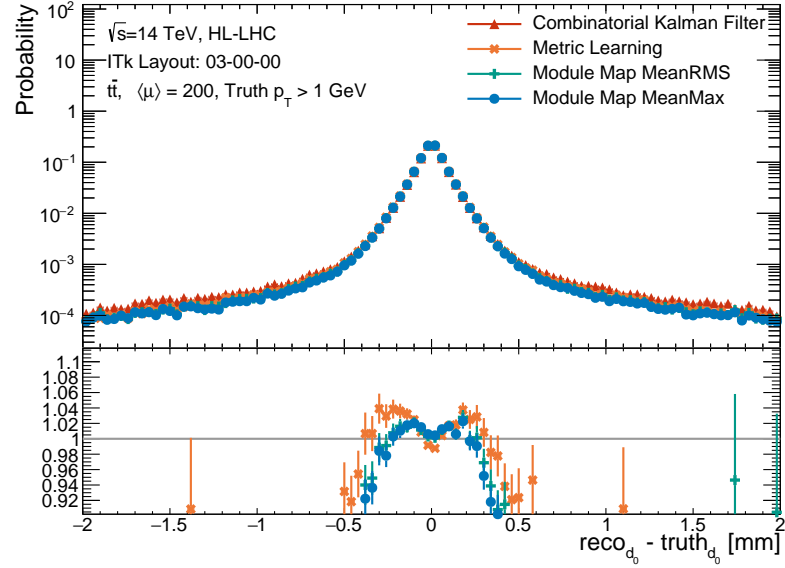
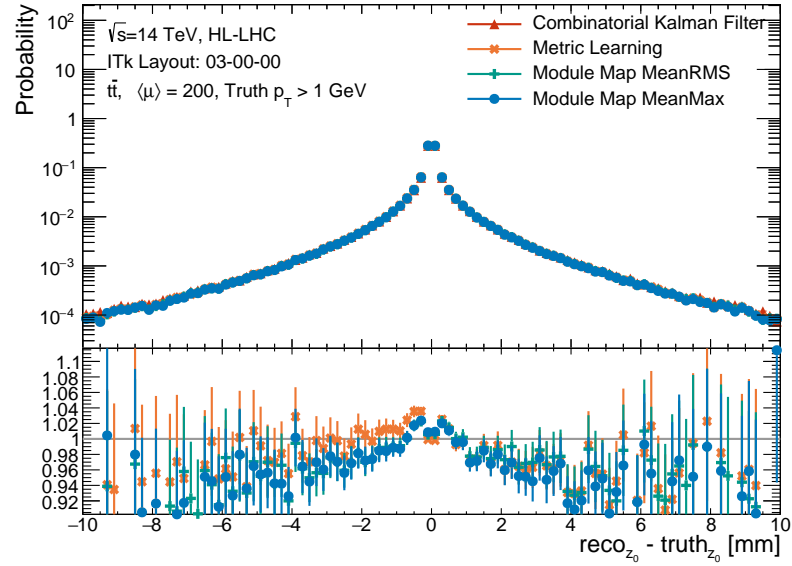
**Figure 11.5:** The proportion of reconstructed tracks reconstructed by the GNN4ITk and CKF chains having matching probability less than 0.5 as a function of the track pseudorapidity  $\eta$  (a) and the truth pile-up (b). The bottom plots show the ratio of the GNN-based curves to the CKF-based curve.

### 3355 11.3.4 Parameter resolution

3356     Track parameter resolution quantifies how well the reconstructed track candidate rep-  
 3357     resents the underlying truth particle, and is thus an important aspect of tracking. It is  
 3358     evaluated by comparing the parameters at the perigee surface extracted from the global  $\chi^2$   
 3359     fit discussed in section 11.1 and the corresponding truth value using equation 7.11. In MC  
 3360     simulation, the truth impact parameters are specified by the primary vertex position, and  
 3361     the truth kinematics the momentum at the vertex. The are generated along the particles  
 3362     and stored for tracking validation.

3363     The resolution of the longitudinal ( $z_0$ ) and transverse ( $d_0$ ) impact parameters of the  
 3364     track candidates produced by both the GNN- and CKF-based algorithms is shown in figure  
 3365     11.6. The vertical axis in these plots displays the number of matched track–particle pairs  
 3366     normalized to unity. All track builders show a spectrum peaking at  $\sigma(d_0) = 0$  and  $\sigma(z_0) = 0$ .  
 3367     In general, the GNN-based algorithms produce a larger proportion of tracks whose resolution  
 3368     concentrates around 0 for both impact parameters than does the CKF. Despite having higher  
 3369     efficiency, i.e. reconstructing more particles, the GNN-based track candidates are less tail-  
 3370     heavy. In other words, the excess tracks found by the GNN4ITk are overwhelmingly good-  
 3371     quality tracks accurately characterizing the impact parameters of the underlying particle.  
 3372     The distributions from the two Module Map variants appear similar, while that of the Metric  
 3373     Learning variant is slightly more tail-heavy.

3374     The good resolution observed for the GNN-based algorithm can be explained by the  
 3375     efficiency in finding the hit on the innermost pixel layer, which provides a strong constraint  
 3376     on the impact parameters. Figure 11.7 shows the number innermost pixel hits as a function  
 3377     of track pseudorapidity. The Module Map variants build tracks with the same average  
 3378     number of innermost pixel hits as does the CKF, with tracks in the barrel region having  
 3379      $\langle N_{pix,innermost} \rangle = 1$ . The Metric Learning variant is slightly less hit-efficient in the barrel,  
 3380     which would explain its lower resolution.

(a) Transverse impact parameter resolution  $\sigma(d_0)$ (b) Longitudinal impact parameter resolution  $\sigma(z_0)$ 

**Figure 11.6:** Transverse (a) and longitudinal (b) impact parameter resolution shown as histograms of  $\sigma(d_0)$  and  $\sigma(z_0)$  respectively. Note that the resolution of parameter  $x$  is inversely proportional to  $\sigma(x)$ .

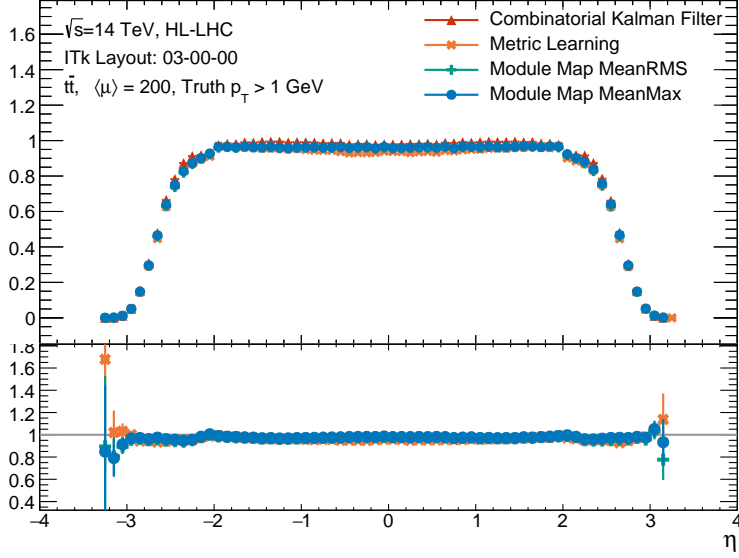


**Figure 11.7:** The number of hits from the inner most pixel layer as a function of reconstructed pseudorapidity  $\eta$ .

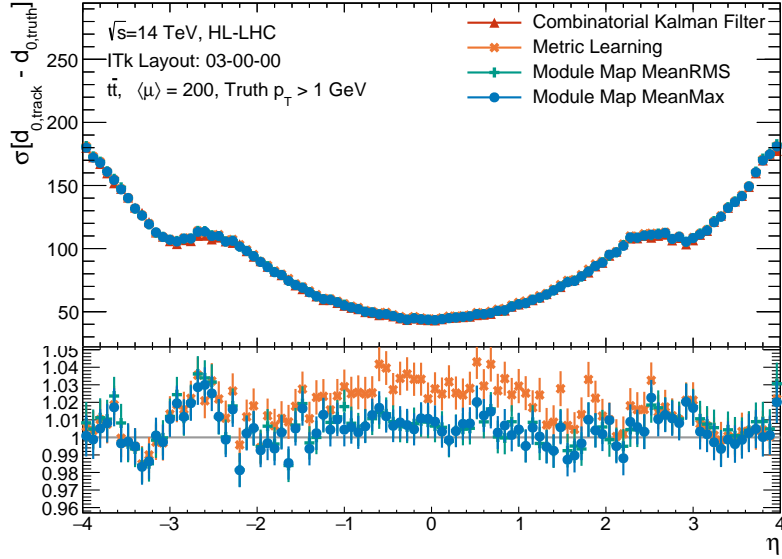


**Figure 11.8:** Transverse impact parameter resolution  $\sigma(d_0)$  of as a function of truth  $\eta$ , evaluated on tracks reconstructed by the GNN4ITk and the CKF chains. The bottom plots show the ratio of the GNN-based curves to the CKF-based curve.

Another measure of resolution is the RMS of the core of the distribution of the difference between the reconstructed and true values of the parameter. Figures 11.8 and 11.9 respectively show the RMS of the  $(d_{0,reco} - d_{0,truth})$  distribution and the the  $(z_{0,track} - z_{0,truth})$  distribution, measured in  $\mu\text{m}$ , as a function of  $\eta$ . Over the entire  $\eta$  range, the resolution of the Module Map variants is in good agreement with that of the CKF, while that of the Metric Learning is slightly degraded in the barrel region. Here we can clearly observe the correlation between the number of innermost pixel hits and the impact parameter resolution, as the degradation occurs where the former quantity is the most deficient among the the Metric Learning track candidates.

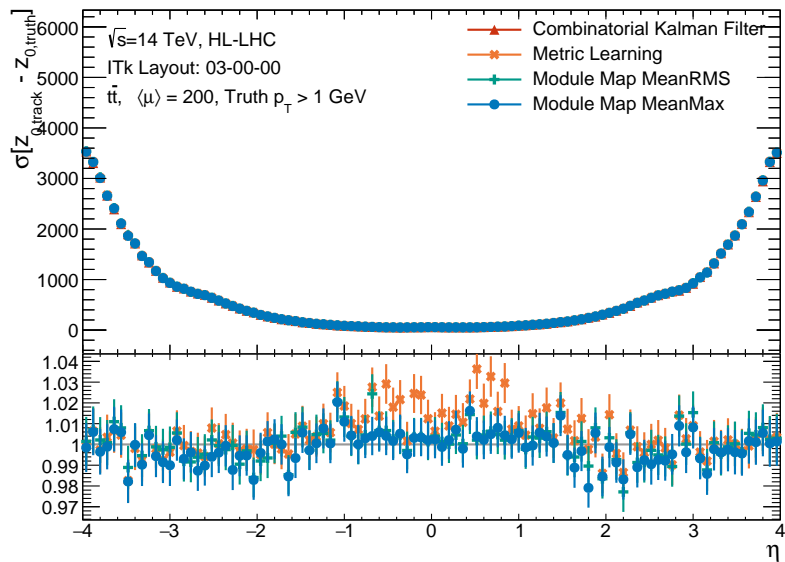


**Figure 11.9:** Longitudinal impact parameter resolution  $\sigma(z_0)$  of as a function of truth  $\eta$ , evaluated on tracks reconstructed by the GNN4ITk and the CKF chains. The bottom plots show the ratio of the GNN-based curves to the CKF-based curve.

The transverse momentum resolution as a histogram is shown in figure 11.10a and as a function of  $\eta$  in figure 11.10b. Unlike the other parameters' resolution, the dimensionless transverse momentum resolution is computed as

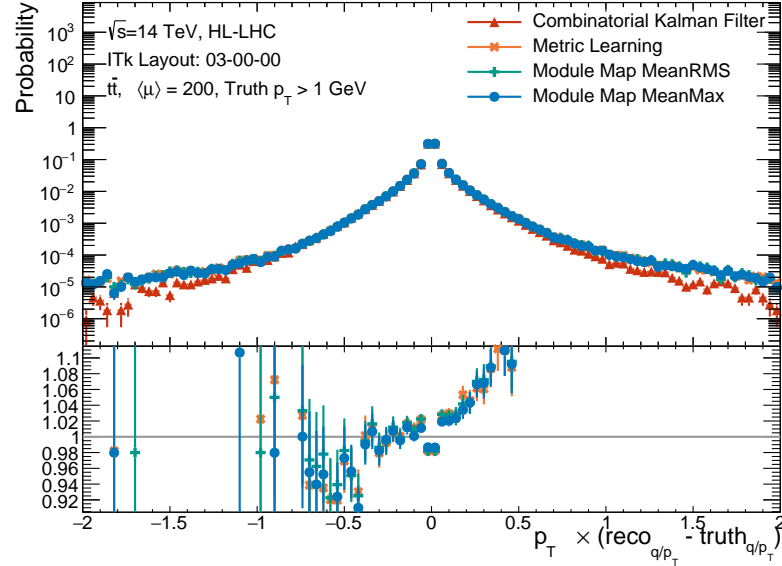
$$\sigma(p_T) = p_{T,truth} \times \left( \frac{q}{p_{T,reco}} - \frac{q}{p_{T,truth}} \right).$$

While other track parameters are directly obtained from the  $\chi^2$  fit, the transverse momentum is derived from the total momentum  $p$  and the azimuthal angle  $\theta$  in the ATLAS parametrization (equation (11.1)). There is no straightforward relationship between its resolution and elements of the global fit. However, given that it is derived from fit parameter  $q/p$ , whose uncertainty is driven by material interaction, one expects lower  $p_T$  resolution with more detector material encountered on the trajectory. This effect is observed on figure 11.10b, viewed in tandem with figure 6.8a, which shows the material budget traversed by a straight track in radiation length as a function of the particle's pseudorapidity. The total radiation length increases generally with  $\eta$ , so the closer to the beamline is the particle, the more its energy—and thus momentum—is eroded, weakening the constraints on  $p_T$ . In consequence, the  $p_T$  resolution decreases monotonically with  $\eta$ .

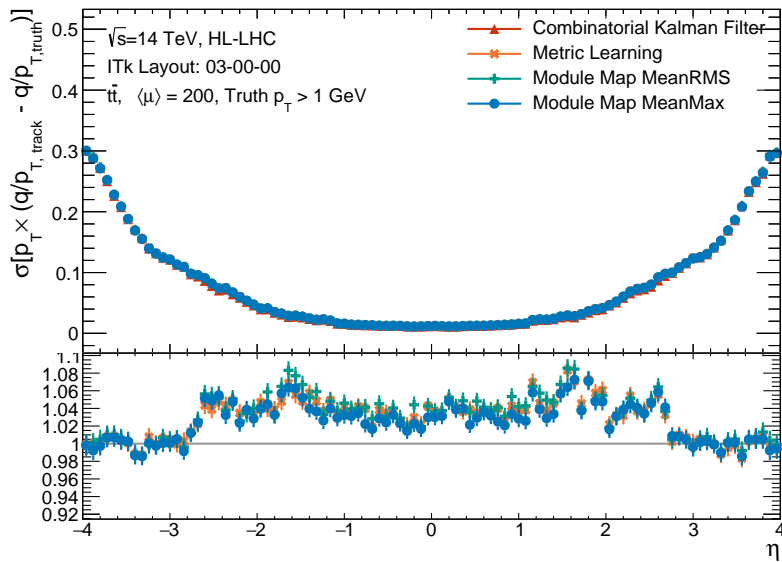
The transverse momentum is proportional to the radius of the curved trajectory, which in turn is geometrically constrained by the hits found between the outermost hits of the track candidate<sup>V</sup>. Therefore, the  $p_T$  resolution generally improves with the number of measurements and degrades with the number of holes of the track candidate. In light of this principle, the difference in  $p_T$  resolution between the GNN4ITk and the CKF may be elucidated. On figure 11.10b, the observed  $p_T$  resolution of the GNN4ITk is similar to that of the CKF in the all-pixel region, for  $|\eta| > 2.6$ . Both algorithms find relatively long tracks in this region, having on average 13–14 hits, shown in figure 11.11a. Track candidates from the GNN4ITk are slightly shorter than those from the CKF. However, these the former contains on average

---

<sup>V</sup>Intuitively, imagine fitting a circle passing through two outermost points. If no intermediate points exists, any of infinitely many possible circles is equally likely, hence null constraint. If an intermediate measurement exists with some measurement error, the closer a circle passes by the points, the more likely hit is. More intermediate measurements provide better constraining power, hence better resolution.



(a) Transverse momentum resolution  $p_T \times \left( \frac{q}{p_{T,reco}} - \frac{q}{p_{T,truth}} \right)$

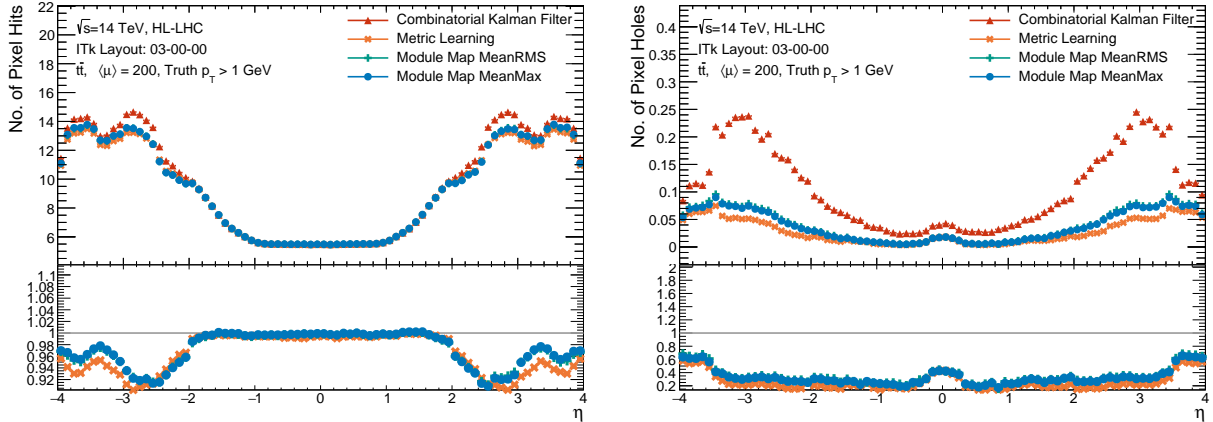


(b) Transverse momentum resolution  $p_T \times \left( \frac{q}{p_{T,reco}} - \frac{q}{p_{T,truth}} \right)$  as a function of  $\eta$

**Figure 11.10:** Transverse momentum resolution shown as a histogram of  $\sigma(p_T)$  (a) and a function of the truth pseudorapidity  $\eta$  (b).

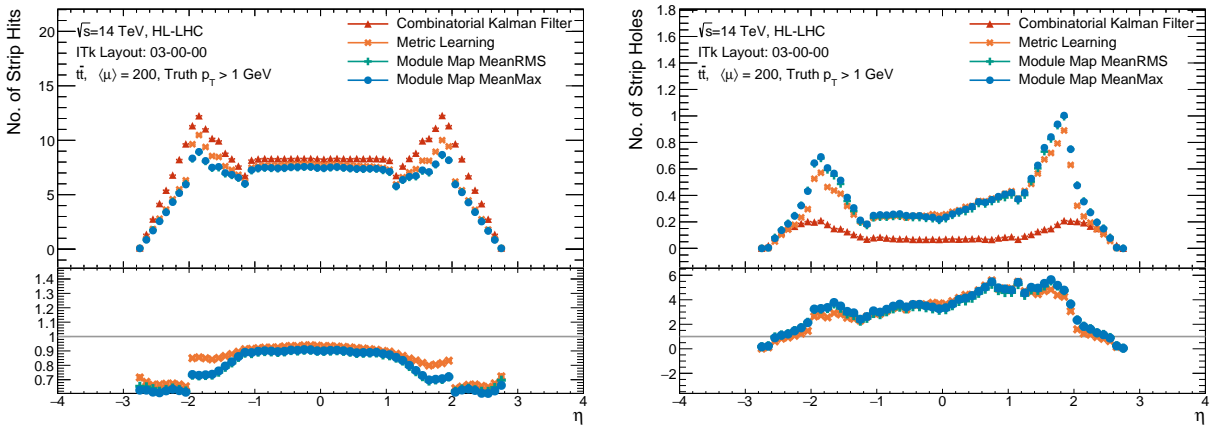
3410 fewer holes, as seen on figure 11.11b. In other words, pixel-only GNN-tracks are shorter,  
3411 but skip fewer layers than do the CKF counterparts. Though not simply quantifiable, these  
3412 factors have opposite impacts on the  $p_T$  resolution and likely yield similar performance in  
3413 this region in effect.

3414 On the other hand, in the barrel ( $|\eta| < 2$ ) and transition regions ( $2 < |\eta| < 2.6$ ), the  $p_T$   
3415 resolution of all GNN-based variants is lower than that of the CKF. The RMS width of the  
3416  $\sigma(p_T)$ -distribution from the GNN4ITk is at worst 8% larger than from CKF. In this region,  
3417 the GNN-based tracks contain fewer clusters and more holes than the CKF-based tracks. The  
3418 gap is particularly pronounced in the strip detector, due to the presence of single clusters. In  
3419 the barrel, despite the same average number of pixel clusters and negligible numbers of pixel  
3420 holes, the GNN4ITk finds about 90% the average number of strip hits found by the CKF,  
3421 and leaves up to 5 times the number of holes left by the latter. In the transition region,  
3422 this trend repeats. The combination of cluster deficiency and enrichment of holes explains  
3423 the degraded  $p_T$  resolution in this region. In general, the GNN, being trained on incomplete  
3424 data, performs worse than the CKF does in the strip detector. In addition, the relaxed track  
3425 selection cuts in  $|\eta| < 2.6$ -range allow short and layer-skipping GNN tracks to pass through,  
3426 contributing to their increased abundance. This is the trade-off we make in exchange for  
3427 better efficiency.



(a) Average number of pixel clusters on selected track candidates.

(b) Average number of pixel holes on selected track candidates.



(c) Average number of strip clusters on selected track candidates

(d) Average number of strip holes on selected track candidates

**Figure 11.11:** Hit content of selected track candidates, demonstrated by the average number pixel clusters (a), pixel holes (b), strip clusters (c) and strip holes (d). These quantities are shown as functions of the reconstructed pseudorapidity  $\eta$ .

3428 In accordance with our discussion on figure 11.10b, the  $\eta$ -independent GNN-based dis-  
 3429 tributions of  $\sigma(p_T)$  is manifestly wider than corresponding CKF-based distribution. The tail-  
 3430 heavy histograms verify that the GNN4ITk yields lower  $p_T$  resolution than does the CKF.  
 3431 Notably, the GNN-based distributions are not symmetric around  $\sigma(p_T) = 0$ , but instead

<sup>3432</sup> leaning more heavily toward positive values of  $\sigma(p_T)$ . Although occurring with low statistics,  
<sup>3433</sup> this asymmetry is apparent and merits further investigation. We hypothesize that the  
<sup>3434</sup> asymmetric distribution of strip holes observed in figure 11.11d could contribute to this  
<sup>3435</sup> phenomenon, but more careful inspection is needed.

## 3436 Chapter 12

### 3437 Computational performance

3438 In the previous chapter, we have shown that the GNN4ITk pipeline achieves tracking  
3439 performance competitive to that of the CKF chain. An equally important aspect of a track  
3440 reconstruction algorithm, as previously stated, is speed and resource consumption. After all,  
3441 the bottleneck caused by the current CPU-intensive track finder under HL-LHC conditions  
3442 is the primary motivation to develop a GPU-based alternative. In this regard, this thesis  
3443 documents the first attempt to evaluate and optimize the computing performance on full-  
3444 simulation data with realistic ITk geometry. In comparison, previous publications have either  
3445 focused entirely on the physics performance [162, 157], or evaluated computing performance  
3446 on an open dataset based on simplified geometry [141]. This chapter presents a number  
3447 of techniques to accelerate the edge classification inference, the key part of the GNN4ITk  
3448 algorithm. The most recent results on the pipeline latency is summarized and discussed with  
3449 respect to that of the CKF.

3450 It should be noted, however, that the computational performance of this technique un-  
3451 dergoes rapid developments, and thus this chapter aims to provide a snapshot of the progress  
3452 at the time of writing, rather than the finished product. A fully optimized algorithm will  
3453 likely be different from its present status. As such, we will identify several directions both  
3454 currently undertaken and for future studies.

3455 **12.1 An inference pipeline**

3456 As shown in figure 8.1 and explained in chapters 8, 9, and 10, the GNN4ITk is a multi-  
3457 stage algorithm, in which the output from one stage becomes the input to the next. It is  
3458 natural that these stages are developed and optimized independently. In production, the data  
3459 must flow seamlessly through all stages to avoid unnecessary overhead from intermediate I/O  
3460 and data transfer between CPU and GPU memories. [A figure here to illustrate this] The  
3461 data containing space point input is prepared by reading and preprocessing an event already  
3462 save on disk, then transferred to the GPU only once. It stays on the GPU, gets treated in  
3463 sequence by the models, yielding a collection of track candidates, each as an array of hit  
3464 indices. After the track building stage, the output transferred back to the CPU for track fit,  
3465 and the GPU memory liberated to process the next event.

3466 An inference pipeline in PYTHON, as a part of our R&D software framework, was de-  
3467 veloped to evaluate the latency at each stage of the algorithm and the overall inference  
3468 time.

3469 **12.2 Neural Network optimization techniques**

3470 Graph neural networks are the key engine for pattern recognition in the GNN4ITk  
3471 pipeline. They are also the easiest to accelerate, as many techniques are well established  
3472 and integrated into standard PYTHON libraries. We detail in this section two optimizations  
3473 which in combination significantly enhance the inference speed of the INTERACTIONGNN,  
3474 starting with Automated Mixed Precision, followed by Just-In-Time compilation.

### 3475 12.2.1 Automatic mixed precision (AMP)

3476 Reduced precision is a common technique in machine learning to enhance latency and  
3477 reduce memory footprint. A number represented by binary form is characterized by three  
3478 components, namely the sign, the exponent, and the mantissa, each of which is quantified  
3479 by a number of bits, depending on the data format. The sign, represented by a single bit,  
3480 is self-explanatory. The exponent determines the range of the number that a particular  
3481 format can represent, and the mantissa the precision with which a number is characterized.  
3482 The more bits are dedicated to the exponent, the wider is the range. Similarly, the more  
3483 bits reserved for the mantissa, the more decimal points a number can have. By default,  
3484 arithmetic operations employed in training neural networks are done in FP32, or single-  
3485 precision. In this format, a number is represented by 32 bits. The first bit is dedicated for  
3486 the sign, the next 8 bits for the exponent, and the remaining 23 bits for the digits that make  
3487 up the number. The 8 exponential bits can represent numbers from 0 to 256, thus enabling  
3488 a logarithmic<sup>1</sup> range of  $[-126, 127]$ , with some values reserved for special numbers such as  
3489 infinities, NaNs, etc. Roughly speaking, the 23 mantissa bits allow to express numbers with  
3490 lower threshold of  $2^{-23}$  in precision.

3491 However, during inference, such a wide range and high precision may not be necessary to  
3492 achieve good accuracy, since no gradient calculation, which is prone to numerical explosion  
3493 and vanishing, takes place. If the network output is stable under smaller bit widths, it is  
3494 possible to decrease memory footprint, improve computational efficiency, and reduce power  
3495 consumption by simply lowering the precision. We examine the latency and accuracy of  
3496 the INTERACTIONGN under FP16, or half-precision, in comparison to the baseline single-  
3497 precision. [Figure]

---

<sup>1</sup>base 2

### 3498 12.2.2 Just-In-Time (JIT) compilation

3499 Compilation is a mechanism to optimize the performance and deployability of deep learn-  
3500 ing models by transforming dynamic PYTHON code into an intermediate representation that  
3501 can be efficiently executed. PYTORCH [163]’s eager execution model is highly expressive and  
3502 user-friendly but also incurs significant overhead due to the dynamic nature of PYTHON and  
3503 the interpreter. Just-In-time compilation addresses this limitation by capturing, transforming,  
3504 and optimizing the execution of PYTORCH models at runtime, thereby delivering substantial  
3505 speedups while maintaining full compatibility with native PYTHON constructs.

3506 Under the hood, PYTORCH performs a series of sophisticated transformations to analyze  
3507 the computational graph<sup>II</sup> for efficient execution on both CPUs and GPUs. The first step  
3508 translates the model into a graph of symbolic functional transformations (FX), in which  
3509 each node represents the sequence of computations. The FX nodes are then converted  
3510 into a lower-level representation that reflects the underlying tensor operations, followed by  
3511 partitioning the FX graph into subgraphs suitable for kernel fusion. A large contribution to  
3512 the overall acceleration comes from merging multiple pointwise and elementwise operations  
3513 in each FX subgraph into a single kernel, reducing memory reads/writes and kernel launch  
3514 overhead. As a simple example, consider a series of three computations shown in algorithm  
6. Without compilation, they are executed separately, starting with the exponent, followed

---

**Algorithm 6:** An example of eager computation

---

Given input  $x$

$x \leftarrow \exp(x);$

$x \leftarrow x + 3;$

$x \leftarrow \text{ReLU}(x)$

---

3515

3516 by the addition, and finally the activation, each step consuming an intermediate memory

---

<sup>II</sup>A model is essentially a computational graph, to be distinguished from the graph data on which it operates.

buffer and dispatch. With compilation, however, they are fused into a single kernel yielding a

---

**Algorithm 7:** Compiled computation

---

```
Given input x
for (i=0; i < N; ++i) {
    out[i] = relu( exp( x[i] ) + 3.0 );
}
```

---

3517

3518 single-step computation instead of three separate ones, thus eliminating intermediate tensor  
 3519 allocations and kernel launch overhead. Further miscellaneous optimizations are carried  
 3520 out, and finally GPU-backend code is emitted for use. Remarkably, this complex analysis  
 3521 is entirely automated by PYTORCH, such that minimal code change is needed to compile  
 3522 an eager model. As this is an active area of development, further optimizations will likely  
 3523 become available.

3524 **12.3 Optimized performance**

3525 The computational efficiency gain from reduced precision and compilation of the INTER-  
 3526 ACTIONGNN is measured on three GPU platforms: the NVIDIA A100 Tensor Core GPUs  
 3527 with 40GB and 80GB memory, and the more advanced H100 model with 80GB memory.  
 3528 These measurements are conducted on the same 1000  $t\bar{t}$  events used in the previous chapter.  
 3529 The baseline corresponds to eager computation with no optimization. The improvement  
 3530 over the baseline automatic mixed precision (AMP) and compilation is separately measured.  
 3531 Because the two techniques are completely independent, we can perform the inference on  
 3532 a compiled model under reduced precision, compounding their effects. The combined im-  
 3533 provement is also measured. The average execution time and peak memory consumption as  
 3534 functions of the optimization method are shown in figure 12.1.

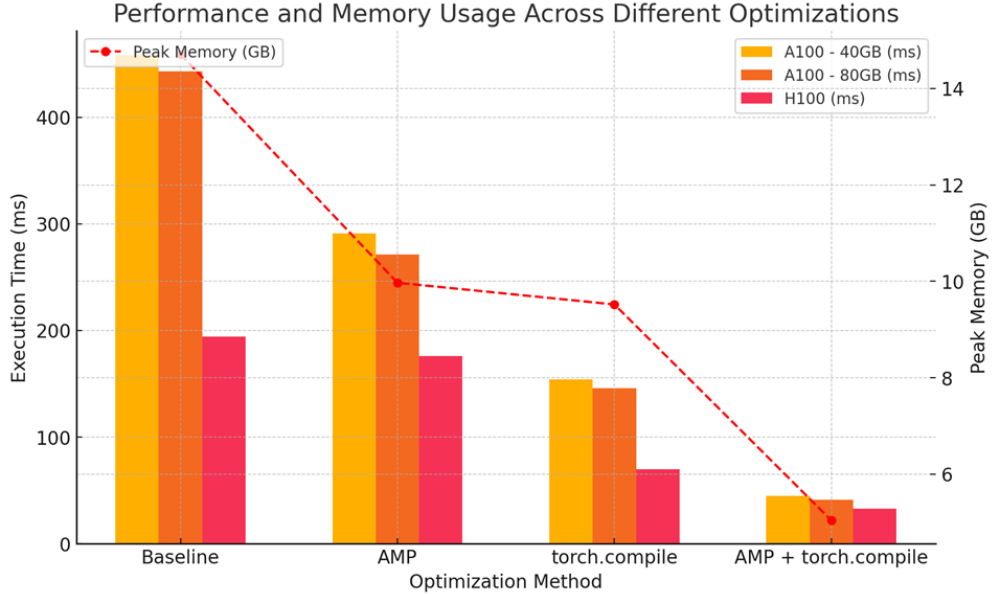


**Figure 12.1:** Computational efficiency of the INTERACTIONGNN in terms of the execution time (left vertical axis) and peak memory (right vertical axis), measured using the baseline configuration, and configuration optimized with automated mixed precision (AMP), Just-In-time computation (JIT), and a combination of the two techniques. All measurements use graphs constructed with the Module Map MinMax method.

3535        The baseline configuration shows a latency of  $\approx 600$  ms/event on the A100 platform,  
 3536   and 264 ms/event on the H100 platform. The H100's better performance is due to en-  
 3537   hanced floating-point operation efficiency on FP32, namely 67 TFLOPS compared to 19.5  
 3538   TFLOPS on the A100. Under reduced precision, the latency is reduced by approximately  
 3539   1/3 compared to the baseline on the A100, reaching on average 391 ms/event (40GB) and  
 3540   362 ms/event (80GB), but only by a small margin on the H100, reaching 239 ms/event.  
 3541   With JIT compilation, the execution time is enhanced to  $\approx 200$  ms/event on both A100  
 3542   platforms, and 92 ms/event on the H100. Under the combined effect of both techniques, the  
 3543   execution time is significantly reduced to  $\leq 60$  ms/event across all platform.

3544        Table 12.1 shows the improvement in inference speed with respect to eager computation  
 3545   at full precision of each optimization. The A100 and H100 platforms respectively benefit

3546 from up to an 11x and 6x boost in efficiency. Remarkably, while the next-generation H100  
 3547 outperforms the older A100-80GB by a factor of 2.25 in speed, this gap is shrunk to 1.40 by  
 3548 these optimizations. The larger enhancement of the A100 is an important benefit, because  
 3549 it is less expensive and power hungry than the new-generation counterpart, and hence more  
 3550 suitable for budget-constrained scientific computing. Interestingly, the performance boost  
 3551 delivered by the combined technique exceeds the product of the two underlying factors.

Optimization	A100-40GB	A100-80GB	H100-80GB
AMP	1.57	<b>1.63</b>	1.10
Compilation	2.97	<b>3.02</b>	2.77
Combined	9.69	<b>10.58</b>	5.92

**Table 12.1:** Latency improvement over eager computation at full precision of each optimization, measured using the baseline configuration, and configurations optimized with automated mixed precision (AMP), JIT compilation, and a combination of both techniques. All measurements use graphs constructed with the Module Map MeanRMS method.

3552 Similarly, the peak memory consumption is significantly improved with the combined  
 3553 optimization. Shown in figure 12.1, the peak consumption on the A100 decreases from  
 3554 19.16GB in the baseline to 6.48GB in the combined configuration, a factor of almost 3  
 3555 smaller. Thanks to the reduced memory footprint, it becomes possible to simultaneously  
 3556 fit several events on the GPU and enhance the inference throughput, a logical next step for  
 3557 future computational optimization. This direction is being explore using a *inference-as-a-*  
 3558 *service* approach, which optimizes the GPU utilization by batching multiple inference events  
 3559 and processing at the same time [164].

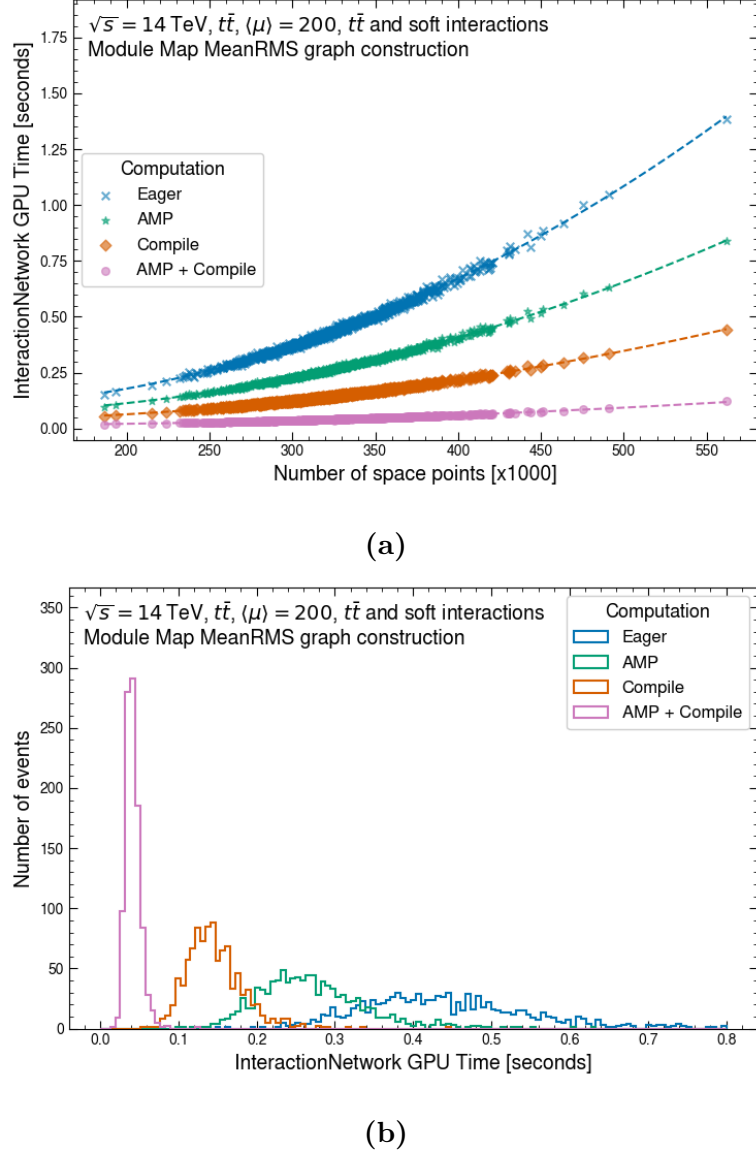


**Figure 12.2:** GPU time of the INTERACTIONGNN as a function of the number of space points in a  $t\bar{t}$  event (a) and as a histogram (b), measured using the baseline configuration, and configurations optimized with automated mixed precision (AMP), JIT compilation, and a combination of both techniques. Each dashed line in (a) displays the best-fit second-order polynomial to the corresponding configuration. The fitted coefficients are exhibited in table 12.2. All measurements are performed on an NVIDIA-A100 GPU with 80 GB of memory, using graphs constructed with the Module Map MeanRMS method.

Computation	A	B	C
Eager	5.56	$-8.73 \times 10^{-1}$	$1.30 \times 10^{-1}$
AMP	3.36	$-5.40 \times 10^{-1}$	$8.87 \times 10^{-2}$
Compile	1.73	$-2.67 \times 10^{-1}$	$4.76 \times 10^{-2}$
AMP + Compile	0.457	$-7.95 \times 10^{-2}$	$1.87 \times 10^{-2}$

**Table 12.2:** The coefficients of a second-order polynomial fit to the GPU time shown in figure 12.2 for each optimization technique. The GPU time  $t$  in units of seconds is assumed to depend on  $x = \frac{|V|}{10^6}$ , where  $V$  is the set of nodes, as  $t = Ax^2 + Bx + C$ .

3560        The event-level GPU run time as a function of the event size measured in the number of  
 3561        space points (graph nodes) along its best-fit second-order polynomial is shown in figure 12.2a,  
 3562        and the fitted coefficients in table 12.2. The majority of events contain 250,000 to 425,000  
 3563        nodes, and their GPU time exhibits a well-defined scaling behaviour with respect to the  
 3564        number of space points in the event. The dependence on space point number of GPU time  
 3565        scales quadratically, with a small linear component. Events far from the distribution core  
 3566        are well-described by the fitted curve, and no significant outliers are observed. The scaling  
 3567        behaviour is significantly improved with each optimization technique. In comparison to that  
 3568        of eager execution, the execution time of the combined AMP and Compilation execution  
 3569        scales much slower with event size, which is approximately proportional to true pile-up.  
 3570        This is evident, given the second-order coefficient of obtained from the latter  $A_{AMP+Compile} =$   
 3571        0.457, being an order of magnitude smaller than former's corresponding coefficient  $A_{Eager} =$   
 3572        5.56. The execution time of the optimized code is thus not only small but also stays small  
 3573        over the typical range of pile-up.

3574        The latency reduction from these computational optimizations is also evident from both  
 3575        the mean and spread of the GPU time distribution observed in each scenario, demonstrated  
 3576        in figure 12.2b. In the combined optimization, the distribution averages to  $42 \pm 9$  ms, with  
 3577        a range of 103 ms, while in the eager baseline, the distribution centers at  $443 \pm 117$  ms, with

3578 a range of 1231 ms. The former only peaks at a lower latency, it is also much narrower  
 3579 than the latter. This weak scaling makes the computation less susceptible to large events  
 3580 outside the core distribution, as shown in figure 12.2a above  $|V| = 4.5 \times 10^5$ .

## 3581 12.4 Pipeline computational performance

3582 The average latency of each stage in the GNN4ITk algorithm is shown in table 12.3,  
 3583 along with the average total execution time. The edge classification stage is measured  
 3584 with combined AMP and JIT optimization in all three variants. Among the stages, graph  
 3585 segmentation is the slowest, contributing nearly 60% of the total run time, while graph  
 3586 construction and edge classification each account for 20%. The difference in latency can be  
 3587 attributed to the different hardware on which these stages take place. Graph construction  
 3588 in the Module Map method is carried out on the GPU, by means of a custom CUDA  
 3589 kernel that highly parallelizes many steps of the algorithm. Edge classification leverages a  
 3590 graph neural network whose building blocks (the feed-forward multi-layer perceptron) are  
 3591 natively suitable to run on the GPU, and further benefit from the optimizations detailed in  
 3592 section 12.2. As a result, both stages are optimized for and performed on the GPU, and  
 3593 are thus massively accelerated. In comparison, the Walkthrough algorithm used in graph  
 3594 segmentation, originally conceived as an *ad hoc* routine, contains many loops and logical  
 3595 IF-THEN statements (see section 10.2), and is thus difficult to parallelize. Although much  
 3596 effort has been put into optimizing the current implementation, a mechanism redesign that  
 3597 prioritizes parallelizability is necessary to accelerate it on the GPU and bring the entire  
 3598 GNN4ITk algorithm onto a single hardware architecture. As of writing, a CUDA-based  
 3599 version of the Walkthrough is under development, promising better latency in the future.

3600 Of the two graph construction approaches, Module Map is significantly faster than Metric  
 3601 Learning. The former is carried out by a custom CUDA-kernel which maximally parallelizes  
 3602 all steps of the graph creation on the GPU, most notably the MERGE/JOIN operations of data

Stage	Latency [ms/event]		
	MeanRMS	MinMax	Metric Learning
Graph construction	$41 \pm 10$	$41 \pm 11$	$932 \pm 92$
Edge classification	$42 \pm 9$	$53 \pm 12$	$47 \pm 10$
Graph segmentation	$120 \pm 93$	$120 \pm 93$	
Total	$203 \pm 94$		

**Table 12.3:** Per-event run time of each stage in the GNN4ITk algorithm. The latency of graph construction and edge classification is evaluated on an NVIDIA-A100 GPU with 80GB of memory, and of graph segmentation on the AMD EPYC 7763 CPU, using graphs constructed with the Module Map MeanRMS method.

3603 frames, which consume considerable computation on the CPU but are greatly accelerated  
 3604 on the GPU [165]. On the other hand, the latter’s graph construction latency is the sum of  
 3605 the metric learning and filter steps, both of which, as of writing, have not been optimized.  
 3606 The metric learning step suffers from a lengthy kNN search in high a 12-dimensional space,  
 3607 and the filter step operates on large graphs of  $|V| \sim 6 \times 10^6$  edges. These shortcomings  
 3608 are however optimizable, and methods to address them are being investigated. In the edge  
 3609 classification step, both graph construction approaches demonstrate similar speed, ranging  
 3610 from 42 to 53 ms/event. Their difference in latency is evident from the average graph size,  
 3611 with  $|E|_{\text{MinMax}} > |E|_{\text{ML}} > |E|_{\text{MeanRMS}}$ , and correspondingly  $t_{\text{MinMax}} > t_{\text{ML}} > t_{\text{MeanRMS}}$ , where  
 3612  $E$  is the edge set and  $t$  the latency. In the graph segmentation step, after fake edges are  
 3613 removed by a loose GNN score cut, the remaining graphs have similar edge set among the  
 3614 three variants, and their track building time is largely in accordance.

3615 A comparison between the GNN- and the CKF-based track finders in terms of computing  
 3616 performance is unfortunately not straightforward. The two algorithms by design operates  
 3617 on different hardware, the CKF on CPUs and the GNN on GPUs. The lack of a common  
 3618 benchmark is the main challenge, which stems from differences in architecture, programming

3619 models, and performance goals. For example, CPUs are optimized for low-latency execution  
 3620 of sequential tasks with a control flow, whereas GPUs for high-throughput executions of  
 3621 parallelized code. These factors complicate the establishment of a fair and standardized  
 3622 metrics across the computing platforms. CPU performance is usually measured by the  
 3623 latency per task, and GPU performance by FLoating-point Operations Per Second (FLOPS).  
 3624 Of course, one could naively compare the per-event latency of the two algorithms, and  
 3625 immediately runs into the question: ***which*** latency? As we have seen in the previous section,  
 3626 the GNN latency varies widely with different GPU platforms, and the most performant  
 3627 platform may not be the choice for production infrastructure, giving little significance to  
 3628 this comparison. Quoting the latency of the CKF on different CPUs suffers from the same  
 3629 problem.

3630 Ultimately, the latency alone is insufficient to make a decision on the tracking technology  
 3631 in HL-HLC. It is not enough to answer the question “*How fast can we reconstruct tracks?*”,  
 3632 but **How much does it cost to reach a certain event/second throughput using**  
 3633 **each algorithm?** Therefore, a cost analysis taking into account all factors such as pro-  
 3634 curement, inherent throughput, latency, energy consumption, etc. is needed. It necessitates  
 3635 investigations much deeper than the scope of the scope of this thesis. For the moment, we  
 3636 refrain from making a direct comparison in computing performance between the two track  
 3637 finders.

## 3638 12.5 Toward computational performance in production environ- 3639 ment

3640 The result in section 12.4 representing the current computational performance of the  
 3641 GNN4ITk algorithm, is obtained from inference in a development environment. Most of  
 3642 the source code is implemented in PYTHON, and deep-learning models are written with  
 3643 PYTORCH. The Module Map, though implemented in C++ and CUDA, is incorporated via

3644 a python-binding into the inference pipeline. The Walkthrough mechanism, though highly  
3645 optimized by Just-In-Time compiling many components in a manner similar to C++ using  
3646 NUMBA[166], is still implemented in PYTHON code. As a syntactically simple language rich  
3647 in well-supported libraries, PYTHON is suitable for research and development, but it is not  
3648 the language of choice for production systems, which prioritize computational performance.  
3649 In fact, the legacy analysis software and the future tracking toolkit employed by ATLAS are  
3650 both written in C++. Therefore, table 12.3 serves as the algorithm’s baseline latency, not  
3651 measurements in a realistic production environment. As compiled C++ code is typically  
3652 faster than the corresponding PYTHON code, we expect even better performance than so far  
3653 demonstrated.

3654 Further developments are needed to achieve competitive computing performance. The  
3655 entire pipeline must be implemented in C++ and ported to ATHENA[144], enabling measure-  
3656 ments and optimizations in production environment. All three stages of the Module Map  
3657 variant have been integrated into the ACTS framework [138], which will become the tracking  
3658 component of the ATLAS software. The graph construction stage of the Metric Learning  
3659 remains to be accelerated and integrated. The slowest component of this step is the k-  
3660 nearest-neighbor search which takes  $\approx 400$  ms/event, due to the rather large 12-dimensional  
3661 embedding space. A possible method is to reduce the embedding dimensions by encourag-  
3662 ing one or more dimensions to take a constant value using an extra loss term in training.  
3663 During inference, the kNN search can ignore these dimension in the distance calculation,  
3664 and therefore save time. The large number of edges, likely due to the current method being  
3665 sub-optimal, is also a huge bottleneck, requiring a filter step to eliminate easy fake edges.  
3666 As Metric Learning is a mature technique of machine learning, more sophisticated models  
3667 can better discriminate target hits from background, allowing to build smaller graphs and  
3668 possibly bypass the Filter step.

## 3669 Chapter 13

### 3670 Conclusion

3671 This thesis presents a combination of a wide range of searches targeting experimental sig-  
 3672 natures with and without a missing transverse momentum  $E_T^{\text{miss}}$  and an interpretation in the  
 3673 context of a Two-Higgs-Doublet Model extended by a pseudo-scalar mediator (2HDM+ $a$ )  
 3674 between the visible and dark sectors. The searches use up to  $139 \text{ fb}^{-1}$  of proton-proton  
 3675 collision data at a center-of-mass energy  $\sqrt{s} = 13 \text{ TeV}$  recorded by the ATLAS detector  
 3676 during LHC Run 2 between 2015 and 2018. The most sensitive analyses, including searches  
 3677 for large  $E_T^{\text{miss}}$  produced in association with a leptonically decaying  $Z$ -boson ( $E_T^{\text{miss}} + Z(\ell\ell)$ )  
 3678 and with a SM Higgs boson decaying to a pair of  $b$ -quarks ( $E_T^{\text{miss}} + h(b\bar{b})$ ), and a search for  
 3679 associated production of a top and a bottom quarks with a charged Higgs boson decaying to  
 3680 a top and a bottom quark ( $tbH^\pm(tb)$ ) are statistically combined, and constraints from other  
 3681 searches are overlaid in the summary. No significant deviations from SM predictions are  
 3682 observed, and 95% confidence-level upper limits on the 2HDM+ $a$  for a variety of benchmark  
 3683 scenarios, including those based on the recommendations of the LHC Dark Matter Working  
 3684 Group and several new ones exploring the model's rich phenomenology, are established.

3685 Large regions of the parameter space are excluded, thanks to the combined sensitivity  
 3686 of the  $E_T^{\text{miss}} + X$  and  $tbH^\pm(tb)$  signatures. The  $E_T^{\text{miss}} + Z(\ell\ell)$  and  $E_T^{\text{miss}} + h(b\bar{b})$  searches  
 3687 drive the sensitivity in at high heavy Higgs boson mass ( $m_A = m_H = m_{H^\pm}$ ), while the  
 3688  $tbH^\pm(tb)$  search is most sensitive at low  $m_A$  across the full mediator mass ( $m_a$ ) range. The  
 3689 latter also extends the exclusion region in  $\tan\beta$  across all  $m_a$ . The statistically combined

3690 result provides better sensitivity to the 2HDM+ $a$  than that derived from each individual  
 3691 search. This analysis represents an improvement over the summary based on  $36\text{ fb}^{-1}$  of data  
 3692 from LHC Run 1, by statistically combining the  $t b H^\pm(t b)$  channel which was previously not  
 3693 considered, by including new benchmark scenarios, and by incorporating a larger amount  
 3694 of data. Nevertheless, a large part of the parameter space remains unexcluded and awaits  
 3695 future analyses using larger datasets.

3696 In general, the sensitivity of searches for BSM signals, as well as precision measurements  
 3697 of SM processes is statistically constrained. The High Luminosity Large Hadron Collider  
 3698 (HL-LHC) promises an order of magnitude increase in collision data compared to that ac-  
 3699 quired over the three nominal LHC Runs, which would greatly benefits all physics programs  
 3700 at each of the general-purpose experiments. Nevertheless, reaching this goal requires consid-  
 3701 erable upgrades in event reconstruction. Charged-particle track reconstruction, in particular,  
 3702 faces numerous challenges from the increased expected pile-up multiplicity ( $\langle \mu \rangle$ ), for which  
 3703 a GPU-based new algorithm is a potential solution. We investigate an algorithm based on  
 3704 Graph Neural Networks (GNNs) for tracking under HL-LHC conditions. Using  $t\bar{t}$  collision  
 3705 event simulated simulated at  $\langle \mu \rangle = 200$  with realistic ITk layout, we optimized all stages  
 3706 of the algorithm, including graph construction, edge classification and graph segmentation.  
 3707 Compared to previous publications, this thesis demonstrates a comprehensive apple-to-apple  
 3708 comparison to the traditional technique in important tracking metrics, as well as measure-  
 3709 ments and optimizations of the computing performance.

3710 The efficiency on target particles in  $t\bar{t}$  samples of exceeds that of the Combinatorial  
 3711 Kalman Filter (CKF) at low transverse momentum  $p_T$ , and is competitive at high  $p_T$ . At  
 3712 the same time, the proportion of track candidates having the highest matching probability  
 3713 less than 50% is significantly reduced. Good impact parameter resolution is observed, but  
 3714 the momentum resolution has yet to reach the same level of CKF. The fastest configuration  
 3715 of the algorithm, in which the first two stages are carried out on the GPU and the last on  
 3716 the CPU, has a total run time of  $\approx 200$  ms/event.

Despite the impressive performance, future work is needed to improve and demonstrate the algorithm. First, the object-level performance must be evaluated to understand potential impacts on the reconstruction and identification of various physics objects. For example, the efficiency and parameter resolution of tracks inside  $b$ -quark jets is an indicator of  $b$ -tagging performance, whereas samples containing single muons, electrons, and pions help isolate the performance when various levels of material interactions are involved, as well as track quality at fixed transverse momenta. Single-cluster hits should also be reintroduced into the track candidates constructed by the GNN-chain to improve momentum resolution. Second, all stages the algorithm must be implemented to run on the GPU and fully integrated into Athena via the ACTS framework. In particular, the graph segmentation which runs on the CPU and the metric learning technique based on costly kNN searches are identified as bottlenecks, which ongoing developments will address. Other incremental improvements, such as model size reduction and quantization, could shave away both inference time and memory consumption, enhancing algorithmic frugality and economic competitiveness.

## <sup>3731</sup> Bibliography

- <sup>3732</sup> [1] Edvige Corbelli and Paolo Salucci,  
<sup>3733</sup> *The Extended Rotation Curve and the Dark Matter Halo of M33*,  
<sup>3734</sup> Mon. Not. Roy. Astron. Soc. **311** (2000) 441, arXiv: astro-ph/9909252  
<sup>3735</sup> (cit. on p. 16).
- <sup>3736</sup> [2] V. C. Rubin et al., *Rotational properties of 21 SC galaxies with a large range of*  
<sup>3737</sup> *luminosities and radii, from NGC 4605 ( $R=4\text{kpc}$ ) to UGC 2885 ( $R=122\text{kpc}$ )*,  
<sup>3738</sup> Astrophysical Journal **238** (1980) 471 (cit. on p. 16).
- <sup>3739</sup> [3] K. G. Begeman, A. H. Broeils, and R. H. Sanders,  
<sup>3740</sup> *Extended rotation curves of spiral galaxies: Dark haloes and modified dynamics*,  
<sup>3741</sup> MNRAS **249** (1991) 523 (cit. on p. 16).
- <sup>3742</sup> [4] G. Hinshaw et al., *Nine-Year Wilkinson Microwave Anisotropy Probe (WMAP)*  
<sup>3743</sup> *Observations: Cosmological Parameter Results*, Astrophys. J. Suppl. **208** (2013) 19,  
<sup>3744</sup> arXiv: 1212.5226 [astro-ph.CO] (cit. on p. 16).
- <sup>3745</sup> [5] Planck Collaboration,  
<sup>3746</sup> *Planck 2018 results. I. Overview and the cosmological legacy of Planck*,  
<sup>3747</sup> Astron. Astrophys. **641** (2020) A1, arXiv: 1807.06205 [astro-ph.CO]  
<sup>3748</sup> (cit. on p. 16).
- <sup>3749</sup> [6] Virginia Trimble, *Existence and Nature of Dark Matter in the Universe*,  
<sup>3750</sup> Ann. Rev. Astron. Astrophys. **25** (1987) 425 (cit. on p. 16).

- 3751 [7] G. Bertone, D. Hooper, and J. Silk,  
 3752 *Particle dark matter: evidence, candidates and constraints*,  
 3753 Phys. Rept. **405** (2005) 279 (cit. on p. 16).
- 3754 [8] Jonathan L. Feng,  
 3755 *Dark Matter Candidates from Particle Physics and Methods of Detection*,  
 3756 Ann. Rev. Astron. Astrophys. **48** (2010) 495 (cit. on p. 16).
- 3757 [9] Danyer Perez Adan, *Dark Matter searches at CMS and ATLAS*, 2023,  
 3758 arXiv: 2301.10141 [hep-ex], URL: <https://arxiv.org/abs/2301.10141>  
 3759 (cit. on p. 16).
- 3760 [10] Gary Steigman and Michael S. Turner,  
 3761 *Cosmological Constraints on the Properties of Weakly Interacting Massive Particles*,  
 3762 Nucl. Phys. B **253** (1985) 375 (cit. on p. 16).
- 3763 [11] Martin Bauer, Ulrich Haisch, and Felix Kahlhoefer,  
 3764 *Simplified dark matter models with two Higgs doublets: I. Pseudoscalar mediators*,  
 3765 JHEP **05** (2017) 138, arXiv: 1701.07427 [hep-ph]  
 3766 (cit. on pp. 17, 44, 45, 47, 48, 51, 79, 83).
- 3767 [12] Tomohiro Abe et al.,  
 3768 *LHC Dark Matter Working Group: Next-generation spin-0 dark matter models*,  
 3769 Phys. Dark Univ. **27** (2020) 100351, arXiv: 1810.09420 [hep-ex]  
 3770 (cit. on pp. 17, 29, 44, 47–49, 52, 86, 102).
- 3771 [13] ATLAS Collaboration,  
 3772 *Search for dark matter produced in association with a Standard Model Higgs boson*  
 3773 *decaying into b-quarks using the full Run 2 dataset from the ATLAS detector*,  
 3774 JHEP **11** (2021) 209, arXiv: 2108.13391 [hep-ex] (cit. on pp. 17, 54, 57, 59).
- 3775 [14] ATLAS Collaboration,  
 3776 *Search for associated production of a Z boson with an invisibly decaying Higgs boson*  
 3777 *or dark matter candidates at  $\sqrt{s} = 13 \text{ TeV}$  with the ATLAS detector*,

- 3778 Phys. Lett. B **829** (2021) 137066, arXiv: 2111.08372 [hep-ex]  
 3779 (cit. on pp. 17, 54, 55, 65).
- 3780 [15] ATLAS Collaboration, *Search for charged Higgs bosons decaying into a top quark*  
 3781 *and a bottom quark at  $\sqrt{s} = 13 \text{ TeV}$  with the ATLAS detector*, JHEP **06** (2021) 145,  
 3782 arXiv: 2102.10076 [hep-ex] (cit. on pp. 17, 54, 67).
- 3783 [16] O. Aberle et al.,  
 3784 *High-Luminosity Large Hadron Collider (HL-LHC): Technical design report*,  
 3785 CERN Yellow Reports: Monographs, Geneva: CERN, 2020,  
 3786 URL: <https://cds.cern.ch/record/2749422> (cit. on p. 17).
- 3787 [17] Sheldon L. Glashow, *Partial-symmetries of weak interactions*,  
 3788 Nuclear Physics **22** (1961) 579, ISSN: 0029-5582, URL:  
 3789 <https://www.sciencedirect.com/science/article/pii/0029558261904692>  
 3790 (cit. on p. 20).
- 3791 [18] Steven Weinberg, *A Model of Leptons*, Phys. Rev. Lett. **19** (21 1967) 1264,  
 3792 URL: <https://link.aps.org/doi/10.1103/PhysRevLett.19.1264> (cit. on p. 20).
- 3793 [19] Michael E. Peskin, *An introduction to quantum field theory*, CRC Press, 2018  
 3794 (cit. on p. 20).
- 3795 [20] Francis Halzen and Alan Douglas Martin,  
 3796 *Quarks and leptons: An introductory course in modern particle physics*,  
 3797 John Wiley, 2016 (cit. on p. 20).
- 3798 [21] Matthew Dean Schwartz, *Quantum Field Theory and the standard model*,  
 3799 Cambridge University Press, 2014 (cit. on p. 20).
- 3800 [22] Particle Data Group, P.A. Zyla, et al., *Review of Particle Physics*,  
 3801 PTEP **2020** (2020) 083C01 (cit. on pp. 29, 105, 107, 110, 113).

- 3802 [23] H.E. Haber and G.L. Kane,  
 3803 *The search for supersymmetry: Probing physics beyond the standard model*,  
 3804 Physics Reports **117** (1985) 75, ISSN: 0370-1573, URL:  
 3805 <https://www.sciencedirect.com/science/article/pii/0370157385900511>  
 3806 (cit. on p. 29).
- 3807 [24] Michael Joyce, Tomislav Prokopec, and Neil Turok,  
 3808 *Nonlocal electroweak baryogenesis. II. The classical regime*,  
 3809 Physical Review D **53** (1996) 2958, ISSN: 1089-4918,  
 3810 URL: <http://dx.doi.org/10.1103/PhysRevD.53.2958> (cit. on p. 29).
- 3811 [25] K. Funakubo, A. Kakuto, and K. Takenaga, *The Effective Potential of Electroweak*  
 3812 *Theory with Two Massless Higgs Doublets at Finite Temperature*,  
 3813 Progress of Theoretical Physics **91** (1994) 341, ISSN: 1347-4081,  
 3814 URL: <http://dx.doi.org/10.1143/ptp/91.2.341> (cit. on p. 29).
- 3815 [26] James M. Cline, Kimmo Kainulainen, and Axel P. Vischer, *Dynamics of*  
 3816 *two-Higgs-doublet violation and baryogenesis at the electroweak phase transition*,  
 3817 Physical Review D **54** (1996) 2451, ISSN: 1089-4918,  
 3818 URL: <http://dx.doi.org/10.1103/PhysRevD.54.2451> (cit. on p. 29).
- 3819 [27] James M. Cline and Pierre-Anthony Lemieux,  
 3820 *Electroweak phase transition in two Higgs doublet models*,  
 3821 Phys. Rev. D **55** (6 1997) 3873,  
 3822 URL: <https://link.aps.org/doi/10.1103/PhysRevD.55.3873> (cit. on p. 29).
- 3823 [28] M. Laine and K. Rummukainen, *Two Higgs doublet dynamics at the electroweak*  
 3824 *phase transition: a non-perturbative study*, Nuclear Physics B **597** (2001) 23,  
 3825 ISSN: 0550-3213, URL:  
 3826 <https://www.sciencedirect.com/science/article/pii/S0550321300007367>  
 3827 (cit. on p. 29).

- 3828 [29] Lars Fromme, Stephan J. Huber, and Michael Seniuch,  
 3829 *Baryogenesis in the two-Higgs doublet model*,  
 3830 Journal of High Energy Physics **2006** (2006) 038,  
 3831 URL: <https://dx.doi.org/10.1088/1126-6708/2006/11/038> (cit. on p. 29).
- 3832 [30] G.C. Branco et al., *Theory and phenomenology of two-Higgs-doublet models*,  
 3833 Physics Reports **516** (2012) 1, ISSN: 0370-1573,  
 3834 URL: <http://dx.doi.org/10.1016/j.physrep.2012.02.002> (cit. on p. 29).
- 3835 [31] Joao Pequenao, “Computer generated image of the whole ATLAS detector”, 2008,  
 3836 URL: <https://cds.cern.ch/record/1095924> (cit. on p. 32).
- 3837 [32] L. Blanquart et al., *FE-I2: a front-end readout chip designed in a commercial*  
 3838 *0.25-/spl mu/m process for the ATLAS pixel detector at LHC*,  
 3839 IEEE Transactions on Nuclear Science **51** (2004) 1358 (cit. on p. 34).
- 3840 [33] The ATLAS Collaboration, *ATLAS pixel detector electronics and sensors*,  
 3841 Journal of Instrumentation **3** (2008) P07007,  
 3842 URL: <https://dx.doi.org/10.1088/1748-0221/3/07/P07007> (cit. on p. 35).
- 3843 [34] ATLAS Collaboration, *ATLAS Inner Detector: Technical Design Report, Volume 1*,  
 3844 ATLAS-TDR-4; CERN-LHCC-97-016, 1997,  
 3845 URL: <https://cds.cern.ch/record/331063> (cit. on p. 35).
- 3846 [35] ATLAS Collaboration, *ATLAS Inner Detector: Technical Design Report, Volume 2*,  
 3847 ATLAS-TDR-5, CERN-LHCC-97-017, 1997,  
 3848 URL: <https://cds.cern.ch/record/331064> (cit. on p. 35).
- 3849 [36] Gaetano Barone, *ATLAS silicon microstrip tracker operation and performance*,  
 3850 Nuclear Instruments and Methods in Physics Research Section A: Accelerators,  
 3851 Spectrometers, Detectors and Associated Equipment **732** (2013) 57, Vienna  
 3852 Conference on Instrumentation 2013, ISSN: 0168-9002, URL:  
 3853 <https://www.sciencedirect.com/science/article/pii/S0168900213007171>  
 3854 (cit. on p. 35).

- 3855 [37] D. Robinson, *The atlas semi-conductor tracker operation and performance*,  
 3856 Nuclear Instruments and Methods in Physics Research Section A: Accelerators,  
 3857 Spectrometers, Detectors and Associated Equipment **699** (2013) 139 (cit. on p. 36).
- 3858 [38] The ATLAS Collaboration,  
 3859 *The ATLAS Experiment at the CERN Large Hadron Collider*,  
 3860 Journal of Instrumentation **3** (2008) S08003,  
 3861 URL: <https://dx.doi.org/10.1088/1748-0221/3/08/S08003> (cit. on p. 38).
- 3862 [39] ATLAS Collaboration, *ATLAS Muon Spectrometer: Technical Design Report*,  
 3863 ATLAS-TDR-10; CERN-LHCC-97-022, CERN, 1997,  
 3864 URL: <https://cds.cern.ch/record/331068> (cit. on p. 40).
- 3865 [40] The ATLAS Collaboration,  
 3866 *Combination and summary of ATLAS dark matter searches interpreted in a 2HDM*  
 3867 *with a pseudo-scalar mediator using 139 fb-1 of  $\sqrt{s} = 13$  TeV pp collision data*,  
 3868 Science Bulletin **69** (2024) 3005, ISSN: 2095-9273, URL:  
 3869 <https://www.sciencedirect.com/science/article/pii/S2095927324003992>  
 3870 (cit. on pp. 41, 49–51, 54, 76, 78, 81, 82, 84, 87, 89).
- 3871 [41] Matthew R. Buckley, David Feld, and Dorival Goncalves,  
 3872 *Scalar Simplified Models for Dark Matter*, Phys. Rev. D **91** (2015) 015017,  
 3873 arXiv: 1410.6497 [hep-ph] (cit. on p. 41).
- 3874 [42] Daniel Abercrombie et al., *Dark Matter benchmark models for early LHC Run-2*  
 3875 *Searches: Report of the ATLAS/CMS Dark Matter Forum*,  
 3876 Phys. Dark Univ. **27** (2020) 100371, ed. by Antonio Boveia, Caterina Doglioni,  
 3877 Steven Lowette, Sarah Malik, and Stephen Mrenna, arXiv: 1507.00966 [hep-ex]  
 3878 (cit. on p. 41).
- 3879 [43] John F. Gunion and Howard E. Haber,  
 3880 *The CP conserving two Higgs doublet model: The Approach to the decoupling limit*,  
 3881 Phys. Rev. D **67** (2003) 075019, arXiv: hep-ph/0207010 (cit. on p. 42).

- 3882 [44] Mikolaj Misiak and Matthias Steinhauser, *Weak radiative decays of the  $B$  meson*  
 3883 *and bounds on  $M_{H^\pm}$  in the Two-Higgs-Doublet Model,*  
 3884 Eur. Phys. J. C **77** (2017) 201, arXiv: 1702.04571 [hep-ph] (cit. on p. 47).
- 3885 [45] ATLAS Collaboration, *Constraints on mediator-based dark matter and scalar dark*  
 3886 *energy models using  $\sqrt{s} = 13\text{ TeV}$  pp collision data collected by the ATLAS detector,*  
 3887 JHEP **05** (2019) 142, arXiv: 1903.01400 [hep-ex]  
 3888 (cit. on pp. 48, 49, 80, 83, 85, 86).
- 3889 [46] Spyros Argyropoulos and Ulrich Haisch,  
 3890 *Benchmarking LHC searches for light 2HDM+a pseudoscalars,*  
 3891 SciPost Phys. **13** (2022) 007, arXiv: 2202.12631 [hep-ph] (cit. on pp. 48, 49).
- 3892 [47] Ulrich Haisch and Giacomo Polesello,  
 3893 *Searching for heavy Higgs bosons in the  $t\bar{t}Z$  and  $tbW$  final states,*  
 3894 JHEP **09** (2018) 151, arXiv: 1807.07734 [hep-ph] (cit. on p. 48).
- 3895 [48] Priscilla Pani and Giacomo Polesello,  
 3896 *Dark matter production in association with a single top-quark at the LHC in a*  
 3897 *two-Higgs-doublet model with a pseudoscalar mediator,*  
 3898 Phys. Dark Univ. **21** (2018) 8, arXiv: 1712.03874 [hep-ph] (cit. on pp. 49, 81).
- 3899 [49] ATLAS Collaboration,  
 3900 *ATLAS data quality operations and performance for 2015–2018 data-taking,*  
 3901 JINST **15** (2020) P04003, arXiv: 1911.04632 [physics.ins-det] (cit. on p. 49).
- 3902 [50] Celine Degrande et al., *UFO - The Universal FeynRules Output,*  
 3903 Comput. Phys. Commun. **183** (2012) 1201, arXiv: 1108.2040 [hep-ph]  
 3904 (cit. on p. 50).
- 3905 [51] Celine Degrande, Maria Ubiali, Marius Wiesemann, and Marco Zaro,  
 3906 *Heavy charged Higgs boson production at the LHC*, JHEP **10** (2015) 145,  
 3907 arXiv: 1507.02549 [hep-ph] (cit. on p. 51).

- 3908 [52] J. Alwall et al., *The automated computation of tree-level and next-to-leading order*  
 3909 *differential cross sections, and their matching to parton shower simulations,*  
 3910 *JHEP* **07** (2014) 079, arXiv: 1405.0301 [hep-ph] (cit. on p. 50).
- 3911 [53] Torbjörn Sjöstrand et al., *An introduction to PYTHIA 8.2,*  
 3912 *Comput. Phys. Commun.* **191** (2015) 159, arXiv: 1410.3012 [hep-ph]  
 3913 (cit. on pp. 50, 114).
- 3914 [54] ATLAS Collaboration, *ATLAS Pythia 8 tunes to 7 TeV data,*  
 3915 ATL-PHYS-PUB-2014-021, 2014, URL: <https://cds.cern.ch/record/1966419>  
 3916 (cit. on pp. 51, 114).
- 3917 [55] The NNPDF Collaboration, Richard D. Ball, et al.,  
 3918 *Parton distributions for the LHC run II*, *JHEP* **04** (2015) 040,  
 3919 arXiv: 1410.8849 [hep-ph] (cit. on pp. 51, 114).
- 3920 [56] ATLAS Collaboration, *Summary of ATLAS Pythia 8 tunes,*  
 3921 ATL-PHYS-PUB-2012-003, 2012, URL: <https://cds.cern.ch/record/1474107>  
 3922 (cit. on p. 52).
- 3923 [57] A. D. Martin, W. J. Stirling, R. S. Thorne, and G. Watt,  
 3924 *Parton distributions for the LHC*, *Eur. Phys. J. C* **63** (2009) 189,  
 3925 arXiv: 0901.0002 [hep-ph] (cit. on p. 52).
- 3926 [58] S. Agostinelli et al., *GEANT4 – a simulation toolkit,*  
 3927 *Nucl. Instrum. Meth. A* **506** (2003) 250 (cit. on pp. 52, 100).
- 3928 [59] ATLAS Collaboration, *The ATLAS Simulation Infrastructure,*  
 3929 *Eur. Phys. J. C* **70** (2010) 823, arXiv: 1005.4568 [physics.ins-det]  
 3930 (cit. on p. 52).
- 3931 [60] ATLAS Collaboration, *The simulation principle and performance of the ATLAS fast*  
 3932 *calorimeter simulation FastCaloSim*, ATL-PHYS-PUB-2010-013, 2010,  
 3933 URL: <https://cds.cern.ch/record/1300517> (cit. on p. 52).

- 3934 [61] Olivier Mattelaer,  
 3935 *On the maximal use of Monte Carlo samples: re-weighting events at NLO accuracy,*  
 3936 Eur. Phys. J. C **76** (2016) 674, arXiv: 1607.00763 [hep-ph] (cit. on p. 52).
- 3937 [62] ATLAS Collaboration, *Search for dark matter in events with missing transverse*  
 3938 *momentum and a Higgs boson decaying into two photons in pp collisions at*  
 3939  *$\sqrt{s} = 13 \text{ TeV}$  with the ATLAS detector*, JHEP **10** (2021) 013,  
 3940 arXiv: 2104.13240 [hep-ex] (cit. on pp. 54, 60).
- 3941 [63] ATLAS Collaboration, *Search for dark matter produced in association with a Higgs*  
 3942 *boson decaying to tau leptons at  $\sqrt{s} = 13 \text{ TeV}$  with the ATLAS detector*, (2023),  
 3943 arXiv: 2305.12938 [hep-ex] (cit. on pp. 54, 61, 63).
- 3944 [64] ATLAS Collaboration,  
 3945 *Search for dark matter produced in association with a single top quark and an*  
 3946 *energetic W boson in  $\sqrt{s} = 13 \text{ TeV}$  pp collisions with the ATLAS detector*, (2022),  
 3947 arXiv: 2211.13138 [hep-ex] (cit. on pp. 54, 62).
- 3948 [65] ATLAS Collaboration,  
 3949 *Search for new phenomena in events with an energetic jet and missing transverse*  
 3950 *momentum in pp collisions at  $\sqrt{s} = 13 \text{ TeV}$  with the ATLAS detector*,  
 3951 Phys. Rev. D **103** (2021) 112006, arXiv: 2102.10874 [hep-ex]  
 3952 (cit. on pp. 54, 64, 65).
- 3953 [66] ATLAS Collaboration,  
 3954 *Combination of searches for invisible decays of the Higgs boson using  $139 \text{ fb}^{-1}$  of*  
 3955 *proton-proton collision data at  $\sqrt{s} = 13 \text{ TeV}$  collected with the ATLAS experiment*,  
 3956 arXiv: 2301.10731 [hep-ex] (cit. on pp. 54, 65).
- 3957 [67] ATLAS Collaboration, *Search for dark matter in events with a hadronically decaying*  
 3958 *vector boson and missing transverse momentum in pp collisions at  $\sqrt{s} = 13 \text{ TeV}$*   
 3959 *with the ATLAS detector*, JHEP **10** (2018) 180, arXiv: 1807.11471 [hep-ex]  
 3960 (cit. on pp. 54, 66).

- [3961] [68] ATLAS Collaboration, *Search for dark matter produced in association with bottom*  
 [3962] *or top quarks in  $\sqrt{s} = 13 \text{ TeV}$  pp collisions with the ATLAS detector,*  
 [3963] Eur. Phys. J. C **78** (2018) 18, arXiv: 1710.11412 [hep-ex] (cit. on pp. 54, 66, 67).
- [3964] [69] ATLAS Collaboration, *Search for top-squark pair production in final states with one*  
 [3965] *lepton, jets, and missing transverse momentum using  $36 \text{ fb}^{-1}$  of  $\sqrt{s} = 13 \text{ TeV}$  pp*  
 [3966] *collision data with the ATLAS detector*, JHEP **06** (2018) 108,  
 [3967] arXiv: 1711.11520 [hep-ex] (cit. on pp. 54, 67).
- [3968] [70] ATLAS Collaboration, *Search for  $t\bar{t}H/A \rightarrow t\bar{t}t\bar{t}$  production in the multilepton final*  
 [3969] *state in proton–proton collisions at  $\sqrt{s} = 13 \text{ TeV}$  with the ATLAS detector*, (2022),  
 [3970] arXiv: 2211.01136 [hep-ex] (cit. on pp. 54, 68).
- [3971] [71] ATLAS Collaboration,  
 [3972] *Search for Higgs boson decays into a pair of pseudoscalar particles in the  $bb\mu\mu$  final*  
 [3973] *state with the ATLAS detector in pp collisions at  $\sqrt{s} = 13 \text{ TeV}$ ,*  
 [3974] Phys. Rev. D **105** (2021) 012006, arXiv: 2110.00313 [hep-ex] (cit. on pp. 54, 70).
- [3975] [72] ATLAS Collaboration, *Search for the Higgs boson produced in association with a*  
 [3976] *vector boson and decaying into two spin-zero particles in the  $H \rightarrow aa \rightarrow 4b$  channel*  
 [3977] *in pp collisions at  $\sqrt{s} = 13 \text{ TeV}$  with the ATLAS detector*, JHEP **10** (2018) 031,  
 [3978] arXiv: 1806.07355 [hep-ex] (cit. on pp. 54, 70).
- [3979] [73] ATLAS Collaboration, *Search for Higgs bosons decaying to  $aa$  in the  $\mu\mu\tau\tau$  final*  
 [3980] *state in pp collisions at  $\sqrt{s} = 8 \text{ TeV}$  with the ATLAS experiment*,  
 [3981] Phys. Rev. D **92** (2015) 052002, arXiv: 1505.01609 [hep-ex]  
 [3982] (cit. on pp. 54, 70, 88).
- [3983] [74] ATLAS Collaboration, *Search for Higgs boson decays to beyond-the-Standard-Model*  
 [3984] *light bosons in four-lepton events with the ATLAS detector at  $\sqrt{s} = 13 \text{ TeV}$* ,  
 [3985] JHEP **06** (2018) 166, arXiv: 1802.03388 [hep-ex] (cit. on pp. 54, 70).

- 3986 [75] ATLAS Collaboration, *Search for Higgs bosons decaying into new spin-0 or spin-1*  
 3987 *particles in four-lepton final states with the ATLAS detector with  $139\text{ fb}^{-1}$  of  $pp$*   
 3988 *collision data at  $\sqrt{s} = 13\text{ TeV}$* , JHEP **03** (2021) 041, arXiv: 2110.13673 [hep-ex]  
 3989 (cit. on pp. 54, 70).
- 3990 [76] Matteo Cacciari, Gavin P. Salam, and Gregory Soyez,  
 3991 *The anti- $k_t$  jet clustering algorithm*, JHEP **04** (2008) 063,  
 3992 arXiv: 0802.1189 [hep-ph] (cit. on p. 53).
- 3993 [77] Matteo Cacciari, Gavin P. Salam, and Gregory Soyez, *FastJet user manual*,  
 3994 Eur. Phys. J. C **72** (2012) 1896, arXiv: 1111.6097 [hep-ph] (cit. on p. 53).
- 3995 [78] ATLAS Collaboration,  
 3996 *Jet reconstruction and performance using particle flow with the ATLAS Detector*,  
 3997 Eur. Phys. J. C **77** (2017) 466, arXiv: 1703.10485 [hep-ex] (cit. on p. 53).
- 3998 [79] ATLAS Collaboration, *Jet energy scale and resolution measured in proton-proton*  
 3999 *collisions at  $\sqrt{s} = 13\text{ TeV}$  with the ATLAS detector*, Eur. Phys. J. C **81** (2020) 689,  
 4000 arXiv: 2007.02645 [hep-ex] (cit. on p. 53).
- 4001 [80] ATLAS Collaboration,  
 4002 *ATLAS flavour-tagging algorithms for the LHC Run 2  $pp$  collision dataset*, (2022),  
 4003 arXiv: 2211.16345 [physics.data-an] (cit. on p. 53).
- 4004 [81] ATLAS Collaboration, *ATLAS b-jet identification performance and efficiency*  
 4005 *measurement with  $t\bar{t}$  events in  $pp$  collisions at  $\sqrt{s} = 13\text{ TeV}$* ,  
 4006 Eur. Phys. J. C **79** (2019) 970, arXiv: 1907.05120 [hep-ex] (cit. on p. 53).
- 4007 [82] ATLAS Collaboration, *Electron and photon performance measurements with the*  
 4008 *ATLAS detector using the 2015–2017 LHC proton-proton collision data*,  
 4009 JINST **14** (2019) P12006, arXiv: 1908.00005 [hep-ex] (cit. on p. 53).

- 4010 [83] ATLAS Collaboration, *Electron and photon reconstruction and performance in*  
 4011 *ATLAS using a dynamical, topological cell clustering-based approach*,  
 4012 ATL-PHYS-PUB-2017-022, 2017, URL: <https://cds.cern.ch/record/2298955>  
 4013 (cit. on p. 53).
- 4014 [84] ATLAS Collaboration, *Muon reconstruction performance of the ATLAS detector in*  
 4015 *proton–proton collision data at  $\sqrt{s} = 13 \text{ TeV}$* , Eur. Phys. J. C **76** (2016) 292,  
 4016 arXiv: 1603.05598 [hep-ex] (cit. on p. 53).
- 4017 [85] ATLAS Collaboration,  
 4018 *Reconstruction, Energy Calibration, and Identification of Hadronically Decaying Tau*  
 4019 *Leptons in the ATLAS Experiment for Run-2 of the LHC*,  
 4020 ATL-PHYS-PUB-2015-045, 2015, URL: <https://cds.cern.ch/record/2064383>  
 4021 (cit. on p. 54).
- 4022 [86] ATLAS Collaboration,  
 4023 *Measurement of the tau lepton reconstruction and identification performance in the*  
 4024 *ATLAS experiment using pp collisions at  $\sqrt{s} = 13 \text{ TeV}$* , ATLAS-CONF-2017-029,  
 4025 2017, URL: <https://cds.cern.ch/record/2261772> (cit. on p. 54).
- 4026 [87] ATLAS Collaboration, *Local Hadronic Calibration*, ATL-LARG-PUB-2009-001-2,  
 4027 ATL-COM-LARG-2008-006, ATL-LARG-PUB-2009-001, 2008,  
 4028 URL: <https://cds.cern.ch/record/1112035> (cit. on p. 54).
- 4029 [88] ATLAS Collaboration, *Performance of missing transverse momentum reconstruction*  
 4030 *with the ATLAS detector using proton–proton collisions at  $\sqrt{s} = 13 \text{ TeV}$* ,  
 4031 Eur. Phys. J. C **78** (2018) 903, arXiv: 1802.08168 [hep-ex] (cit. on p. 54).
- 4032 [89] ATLAS Collaboration,  
 4033 *Object-based missing transverse momentum significance in the ATLAS Detector*,  
 4034 ATLAS-CONF-2018-038, 2018, URL: <https://cds.cern.ch/record/2630948>  
 4035 (cit. on p. 56).

- 4036 [90] ATLAS Collaboration, *The ATLAS Tau Trigger in Run 2*, ATLAS-CONF-2017-061,  
 4037 2017, URL: <https://cds.cern.ch/record/2274201> (cit. on p. 61).
- 4038 [91] ATLAS Collaboration, *Search for dark matter produced in association with a single*  
 4039 *top quark in  $\sqrt{s} = 13 \text{ TeV}$  pp collisions with the ATLAS detector*,  
 4040 Eur. Phys. J. C **81** (2020) 860, arXiv: 2011.09308 [hep-ex] (cit. on pp. 62, 79, 81).
- 4041 [92] ATLAS Collaboration,  
 4042 *Search for invisible Higgs-boson decays in events with vector-boson fusion signatures*  
 4043 *using  $139 \text{ fb}^{-1}$  of proton–proton data recorded by the ATLAS experiment*,  
 4044 JHEP **08** (2022) 104, arXiv: 2202.07953 [hep-ex] (cit. on p. 65).
- 4045 [93] ATLAS Collaboration,  
 4046 *Observation of electroweak production of two jets in association with an isolated*  
 4047 *photon and missing transverse momentum, and search for a Higgs boson decaying*  
 4048 *into invisible particles at 13 TeV with the ATLAS detector*,  
 4049 Eur. Phys. J. C **82** (2021) 105, arXiv: 2109.00925 [hep-ex] (cit. on p. 65).
- 4050 [94] ATLAS Collaboration, *Constraints on spin-0 dark matter mediators and invisible*  
 4051 *Higgs decays using ATLAS 13 TeV pp collision data with two top quarks and missing*  
 4052 *transverse momentum in the final state*, (2022), arXiv: 2211.05426 [hep-ex]  
 4053 (cit. on p. 65).
- 4054 [95] ATLAS Collaboration, *Constraints on new phenomena via Higgs boson couplings*  
 4055 *and invisible decays with the ATLAS detector*, JHEP **11** (2015) 206,  
 4056 arXiv: 1509.00672 [hep-ex] (cit. on p. 65).
- 4057 [96] ATLAS Collaboration,  
 4058 *Improvements in  $t\bar{t}$  modelling using NLO+PS Monte Carlo generators for Run 2*,  
 4059 ATL-PHYS-PUB-2018-009, 2018, URL: <https://cds.cern.ch/record/2630327>  
 4060 (cit. on p. 68).

- 4061 [97] ATLAS Collaboration,  
 4062 *Measurements of top-quark pair single- and double-differential cross-sections in the*  
 4063 *all-hadronic channel in pp collisions at  $\sqrt{s} = 13$  TeV using the ATLAS detector,*  
 4064 JHEP **01** (2021) 033, arXiv: 2006.09274 [hep-ex] (cit. on p. 68).
- 4065 [98] Pierre Baldi, Kyle Cranmer, Taylor Faustett, Peter Sadowski, and Daniel Whiteson,  
 4066 *Parameterized neural networks for high-energy physics,*  
 4067 Eur. Phys. J. C **76** (2016) 235, arXiv: 1601.07913 [hep-ex] (cit. on p. 69).
- 4068 [99] ATLAS Collaboration, *Luminosity determination in pp collisions at  $\sqrt{s} = 13$  TeV*  
 4069 *using the ATLAS detector at the LHC*, ATLAS-CONF-2019-021, 2019,  
 4070 URL: <https://cds.cern.ch/record/2677054> (cit. on p. 71).
- 4071 [100] Jon Butterworth et al., *PDF4LHC recommendations for LHC Run II*,  
 4072 J. Phys. G **43** (2016) 023001, arXiv: 1510.03865 [hep-ph] (cit. on p. 71).
- 4073 [101] Glen Cowan, Kyle Cranmer, Eilam Gross, and Ofer Vitells,  
 4074 *Asymptotic formulae for likelihood-based tests of new physics*,  
 4075 Eur. Phys. J. C **71** (2011) 1554, arXiv: 1007.1727 [physics.data-an]  
 4076 (cit. on pp. 72, 73), Erratum: Eur. Phys. J. C **73** (2013) 2501.
- 4077 [102] Alexander L. Read, *Presentation of search results: the  $CL_S$  technique*,  
 4078 J. Phys. G **28** (2002) 2693 (cit. on p. 73).
- 4079 [103] Abdelhak Djouadi, Manuel Drees, and Jean-Loic Kneur,  
 4080 *Neutralino dark matter in mSUGRA: Reopening the light Higgs pole window*,  
 4081 Phys. Lett. B **624** (2005) 60, arXiv: hep-ph/0504090 [hep-ph] (cit. on p. 86).
- 4082 [104] E. A. Bagnaschi et al., *Supersymmetric dark matter after LHC Run 1*,  
 4083 Eur. Phys. J. C **75** (2015) 500, arXiv: 1508.01173 [hep-ph] (cit. on p. 86).
- 4084 [105] Federico Ambrogi et al.,  
 4085 *MadDM v.3.0: a Comprehensive Tool for Dark Matter Studies*,  
 4086 Phys. Dark Univ. **24** (2019) 100249, arXiv: 1804.00044 [hep-ph]  
 4087 (cit. on pp. 87, 89).

- 4088 [106] The ATLAS Collaboration,  
 4089     *Software Performance of the ATLAS Track Reconstruction for LHC Run 3*,  
 4090     Computing and Software for Big Science **8** (2024), ISSN: 2510-2044,  
 4091     URL: <http://dx.doi.org/10.1007/s41781-023-00111-y> (cit. on p. 94).
- 4092 [107] The ATLAS collaboration, *Expected tracking performance of the ATLAS Inner*  
 4093     *Tracker at the High-Luminosity LHC*, Journal of Instrumentation **20** (2025) P02018,  
 4094     URL: <https://dx.doi.org/10.1088/1748-0221/20/02/P02018>  
 4095     (cit. on pp. 97, 99, 100, 102, 112, 114, 188–190, 193, 194).
- 4096 [108] ATLAS Collaboration,  
 4097     *ATLAS Inner Tracker Strip Detector: Technical Design Report*,  
 4098     ATLAS-TDR-025; CERN-LHCC-2017-005, 2017,  
 4099     URL: <https://cds.cern.ch/record/2257755> (cit. on pp. 97, 100, 101, 112).
- 4100 [109] ATLAS Collaboration,  
 4101     *ATLAS Inner Tracker Pixel Detector: Technical Design Report*,  
 4102     ATLAS-TDR-030; CERN-LHCC-2017-021, 2017,  
 4103     URL: <https://cds.cern.ch/record/2285585> (cit. on pp. 97, 103, 104).
- 4104 [110] Gert Moliere, *Theorie der Streuung schneller geladener. Teichen I. Einzelstreuung*  
 4105     *am abgeschirmten Coulomb-Feld.* Z. Zeitsch. f. Naturforsch. **2a** (2014) 133  
 4106     (cit. on p. 111).
- 4107 [111] G. Moliere, *Theory of the scattering of fast charged particles. 2. Repeated and*  
 4108     *multiple scattering*, Z. Naturforsch. A **3** (1948) 78 (cit. on p. 111).
- 4109 [112] H. A. Bethe, *Molière's Theory of Multiple Scattering*, Phys. Rev. **89** (6 1953) 1256,  
 4110     URL: <https://link.aps.org/doi/10.1103/PhysRev.89.1256> (cit. on p. 111).
- 4111 [113] William T. Scott,  
 4112     *The Theory of Small-Angle Multiple Scattering of Fast Charged Particles*,  
 4113     Rev. Mod. Phys. **35** (2 1963) 231,  
 4114     URL: <https://link.aps.org/doi/10.1103/RevModPhys.35.231> (cit. on p. 111).

- <sup>4115</sup> [114] Bruno Rossi and Kenneth Greisen, *Cosmic-Ray Theory*,  
<sup>4116</sup> Reviews of Modern Physics **13** (1941) 240 (cit. on p. 111).
- <sup>4117</sup> [115] Virgil L. Highland, *Some practical remarks on multiple scattering*,  
<sup>4118</sup> Nuclear Instruments and Methods **129** (1975) 497 (cit. on p. 111).
- <sup>4119</sup> [116] Gerald R. Lynch and Orin I. Dahl, *Approximations to multiple Coulomb scattering*,  
<sup>4120</sup> Nuclear Instruments and Methods in Physics Research Section B: Beam Interactions  
<sup>4121</sup> with Materials and Atoms **58** (1991) 6 (cit. on p. 111).
- <sup>4122</sup> [117] Stefano Frixione and Bryan R. Webber,  
<sup>4123</sup> *Matching NLO QCD computations and parton shower simulations*,  
<sup>4124</sup> JHEP **06** (2002) 029, arXiv: hep-ph/0204244 (cit. on p. 114).
- <sup>4125</sup> [118] Stefano Frixione, Paolo Nason, and Carlo Oleari, *Matching NLO QCD computations*  
<sup>4126</sup> *with parton shower simulations: the POWHEG method*, JHEP **11** (2007) 070,  
<sup>4127</sup> arXiv: 0709.2092 [hep-ph] (cit. on p. 114).
- <sup>4128</sup> [119] Paolo Nason,  
<sup>4129</sup> *A new method for combining NLO QCD with shower Monte Carlo algorithms*,  
<sup>4130</sup> JHEP **11** (2004) 040, arXiv: hep-ph/0409146 (cit. on p. 114).
- <sup>4131</sup> [120] Simone Alioli, Paolo Nason, Carlo Oleari, and Emanuele Re,  
<sup>4132</sup> *A general framework for implementing NLO calculations in shower Monte Carlo*  
<sup>4133</sup> *programs: the POWHEG BOX*, JHEP **06** (2010) 043, arXiv: 1002.2581 [hep-ph]  
<sup>4134</sup> (cit. on p. 114).
- <sup>4135</sup> [121] ATLAS Collaboration, *Studies on top-quark Monte Carlo modelling for Top2016*,  
<sup>4136</sup> ATL-PHYS-PUB-2016-020, 2016, URL: <https://cds.cern.ch/record/2216168>  
<sup>4137</sup> (cit. on p. 114).
- <sup>4138</sup> [122] NNPDF Collaboration, Richard D. Ball, et al., *Parton distributions with LHC data*,  
<sup>4139</sup> Nucl. Phys. B **867** (2013) 244, arXiv: 1207.1303 [hep-ph] (cit. on p. 114).

- <sup>4140</sup> [123] D. J. Lange, *The EvtGen particle decay simulation package*,  
<sup>4141</sup> Nucl. Instrum. Meth. A **462** (2001) 152 (cit. on p. 114).
- <sup>4142</sup> [124] Paul Gessinger-Befurt, *Development and improvement of track reconstruction*  
<sup>4143</sup> *software and search for disappearing tracks with the ATLAS experiment*,  
<sup>4144</sup> Doctoral Dissertation: Johannes Gutenberg-Universität Mainz, 2021  
<sup>4145</sup> (cit. on pp. 116–118).
- <sup>4146</sup> [125] Azriel Rosenfeld and John L. Pfaltz,  
<sup>4147</sup> *Sequential Operations in Digital Picture Processing*, J. ACM **13** (1966) 471,  
<sup>4148</sup> ISSN: 0004-5411, URL: <https://doi.org/10.1145/321356.321357> (cit. on p. 116).
- <sup>4149</sup> [126] The ATLAS collaboration,  
<sup>4150</sup> *A neural network clustering algorithm for the ATLAS silicon pixel detector*,  
<sup>4151</sup> Journal of Instrumentation **9** (2014) P09009,  
<sup>4152</sup> URL: <https://dx.doi.org/10.1088/1748-0221/9/09/P09009> (cit. on p. 116).
- <sup>4153</sup> [127] R. L. Plackett, *A Historical Note on the Method of Least Squares*,  
<sup>4154</sup> Biometrika **36** (1949) 458, ISSN: 00063444, 14643510,  
<sup>4155</sup> URL: <http://www.jstor.org/stable/2332682> (visited on 05/22/2025)  
<sup>4156</sup> (cit. on p. 122).
- <sup>4157</sup> [128] M Regler, R Fruhwirth, R K Bock, H Grote, and D Notz,  
<sup>4158</sup> *Cambridge monographs on particle physics, nuclear physics and cosmology: Data*  
<sup>4159</sup> *analysis techniques for high-energy physics series number 11*, en, 2nd ed.,  
<sup>4160</sup> Cambridge monographs on particle physics, nuclear physics and cosmology,  
<sup>4161</sup> Cambridge, England: Cambridge University Press, 2000 (cit. on p. 123).
- <sup>4162</sup> [129] R Mankel,  
<sup>4163</sup> *Pattern recognition and event reconstruction in particle physics experiments*,  
<sup>4164</sup> Reports on Progress in Physics **67** (2004) 553, ISSN: 1361-6633,  
<sup>4165</sup> URL: <https://dx.doi.org/10.1088/0034-4885/67/4/R03> (cit. on p. 123).

- 4166 [130] Pierre Billoir, *Track fitting with multiple scattering: A new method*,  
 4167 Nuclear Instruments and Methods in Physics Research **225** (1984) 352,  
 4168 ISSN: 0167-5087, URL:  
 4169 <https://www.sciencedirect.com/science/article/pii/0167508784902746>  
 4170 (cit. on p. 123).
- 4171 [131] R. Frühwirth, *Application of Kalman filtering to track and vertex fitting*,  
 4172 Nuclear Instruments and Methods in Physics Research Section A: Accelerators,  
 4173 Spectrometers, Detectors and Associated Equipment **262** (1987) 444,  
 4174 ISSN: 0168-9002, URL:  
 4175 <https://www.sciencedirect.com/science/article/pii/0168900287908874>  
 4176 (cit. on p. 123).
- 4177 [132] The ATLAS Collaboration, *ATLAS HL-LHC Computing Conceptual Design Report*,  
 4178 tech. rep., CERN, 2020, URL: <https://cds.cern.ch/record/2729668>  
 4179 (cit. on p. 127).
- 4180 [133] ATLAS Collaboration, *Fast Track Reconstruction for HL-LHC*,  
 4181 ATL-PHYS-PUB-2019-041, 2019, URL: <https://cds.cern.ch/record/2693670>  
 4182 (cit. on pp. 128, 129).
- 4183 [134] The ATLAS Collaboration, *ATLAS Software and Computing HL-LHC Roadmap*,  
 4184 tech. rep., CERN, 2022, URL: <https://cds.cern.ch/record/2802918>  
 4185 (cit. on p. 128).
- 4186 [135] The ATLAS Collaboration,  
 4187 *AtlFast3: The Next Generation of Fast Simulation in ATLAS*,  
 4188 Computing and Software for Big Science **6** (2022), ISSN: 2510-2044,  
 4189 URL: <http://dx.doi.org/10.1007/s41781-021-00079-7> (cit. on p. 128).
- 4190 [136] The ATLAS Collaboration,  
 4191 *Jet reconstruction and performance using particle flow with the ATLAS Detector*,

- 4192        The European Physical Journal C **77** (2017) 466,  
4193        URL: <https://doi.org/10.1140/epjc/s10052-017-5031-2> (cit. on p. 128).
- 4194 [137] Arnaud Duperrin,  
4195        *Flavour tagging with graph neural networks with the ATLAS detector*, tech. rep.,  
4196        6 pages, 2 figures, 1 table, Presented at DIS2023: XXX International Workshop on  
4197        Deep-Inelastic Scattering and Related Subjects, Michigan State University, USA,  
4198        27-31 March 2023: CERN, 2023, arXiv: 2306.04415,  
4199        URL: <https://cds.cern.ch/record/2860610> (cit. on p. 129).
- 4200 [138] Andreas Salzburger et al., *acts-project/acts: v41.0.0*, version v41.0.0, 2025,  
4201        URL: <https://doi.org/10.5281/zenodo.15260074> (cit. on pp. 129, 221).
- 4202 [139] Steven Farrell et al., *Novel deep learning methods for track reconstruction*, 2018,  
4203        arXiv: 1810.06111 [hep-ex], URL: <https://arxiv.org/abs/1810.06111>  
4204        (cit. on p. 130).
- 4205 [140] Anaderi et al., *TrackML Particle Tracking Challenge*,  
4206        <https://kaggle.com/competitions/trackml-particle-identification>,  
4207        Kaggle, 2018 (cit. on pp. 130, 159).
- 4208 [141] Xiangyang Ju et al.,  
4209        *Performance of a geometric deep learning pipeline for HL-LHC particle tracking*,  
4210        The European Physical Journal C **81** (2021) 876,  
4211        URL: <https://doi.org/10.1140/epjc/s10052-021-09675-8>  
4212        (cit. on pp. 130, 159, 162, 209).
- 4213 [142] Nicholas Choma et al.,  
4214        *Track Seeding and Labelling with Embedded-space Graph Neural Networks*, 2020,  
4215        arXiv: 2007.00149 [physics.ins-det],  
4216        URL: <https://arxiv.org/abs/2007.00149> (cit. on p. 130).

- 4217 [143] Sylvain Caillou et al., *ATLAS ITk Track Reconstruction with a GNN-based pipeline*,  
 4218 tech. rep., CERN, 2022, URL: <https://cds.cern.ch/record/2815578>  
 4219 (cit. on p. 130).
- 4220 [144] ATLAS Collaboration, *Athena*, version 21.0.127, 2021,  
 4221 URL: <https://doi.org/10.5281/zenodo.4772550> (cit. on pp. 131, 166, 188, 221).
- 4222 [145] Di Feng, Ali Harakeh, Steven L. Waslander, and Klaus Dietmayer, *A Review and*  
 4223 *Comparative Study on Probabilistic Object Detection in Autonomous Driving*,  
 4224 IEEE Transactions on Intelligent Transportation Systems **23** (2022) 9961,  
 4225 ISSN: 1558-0016, URL: <http://dx.doi.org/10.1109/TITS.2021.3096854>  
 4226 (cit. on p. 131).
- 4227 [146] Benyamin Ghojogh, Ali Ghodsi, Fakhri Karray, and Mark Crowley,  
 4228 *Spectral, Probabilistic, and Deep Metric Learning: Tutorial and Survey*, 2022,  
 4229 arXiv: 2201.09267 [stat.ML], URL: <https://arxiv.org/abs/2201.09267>  
 4230 (cit. on p. 140).
- 4231 [147] Mahmut KAYA and Hasan Şakir BİLGE, *Deep Metric Learning: A Survey*,  
 4232 Symmetry **11** (2019), ISSN: 2073-8994,  
 4233 URL: <https://www.mdpi.com/2073-8994/11/9/1066> (cit. on pp. 140–142).
- 4234 [148] Brian Kulis, 2013 (cit. on p. 140).
- 4235 [149] R. L. Vasilev and A. G. D'yakonov,  
 4236 *Deep Metric Learning: Loss Functions Comparison*,  
 4237 Doklady Mathematics **108** (2023) S215,  
 4238 URL: <https://doi.org/10.1134/S1064562423701053> (cit. on p. 142).
- 4239 [150] Joshua Robinson, Ching-Yao Chuang, Suvrit Sra, and Stefanie Jegelka,  
 4240 *Contrastive Learning with Hard Negative Samples*, 2021,  
 4241 arXiv: 2010.04592 [cs.LG], URL: <https://arxiv.org/abs/2010.04592>  
 4242 (cit. on p. 142).

- 4243 [151] Thomas N. Kipf and Max Welling,  
 4244 *Semi-Supervised Classification with Graph Convolutional Networks*, 2017,  
 4245 arXiv: 1609.02907 [cs.LG], URL: <https://arxiv.org/abs/1609.02907>  
 4246 (cit. on p. 149).
- 4247 [152] Petar Veličković et al., *Graph Attention Networks*, 2018,  
 4248 arXiv: 1710.10903 [stat.ML], URL: <https://arxiv.org/abs/1710.10903>  
 4249 (cit. on p. 149).
- 4250 [153] William L. Hamilton, Rex Ying, and Jure Leskovec,  
 4251 *Inductive Representation Learning on Large Graphs*, 2018,  
 4252 arXiv: 1706.02216 [cs.SI], URL: <https://arxiv.org/abs/1706.02216>  
 4253 (cit. on pp. 149–153).
- 4254 [154] Keyulu Xu, Weihua Hu, Jure Leskovec, and Stefanie Jegelka,  
 4255 *How Powerful are Graph Neural Networks?*, 2019, arXiv: 1810.00826 [cs.LG],  
 4256 URL: <https://arxiv.org/abs/1810.00826> (cit. on p. 149).
- 4257 [155] Abien Fred Agarap, *Deep Learning using Rectified Linear Units (ReLU)*, 2019,  
 4258 arXiv: 1803.08375 [cs.NE], URL: <https://arxiv.org/abs/1803.08375>  
 4259 (cit. on p. 156).
- 4260 [156] Peter W. Battaglia, Razvan Pascanu, Matthew Lai, Danilo Rezende, and  
 4261 Koray Kavukcuoglu,  
 4262 *Interaction Networks for Learning about Objects, Relations and Physics*, 2016,  
 4263 arXiv: 1612.00222 [cs.AI], URL: <https://arxiv.org/abs/1612.00222>  
 4264 (cit. on pp. 159, 161, 162).
- 4265 [157] Caillou, Sylvain et al.,  
 4266 *Physics Performance of the ATLAS GNN4ITk Track Reconstruction Chain*,  
 4267 EPJ Web of Conf. **295** (2024) 03030,  
 4268 URL: <https://doi.org/10.1051/epjconf/202429503030> (cit. on pp. 164, 209).

- 4269 [158] Aric A. Hagberg, Daniel A. Schult, and Pieter J. Swart,  
 4270 “Exploring Network Structure, Dynamics, and Function using NetworkX”,  
 4271 *Proceedings of the 7th Python in Science Conference*,  
 4272 ed. by Gaël Varoquaux, Travis Vaught, and Jarrod Millman,  
 4273 Pasadena, CA USA, 2008 11 (cit. on p. 176).
- 4274 [159] P F Åkesson et al., *ATLAS Tracking Event Data Model*, tech. rep.,  
 4275 All figures including auxiliary figures are available at  
 4276 <https://atlas.web.cern.ch/Atlas/GROUPS/PHYSICS/PUBNOTES/ATL-SOFT-PUB-2006-004>: CERN, 2006, URL: <https://cds.cern.ch/record/973401>  
 4277 (cit. on p. 183).
- 4279 [160] T G Cornelissen et al.,  
 4280 *Updates of the ATLAS Tracking Event Data Model (Release 13)*, tech. rep.,  
 4281 All figures including auxiliary figures are available at  
 4282 <https://atlas.web.cern.ch/Atlas/GROUPS/PHYSICS/PUBNOTES/ATL-SOFT-PUB-2007-003>: CERN, 2007, URL: <https://cds.cern.ch/record/1038095>  
 4284 (cit. on p. 184).
- 4285 [161] M. Hansroul, H. Jeremie, and D. Savard,  
 4286 *Fast circle fit with the conformal mapping method*,  
 4287 Nuclear Instruments and Methods in Physics Research Section A: Accelerators,  
 4288 Spectrometers, Detectors and Associated Equipment **270** (1988) 498,  
 4289 ISSN: 0168-9002, URL:  
 4290 <https://www.sciencedirect.com/science/article/pii/016890028890722X>  
 4291 (cit. on p. 186).
- 4292 [162] Jared Dynes Burleson et al.,  
 4293 *Physics Performance of the ATLAS GNN4ITk Track Reconstruction Chain*,  
 4294 tech. rep., CERN, 2023, URL: <https://cds.cern.ch/record/2882507>  
 4295 (cit. on p. 209).

- 4296 [163] Adam Paszke et al.,  
4297 *PyTorch: An Imperative Style, High-Performance Deep Learning Library*, 2019,  
4298 arXiv: 1912.01703 [cs.LG], URL: <https://arxiv.org/abs/1912.01703>  
4299 (cit. on p. 212).
- 4300 [164] Haoran Zhao et al., *Track reconstruction as a service for collider physics*, 2025,  
4301 arXiv: 2501.05520 [physics.ins-det],  
4302 URL: <https://arxiv.org/abs/2501.05520> (cit. on p. 215).
- 4303 [165] Ahmedur Rahman Shovon, Landon Richard Dyken, Oded Green, Thomas Gilray,  
4304 and Sidharth Kumar, “Accelerating Datalog applications with cuDF”,  
4305 *2022 IEEE/ACM Workshop on Irregular Applications: Architectures and Algorithms*  
4306 (*IA3*), 2022 41 (cit. on p. 219).
- 4307 [166] Siu Kwan Lam, Antoine Pitrou, and Stanley Seibert,  
4308 “Numba: a LLVM-based Python JIT compiler”,  
4309 *Proceedings of the Second Workshop on the LLVM Compiler Infrastructure in HPC*,  
4310 LLVM ’15, Austin, Texas: Association for Computing Machinery, 2015,  
4311 ISBN: 9781450340052, URL: <https://doi.org/10.1145/2833157.2833162>  
4312 (cit. on p. 221).